POLYPUBLIE
Polytechnique Montréal

POLYTECHNIQUE MONTRÉAL
UNIVERSITÉ D'INGÉNIERIE

Titre: Title:	Interfaces and deformation behaviour of aluminium matrix composites
Auteur: Author:	Weimin Zhong
Date:	1995
Type:	Mémoire ou thèse / Dissertation or Thesis
Référence: Citation:	Zhong, W. (1995). Interfaces and deformation behaviour of aluminium matrix composites [Thèse de doctorat, École Polytechnique de Montréal]. PolyPublie. https://publications.polymtl.ca/31609/

Document en libre accès dans PolyPublie
Open Access document in PolyPublie

URL de PolyPublie: PolyPublie URL:	https://publications.polymtl.ca/31609/
Directeurs de recherche: Advisors:	Gilles L'Espérance
Programme: Program:	Non spécifié

Ce fichier a été téléchargé à partir de PolyPublie, le dépôt institutionnel de Polytechnique Montréal
This file has been downloaded from PolyPublie, the institutional repository of Polytechnique Montréal

https://publications.polymtl.ca

UNIVERSITÉ DE MONTRÉAL

INTERFACES AND DEFORMATION BEHAVIOUR OF ALUMINIUM MATRIX COMPOSITES

ZHONG WEIMIN

DÉPARTEMENT DE MÉTALLURGIE ET DE GÉNIE DES MATÉRIAUX

ÉCOLE POLYTECHNIQUE DE MONTRÉAL

THÈSE PRÉSENTÉE EN VUE DE L'OBTENTION

DU DIPLÔME DE PHILOSOPHIAE DOCTOR (Ph.D.)

(GÉNIE MÉTALLURGIQUE)

Octobre 1995

© ZHONG Weimin, 1995

National Library of Canada
Bibliothèque nationale du Canada

Acquisitions and Bibliographic Services Branch
Direction des acquisitions et des services bibliographiques

395 Wellington Street
Ottawa, Ontario
K1A 0N4

395, rue Wellington
Ottawa (Ontario)
K1A 0N4

Your file Votre référence

Our file Notre référence

The author has granted an irrevocable non-exclusive licence allowing the National Library of Canada to reproduce, loan, distribute or sell copies of his/her thesis by any means and in any form or format, making this thesis available to interested persons.

L'auteur a accordé une licence irrévocable et non exclusive permettant à la Bibliothèque nationale du Canada de reproduire, prêter, distribuer ou vendre des copies de sa thèse de quelque manière et sous quelque forme que ce soit pour mettre des exemplaires de cette thèse à la disposition des personnes intéressées.

The author retains ownership of the copyright in his/her thesis. Neither the thesis nor substantial extracts from it may be printed or otherwise reproduced without his/her permission.

L'auteur conserve la propriété du droit d'auteur qui protège sa thèse. Ni la thèse ni des extraits substantiels de celle-ci ne doivent être imprimés ou autrement reproduits sans son autorisation.

ISBN 0-612-11473-2

Canada

Name ZHONG WEIMIN

Dissertation Abstracts International is arranged by broad, general subject categories. Please select the one subject which most nearly describes the content of your dissertation. Enter the corresponding four-digit code in the spaces provided.

Materials Science — SUBJECT TERM

0794 — SUBJECT CODE

U·M·I

Subject Categories

THE HUMANITIES AND SOCIAL SCIENCES

COMMUNICATIONS AND THE ARTS
Architecture 0729
Art History 0377
Cinema 0900
Dance 0378
Fine Arts 0357
Information Science 0723
Journalism 0391
Library Science 0399
Mass Communications 0708
Music 0413
Speech Communication 0459
Theater 0465

EDUCATION
General 0515
Administration 0514
Adult and Continuing 0516
Agricultural 0517
Art 0273
Bilingual and Multicultural 0282
Business 0688
Community College 0275
Curriculum and Instruction 0727
Early Childhood 0518
Elementary 0524
Finance 0277
Guidance and Counseling 0519
Health 0680
Higher 0745
History of 0520
Home Economics 0278
Industrial 0521
Language and Literature 0279
Mathematics 0280
Music 0522
Philosophy of 0998
Physical 0523
Psychology 0525
Reading 0535
Religious 0527
Sciences 0714
Secondary 0533
Social Sciences 0534
Sociology of 0340
Special 0529
Teacher Training 0530
Technology 0710
Tests and Measurements 0288
Vocational 0747

LANGUAGE, LITERATURE AND LINGUISTICS
Language
- General 0679
- Ancient 0289
- Linguistics 0290
- Modern 0291

Literature
- General 0401
- Classical 0294
- Comparative 0295
- Medieval 0297
- Modern 0298
- African 0316
- American 0591
- Asian 0305
- Canadian (English) 0352
- Canadian (French) 0355
- English 0593
- Germanic 0311
- Latin American 0312
- Middle Eastern 0315
- Romance 0313
- Slavic and East European 0314

PHILOSOPHY, RELIGION AND THEOLOGY
Philosophy 0422
Religion
- General 0318
- Biblical Studies 0321
- Clergy 0319
- History of 0320
- Philosophy of 0322

Theology 0469

SOCIAL SCIENCES
American Studies 0323
Anthropology
- Archaeology 0324
- Cultural 0326
- Physical 0327

Business Administration
- General 0310
- Accounting 0272
- Banking 0770
- Management 0454
- Marketing 0338

Canadian Studies 0385
Economics
- General 0501
- Agricultural 0503
- Commerce-Business 0505
- Finance 0508
- History 0509
- Labor 0510
- Theory 0511

Folklore 0358
Geography 0366
Gerontology 0351
History
- General 0578
- Ancient 0579
- Medieval 0581
- Modern 0582
- Black 0328
- African 0331
- Asia, Australia and Oceania 0332
- Canadian 0334
- European 0335
- Latin American 0336
- Middle Eastern 0333
- United States 0337

History of Science 0585
Law 0398
Political Science
- General 0615
- International Law and Relations 0616
- Public Administration 0617

Recreation 0814
Social Work 0452
Sociology
- General 0626
- Criminology and Penology 0627
- Demography 0938
- Ethnic and Racial Studies 0631
- Individual and Family Studies 0628
- Industrial and Labor Relations 0629
- Public and Social Welfare 0630
- Social Structure and Development 0700
- Theory and Methods 0344

Transportation 0709
Urban and Regional Planning 0999
Women's Studies 0453

THE SCIENCES AND ENGINEERING

BIOLOGICAL SCIENCES
Agriculture
- General 0473
- Agronomy 0285
- Animal Culture and Nutrition 0475
- Animal Pathology 0476
- Food Science and Technology 0359
- Forestry and Wildlife 0478
- Plant Culture 0479
- Plant Pathology 0480
- Plant Physiology 0817
- Range Management 0777
- Wood Technology 0746

Biology
- General 0306
- Anatomy 0287
- Biostatistics 0308
- Botany 0309
- Cell 0379
- Ecology 0329
- Entomology 0353
- Genetics 0369
- Limnology 0793
- Microbiology 0410
- Molecular 0307
- Neuroscience 0317
- Oceanography 0416
- Physiology 0433
- Radiation 0821
- Veterinary Science 0778
- Zoology 0472

Biophysics
- General 0786
- Medical 0760

EARTH SCIENCES
Biogeochemistry 0425
Geochemistry 0996
Geodesy 0370
Geology 0372
Geophysics 0373
Hydrology 0388
Mineralogy 0411
Paleobotany 0345
Paleoecology 0426
Paleontology 0418
Paleozoology 0985
Palynology 0427
Physical Geography 0368
Physical Oceanography 0415

HEALTH AND ENVIRONMENTAL SCIENCES
Environmental Sciences 0768
Health Sciences
- General 0566
- Audiology 0300
- Chemotherapy 0992
- Dentistry 0567
- Education 0350
- Hospital Management 0769
- Human Development 0758
- Immunology 0982
- Medicine and Surgery 0564
- Mental Health 0347
- Nursing 0569
- Nutrition 0570
- Obstetrics and Gynecology 0380
- Occupational Health and Therapy 0354
- Ophthalmology 0381
- Pathology 0571
- Pharmacology 0419
- Pharmacy 0572
- Physical Therapy 0382
- Public Health 0573
- Radiology 0574
- Recreation 0575
- Speech Pathology 0460
- Toxicology 0383

Home Economics 0386

PHYSICAL SCIENCES

Pure Sciences

Chemistry
- General 0485
- Agricultural 0749
- Analytical 0486
- Biochemistry 0487
- Inorganic 0488
- Nuclear 0738
- Organic 0490
- Pharmaceutical 0491
- Physical 0494
- Polymer 0495
- Radiation 0754

Mathematics 0405
Physics
- General 0605
- Acoustics 0986
- Astronomy and Astrophysics 0606
- Atmospheric Science 0608
- Atomic 0748
- Electronics and Electricity 0607
- Elementary Particles and High Energy 0798
- Fluid and Plasma 0759
- Molecular 0609
- Nuclear 0610
- Optics 0752
- Radiation 0756
- Solid State 0611

Statistics 0463

Applied Sciences

Applied Mechanics 0346
Computer Science 0984
Engineering
- General 0537
- Aerospace 0538
- Agricultural 0539
- Automotive 0540
- Biomedical 0541
- Chemical 0542
- Civil 0543
- Electronics and Electrical 0544
- Heat and Thermodynamics 0348
- Hydraulic 0545
- Industrial 0546
- Marine 0547
- Materials Science 0794
- Mechanical 0548
- Metallurgy 0743
- Mining 0551
- Nuclear 0552
- Packaging 0549
- Petroleum 0765
- Sanitary and Municipal 0554
- System Science 0790

Geotechnology 0428
Operations Research 0796
Plastics Technology 0795
Textile Technology 0994

PSYCHOLOGY
General 0621
Behavioral 0384
Clinical 0622
Developmental 0620
Experimental 0623
Industrial 0624
Personality 0625
Physiological 0989
Psychobiology 0349
Psychometrics 0632
Social 0451

Nom ZHONG Weimia

Dissertation Abstracts International est organisé en catégories de sujets. Veuillez s.v.p. choisir le sujet qui décrit le mieux votre thèse et inscrivez le code numérique approprié dans l'espace réservé ci-dessous.

Science des matériaux — SUJET

0794 — CODE DE SUJET

U·M·I

Catégories par sujets

HUMANITÉS ET SCIENCES SOCIALES

COMMUNICATIONS ET LES ARTS
Architecture 0729
Beaux-arts 0357
Bibliothéconomie 0399
Cinéma 0900
Communication verbale 0459
Communications 0708
Danse 0378
Histoire de l'art 0377
Journalisme 0391
Musique 0413
Sciences de l'information 0723
Théâtre 0465

ÉDUCATION
Généralités 515
Administration 0514
Art 0273
Collèges communautaires 0275
Commerce 0688
Économie domestique 0278
Éducation permanente 0516
Éducation préscolaire 0518
Éducation sanitaire 0680
Enseignement agricole 0517
Enseignement bilingue et multiculturel 0282
Enseignement industriel 0521
Enseignement primaire. 0524
Enseignement professionnel 0747
Enseignement religieux 0527
Enseignement secondaire 0533
Enseignement spécial 0529
Enseignement supérieur 0745
Évaluation 0288
Finances 0277
Formation des enseignants 0530
Histoire de l'éducation 0520
Langues et littérature 0279
Lecture 0535
Mathématiques 0280
Musique 0522
Orientation et consultation 0519
Philosophie de l'éducation 0998
Physique 0523
Programmes d'études et enseignement 0727
Psychologie 0525
Sciences 0714
Sciences sociales 0534
Sociologie de l'éducation 0340
Technologie 0710

LANGUE, LITTÉRATURE ET LINGUISTIQUE
Langues
- Généralités 0679
- Anciennes 0289
- Linguistique 0290
- Modernes 0291

Littérature
- Généralités 0401
- Anciennes 0294
- Comparée 0295
- Médiévale 0297
- Moderne 0298
- Africaine 0316
- Américaine 0591
- Anglaise 0593
- Asiatique 0305
- Canadienne (Anglaise) 0352
- Canadienne (Française) 0355
- Germanique 0311
- Latino-américaine 0312
- Moyen-orientale 0315
- Romane 0313
- Slave et est-européenne 0314

PHILOSOPHIE, RELIGION ET THÉOLOGIE
Philosophie 0422
Religion
- Généralités 0318
- Clergé 0319
- Études bibliques 0321
- Histoire des religions 0320
- Philosophie de la religion 0322

Théologie 0469

SCIENCES SOCIALES
Anthropologie
- Archéologie 0324
- Culturelle 0326
- Physique 0327

Droit 0398
Économie
- Généralités 0501
- Commerce-Affaires 0505
- Économie agricole 0503
- Économie du travail 0510
- Finances 0508
- Histoire 0509
- Théorie 0511

Études américaines 0323
Études canadiennes 0385
Études féministes 0453
Folklore 0358
Géographie 0366
Gérontologie 0351
Gestion des affaires
- Généralités 0310
- Administration 0454
- Banques 0770
- Comptabilité 0272
- Marketing 0338

Histoire
- Histoire générale 0578
- Ancienne 0579
- Médiévale 0581
- Moderne 0582
- Histoire des noirs 0328
- Africaine 0331
- Canadienne 0334
- États-Unis 0337
- Européenne 0335
- Moyen-orientale 0333
- Latino-américaine 0336
- Asie, Australie et Océanie 0332

Histoire des sciences 0585
Loisirs 0814
Planification urbaine et régionale 0999
Science politique
- Généralités 0615
- Administration publique 0617
- Droit et relations internationales 0616

Sociologie
- Généralités 0626
- Aide et bien-âtre social 0630
- Criminologie et établissements pénitentiaires 0627
- Démographie 0938
- Études de l' individu et de la famille 0628
- Études des relations interethniques et des relations raciales 0631
- Structure et développement social 0700
- Théorie et méthodes. 0344
- Travail et relations industrielles 0629

Transports 0709
Travail social 0452

SCIENCES ET INGÉNIERIE

SCIENCES BIOLOGIQUES
Agriculture
- Généralités 0473
- Agronomie. 0285
- Alimentation et technologie alimentaire 0359
- Culture 0479
- Élevage et alimentation 0475
- Exploitation des pâturages 0777
- Pathologie animale 0476
- Pathologie végétale 0480
- Physiologie végétale 0817
- Sylviculture et faune 0478
- Technologie du bois 0746

Biologie
- Généralités 0306
- Anatomie 0287
- Biologie (Statistiques) 0308
- Biologie moléculaire 0307
- Botanique 0309
- Cellule 0379
- Écologie 0329
- Entomologie 0353
- Génétique 0369
- Limnologie 0793
- Microbiologie 0410
- Neurologie 0317
- Océanographie 0416
- Physiologie 0433
- Radiation 0821
- Science vétérinaire 0778
- Zoologie 0472

Biophysique
- Généralités 0786
- Medicale 0760

SCIENCES DE LA TERRE
Biogéochimie 0425
Géochimie 0996
Géodésie 0370
Géographie physique 0368
Géologie 0372
Géophysique 0373
Hydrologie 0388
Minéralogie 0411
Océanographie physique 0415
Paléobotanique 0345
Paléoécologie 0426
Paléontologie 0418
Paléozoologie 0985
Palynologie 0427

SCIENCES DE LA SANTÉ ET DE L'ENVIRONNEMENT
Économie domestique 0386
Sciences de l'environnement 0768
Sciences de la santé
- Généralités 0566
- Administration des hôpitaux 0769
- Alimentation et nutrition 0570
- Audiologie 0300
- Chimiothérapie 0992
- Dentisterie 0567
- Développement humain 0758
- Enseignement 0350
- Immunologie 0982
- Loisirs 0575
- Médecine du travail et thérapie 0354
- Médecine et chirurgie 0564
- Obstétrique et gynécologie 0380
- Ophtalmologie 0381
- Orthophonie 0460
- Pathologie 0571
- Pharmacie 0572
- Pharmacologie 0419
- Physiothérapie 0382
- Radiologie 0574
- Santé mentale 0347
- Santé publique 0573
- Soins infirmiers 0569
- Toxicologie 0383

SCIENCES PHYSIQUES
Sciences Pures

Chimie
- Généralités 0485
- Biochimie 487
- Chimie agricole 0749
- Chimie analytique 0486
- Chimie minérale 0488
- Chimie nucléaire 0738
- Chimie organique 0490
- Chimie pharmaceutique 0491
- Physique 0494
- PolymÈres 0495
- Radiation 0754

Mathématiques 0405
Physique
- Généralités 0605
- Acoustique 0986
- Astronomie et astrophysique 0606
- Électronique et électricité 0607
- Fluides et plasma 0759
- Météorologie 0608
- Optique 0752
- Particules (Physique nucléaire) 0798
- Physique atomique 0748
- Physique de l'état solide 0611
- Physique moléculaire 0609
- Physique nucléaire 0610
- Radiation 0756

Statistiques 0463

Sciences Appliqués Et Technologie

Informatique 0984
Ingénierie
- Généralités 0537
- Agricole 0539
- Automobile 0540
- Biomédicale 0541
- Chaleur et ther modynamique 0348
- Conditionnement (Emballage) 0549
- Génie aérospatial 0538
- Génie chimique 0542
- Génie civil 0543
- Génie électronique et électrique 0544
- Génie industriel 0546
- Génie mécanique 0548
- Génie nucléaire 0552
- Ingénierie des systèmes 0790
- Mécanique navale 0547
- Métallurgie 0743
- Science des matériaux 0794
- Technique du pétrole 0765
- Technique minière 0551
- Techniques sanitaires et municipales 0554
- Technologie hydraulique 0545

Mécanique appliquée 0346
Géotechnologie 0428
Matières plastiques (Technologie) 0795
Recherche opérationnelle 0796
Textiles et tissus (Technologie) 0794

PSYCHOLOGIE
Généralités 0621
Personnalité 0625
Psychobiologie 0349
Psychologie clinique 0622
Psychologie du comportement 0384
Psychologie du développement 0620
Psychologie expérimentale 0623
Psychologie industrielle 0624
Psychologie physiologique 0989
Psychologie sociale 0451
Psychométrie 0632

UNIVERSITÉ DE MONTRÉAL

ÉCOLE POLYTECHNIQUE DE MONTRÉAL

Cette thèse intitulée:

INTERFACES AND DEFORMATION BEHAVIOUR OF

ALUMINIUM MATRIX COMPOSITES

présentée par: ZHONG Weimin

en vue de l'obtention du diplôme de: Philosophiae Doctor

a été dûment acceptée par le jury d'examen constitué de:

M. AJERSCH Frank, Ph.D., président

M. L'ESPERANCE Gilles, Ph.D., membre et directeur de recherche

M. SUÉRY Michel, Ph.D., membre et co-directeur de recherche

M. BAÏLON Jean-Paul, Ph.D., membre

M. MASOUNAVE, Jacques, Ph.D., Membre

To my wife Hong Wang

and my son Michael

ACKNOWLEDGMENTS

First of all, I would like to give my special thanks to Professor G. L'Espérance who gave me an opportunity to do my Ph.D. in Ecole Polytechnique and has supported and guided me through all my Ph.D. studies. He is by all means a great open-minded professor. He always encourages me to go ahead with my ideas and to be the best. He always show me the right directions in my research. I have learned from him not only the knowledge but also the way of thinking as a scientist. I really enjoy working with him and I especially enjoy discussing our research with him.

I would also like to thank Prof. M. Suéry and his group members such as E. Goiffon, J.J. Blandin, L. Salvo and L. Nguyen in Génie Physique et Mécanique des Matériaux, GPM^2, Institut National Polytechnique de Grenoble, France. Prof. Suéry is also a marvellous professor who gave me help when I need it. His valuable comments contributed substantially to the final form of this thesis.

At the same time, I would like to thank all the professors, technicians and colleagues in our department, especially, those in CM^2. I would like to thank Elise Campeau, Rene Veillette, Josee Laviolette, Jacques Desrocher, Z. Tong, P. Wu. E. Baril, E. Boutin and C. Blais. I also want to thank Karen Adams for correcting my English.

I gratefully acknowledge NATO International Scientific Exchange Programmes for financially supporting this project (Grant no. CRG 900950).

Finally, I would like to thank my wife Hong, who has given me the love and all the support I need through these years, and has devoted all herself taking care of the family and letting me concentrate on my researches.

To my beloved wife, my parents, as well as my son Michael.

Weimin Zhong

October, 1995

RÉSUMÉ

Dans cette thèse, la nature physique et chimique des interfaces entre les particules de renforcement et la matrice d'aluminium est étudiée. Le mode de déformation et de rupture du composite est présenté à différentes températures comme la température ambiante, 350°C et 550°C.

Dans le chapitre 2, les mécanismes de réactions aux interfaces entre les différentes particules comme le SiC tel que reçu, SiC oxydé ou Al_2O_3 et la matrice d'aluminium 5083 sont discutés abondamment dans les sections 2.1, 2.2, 2.3. Les facteurs thermodynamiques et cinétiques sont considérés. On étudie le rôle protecteur de la couche de SiO_2 et la formation de nouvelles couches polycristallines MgO ou $MgAl_2O_4$ à la surface des particules. Les composites ont été fabriqués par la méthode de compocasting; certains d'entre eux ont été refondus à 800°C pour différents temps. Les techniques suivantes ont été utilisées pour caractériser les produits de réaction aux interfaces, la microscopie électronique à balayage (MEB), la microscopie électronique en transmission (MET), la spectrométrie des rayons X par dispersion d'énergie (EDS) et la spectrométrie des pertes d'énergie des électrons transmis (PEELS). Dans la section 2.4, la ségrégation du Mg et du Cu aux interfaces est déterminée par une technique de déconvolution qui améliore la résolution spatiale de l'analyse rayons X sans augmenter l'erreur statistique. La ségrégation du Mg et du Cu aux interfaces entre les whiskers et la matrice d'un alliage d'aluminium 2124 a été observée. Tel que discuté dans la section

2.5, les contraintes résiduelles dans une matrice d'aluminium ont été déterminées en utilisant la technique de diffraction du faisceau d'électrons convergent (DFEC) avec le microscope électronique en transmission. Cette technique nous permet de déterminer la contrainte résiduelle et l'état de contrainte dans une région aussi petite que 50 nm.

Dans le chapitre 3, on présente la recristallisation du composite lors de l'extrusion à haute température et le comportement de celui-ci lors de la déformation à des températures telles que la température ambiante, 350°C et 550°C. On discute des mécanismes de renforcement et de rupture pour différents composites à plusieurs températures et ensuite, on les relie à la nature des interfaces du composite avec les différentes particules de renforcement. Les mécanismes de déformation et de rupture de l'alliage d'aluminium monolithique 5083 et du composite tel que coulé sont comparés aux composites extrudés. Dans la section 3.1, on discute de la restauration dynamique de l'alliage d'aluminium monolithique 5083 et la recristallisation dynamique des différents composites lors de l'extrusion. Les mécanismes de renforcement des composites déformés à différentes températures sont présentés dans la section 3.2. La section 3.3 présente les photographies des faciès de rupture et les mécanismes de rupture des composites tels que coulés et extrudés et aussi pour l'alliage d'aluminium monolithique. Finalement, l'effet Portevin-Le Chatelier observé lors des essais de traction des composites et de l'alliage 5083 est présenté.

Les contributions majeures de cette thèse sont les suivantes. Premièrement, les résultats de l'étude de la nature des interfaces entre les particules de renforcement et les matrices d'aluminium. Généralement, l'attaque des particules de SiC par l'aluminium liquide lors de la fabrication n'est pas observé. Cependant, une réaction s'est produite à l'interface entre la couche de SiO_2 à la surface des particules et le Mg dans la matrice. La réaction est très lente entre les particules de Al_2O_3 et le Mg d'une matrice d'aluminium 5083. La conséquence de la réaction à l'interface est la formation d'une couche de petits cristaux de MgO d'une taille d'environ 5-20 nm (aussi $MgAl_2O_4$) à la surface des particules. L'épaisseur de la zone de réaction est environ 30-50 nm pour les particules de SiC tel que reçu, 50-80 nm pour Al_2O_3p et environ 100-200 nm pour les SiCp oxydés artificiellement (avec 3.04% poids de SiO_2). Puisque la réaction d'interface consomme du Mg, il est évident que le niveau de Mg dans la matrice variera en fonction du type de renforcement et de l'épaisseur de la zone de réaction. Il a été montré qu'il y a une ségrégation du Mg ou du Cu aux interfaces et des contraintes résiduelles importantes dans la matrice proche des particules de renforcement. Les différentes natures des interfaces dans les différents composites peuvent causer une différence dans le mode de déformation et de rupture de ces composites.

Deuxièmement, les résultats pour l'étude du mode de déformation et de rupture des composites. Lors de l'extrusion, on peut remarquer qu'il y a de la recristallisation dynamique due à la grande quantité de particules de renforcement dans la matrice. Donc, la microstructure après extrusion est modifiée et il y a apparition de petits grains (5 μm)

dans la matrice. La UTS des composites extrudés peut atteindre 360 à 400 MPa et la limite ultime d'élongation est près de 10% à la température ambiante. Ces valeurs sont beaucoup plus grandes que celles d'un composite tel que coulé. Un grand nombre de dislocations, des grains de petites tailles et un transfert de charge de la matrice aux particules contribuent au renforcement des composites. Les photographies des faciès de ruptures des composites extrudés sont différentes de celles des composites tels que coulés. Il est montré que l'extrusion ne change pas seulement la microstructure des composites, mais aussi le mode de rupture des composites.

La déformation à la température ambiante est influencée par la nature des interfaces ou le type de particules; cependant, elle est contrôlée principalement par le mécanisme de déformation à haute température. Par exemple, à la température ambiante, la UTS et la limite ultime d'élongation du composite renforcé par des particules de SiC oxydées artificiellement est réduite, alors qu'à haute température, comme 350 et 550°C, elles sont similaires à celle des composites renforcés par des particules de SiC ou Al_2O_3. De plus, l'effet Portevin-Le Chatelier (PLC) observé pour des composites déformés à la température ambiante est aussi relié au type de particules de renforcement. Par contre, le mécanisme de rupture des composites est modifié avec un changement de la température de déformation.

ABSTRACT

Metal matrix composites (MMCs) have considerably improved over the past 20 years. However, aluminum alloy matrix composites are the only ones that have become widely available, due to their relatively low price, high strength/density ratio, high stiffness/density ratio and high wear resistance. The fabrication cost of the composites reinforced by SiC or Al_2O_3 particles is lower than that of composites reinforced by fibres or whiskers. Particle reinforced composites also have the advantages of workability, isotropic mechanical properties and formability, although problems with toughness and fatigue still exist. The mechanical properties of the composites are usually affected by the following factors: fabrication process, reinforcements/matrix interfaces, volume fraction, size, shape and distribution of the reinforcements, and the microstructure and properties of the matrices. Therefore, in this thesis, the major objectives of our research include the following aspects:

1. To fabricate 5083 aluminium matrix composites reinforced by SiC, Al_2O_3 and oxidized SiC particles using the compocasting method.

2. To characterize the reaction products at the reinforcements/matrix interfaces using TEM, SEM, EDS, EELS and AES and to understand the reaction mechanisms between 5083Al/SiCp, 5083Al/oxidized SiCp and 5083Al/Al_2O_3p.

3. To develop and use some new techniques (convergent beam diffraction and graphical deconvolution of X-ray analysis) to measure the residual stress and to determine the segregation of Mg or Cu solutes at the interfaces.

4. To study the effect of thermomechanical processing on the microstructure and the mechanical properties of the composites.

5. To study the deformation and fracture mechanisms of the composites at various temperatures (e.g. 25°C, 350°C and 550°C).

The 5083 aluminium alloy is a solute and deformation hardening and weldable alloy. It has moderate-strength and good corrosion resistance. Tensile strength is about 303 MPa; yield strength is about 193 MPa and the elongation to fracture is about 16% in the H112 state. Moreover, it has the potential to be deformed superplastically. Therefore, it was chosen as the matrix alloy in our study.

With the permission of the École Polytechnique and the Département de Métallurgie et de Génie des Matériaux, this thesis is written in English. The experimental results and discussions in the thesis presented as a collection of several papers accepted or submitted for publications. Each paper is one section in a chapter.

In chapter 2, experimental results and a discussion related to interfacial

phenomena in aluminum matrix composites are presented. It consists of the following papers and sections:

2.1. "Interfacial Reactions in 5083Al/SiCp Composites During Fabrication and Remelting", W.M. Zhong, G. L'Esperance, M. Suery, Metall. Trans. A vol.26A, Oct.(1995), p.2637

2.2. "Interfacial Reactions in 5083Al/Al_2O_3p Composites During Fabrication and Remelting", W.M. Zhong, G. L'Esperance, M. Suery, Metall. Trans. A vol.26A, Oct.(1995), p.2625

2.3. "Effect of Dynamic Mg Content on Interfacial Reactions of Al-Mg (5083)/Al_2O_3p Composites", G. L'Esperance, W.M. Zhong and M. Suery, (to be submitted to Scripta Metall.)

2.4. "True Composition Profile Obtained by A Graphical Deconvolution Technique in AEM/STEM", W.M. Zhong, G. L'Esperance, presented at the Annual Meeting of the Microscopical Society of Canada, Montreal, June, 1994

2.5. "Determination of the Residual Stresses and Stress State in Al-1%Mg/SiCp Composites Using CBED Technique", W.M. Zhong, G. L'Esperance, presented at the Third Canadian Materials Science Conf., Kingston, June, 1991

In chapter 3, the deformation behaviour of aluminum matrix composites are

studied intensively. It consists of following papers and sections;

3.1. "Effect of Thermomechanical Processing on the Microstructure and the Mechanical Properties of Al-Mg (5083)/Particles Composites", **part I-** dynamic recrystallization of the composites, W.M. Zhong, E. Goiffon, G. L'Esperance, J.J. Blandin, M. Suery, Mater. Sci. & Eng., 1995 (accepted)

3.2. "Effect of Thermomechanical Processing on the Microstructure and the Mechanical Properties of Al-Mg (5083)/Particles Composites", **part II-** tensile properties at different temperatures, W.M. Zhong, G. L'Esperance and M. Suery, Mater. Sci. & Eng., 1995 (accepted)

3.3. "Effect of Thermomechanical Processing on the Microstructure and the Mechanical Properties of Al-Mg (5083)/Particles Composites", **part III-** fracture mechanism of the composites), W.M. Zhong, G. L'Esperance and M. Suery, Mater. Sci. & Eng., 1995 (accepted)

3.4. "The Portevin-Le Chatelier Effect in a 5083 Al Alloy and Al Matrix Composites", W.M. Zhong, G. L'Esperance and M. Suery, (to be submitted to Scripta Metall.)

As mentioned above, the composites were fabricated using the modified compocasting technique. The 5083-Al alloy was first heated to the semi-solid state in the temperature range from 600 to 640 °C. The reinforcing particles were then

incorporated into the vigorously agitated alloy. Approximately 5 minutes were required to add all the particles. Finally, the alloy was completely remelted at 720°C for 5 minutes and solidified under a pressure of 100 MPa. The particles used were Al_2O_3 and SiC. The SiC particles are either in an as-received condition or in an artificially oxidized condition. Oxidation was carried out in air at 1100°C for two different times (about 1 hour and 12 hours) using a SiC crucible heated with an induction furnace. The SiO_2 layer formed in this way was continuous and the amount of SiO_2 determined by wet chemical analysis, was 3.04 wt% and 14.06 wt% of the particle weight for oxidation times of 1 hour and 12 hours respectively. A total of 15 vol% of SiCp was used (with a diameter of 13 μm). The remelting experiments were performed in an induction furnace using a small graphite crucible, under Ar atmosphere. The samples were reheated to 800°C and held for 30 minutes or 4 hours. The composition of the alloy used is: 4.1 wt%Mg - 0.56 wt%Mn - 0.12 wt%Cr - 0.19 wt%Fe - 0.15 wt%Si - 0.04 wt%Cu - 0.02 wt%Ti - (balance) Al.

The ingots with a size of ϕ50 x 100 mm were extruded at 480°C with an extrusion ratio of 16:1. The final diameter of the extruded bars was 15 mm. Tensile tests were performed at constant cross-head velocities at 25°C, 350°C and 550°C. The initial strain rate was $1.6 \times 10^{-3} s^{-1}$ at 25°C and $1.2 \times 10^{-4} s^{-1}$ at 350°C and 550°C. The tensile samples had an initial 25 mm gauge length and a 4 mm diameter. Instron 1125 and Zwick 1474 tensile machines were used.

Scanning electron microscopes (SEM, JEOL-840 and JEOL-820) and transmission electron microscopes (TEM, CM30-PHILIPS and JEOL-2000FX) electron microscopes were used. The interface microstructure was examined by using bright field images (BF), dark field images (DF), selected area diffraction (SAD), microdiffraction, electron energy loss and energy dispersive X-ray spectroscopies (EELS, EDS). The TEM thin foils were prepared by ion milling at 15° with a voltage of 5 kV after mechanical polishing and dimpling.

The important conclusions obtained from the studies of the 5083 Al matrix composites can be summarized here.

1 MATERIALS CASTING AND INTERFACES

(1) In the as-cast composites, there is no attack of SiCp by molten Al whether the SiCp has been artificially oxidized or not prior to their incorporation, due to the relatively low incorporation temperature and the short holding time when the alloy is completely molten during fabrication using the compocasting method.

A reaction zone, consisting mainly of fine MgO crystals (5-20 nm), is found at the interface between the matrix and different reinforcements (including SiCp and Al_2O_3p particles). The thickness of the reaction zone increases with the thickness of the SiO_2 layer from about 30 nm to 200 nm and 500 nm for as-received SiCp, 3.04 wt% oxidized

SiCp and 14.06 wt% oxidized SiCp respectively. At the interface between the matrix and Al_2O_3p, the width of the reaction zone is about 50-80 nm.

(2) In remelted composites with as-received SiCp, the particles are heavily attacked. However, attack of SiCp by molten Al is decreased with increasing thickness of the SiO_2 layer.

It is found that the possibility of obtaining $MgAl_2O_4$ during interfacial reactions increases with the thickness of the SiO_2 layer. The nature of the reaction product is related to the "dynamic" concentration of Mg in the matrix. Similar results are obtained in the reaction between Al_2O_3 and the matrix. MgO is formed at the beginning and $MgAl_2O_4$ eventually appears as the reaction proceeds.

(3) The newly formed MgO (or spinel) crystal boundaries are believed to be the diffusion paths (or channels) for the interfacial reactions to proceed. It was found that the reaction between Mg and Al_2O_3 is more difficult than that between Mg and SiO_2 because the former reaction leads to a volume expansion whilst the latter is asociated with a contraction. Moreover, the formation of MgO from SiO_2 will lead to less volume contraction and the formation of MgO from Al_2O_3 will result in a larger volume expansion compared to that of $MgAl_2O_4$ crystals. Thus, the diffusion paths between the MgO crystals will be narrower than that between $MgAl_2O_4$ crystals. Furthermore, MgO forms more easily when the Mg content in the matrix is high. Therefore, with a higher

Mg content in the matrix, a denser MgO reaction zone will be formed more readily, and thus, will protect the particles better than the $MgAl_2O_4$ reaction zone.

(4) Segregation of Mg and Cu at the interfaces of aluminium alloys/SiCp or Si_3N_4w composites has been demonstrated using a graphical deconvolution method. Segregation of Mg or Cu at interfaces leads to a local decrease of the melting point of the matrix, resulting in the presence of a small amount of liquid phase around the particles during deformation of the composites at high temperatures.

(5) The residual stresses near the reinforcing particles were measured using the CBED technique. The effective stresses calculated by the Von Mises yield criterion are near the yield limit of the matrix and are larger near the SiCp and near the corners of the particles.

2 DEFORMATION AND FRACTURE BEHAVIOURS

(1) Large scale dynamic recrystallization was observed in all the extruded composites studied. The average grain size was about 5 μm. Reinforcing particles enhance the nucleation of the recrystallization and more than one grain was nucleated by a particle. In contrast, the microstructure of the extruded monolithic 5083 Al alloy consists mainly of a recovered microstructure.

(2) In the 5083/SiCp and 5083/Al_2O_3 composites, extrusion increases both the UTS (to about 400 MPa) and the elongation to fracture (to about 10%) at room temperature. The microhardness of the extruded composites is also increased. Increasing the reinforcement strength will increase both the UTS and the elongation to fracture. Artificial oxidation of the SiC particles (with 3.04 wt% SiO_2) reduces both the UTS and the elongation to fracture of the composites.

(3) At temperatures of 350°C and 550°C, the UTS of the composites decreases and the elongation to fracture increases to about 50%. Elongation to fracture does not increase as much as expected from the increase in the strain rate sensitivity when the deformation temperature increases from 350°C to 550°C, due to the greater possibility of cavitation at 550°C. The effect of different types of particles on the mechanical properties of the composites and on the fracture mechanisms is not obvious at higher temperatures.

(4) A change in the microstructure of the composites by extrusion corresponds to a change in the fracture mechanisms.

In as-cast composites, decohesion of the matrix/particle interface, cavities formed during solidification and fracture along the dendrite boundaries are all sources of void nucleation. Because of the large number of potential void nucleation sites in as-cast composites, premature fracture occurs during tensile testing.

In as-extruded composites, fracture of the reinforcing particles is the main source of void nucleation. Final failure occurs by shear coalescence of the small void sheets in matrix between the large reinforcing particles (or clusters of particles). The large voids caused by reinforcing particles induce localized deformation in the matrix which accelerates the nucleation, growth and coalescence of the small voids in the matrix. Retarding the formation of the large voids, by improving the quality of reinforcing particles and increasing the interfacial bond strength between the matrix and reinforcements, for example, will increase both the strength and the elongation to fracture of the composites. As mentioned previously, composites with artificially oxidized SiCp particles have lower UTS and elongation to fracture compared to composites with as-received SiC particles. This is explained by the degradation of SiC particles during the oxidation and the thicker interfacial reaction zone consuming more Mg from the matrix thus reducing solute strengthening.

(5) At high deformation temperatures (350°C and 550°C), fracture of the composites is caused by interfacial decohesion between the reaction zone on the surface of the particle and the matrix. Both dimple fracture and intergranular fracture are observed at 350°C. At 550°C, the fracture is caused by cavitation at grain boundaries and near particles. Deformation associated with dislocation slip still plays an important role in the deformation mechanisms at 350°C; however, at 550°C, the deformation behaviour is controlled by bulk diffusion, some grain boundary sliding, and particle/matrix interface decohesion. As well, at 550°C, cavitation at grain boundaries

plays an important role in the fracture of composites, whereas, at 350°C, cavitation is greatly associated with reinforcing particles. Thus, more particles were observed on the fracture surface of the composites deformed at 350°C.

(6) The Portevin-Le Chatelier effect is more pronounced in extruded composites than in the monolithic alloy. It is found that factors such as a smaller grain size of the matrix, a higher strength of the reinforcing particles and a larger density of dislocations are related to an increase of the "locking strength". The PLC effect is also related to the interfacial reactions which cause a variation of the Mg content of the matrix.

CONDENSÉ EN FRANÇAIS

Les matériaux composites à matrice métalliques (MCMM) ont connu des améliorations considérables au cours des 20 dernières années. Le principal soutien pour ce type de composites est venu de la part de l'industrie aéronautique pour l'élaboration de structures d'avion et d'équipement aerospatial. Plus récemment, les domaines de l'automobile, de l'électronique et des loisirs se sont tournés vers ce type de matériaux composites.

Les matériaux composites à matrice métallique peuvent être classés selon qu'il soient renforcés par des fibres continues ou discontinues. Les principaux matériaux utilisés comme renfort de la matrice sont: SiC, Al_2O_3, graphite, bore et le tungsténe. Ces types de renfort ont été utilisés dans divers matrices telles que, le aluminium, le magnésium, le cuivre, le titane, les aluminates de titane, le nickel, les aluminates de nickel, les super-alliages de nickel et plusieurs alliages à base de fer. Les composites fabriqués à partir d'alliages d'aluminium sont pratiquement les seuls à être disponibles commercialement dû à leur coût relativement peu élévé. De plus, ce type de matériaux offre les avantages suivants: rapport (ténacité/densité) élevé, (rigidité/densité) élevé et une résistance à l'usure importante.

La fabrication des composites renforcés par des particules de SiC et d'Al_2O_3 est moins dispendieuse que pour les mêmes matériaux renforcés à l'aide de fibres ou de

trichites. Les composites renforcés à l'aide de particules présentent les avantages suivants: propriétés mécaniques isotropes, matériaux bien adaptés pour le design et faciles de mise en oeuvre bien que des limites quant à la ténacité et la fatigue subsistent. Les propriétés mécaniques des composites sont habituellement influencées par les facteurs suivants: procédé de fabrication, interfaces entre le renfort et la matrice de même que la fraction volumique, la taille, la forme et la distribution des renforts. On ne peut également passer outre la microstructure et les différentes propriétés des matrices.

LES OBJECTIFS DE NOTRE RECHERCHE COMPREND LES ASPECTS SUIVANTS:

1. Fabriquer des composites à matrice d'aluminium 5083 renforcés de particules de SiC et Al_2O_3 et de particules oxydées de SiC par la méthode de rhéomoulage.

2. Caractériser les produits de réaction aux interfaces entre les renforts et la matrice en utilisant la microscopie électronique en transmission (MET), la microscopie électronique à balayage (MEB), la spectrométrie des rayons-x par dispersion d'énergie et la spectrométrie électronique Auger afin de comprendre les mécanismes de réaction entre $5083Al/SiC_p$, $5083Al/SiC_p$ oxydé et $5083Al/Al_2O_{3p}$.

3. Développer et utiliser certaines nouvelles techniques de caractérisation telles: la diffraction en faisceau convergent et la déconvolution de profils de ségrégation afin

de mesurer les contraintes résiduelles et de déterminer s'il y a ségrégation de magnésium et de cuivre aux interfaces.

4. Étudier l'effet du traitement thermomécanique sur la microstructure et les propriétés mécaniques.

5. Étudier les mécanismes de déformation et de rupture des composites à plusieurs températures. Des essais de traction ont été effectués à des températures de 25°C, 350°C et 550°C.

L'alliage d'aluminium 5083 est un alliage soudable durci par solution solide et qui peut être durci également par déformation. Il présente une bonne tenue contre la corrosion et une résistance mécanique modérée. En effet, pour cet alliage, la limite de rupture est d'environ 303 MPa, la limite d'élasticité est de 193 MPa et l'allongement à la rupture est de 16% à l'état H112 (106). De plus, cet alliage a la possibilité de pouvoir être déformé par superplasticité. C'est pour ces raisons que nous l'avons choisi comme matrice de notre matériau composite.

Au chapitre 1, nous ferons une revue de plusieurs méthodes importantes de fabrication de MCMM ainsi que de leurs avantages et désavantages. Cette démarche nous aidera à choisir une méthode de fabrication adéquate pour notre expérimentation. Nous réviserons également les recherches portant sur les composites à matrice

d'aluminium. Nous discuterons des réactions chimiques et des processus physiques qui ont lieu entre différents renforts et diférentes matrices. La dernière section du chapitre traitera de la revue des mécanismes de déformation et de rupture de MCMM. Nous discuterons des effets de la microstructure de la matrice, des propriétés des matrices, des propriétés des renforts et de l'effet des interfaces sur les propriétés mécaniques des composites. Nous ferons également un bref survol du comportement des MCMM lors de la déformation à haute température.

Cette thèse est rédigée en anglais avec la permession de l'École Polytechnique et du département de métallurgie et de génie des matériaux. Les résultats expérimentaux et les discussions des chapitres 2 et 3 de cette thèse sont présentés sous forme de plusieurs articles acceptés ou soummis pour publication.

LISTE DES ARTICLES:

1. "Interfacial Reactions in 5083Al/SiCp Composites During Fabrication and Remelting", W.M. Zhong, G. L'Esperance, M. Suery, Metall. Trans. A, vol.26A, Oct.(1995), p.2637
2. "Interfacial Reactions in 5083Al/Al_2O_3p Composites During Fabrication and Remelting", W.M. Zhong, G. L'Esperance, M. Suery, Metall. Trans. A, vol.26A, Oct.(1995), p.2625
3. "Effect of Dynamic Mg Content on Interfacial Reactions of Al-Mg (5083)/Al_2O_3p

Composites", G. L'Esperance, W.M. Zhong M. Suery (submitted to Scripta Metall.)

4. "True Composition Profiles Obtained by A Graphical Deconvolution Technique in AEM/STEM", W.M. Zhong, G. L'Esperance, presented at the Annual Meeting of the Microscopical Society of Canada, Montréal, June, 1994

5. "Determination of the Residual Stresses and Stress State in Al-1%Mg/SiCp Composites Using CBED Technique", W.M. Zhong, G. L'Esperance, presented at the Third Canadian Materials Science Conf., Kingston, June, 1991

6. "Effect of Thermomechanical Processing on the Microstructure and the Mechanical Properties of Al-Mg (5083)/Particles Composites", **part I-** dynamic recrystallization of the composites, W.M. Zhong, E. Goiffon, G. L'Esperance, J.J. Blandin, M. Suery, Mater. Sci. & Eng., 1995 (accepted)

7. "Effect of Thermomechanical Processing on the Microstructure and the Mechanical Properties of Al-Mg (5083)/Particles Composites" **part II-** tensile properties at various temperatures, W.M. Zhong, G. L'Esperance and M. Suery, Mater. Sci. & Eng., 1995 (accepted)

8. "Effect of Thermomechanical Processing on the Microstructure and the Mechanical Properties of Al-Mg (5083)/Particles Composites" **part III-** fracture mechanism of the composites, W.M. Zhong, G. L'Esperance and M. Suery, Mater. Sci. & Eng., 1995 (accepted)

9. "The Portevin-Le Chatelier Effect in an 5083 Al Alloy and Al Matrix Composites", W.M. Zhong, G. L'Esperance, M. Suery (to be submitted to Scripta Metall.)

Le chapitre 4 sont respectivement la discussion et la conclusion. Au chapitre 4, nous discuterons des relations entre la nature chimique des interfaces et les propriétés générales des composites. De ce chapitre découlera une vue d'ensemble de nos résultats et de nos contributions.

LES CONTRIBUTIONS DE NOTRE TRAVAIL DE RECHERCHE DANS LES DOMAINES DES COMPOSITES À MATRICE METALLIQUE INCLUENT LES ASPECTS SUIVANTS:

1. Comprendre les réactions interfaciales entre un alliage Al(Mg) et des particules de SiC et des particules oxydées de SiC. Au cours de la fabrication par rhéomoulage et de la refusion, les réactions subsequentes aux interfaces ne sont pas seulement affectées par la composition de la matrice du composite mais aussi par l'épaisseur de la couche de SiO_2 à la surface des particules de SiC. Les joints de grains de MgO ou de spinelle nouvellement formés sont les principaux chemins de diffusion lors des réactions d'interface entre Al(Mg) et le SiO_2. Nous traitons également du rôle protecteur que joue la couche de SiO_2 sur la particule de SiC contre l'attaque de l'aluminium liquide.

2. Suggérer un mécanisme pouvant expliquer la réaction d'interface entre la matrice Al(Mg) et les particules d'Al_2O_3. Les joints de grains de MgO ou de spinelle sont les principaux chemins de diffusion des réactions d'interface entre Al(Mg) et Al_2O_3. Nous évaluons le rôle protecteur des cristaux de MgO et de $MgAl_2O_4$. Les produits de

réaction semblent être reliés au temps de réaction à température élevée.

3. Développer une technique de déconvolution graphique, améliorant la résolution spatiale des analyses EDS jusquà quelques nanomètres en mode STEM. La ségrégation du Mg à l'interface du renfort a été quantifiée. Des quantités importantes de Mg et Cu ont ségrégé aux interfaces entre la matrice et le renfort. Ceci affecte le comportement de déformation des composites à haute température.

4. Mesurer les contraintes résiduelles près des interfaces à l'aide de la technique de diffraction par illumination convergente. Nous avons observé que les contraintes résiduelles près des particules de SiC sont pratiquement égales à la limite d'élasticité des matériaux formant la matrice. La contrainte anneau est en compression tandis que la contrainte radiale est en tension.

5. Étudier le comportement de restauration et de recristallisation dynamique des MCMM lors de l'extrusion. Les renforts favorisent la recristallisation dynamique. L'extrusion rend la distribution des particules de renfort plus uniforme. Une microstructure fine est obtenue (le size de grain est environ 5 microns) suite à une extrusion à 480°C avec un rapport d'extrusion de 16:1. Les propriétés mécaniques des composites extrudés ont été améliorées. Nous avons également étudié l'effet Portevin-Le Chatelier des composites dont la matrice est composée d'aluminum 5083. Nous avons observé que le comportement Portevin-LeChatelier est influencé par la résistance des

particules de renfort et des réactions d'interface entre la matrice et le renfort. Les composites semblent promouvoir l'effet Portevin-Le Chatelier.

6. Comprendre les mécanismes de rupture des MCMM à différentes températures. À température an haute, la matrice se rompt selon un mécanisme ductile. Pour les composites bruts de coulée, la fissure est initiée principalement par la décohésion de l'interface entre la matrice et les particules. Le mécanisme de rupture change suite à l'extrusion. En effet, la surface de rupture d'échantillons extrudés montre un nombre important de particules fracturées (70%). Les grosses cavités causées par les particules de renforts introduisent des déformations plastiques localisées qui ont pour effet d'accélérer la germination, la croissance et la coalescence des cavités dans la matrice. La germination de ces cavités par rupture des particules de renfort contrôle le processus de fracture. De même, plus la couche oxydée à la surface de la particule de SiC est épaisse, plus les propriétés mécaniques sont mauvaises.

7. Pour des températures de 350°C et 550°C, il n'y a pas de particules brisées. La décohésion de l'interface est la principale cause de formation des microcavités. Les propriétés mécaniques sont principalement controlées par le comportement de la matrice.

TABLE OF CONTENTS

Page

DEDICATION.....iv

ACKNOWLEDGMENTS.....v

RESUME vii

ABSTRACT.....xi

CONDENSÉ EN FRANÇAIS.....xxii

LIST OF FIGURES.....xxxiv

LIST OF TABLES.....xlviii

INTRODUCTION.....1

CHAPTER 1 LITERATURE REVIEW.....9

1.1 Fabrication of Particle Reinforced Metal Composites.....9

1.1.1 Foundry Processes.....9

1.1.2 Powder Metallurgy.....10

1.2 The Interface Between Reinforcement and Matrix in MMCs.....11

1.2.1 The Interfaces between Aluminum Alloys and the Reinforcement of SiC.....11

1.2.2 The Interfaces Between Aluminum Alloys and the Reinforcement of Al_2O_3.....16

1.2.3 Enrichment of Mg at the Interface between Al(Mg) Alloy and Reinforcement.....22

1.2.4 Determination of the True Composition Profile by

Analytical Transmission Electron Microscopy (AEM) 24

1.2.5 Residual Stresses and the Stress State in the Matrix Near the Reinforcements in MMCs.....28

1.3 Deformation Mechanisms in Discontinuously Reinforced MMCs 31

1.3.1 Strengthening Mechanisms.....31

1.3.2 Fracture Mechanisms.....39

1.3.3 The Portevin-Le Chatelier Behaviour in Aluminum Alloys.....46

1.3.4 Deformation at High Temperatures.....47

1.3.4.1 Extrusion of MMCs.....49

1.3.4.2 Superplasticity in Whisker and Particle Reinforced MMCs.....51

CHAPTER 2 INTERFACIAL PHENOMENA IN ALUMINUM MATRIX COMPOSITES.....53

Introduction.....53

2.1 Interfacial Reactions in Al-Mg (5083)/SiCp Composites during Fabrication and Remelting.....55

2.2 Interfacial Reactions in Al-Mg (5083)/Al_2O_3p Composites During Fabrication and Remelting.....98

2.3 Effect of Dynamic Mg Content on Interfacial Reactions of Al-Mg

(5083)/Al_2O_3p Composites during Remelting.....130

2.4 True Composition Profiles Obtained by A Graphical Deconvolution Technique Using Analytical Transmission Electron Microscopy (AEM/STEM).....147

2.5 Determination of Residual Stresses and Stress State in Al-1%Mg/ SiCp Composites Using Convergent Beam Electron Diffraction Technique.....185

2.6 Final Remarks on the Study of Interfaces in MMCs.....214

CHAPTER 3 DEFORMATION AND FRACTURE OF ALUMINUM MATRIX COMPOSITES.....215

Introduction.....215

3.1 Effect of Thermomechanical Processing on the Microstructure and Mechanical Properties of Al-Mg (5083)/SiCp and Al-Mg (5083)/ Al_2O_3p Composites, Part I, Dynamic Recrystallization of the Composites 216

3.2 Effect of Thermomechanical Processing on the Microstructure and Mechanical Properties of Al-Mg (5083)/SiCp and Al-Mg(5083)/ Al_2O_3p Composites, Part II, Tensile Properties at Different Temperatures.....247

3.3 Effect of Thermomechanical Processing on the Microstructure and Mechanical Properties of Al-Mg (5083)/SiCp and Al-Mg(5083)/ Al_2O_3p Composites, Part III, Fracture Mechanisms of the

Composites.....281

3.4 The Portevin-Le Chatelier Effect in an Al-Mg (5083) Monolithic Alloy and Al-Mg (5083)/Particles Reinforced Composites.....314

3.5 Final Remarks in the Study of Deformation and Fracture of the Composites.....328

CHAPTER 4 GENERAL DISCUSSION.....330

4.1 INTRODUCING A SiO_2 LAYER TO THE SURFACE OF SiC PARTICLES.....331

4.2 PROTECTIVE ROLE OF THE INTERFACIAL REACTION PRODUCTS 332

4.3 EFFECT OF SEGREGATION OF SOLUTE ELEMENTS AND RESIDUAL STRESS.....333

4.4 EXTRUSION AND PROPERTIES OF THE COMPOSITES.....334

4.5 THE PORTEVIN-LE CHATELIER EFFECT IN Al-Mg MATRIX COMPOSITES.....336

4.6 FINAL REMARKS ON APPLICATION OF THE COMPOSITES.....337

GENERAL CONCLUSIONS.....339

1 MATERIALS CASTING AND INTERFACES.....339

2 DEFORMATION AND FRACTURE BEHAVIOURS.....341

REFERENCE.....345

LIST OF FIGURES

Chapter 1

Page

Figure 1.1 Composition/Temperature Stability Regions for the Al_2O_3-MgO Equilibria.....19

Figure 1.1 Composition/Temperature Stability Regions for the Al_2O_3-$MgAl_2O_4$ Equilibria.....19

Chapter 2.1

Figure 1 Distribution of SiCp(ARS, 5083/SiCp, as-cast).....79

Figure 2 SiCp boundary is clear, no reaction product is seen at the interface (ARS).....79

Figure 3(a) TEM image of the interface of matrix/SiCp (ARS).....80

Figure 3(b) EDS line-profile at matrix/SiCp interface (ARS).....80

Figure 4 Small MgO crystals are observed at the interface, **(a)** TEM BF image, **(b)** DF image, **(c)** SAD pattern from reaction zone (MgO size 5-10 nm, ARS).....81

Figure 5 SiCp attacked by matrix (RMS, 5083/SiCp, remelted at 800°C for 30 min.).....82

Figure 6 **(a)** TEM BF image, the morphology of the attacked SiCp (RMS)

(b) SAD patterns of B[210]Al_4C_3.....83

Figure 7 **(a)** MgO crystals are observed at the original interface in front of

Al_4C_3 (RMS), **(b)** SAD patterns of MgO polycrystal.....84

Figure 8(a) TEM BF image, **(b)** DF image by (111)MgO, **(c)** SAD

pattern of MgO obtained from the reaction zone (AOX3).....85

Figure 9(a) EDS line profile for AOX3, **(b)** EDS spectrum in the reaction zone...86

Figure 10(a),(b) SEM X-ray maps of the interfaces enriched in Mg and O

(ROX3).....87

Figure 11 After remelting, some particles are attacked (ROX3).....88

Figure 12 EDS spectrum obtained from the matrix/SiCp interface (ROX3)...88

Figure 13(a) TEM BF image of ROX3, **(b)** SAD pattern of MgO, **(c)** Mg_2Si is

found near SiCp, B[110]Mg_2Si 89

Figure 13(d) PEELS spectra obtained from the reaction zone (ROX3),

pure spinel and MgO standards.....90

Figure 14 **(a)** SEM X-ray maps showing the segregation of Mg, O at

the interfaces,

(b) $(Cr,Mn,Fe)_3SiAl_{12}$ (B) and Mg_2Si (D) found in the matrix and near

SiCp (AOX14).....91

Figure 15 **(a)** TEM BF image of the interface (AOX14), **(b)** SAD pattern with

strong MgO rings.....92

Figure 16 **(a)** EDS concentration profile for AOX14, **(b)** EDS spectrum in

reaction zone.....93

Figure 17 **(a)** TEM BF image, Si, Mg_2Si and $MgAl_2O_4$ observed near the reaction zone in the matrix, **(b)** SAD pattern from the reaction zone indicating very strong (111)spinel diffraction, **(c)** SAD pattern of B[110]$MgAl_2O_4$.....94

Figure 18 **(a)** TEM BF image of the reaction zone around SiCp, **(b)** DF image by (111)spinel in ROX14 sample and diffraction patterns of pure MgO**(c)**&pure $MgAl_2O_4$**(d)**.....95

Figure 19 EDS profile at matrix/SiCp interface (ROX14).....96

Figure 20 Effect of SiO_2 on the interfacial reaction products.....97

Chapter 2.2

Figure 1 Distribution of Al_2O_3p (ARO, 5083/Al_2O_3, as-cast).....118

Figure 2 ARO (5083/Al_2O_3, as-cast), **(a)** BF images showing reaction zone inside Al_2O_3p, **(b)** DF image by (200)&(111)MgO diffractio, **(c)** SADP from reaction zone, showing strong MgO diffraction and weak (111)$MgAl_2O_4$ 119

Figure 2 **(d),(e)** Serrated morphology at the boundary of Al_2O_3p **(f)** a MgO crystal protruding out from the Al_2O_3p.....120

Figure 3 EDX concentration profile for ARO.....121

Figure 4 RMO (5083/Al_2O_3 - remelted) reaction layer still invisible by SEM...122

Figure 5 RMO, **(a)** The reaction zone at the interface of Al_2O_3 particle and **(b)** SAD pattern of MgO crystals.....123

Figure 5 **(c)** DF image by (012)$MgAl_{26}O_{40}$, **(d)** SADP of B[121] $MgAl_{26}O_{40}$ **(e)** DF image by (111)MgO, **(f)** SADP of B[112] $MgAl_2O_4$.....124

Figure 6 **(a)(b)** The interface of alumina/matrix and SADP of B[2201]α-Al_2O_3...125

Figure 7 EDX concentration profile for RMO.....126

Figure 8 PEELS spectra obtained from the reaction zone (RMO), pure standard $MgAl_2O_4$ (spinel) and pure MgO crystals.....127

Figure 9 The diagram for reaction mechanism of Al_2O_3p/Al(Mg) Alloy (at 680-800°C).....128

(a) Mg solute comes to the surface of Al_2O_3 particle,

(b) The interdiffusion of Al^{+3} and Mg^{+2} in the surface of Al_2O_3 particle

$$3(Mg^\circ - 2e) = 3Mg^{+2}$$

$$2(Al^{+3} + 3e) = 2Al^\circ$$

(c) MgO or spinel nucleates associated with a volume expansion, Mg (Al) continue to enter or (leave) Al_2O_3 particle along the new phase or MgO crystal boundaries, interdiffusion of cations occurs at the new interface

(d) With increasing time, new MgO or spinel crystals are nucleated further inside Al_2O_3 particle

Chapter 2.3

Figure 1 Fracture surface of the as-cast composite showing an Al_2O_3 particle with a clean surface (5083/Al_2O_3, as-cast).....142

Figure 2(a),(b) SEM images showing $MgAl_2O_4$ crystals on the surface of decohered Al_2O_3 particles (remelting at 800°C for 4 hours).....143

Figure 3(a) Dark field TEM micrograph showing many fine MgO crystals at an interface (5083/Al_2O_3, remelting at 800°C for 0.5 hours)

(b) SAD pattern obtained from reaction zone, showing strong MgO diffraction.....144

Figure 4(a),(b) TEM micrographs showing the large $MgAl_2O_4$ crystals at the interfaces (5083/Al_2O_3, remelting at 800°C for 4 hours)...145

Figure 5 **(a)** SAD patterns and **(b)** computer simulated patterns, showing [1,-1,-2]-$MgAl_2O_4$//[001]-Al_2O_3 with (311)-$MgAl_2O_4$//(-1,2,0)-Al_2O_3 and (1,-1,1)-$MgAl_2O_4$//(110)-Al_2O_3.....146

Chapter 2.4

Fig. 1 The principle of convolution of the electron beam distribution I(r,t) in the thin foil and the segregation distribution (C(y), slab model). From the measured intensity profile $I'_x(y)$ and the calculated electron beam distribution, a "true" solute profile at the boundary can be determined (after Michael [6]).....172

Fig. 2 Schematic representation of electron beam interaction with a grain

boundary in a thin slab specimen. The volume of interaction is modeled as a frustum cone. d_p is the incident probe diameter. B is the diameter of the broadening exit electron beam (after Romig [9]).....173

Fig. 3 (a) Relations among the normal of the foil n_f, the normal of the interface n_s and the direction of the electron beam B...174

Fig. 3 (b) Intersection of the electron beam with the tilted foil surface and the interface 175

Fig. 4 Cross-section of the electron interaction volume in the thin foil, ABCD is the cross-section without distortion, A'B'C'D' is the cross-section with distortion, t=foil thickness...176

Fig. 5 Four integration regions in both (a) no-distortion and (b) distortion models 177

Fig. 6 (a) EDS spectrum obtained at the 2124Al/Si_3N_4 interface.....178

Fig. 6 (b) Mg concentration profile obtained by no-distortion model, C_0=3.5, A=12 nm, d_p=14 nm, X-tilt=10°, Y-tilt=20°, foil thickness=136 nm.....179

Fig. 6 (c) Mg concentration profile obtained by distortion model, C_0=3.9, A=13 nm.....180

Fig. 7 Cu concentration profiles obtained by no-distortion model, showing the effect of C_0 and A profile 1, C_0=3.6, A=24 nm; profile 2, C_0=3.5, A=25 nm 181

Fig. 8 A profile obtained from an interface with high Mg concentration,

C_0=16.5, A=6.5 nm, X-tilt=5°, Y-tilt=20°, d_p=40 nm.....182

Fig. 9 Showing a narrowly extended Mg concentration profile

C_0=3.75, A=5 nm, d_p=20 nm.....183

Fig. 10 **(a)** TEM BF image showing an analyzed interface (5083Al/SiCp)

(b) The convoluted "true" Mg profile (solid curve) obtained

using no-distortion model, C_0=17.5, A=25 nm

* Capr.exp.-- measured apparent concentration

* Capr.cal.-- calculated apparent concentration.....184

Chapter 2.5

Figure 1 Schematic diagram of HOLZ line positions. (a) Section through reciprocal space showing the FOLZ, the projection (g-t) of reflection g onto the diffraction pattern. (b) Section through reciprocal space for [uvw] zone axis. 2ϕ defines the radius of the FOLZ ring. 2Θ, twice the Bragg angle, defines the angle between defect FOLZ lines.....205

Figure 2 (a),(b),(c) TEM micrographs showing the studied interface.

(d) The SAD pattern obtained at zero tilt, foil normal is near B[010]....206

Figure 3 Schematic diagram of the stress volume element (position II is the same as I).....207

Figure 4 (a) HOLZ pattern obtained in the matrix far from SiC particle.

(b) corresponding simulated pattern.....208

Figure 5 (a) HOLZ pattern obtained at position I (see figure 3),

(b) corresponding simulated pattern.....209

Figure 6 (a) HOLZ pattern obtained at position II (see figure 3),

(b) corresponding simulated pattern.....210

Figure 7 (a) HOLZ pattern obtained at position III (see figure 3),

(b) corresponding simulated pattern.....211

Figure 8 The Mg concentration profile near the SiC particle (error bar indicating the statistical error).....212

Figure 9 Relation between lattice parameter and Mg content in Al alloy.....212

Figure 10 HOLZ patterns obtained individually at the positions of 0 nm (a), 50 nm (b), 100 nm (c) from a dislocation.....213

Chapter 3.1

Figure 1 Optical micrographs, (a) As-cast 5083/SiCp (ARS),

(b) As-cast 5083/SiCp (oxidized 3.04%, AOX3).

Samples etched in Kelly's reagent.....233

Figure 2 TEM images of subboundaries in as-cast composites (ARS).....234

Figure 3 Microstructure of extruded 5083 Al alloy (5083E, SEM).....234

Figure 4 (a) TEM image showing the subgrains in extruded 5083Al

alloy (5083E).....235

(b) Corresponding SAD patterns obtained from the different regions shown in figure 4 (a).....236

Figure 5 (a) Recrystallized structure formed near large insoluble inclusions (arrow) in extruded monolithic alloys (5083E),

(b) Corresponding SAD patterns 237

Figure 6 (a) Distribution of particles after extrusion (longitudinal section)

(b) Cracked reinforcing particles after extrusion (extruded 5083/SiCp, ARSE).....238

Figure 7 (a) Equiaxed structure near a SiC particle in an extruded composite (AOX3E).....239

Figure 7 (b) Corresponding SAD patterns (AOX3E).....240

Figure 8 (a) TEM bright field (BF) image of dislocations in an extruded composite,

(b) Weak beam DF image (g_{111},g/3g) (AOX3E).....241

Figure 9 (a) Elongated structure in an extruded composite (AOX3E),

(b) A boundary observed at higher magnification (arrows A&B showing serrated boundaries, C&D showing inclusions).....242

Figure 10 A grain formed between two SiC particles with a serrated boundary in an extruded composite (AOX3E).....243

Figure 11 (a) TEM BF image showing very fine structure (& substructure)

between two reinforcing particles in an extruded composite (ARSE).....244

Figure 11 (b) DF image showing the dislocation structure in a subboundary (ARSE).....245

Figure 11 (c) Corresponding SAD patterns from areas shown in figure 11 (a) (ARSE).....245

Figure 12 Recrystallization nucleated at the junction of several grains in an extruded composite (AOX3E).....246

Chapter 3.2

Fig. 1 Tensile Test Curves at Room Temperature.....271

Fig. 2 Microhardness of the Extruded & the As-cast Composites.....272

Fig. 3 Maximum Strain Rate Sensitivity Measured at Different Temperatures.....273

Fig. 4 SEM Micrograph of a Longitudinal Section (ARSE).....273

Fig. 5 (a),(b) SEM Micrographs Showing the Morphology of SiC Particles (before incorporation).....273

Fig. 6 (a),(b) TEM Images Obtained at Different Tilts Showing a Crack Passing between MgO Crystals in the Reaction Zone (AOX3E).....274

Fig. 7 (a),(b) Cracks Formed Along Twin Boundaries inside Particles.....275

Fig. 8 Tear Ridges Observed on the Fracture Surface (ARSE tested at 350°C).....276

Fig. 9 Intergranular Fracture Observed (AOX3E tested at 350°C).....276

Fig. 10 Void Formed by Interface Decohesion (AOX3E tested at 350°C).....276

Fig. 11 X-ray Spectra Obtained from the Surface of a Decohered SiC Particle at Different Accelerating Voltages.....277

Fig. 12 Auger Depth Profile Obtained from the Surface of a Decohered Al_2O_3 Particle.....277

Fig. 13 TEM Image Illustrating that the Decohesion Occurs at the Matrix/Reaction Zone Interface (AOX3E tested at 350°C).....277

Fig. 14 Longitudinal Section Showing the Nucleation and Coalescence of Voids (ARSE, 350°C).....278

Fig. 15 Ratio of the Number of Particles on the Fracture Surface to that on Polished Surface.....278

Fig. 16 Distribution of Damage at Different Temperatures.....279

Fig. 17 Fracture Surface Observed after Testing at 550°C (ARSE).....279

Fig. 18 Surface of Decohered Particle Observed on a Fracture Surface (ARSE).....280

Fig. 19 Longitudinal Section of a ARSE Sample Tested at 550°C (1 mm from the fracture surface).....280

Fig. 20 **(a)** Fibres Observed on a Grain Surface of a Fractured Sample (ARSE tested at 550°C)

(b) X-ray Maps of Al and Mg, Showing that the Fibres Are Enriched in Mg.....281

Chapter 3.3

Fig. 1 Optical Macrographs of the Fracture Surfaces of Composites,
(a)-Extruded (ARSE), (b)-As-cast (AOX3).....303

Fig. 2 Fracture Surfaces of Extruded Composites (at Room
Temperature), Reinforced by As-received SiC ((a), ARSE)
and Al_2O_3 Particles ((b), AROE) Respectively.....303

Fig. 3 Fracture Surfaces of Extruded Composites,
Matching Pairs: (a)-(b)&(c)-(d),
Stereo-Pairs: (a)-(c)&(b)-(d) (ARSE).....304

Fig. 4 Fracture Surfaces of Extruded Composites,
Matching Pairs: (a)-(b)&(c)-(d),
Stereo-Pairs: (a)-(c)&(b)-(d) (AOX3E).....305

Fig. 5 Fracture Surfaces of Extruded Composites,
Matching Pairs: (a)-(b)&(c)-(d),
Stereo-Pairs: (a)-(c)&(b)-(d) (AROE).....306

Fig. 6 Schematic Diagram of Dimple Formation.....307

Fig. 7 SEM Micrograph Showing Small Elongated Dimples Caused by
(Fe, Mn)-Rich Inclusions (ARSE).....307

Fig. 8 (a),(b) Deep Dimple with Fine Striations on Its Wall
(SEM Stereo-Pairs, AOX3E, 25°C).....308

Fig. 9 Decohered Particle on a Fracture Surface (AROE, 25°).....308

Fig. 10 TEM Micrograph Showing the Site of Decohesion (Arrow Indicating
the Reaction Zone, AOX3E).....308

Fig. 11 SEM Micrograph of Longitudinal Section, Showing the Nucleation of Voids (ARSE).....309

Fig. 12 SEM Micrograph of Longitudinal Section (1 mm from the Fracture Surface (AOX3E, 25°C)).....309

Fig.13 Particles (P) at Different Height Levels Joined by a Crack Propagating in the Matrix (ARSE).....309

Fig. 14 Fracture Surface of the Extruded Monolithic 5083 Al Alloy.....310

Fig.15 Decohered Particles on the Fracture Surface of the As-cast Composites (AOX3).....310

Fig.16 Secondary Cracks in a Cluster of Particles (AOX3).....310

Fig. 17 (a) Cavity Observed at the Boundaries of the Dendrites

(b) Corresponding X-ray Maps (AOX3).....310

Fig. 18 Crack Formed in an Area with High Density of Particles (As-cast Composites, Longitudinal Section).....311

Fig. 19 Crack Parallel to Tensile Axis (AOX3).....311

Fig. 20 Crack Parallel to Fracture Surface.....311

Fig. 21 Ratio of the Number of Particles on a Fracture Surface to that on a Polished Surface.....312

Fig. 22 Variation of the Number of Damaged Particles as a Function of Distance from the Fracture Surfaces.....312

Fig. 23 Number of Decohered Particles on the Fracture Surfaces.....312

Fig. 24 Schematic Diagram of the Fracture Process in Extruded

Particle-Reinforced Composites.....313

(1) Particles(A) are cracked in **Region I** because of the geometrical factors (size, aspect ratio) and the stress state

(2) Local plastic flow occurs in **Region I** because of the decrease of the constraint. The stress state between two cracked particles is also changed.

(3) **Region II** has to support more loads because of the unloading in **Region I.**

(4) Particles(B), mainly in **Region II**, are cracked

(5) Plastic flow extends across the section in **Region W**

(6) With the increase of plastic deformation in **Region W**, more particles are cracked and shear bands in the matrix between the cracked particles are formed

(7) Coalescence of the small voids in the shear bands results in the final fracture of the composites

Chapter 3.4

Figure 1 Tensile Test Curves Obtained at Room Temperature.....326

Figure 2 Examples of Different Types of Serrations [6].....327

LIST OF TABLES

Chapter 1

Page

Table 1.1 Free Energy Changes for Different Reactions (ΔG in KJ/mole, at 900°C) [23].....18

Table 1.2 Free Energy Changes for Different Reactions (ΔG in KJ/mole, at 727°C) [11].....18

Table 1.3 Predicted Increase in Yield Strength of 20 Vol.% SiCp/1100 Al Matrix and Experimentally Measured Values as a Function of Particle Size.....38

Table 1.4 Predicted Increase in Yield Strength of 6061 Al Alloy/SiCw as a Function of Volume Fraction of SiC Whiskers.....38

Chapter 2.1

Table I Relation between the reaction products and the amount of SiO_2 73

Chapter 2.3

Table I Calculated Amount of Reaction Products Formed with Different Amounts of Al_2O_3 Taking Place in the Reaction.....136

Chapter 2.5

Table 1 The Lattice Parameters Obtained from Simulating of HOLZ Lines.....200

Table 2 Residual Strains and Calculated Residual Stresses (MPa).....200

Chapter 3.1

Table I Composition of the 5083 matrix alloy.....220

Table II Misorientations between Different Regions Obtained from TEM Thin Foils.....227

Chapter 3.2

Table I Properties of Composites Deformed at Different Temperatures.....267

Table II Dislocation Densities in Different Composites.....268

Table III Grain and Subgrain Size in the Different Materials.....268

Table IV Contribution of Different Mechanisms to the Yield Strength (Results Based on Measured Dislocation Densities).....269

Table V Strength Based on Calculated Dislocation Densities

($\Delta\sigma_g$ and $\Delta\sigma_{sg}$ from table IV).....269

Chapter 3.4

Table I Maximum Amplitude (MPa, experimental and calculated) and

Peak Distance of Serrations (measured) for Different Materials.....325

INTRODUCTION

Metal matrix composites (MMCs) have considerably improved over the past 20 years. The initial interest for these composites came from the aerospace industry for airframe and spacecraft structures. More recently, the automotive, electronic and leisure industries have been seriously working with these composites. At the present time, metal matrix composites can be classified into either continuous fibre composites or discontinuously reinforced composites. SiC, Al_2O_3, Graphite, Boron and Tungsten are used as reinforcements. These reinforcements have been introduced into aluminum, magnesium, copper, titanium, titanium aluminides, nickel, nickel aluminides, nickel-based superalloys and various alloys of iron. Aluminum alloy matrix composites are the only ones that have become widely available, due to their relatively low price, high strength/density ratio, high stiffness/density ratio and high wear resistance. The fabrication cost of the composites reinforced by SiC or Al_2O_3 particles is lower than that of composites reinforced by fibres or whiskers. Particle reinforced composites also have the advantages of workability, isotropic mechanical properties and formability, although problems with toughness and fatigue still exist [68,69,76,77,80,81,84]. The mechanical properties of the composites are usually affected by the following factors: fabrication process, reinforcements/matrix interfaces, volume fraction, size, shape and distribution of the reinforcements, and the microstructure and properties of the matrices.

The OBJECTIVE of our research includes the following aspects:

1. To fabricate 5083 aluminium matrix composites reinforced by SiC, Al_2O_3 and oxidized SiC particles using the compocasting method.

2. To characterize the reaction products at the reinforcements/matrix interfaces using TEM, SEM, EDS, EELS and AES and to understand the reaction mechanisms between 5083Al/SiCp, 5083Al/oxidized SiCp and 5083Al/Al_2O_3p.

3. To develop and use some new techniques (convergent beam diffraction and graphical deconvolution of X-ray analysis) to measure the residual stress and to determine the segregation of Mg or Cu solutes at the interfaces.

4. To study the effect of thermomechanical processing on the microstructure and the mechanical properties of the composites.

5. To study the deformation and fracture mechanisms of the composites at various temperatures (tensile tests were carried out at 25°C, 350°C and 550°C).

The 5083 aluminium alloy is a solute hardening and weldable alloy. It has moderate-strength and good corrosion resistance. Tensile strength is about 303 MPa; yield strength is about 193 MPa and the elongation to fracture is about 16% in the H112

state [106]. Moreover, it has the potential to be deformed superplastically [97,104]. Therefore, it was chosen as the matrix alloy in our study.

In the literature review presented in chapter 1, several important fabrication methods of MMCs and their advantages and disadvantages are reviewed in order to select a suitable fabrication method for our experiment. Studies of the interfaces in aluminium matrix composites will also be extensively reviewed. The chemical reactions and physical processes at the interfaces between different reinforcements and different matrices will be discussed. The deformation and fracture mechanisms of MMCs will be reviewed in the last section of the chapter. The effect of matrix microstructure, matrix properties, reinforcement properties and interfacial characteristics on the general composite mechanical properties will be discussed. The high temperature deformation behaviour of MMCs will also be briefly reviewd.

With the permission of the École Polytechnique and the Département de Métallurgie et de Génie des Matériaux, this thesis is written in English. The experimental results and discussions in the thesis presented as a collection of several papers accepted or submitted for publications. Each paper is one section in a chapter.

Thus, in chapter 2, experimental results and a discussion related to interfacial phenomena in aluminum matrix composites are presented. It consists of the following papers and sections:

2.1. "Interfacial Reactions in 5083Al/SiCp Composites During Fabrication and Remelting", W.M. Zhong, G. L'Esperance, M. Suery, Metall. Trans. A vol.26A, Oct.(1995), p.2637

2.2. "Interfacial Reactions in 5083Al/Al_2O_3p Composites During Fabrication and Remelting", W.M. Zhong, G. L'Esperance, M. Suery, Metall. Trans. A vol.26A, Oct.(1995), p.2625

2.3. "Effect of Dynamic Mg Content on Interfacial Reactions of Al-Mg (5083)/Al_2O_3p Composites", G. L'Esperance, W.M. Zhong and M. Suery, (to be submitted to Scripta Metall.)

2.4. "True Composition Profile Obtained by A Graphical Deconvolution Technique in AEM/STEM", W.M. Zhong, G. L'Esperance, presented at the Annual Meeting of the Microscopical Society of Canada, Montreal, June, 1994

2.5. "Determination of the Residual Stresses and Stress State in Al-1%Mg/SiCp Composites Using CBED Technique", W.M. Zhong, G. L'Esperance, presented at the Third Canadian Materials Science Conf., Kingston, June, 1991

In chapter 3, the deformation behaviour of aluminum matrix composites are studied intensively. It consists of following papers and sections;

3.1. "Effect of Thermomechanical Processing on the Microstructure and the

Mechanical Properties of Al-Mg (5083)/Particles Composites", **part I-** dynamic recrystallization of the composites, W.M. Zhong, E. Goiffon, G. L'Esperance, J.J. Blandin, M. Suery, Mater. Sci. & Eng., 1995 (accepted)

3.2. "Effect of Thermomechanical Processing on the Microstructure and the Mechanical Properties of Al-Mg (5083)/Particles Composites", **part II-** tensile properties at various temperatures, W.M. Zhong, G. L'Esperance and M. Suery, Mater. Sci. & Eng., 1995 (accepted)

3.3. "Effect of Thermomechanical Processing on the Microstructure and the Mechanical Properties of Al-Mg (5083)/Particles Composites", **part III-** fracture mechanism of the composites), W.M. Zhong, G. L'Esperance and M. Suery, Mater. Sci. & Eng., 1995 (accepted)

3.4. "Teh Portevin-Le Chatelier Effect in a 5083 Al Alloy and Al Matrix Composites", W.M. Zhong, G. L'Esperance and M. Suery, (to be submitted to Scripta Metall.)

Chapter 4 is the general discussion. In this chapter, we will discuss the relation between the nature of the interfaces and the composite properties. A general conclusion is given in the last section.

The CONTRIBUTIONS of our work to the research and development of composites materials include the following aspects:

1. Understanding of the interfacial reactions between Al (Mg) alloy and SiC particles, and between Al (Mg) alloy and SiO_2 layer on the surfaces of SiC particles. During compocasting and the subsequent remelting, the interfacial reactions are not only affected by the matrix composition of the composites but also by the thickness of the SiO_2 layer on SiC surfaces. The boundaries of the newly formed MgO or spinel crystals are the main diffusion paths during interfacial reaction between Al(Mg) and SiO_2. The role of the SiO_2 layer in protecting SiC particles from attack by liquid Al is examined.

2. Suggestion of a mechanism to explain the interfacial reaction between Al(Mg) matrix and Al_2O_3 particles. The boundaries of the newly formed MgO or spinel crystals are also the main diffusion paths during the interfacial reaction between Al(Mg) and Al_2O_3. The protective role of MgO and $MgAl_2O_4$ crystals in the reaction zone is evaluated. The reaction products are found to be related to the reaction times at high temperatures.

3. Development of a graphical deconvolution technique, improving the spatial resolution of the EDS analysis in STEM to a few nm. Segregation of Mg at the interface of the reinforcement has been quantified. Large amounts of Mg and Cu were found segregating at interfaces between matrices and reinforcements. This affects the high temperature deformation behaviour of the composites.

4. Measurement of the local residual stress near the interface by convergent beam electron diffraction (CBED) technique. It has been found that the residual stress near the SiC particles is near the yield stress of the matrix materials. The hoop stress is compressive and the radial stress is tensile.

5. Study of the dynamic recovery and dynamic recrystallization behaviour in composites during extrusion. The reinforcements enhance the dynamic recrystallization. Extrusion makes the distribution of the reinforcing particles more uniform. A fine microstructure (about 5 μm) of the matrix is obtained after extrusion at 480°C with an extrusion ratio of 16:1. The mechanical properties of the extruded composites are improved.

At 350°C and 550°C, particles are not cracked. Interfacial decohesion is the main source of microvoid formation and the mechanical properties are mainly controlled by the matrix behaviour.

6. Understanding of the fracture mechanisms of composites deformed at different temperatures. At room temperature, the matrix is fractured by a ductile mechanism. The crack is nucleated mainly as a result of matrix/particle interfacial decohesion in as-cast composites. The fracture mechanism is changed after extrusion. A large numbers of particles (about 70%) are cracked on the fracture surface in the extruded samples. The large voids caused by reinforcing particles induce localized plastic deformation in

the matrix which accelerates the nucleation, growth and coalescence of the small voids in the matrix. Void nucleation by fracture of reinforcing particles controls the fracture process. A thicker oxidized layer on the surface of SiC has a negative effect on the mechanical properties.

7. The Portevin-Le Chatelier effect in 5083 Al matrix composites has been studied. It was found that the Portevin-Le Chatelier behaviour is affected by the strength of reinforcing particles and the interfacial reactions between matrix and reinforcements. Composites have been found to be more susceptible to the Portevin-Le Chatelier effect.

CHAPTER 1

LITERATURE REVIEW

1.1 Fabrication of Particle Reinforced Metal Composites

The role of a fabrication process is to mix metallic and ceramic constituents in order to achieve acceptable interface strength and to disperse the particles uniformly in the matrix, while keeping the contamination in gases and inclusions at the lowest level. Different methods have been developed. The main characteristics of the several basic methods will be discussed as the following.

1.1.1 Foundry Processes [2, 23, 87, 88, 89, 105]

This class concerns all the techniques that fabricate MMCs by stirring an alloy above the liquidus, while proceeding to the addition of the reinforcing particles. These techniques correspond to the most inexpensive processes for producing MMCs.

Vortex method: This process is probably the simplest and most instinctive method that can be used for the fabrication of MMCs. The method consists of vigorously stirring an alloy maintained over its melting point, while adding reinforcement in the vortex. Controlled rate of particle addition is critical to avoid

introduction of agglomerates in the melt. For a large amount of particles, addition of particles will take a very long time. The particles with a size finer than 50 μm are rejected easily during fabrication.

Compocasting: This process consists of vigorously stirring a semi-solid alloy, while adding the particles to the surface. The main advantage of stirring the melt between the solidus and liquids is that the partly solidified structure drags the particles along into the melt even if they are not wetted. However, due to the entrapment effect, reinforcement, as well as floating impurities and gases, are engulfed into the vortex. A modified compocasting technique was suggested in which, after addition of the particles to the semi-solid alloy, the melt is completely remelted for a length of times which is short enough to prevent chemical reaction of the particles by the molten matrix, and solidified under a pressure of 100 MPa to avoid the formation of porosity [89].

1.1.2 Powder Metallurgy

Powder metallurgy (PM) presently remains one of the more suitable technologies for the fabrication of high performance MMCs. With PM it is possible to obtain near-net-shape parts with variable concentration or nature of reinforcement and matrix. Composites containing fine particles (smaller than 5 μm) can also be fabricated with a high final quality. Working below the melting point is essential for these materials

to avoid high temperature degradation. However, due to the still relatively expensive manufacturing processes, PM will likely to be limited to low volume high performance applications.

1.2 The Interface Between Reinforcement and Matrix in MMCs

A strong composite often requires a strong interfacial bond to permit load to be transferred from the matrix to the fibres or particles. Moreover, the strength of the interfacial bond is strongly related to the nature of interfaces. Usually, the interfaces of composites are very complex. Chemical reaction, diffusion and new phases or precipitates formed at the interfaces are often observed, and they will affect the mechanical properties of composites [44-45]. Since the interfaces are so important, many studies have been carried out to understand the nature of the interface between different reinforcements and matrixes, under different conditions [16,19,48,50]. Here we will review some studies on the interfaces between aluminum alloys and the reinforcements of SiC and Al_2O_3.

1.2.1 The Interfaces between Aluminum Alloys and the Reinforcement of SiC

In SiC reinforced composites, interfacial reactions not only affect the interface

strength, but also affect the age-hardening behaviour of the matrix [1,2]. Some interfacial reactions can improve the wettability of the solid reinforcement by the liquid, because the adhesion work is increased by the energy released from chemical reactions [3]. However, it will sometimes result in the reaction of the reinforcement and form harmful products (such as Al_4C_3) around the reinforcement [4,5]. Introducing an oxide (SiO_2) layer on the surface of SiC has been reported [2,6,119] to play an important role in preventing SiC from being attacked by Al, improving the wettability and also improving the fracture strain of the composites. Because the interfacial reactions in Al/SiC depend on such fabrication parameters as temperature, atmosphere and chemical composition of both aluminium matrix and SiC reinforcement, they will be different for different fabrication procedures and different composite systems. As it is well known, the reactions between SiCp and liquid Al include the following steps [12,13]:

(a) The chemical reaction (partial dissolution) of SiCp with molten Al

(b) The diffusion of Si and C atoms away from the SiCp surface into the bulk molten Al pool

(c) The formation of compounds when the product of Al and C concentrations or Si and C concentrations exceeds the equilibrium constants

(d) On cooling, further precipitation of compounds due to the decrease of the solubility

(e) The solidification of the matrix

The dissolution kinetics of SiCp in Al is believed to be the rate determining step [12,13]. It controls the reaction at the Al/SiCp interface during manufacture. The dissolution rate of SiC in molten Al has been calculated, and the results showed that at 700°C it is 0.0187 wt%/min. (i.e. it is 0.195 μm/min. for a composite with 20 vol% SiC and is about 0.3 μm/min. at 800°C) [117]. The dissolution rate is found to be controlled by the amount of Si in the Al melt, i.e. the dissolution rate decreases with increasing Si content in Al melt [12,14,15]. As shown by Lloyd et al.[14], the reaction rate was very low in the fabrication temperature range from 650°C - 750°C. No attack was found in A356 alloy after 2 hours at 750°C, indicating that 7 wt% of Si in the matrix was sufficient to prevent extensive Al_4C_3 formation. However, according to the calculation of Selvaduray et al. [15], only 4.35 wt% Si is enough to prevent SiCp from being attacked by Al at 827°C (There are some inconsistencies with the results obtained by Lin et al. [12] (15.5 wt% Si), by Iseki et al. [7] (10 wt% Si) and by Lloyd et al. [14] (7-10 wt% Si)).

Dignard-Bailey et al. [59], in studying the interfaces of 20 vol% SiC particles with Al 2014 alloy (4.4Cu-0.8Si-0.5Mg-0.8Mn-93.5 wt% Al), found that particles of MgO and Al_4C_3 can form at the interfaces during manufacture of the MMCs by a melting process. A serrated interfacial morphology of SiCp was also observed. It was believed to result from a dissolution/growth reaction between SiC and liquid Al. Defects such as stacking faults and dislocations were observed in the SiCp. No further interfacial reaction was reported during extrusion and different heat treatments below

500°C. Arsenault et al. [8], reported the presence of Al inside SiC. By comparing the Al profile with that of Si across the interface, diffusion of Al into SiC was claimed, although it was unlikely from theoretical calculations [8].

Iseki et al.[7] reported that at 1000°C and in a vacuum of 10^{-2}Pa for 1h, Al_4C_3 is formed at the interface of Al and SiC, whereas when the amount of free Si in SiC is increased (to about 10 wt%), there is no longer Al_4C_3 at the interfaces. Arsenault et al.[8] did not find any reaction product at the Al/SiC interface in as-cast pure Al/SiC composite. It was suggested that the bond strength of SiC and Al could possibly be 2 or 3 times stronger than that of Al-Al, if the Al atoms are reconstructed at the interface, and certain orientations or dislocation structures are formed [118]. If the Al atoms are not reconstructed, the adhesive energy between Al and SiC is nearly the same as the surface energy of Al. Nutt [9] found fine crystals of MgO near the interface of SiC whisker/2124 Al alloy (with 1.5 wt% Mg, fabricated by powder metallurgy). Withers and Stobbs [10] found an amorphous phase at the interface of pure Al/SiC in as-cast composites.

A chemical interaction between molten Al and SiO_2 was observed by Brondyke at 700-900°C [120], i.e. $4Al + 3SiO_2 = 2Al_2O_3 + 3Si$. The reaction rate was controlled by the diffusion of Al and Si through the newly formed Al_2O_3. A thin alumina film caused by oxidisation of the molten Al in air also delayed the subsequent reaction between Al and SiO_2 [121, 122]. Marumo and Pask [123] suggested the

reaction process between Al and SiO_2: no oxygen diffusion and no modification of the network of the O^{2-} anions because of its large size. The oxidoreduction reaction occurs by cationic diffusion of Al and Si. Suboxides of aluminium are formed during the interaction. Legoux et al. [1,5,6] have extensively studied the reaction between SiO_2 layer on SiCp and Al alloys (with 0.3 wt%, 1 wt% and 5 wt% Mg). $MgAl_2O_4$ was found to be the reaction product in the materials with 0.3 wt% and 1 wt% Mg, whereas a mixture of fine $MgAl_2O_4$ - MgO crystals was found to be the reaction product in the materials with 5 wt% Mg. Metallic Al diffusion channel was supposed to be the diffusion path through the oxide layer for the in-coming Mg and out-going Si. Stephenson et al.[119] experimentally determined that the reaction tendency and kinetics of Mg and SiO_2 is several times higher than that of Al and SiO_2 at 670-800°C. Thus Mg will promote the interface reaction and lead to the formation of $MgAl_2O_4$ or MgO (when Mg>4.5 wt%) at the interfaces. Then the diffusion path is not clear. B. Hallstedt [11] suggested that the reaction between Mg and SiO_2 which is an energy releasing reaction will lead to a great increase of temperature during the reaction (from about 800 °C to about 2000 °C). According to his calculation, the temperature at the interface can be high enough for the transformation of crystalline SiO_2 into amorphous with the formed MgO in the undercooled liquid state. At high temperature, Mg and Si can diffuse rapidly through the amorphous SiO_2 and the liquid MgO phase. By cooling, MgO fine crystals are formed in the previous SiO_2 layer.

From the above review, it is found that the interfacial reaction products and

reaction mechanisms, reported in different studies, are different. To date, there is no study reported on the system of 5083 Al containing 4.0 to 4.5 wt% Mg reinforced by as-received and oxidized SiC particles, especially for the composites fabricated using compocasting method.

1.2.2 The Interfaces Between Aluminum Alloys and the Reinforcement of Al_2O_3

Since the wettability between Al and Al_2O_3 is not good below 900°C (Munitz [16]), several procedures have been adopted to attempt to incorporate Al_2O_3 into Al matrices.

Levi et al. [23] used a process in which chopped Al_2O_3 fibres were added to vigorously agitated, partially solid metal slurries of Al-Mg or Al-Cu-Mg alloys. They found that incorporation, wetting and bonding of the fibres could be achieved by this technique and that agitation and addition of elements such as Mg or Cu, etc. were essential. They concluded that the bonding was achieved through the formation of a $MgAl_2O_4$ or $CuAl_2O_4$ (spinel) layer by the reaction between the fibres and the Mg or Cu in the liquid Al. Ghosh et al. [24], Quigley [25] and Fishkis [26] have confirmed that $MgAl_2O_4$ was the main reaction product at the interface of Al_2O_3 and Al alloys for Mg contents less than 4 wt%, whereas MgO was found to be present when the Mg

contents were larger than 4 wt% (Pai [27]). The reactions could be:

$$Mg(l) + 2Al(l) + 2O_2 = MgAl_2O_4(s) \quad (1.2.1)$$

$$Mg(l) + 4/3\ Al_2O_3(s) = MgAl_2O_4(s) + 2/3Al(l) \quad (1.2.2)$$

$$MgO(s) + Al_2O_3(s) = MgAl_2O_4(s) \quad (1.2.3)$$

$$2Al(l) + 3/2\ O_2 = Al_2O_3(s) \quad (1.2.4)$$

$$2Mg(l) + O_2 = 2MgO(s) \quad (1.2.5)$$

$$3Mg(l) + Al_2O_3(s) = 3MgO(s) + 2Al(l) \quad (1.2.6)$$

As pointed out by Levi et al. [23], reaction (1.2.2) will be more predominant than reaction (1.2.6) thermodynamically, when Mg content is not greater than 4 wt% in the temperature range from 650 to 900°C (see Tables 1.1 & 1.2). Also, reaction (1.2.3) is difficult because it occurs in the solid state. Thus, reactions (1.2.1) and (2.2.2) determine the formation of $MgAl_2O_3$. Mcleod [35] gave the stability diagrams for MgO-$MgAl_2O_4$ and $MgAl_2O_4$-Al_2O_3 equilibria (see figures 1.1-1.2). According to his diagrams, the required Mg concentration for the formation of MgO is only about 1 wt% at 680°C , whereas at higher temperatures such as 800°C, it is about 1.6 wt% Mg.

Cappleman and Clyne [29], did not find interfacial reaction products at σ-Al_2O_3 fibres/Al-(9.5 ~ 11 wt%) Mg interfaces, owing to the short mixing time during fabrication by infiltration. Petitcorps [30] and Molins [31]

Table 1.1 Free Energy Changes for Different Reactions

(ΔG in KJ/mole, at 900°C) [23]

Reaction	2pctMg	4pctMg	8pctMg
$2[Al]+3/2(O_2)=<Al_2O_3>$	-1388	-1391	-1401
$[Mg]+1/2(O_2)=<MgO>$	-508	-509	-512
$<MgO>+<Al_2O_3>=<MgAl_2O_4>$	-28	-28	-28
$[Mg]+4/3<Al_2O_3>=<MgAl_2O_4>+2/3[Al]$	-39	-43	-52
$[Mg]+1/3<Al_2O_3>=<MgO>+2/3[Al]$	-33	-46	-73
$[Mg]+2[Al]+2(O_2)=<MgAl_2O_4>$	-1888	-1915	-1962

Table 1.2 Free Energy Changes for Different Reactions
(ΔG in KJ/mole, at 727°C) [11]

Reaction	ΔG
$<MgO>+<Al_2O_3>=<MgAl_2O_4>$	-47/mole of MgO
$[Mg]+4/3<Al_2O_3>=<MgAl_2O_4>+2/3[Al]$	-71/mole of Mg
$[Mg]+1/3<Al_2O_3>=<MgO>+2/3[Al]$	-39/mole of Mg
$[Al]+1/4<Al_2O_3>=3/4(Al_2O)$ *	-22/mole of Al
$[Mg]+<SiO_2>=<MgO>+[Si]$	-128/mole of Mg

Symbols: <Solid>, (Gas), [in solution]

* Data obtained from refs.[41], at 800°C

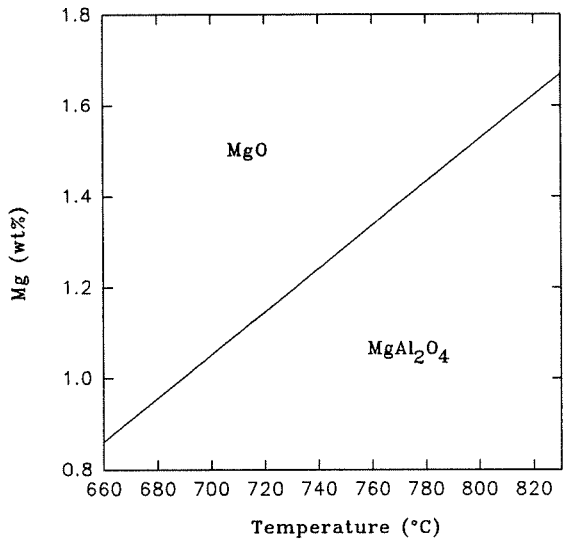

Figure 1.1 Composition/Temperature Stability Regions for the Al_2O_3-MgO Equilibria

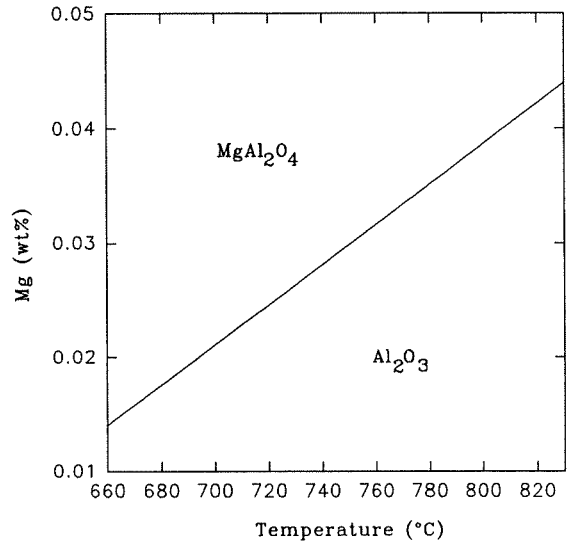

Figure 1.2 Composition/Temperature Stability Regions for the Al_2O_3-$MgAl_2O_4$ Equilibria [ref.35]

studied the Saffil Al_2O_3 fibre (with 3%-4% SiO_2)/Al-Mg (Mg from 0.3~2.2 wt%) system. A mixture of MgO and $MgAl_2O_4$ was observed at interfaces. They suggested that the formation of MgO and $MgAl_2O_4$ arise from the following chemical reactions:

$$SiO_2(s) + 2Mg(l) = 2MgO(s) + Si(s) \quad (1.2.7)$$

$$Mg(l) + 2Al(l) + 2SiO_2(s) = MgAl_2O_4 + 2Si(s) \quad (1.2.8)$$

The reaction between Mg and Al_2O_3 was not emphasized. Hallstedt [11] calculated the reaction kinetics in pure Mg-Al_2O_3 crystal system and concluded that the reaction between Mg(l) and Al_2O_3(s) is impossible during fabrication of the composites because the interdiffusion of Mg^{2+} or Al^{3+} through the MgO or $MgAl_2O_4$ layer is very slow (at 727 °C, $D^{MgO}_{Al} \sim 3x10^{-16} cm^2/s$, $D^{sp}_{Al} \sim 2x10^{-14} cm^2/s$). Karlsen et al. [129] also suggested that trapped air bubbles by particles be the main oxygen source for forming MgO and $MgAl_2O_4$ at Al(Mg)/Al_2O_3 interfaces. Weirauch [147] found no reaction product at the interface of Al-3 wt% Mg/sapphire after 24h at 800°C by optical and scanning electron microscopy, but with 6 wt% of Mg, a mixture of spinel and alpha alumina existed at the interface. A reaction between Al-3 wt% Mg and MgO, forming spinel, was observed under the same conditions. These results should be explained both thermodynamically and kinetically.

Pfeifer [32] studied the interfacial reaction in the α-alumina fibres/magnesium alloy (ZE41A) composite. A reaction layer of MgO with an average thickness of 100 nm

was found. The size of the MgO particles was found to be about 10 nm ~ 100 nm. It is proposed that the growth of the reaction zone was controlled by a "Seepage" mechanism involving infiltration of liquid magnesium between MgO crystals. The reaction zone nucleation starts as the Mg in liquid aluminum first comes in contact with the alumina grains. The MgO grains nucleate and grow on the edges of the alumina grains. MgO nucleation occurs further into the original alumina grains as molten Mg seeps in between already nucleated, and growing MgO grains, and reacts with the Al_2O_3 at the pre-existing reaction zone/Al_2O_3 interface. This seepage process continues until the MgO grains close to the matrix/reaction zone interface have grown large enough to close off the seepage spaces between these grains, or until the molten metal is solidified. This mechanism can explain the formation of the limited thickness of the reaction zone. As shown by Pain [27], the reaction between Al-Mg (4 to 8 wt%) and Al_2O_3 particles can go into the middle of a 80 μm diameter alumina particle without stopping at 720-790°C. Lloyd et al. [128] indicated that the reaction between Mg and Al_2O_3 can even take place in the solid state in 6061/Al_2O_3 composite. It should be noted that the role of aluminium released during these reactions and its diffusion behaviour have not been clearly explained in these studies.

From the previous review, it is evident that the interfacial reactions are different in the various investigated systems. This could be caused by the different fabrication conditions, alloy compositions and volume fractions of the reinforcing materials (Mg consuming increases with the amount of reinforcements) which were used by the various

investigators.

1.2.3 Enrichment of Mg at the Interface between Al(Mg) Alloy and Reinforcement

In many Al-(Mg) matrix based composites, segregation of Mg at the interface between matrix and reinforcement is observed [2,9,16,17,18]. In 5083/SiCp as-cast materials, segregation of Mg is also found. Generally, the segregation can be caused by several mechanisms.

Firstly, as in monolithic Al-Mg alloys (Malis [19]), Mg can segregate at grain boundaries and free surfaces. The segregation of Mg is governed by thermodynamic factors related to the decrease of grain boundary energy, interface energy or surface energy. For example, in quenched samples, non-equilibrium segregation is established by vacancy drag of solutes as defects migrate to the sinks (grain boundaries). In composite materials, the interface between matrix and reinforcement may also act as a vacancy sink during rapid cooling and the Mg solute is dragged into it.

Secondly, the segregation of Mg is caused by the reaction between Mg and the SiO_2 layer on the surface of SiCp or between Mg and the oxygen which was trapped during the fabrication process [2,9]. These reactions form MgO or $MgAl_2O_4$ at the

interfaces [2,9,20] and can improve the wettability and form a diffusion barrier for reaction between liquid Al and SiCp [1,21].

Thirdly, nucleation of the primary solid does not occur on the reinforcement surface during solidification. In the case of an alloy, the solid phase will avoid (or push) the reinforcement as it grows. Consequently, the last portion of the metal to solidify will be located close to or at the reinforcement/matrix interface with the solutes pushed to the interface by the liquid/solid front. Therefore, enrichment of solute (Mg) is observed [17,22].

As pointed out by L'Esperance et al. [101], segregation of Mg at the interface of 2124/Si_3N_4-whisky composite plays an important role in its high strain rate superplastic behaviour. Because the Mg segregation profile often extends over a very small distance (about 10-50 nm), EDS X-ray microanalysis of this segregation often introduces a large statistical error, owing to the small probe size used. Since the limit of the spatial resolution of the microanalysis, it is still not clear whether metallic Al or Mg exist inside SiC and how those solute atoms such as Mg and Cu distribute near reinforcements [8,59,101]. Therefore, a deconvolution technique is required to quantify the Mg or other solute distribution at the interfaces and to determine the presence of solute atoms in the reinforcements.

1.2.4 Determination of the True Composition Profile by Analytical Transmission Electron Microscopy (AEM)

Segregation of solute atoms at the interface between different phases, or that between reinforcing particle and matrix, and at the grain boundaries, often has a tremendous influence on the properties of materials. Nowadays, even though the spatial resolution of microanalysis is as good as about 10 to 50 nm in scanning transmission electron microscopy (STEM) [37], it is still insufficient for many cases. For example, in equilibrium segregation, the segregation layer is generally considered to be confined to within a few nm or a few atomic layers of a boundary [38]. In order to determine the true composition in this layer, a very small probe must be used. However, the decrease of the electron probe size results in a decrease of the total X-ray count and an increase of the analysis statistical errors. At the same time, this causes an increase of both contamination and probe shift. With large probe sizes, the spatial resolution is not good and the measured composition is only an average value for the volume sampled by the electron beam. Thus, the measured composition is usually lower than that of the true composition. A mathematical deconvolution technique has been used in order to obtain the true composition profile as reported in [38,39].

The spatial resolution of X-ray microanalysis in (STEM) is controlled by elastic scattering of the electron probe. The measured characteristic X-ray intensity Ix' is a

convolution of the distribution of electron flux intensity I(v) and the actual solute composition C(v) within the total sampled region of the foil [38,39],

$$Ix' = K\int_V I(V) * C(V)\, dV \ldots\ldots (1.2.9)$$

where K is a constant that describes the efficiency of X-ray generation, emission and detection for a particular element of interest.

Doig and Flewitt (1982) [38] developed an equation which describes the intensity distribution of the electron beam (I) as a function of radial distance (r) from the probe centre at any depth (t) of the specimen:

$$I(r,t) = \frac{Ie}{\pi(2\sigma^2+\beta t^3)} \exp\left(-\frac{r^2}{2\sigma^2+\beta t^3}\right) \ldots\ldots (1.2.10)$$

where Ie is the total incident electron current, σ is the standard deviation of the incident probe current distribution (a measurement of the incident probe size) and $\beta = 500(4E^2/E)(\rho/A)$ nm, E the electron energy (keV).

If the composition profile is only a function of the distance (y) from the analyzed boundary, we can use the following expression [40]:

$$C'(y_i) = \int_0^t \int_{-y}^{+y} \int_{-x}^{+x} I(x,y,t) C(y-y_i)\, dx\, dy\, dt \ldots\ldots (1.2.11)$$

$C'(y_i)$ - experimental composition profile, $C(y)$ - the true composition profile, y_i - the distance between the centre of the electron beam and the peak of composition profile.

There are several ways to determine $C(y)$. First, a physical realistic functional form for $C(y)$ can be assumed and inserted into equation (1.2.11); the values of $C'(y)$ can be calculated and compared with the experimental values [38,39]. The coefficients of $C(y)$ are then adjusted until the calculated values of $C(y)$ provide the best fit to the experimental values. Second, direct deconvolution of the terms $I(x,y,t)$ and $C(y-y_i)$ from the measured $C'(y_i)$ can be accomplished by Fourier analysis [41]. With this method, it is not necessary to assume a composition profile (which is sometimes impossible). However, Rapperport pointed out (1969) [41] that the solution of the equation often has very large errors, when the noise of the input data is large. Also, the calculation of the Fourier transformation is very complicated. With a third approach, Romig [42] used a simple way to convolute (graphically or numerically) the X-ray generation function with an assumed actual composition profile in order to calculate the observed composition profile and to avoid the difficulty of the explicit deconvolution.

According to Romig [42,43], the convolution process simply involves integrating the area under the assumed composition profile intersected by the cross section of the X-ray generation volume at a certain position, and rating the result to the total area of

the cross section of the X-ray generation volume. The ratios of the integrated areas will change as the beam is moved across the interface. A direct plot of the ratios versus the beam positions will determine the convoluted profile [41]. The X-ray generation volume can be determined by either the single scattering model or Monte-Carlo simulations [43]. The measured X-ray intensity for the solute element is plotted as a function of beam position to produce the convoluted composition profile. Usually, the error function profile or a slab profile is used as the assumed "true" composition profile.

The problem in using the slab profile is that when the ratios of the areas are used to do the convolution, the thickness of the slab must be very small relative to the diameter of the X-ray generation volume. If the thickness (δ) of the slab is thicker than one third or fourth of the diameter of the X-ray generation volume, the error from these calculations become significant. Some mistakes were found in calculating the area of the intersection and the volume of X-ray generation [42, 43]. The integration intersection area was only the half of the hyperbola [42] and the calculated X-ray generation volume [43] was four times larger than the true volume because of the errors made in the calculations. Thus, it can be seen that the calculated thickness of the solute enriched layer in reference [42] was only half of that in reference [43] and both of them were larger than that obtained using Auger spectrometry (the apparent and actual compositions in both reference are the same).

1.2.5 Residual Stresses and the Stress State in the Matrix Near the Reinforcements in MMCs

In SiC or Al_2O_3 reinforced Al alloys, owing to the large difference (6:1) between the thermal expansion coefficient of the matrix and that of the reinforcement, a misfit strain between the SiC or Al_2O_3 and the matrix is produced during temperature changes. In certain cases, such as where the composite is cooled from elevated temperatures of annealing or processing, the misfit strain can be very large. As a result, a large number of dislocations will be produced and elastic residual stresses will also exist in the matrix near the reinforcement after cooling down to room temperature [45]. The aging behaviour and other mechanical properties of the composites will then be affected. R.J. Arsenault and his co-workers [91] have observed in-situ the generation of dislocations near SiC due to the different thermal contraction using high voltage electron microscopy. The density of dislocations observed in in-situ TEM foils was about $10^{13}/m^2$ after cooling down from about 400°C. A simple prismatic punching model was developed to account for the relative dislocation density due to the different thermal contraction. The theoretical estimation was claimed to agree with the experimental results. Flom et al. [90] also measured the plastic strains and the extent of the plastic zone due to different thermal expansion by direct observation of slip bands on the polished surface of Al/SiCp composites using Zeiss interference microscopy. The combined plastic shear strains at the Al-SiC interface were found to be about 1-1.32%.

Stobbs et al. [108] found that the density and the orientation of the precipitates near the SiC particle in 2024 Al alloy are affected by the residual stresses around the SiC particles.

According to Lloyd [46], there is currently no satisfactory model to theoretically evaluate residual stresses. A. Levy (1990) used an elastoplastic finite element analysis method to characterize the magnitude of the residual stresses in 20 vol% SiCw/5456 aluminum alloys. He found that the longitudinal stress is in compression near the whisker ends and in tension near the centres. He did not, however, confirm his predictions by experimental results [47]. The calculations of Teodosiu et al. also showed that the radial residual stress is compressive and that the hoop stress is tensile near the particle in particle reinforced composites [58]. Almost all the theoretical models are based on assumptions such as the particles are spherical and are uniformly distributed etc. [56,57,58]. Theoretical models are therefore generally very much simplified. Attempts have also been made to determine the local residual stress experimentally. For example, X-ray diffraction [151,152] and neutron diffraction [153] have been used, but their spatial resolution is often more than a few μm to a hundred μm. Thus, only bulk average stresses are determined. In pure Al/SiC-particles composites, a tensile average stress of 33 MPa was measured using X-ray diffraction by Sun et al. [151]. Kuntz et al. found that the stress values near reinforcements (130 MPa) measured by X-ray diffraction were usually lower than that obtained by calculations (180 MPa) and they were below the yield stress of the metal matrix [152].

However, it was noticed that the analyzed volume in above study was 50 x 50 x 1000 μm^3. Moreover, usually the penetration depth of neutrons is larger than that of X-ray. Ashby-Brown contrast and Moirè fringe images in TEM can be used to determine the strain field and the stresses around small precipitates, but it can only be used in samples with particles smaller than the foil thickness [48,52]. The convergent beam electron diffraction (CBED) technique in TEM has been developed to measure changes in the lattice parameter and thus the residual strain in materials. The analyzed area is defined by the incident probe (which usually can be as small as a few nanometres) [49]. The limit of the measurement accuracy could be $\pm$ 0.0005 Å or $\pm$ 0.03° [50]. However, the interpretation of the CBED pattern is still not easy, because the change of parameter caused by elastic residual stresses is often too small to produce an observable shift of the HOLZ lines. Moreover, relaxation of the residual stresses in a TEM thin foil makes the interpretation of the stress state in materials even more difficult. As a result, the measured misfit strain is often different from that in bulk specimens [53]. S.J. Rozeveld measured the residual strains in Al-SiCw composite using the CBED technique. His results showed that the residual strains near the ends of the whiskers approach the yield limit of the matrix. It is not possible, however, from his results, to know the strain direction. Moreover, the magnitude and the direction of the residual stresses are not known. Another important aspect, which should considered when using the CBED technique in composites, is the segregation of solute atoms near the interfaces (for example the segregation of Mg) as this will also affect the local lattice parameter.

1.3 Deformation Mechanisms in Discontinuously Reinforced MMCs

1.3.1 Strengthening Mechanisms

Although discontinuously reinforced composites generally have a strength inferior to that of composites with continuous fibre reinforcements, they have several advantages: the properties are often isotropic, they can be mechanically worked with processes similar to those of conventional wrought alloys and they are considerably cheaper. As increasing amounts of strong ceramic particles are introduced into a metallic matrix, the elastic modulus increases and the density changes, both in a predictable way [67,80,87]. The yield stress and UTS usually increase (about 100 to 150 MPa) [67,78,82,83,85]. A much larger initial rate of work hardening is obtained [64,68]. However, the ductility and fracture toughness generally decrease significantly [67,69,78,84]. The most obvious improvement in the mechanical properties is the specific stiffness, which may be as much as twice that of a conventional wrought alloy [87]. In order to maintain the fracture toughness to an acceptable level, the volume fraction of the reinforcement should not be higher than 30% [67]. The strength of metals containing long fibres can be successfully modelled by the shear lag model (Kelly & Macmillan 1986) [109] which was originally developed by Cox [110]. The role of the matrix is to transfer the applied stress to the fibres, and the UTS is reached when the fibres fracture. If a composite contains strong aligned fibres of less than a critical length, then the UTS is reached when debonding between the fibres and the matrix

occurs and that the fibres are pulled out of the matrix. The yield stress of the composite is then given by the following equation:

$$\sigma_{cy} = \sigma_{my}(1-V_f)+\tau_i V_f L/d \qquad .....(1.3.1)$$

where σ_{my} is the matrix yield stress, and L and d are the length and diameter of the fibres respectively, V_f is the volume fraction of the fibres and τ_i is the interface shear strength between the fibre and the matrix which is supposed to be half of the σ_{my}. In discontinuously reinforced composites, both the shear lag and the Eshelby models are used to estimate the stiffness and yield stress [87]. Both of them, generally predict a yield stress which is much less than that determined experimentally with a decrease of the aspect ratio (smaller than 4). Nardone and Prewo [75] have pointed out that equation (2.3.1), often referred to as a shear lag analysis, considers only load transfer to the fibre via the shear forces, and that tensile load transfer at the fibre ends is ignored. Their modified shear lag model gives the composite yield stress as:

$$\sigma_{cy} = \sigma_{my}[\ 0.5V_f(L/d + 2) + (1-V_f)] \ .....(1.3.2)$$

In the case of a SiC platelet,

$$\sigma_{cy} = \sigma_{my}\{\ V_f[1+(L_2+t)s/4L_2] + (1-V_f)\}...(1.3.3)$$

where $s=2L_1/t$ with $2L_1$ equal to the length of the platelet edge parallel to the applied stress and t is the thickness of the platelet and L_2 is the width of the platelet. As pointed out by M. Taya and R.J. Arsenault [79,87], this modified model still underestimates the material strength.

Arsenault and Fisher (1983) proposed that the increased strength observed in Al/SiC composites could be accounted for by a high dislocation density in the aluminum matrix due to the large difference in CTE [79]. According to their prismatic punching model [91], the increase in yield strength $\Delta\sigma$ is calculated by:

$$\Delta\sigma = \alpha\mu b\rho^{1/2} \quad \text{.....(1.3.4)}$$

$$\Delta\sigma = \alpha\mu b\ [V_r B\epsilon/(1-V_r)bt]^{1/2} \quad \text{.....(1.3.5)}$$

$$\epsilon = \Delta CTE*\Delta T/2 \quad \text{.....(1.3.6)}$$

where α is a numerical constant, μ is the shear modulus of the matrix, b is the Burgers vector and ρ is the dislocation density. B is a constant which depends on the shape of the reinforcement, V_r is the volume fraction of the reinforcement and t is the minimum dimension of the reinforcement. ΔCTE and ΔT are changes of CTE and temperatures.

Derby and Walker (1988) [93] have investigated the hardness increment of Al-SiC particle composites as a function of quenching temperature and volume fraction. They found an approximate linear relationship between hardness increment and the

temperature drop on quenching and between the hardness increment and the volume fraction. They ascribed this hardness increment to dislocations generated on quenching. There is a large difference between the yield stress and work hardening rates of composite specimens quenched from 550°C and from 200°C. However, calculation of the increase of the strength by equations (1.3.4)-(1.3.6) gives an increment on quenching from 550 °C of 20 MPa, which is considerably less than the experimental values of 100 to 200 MPa [78]. This discrepancy suggests that the interpretation of the strengthening of the composite as a result of quenching in terms of the dislocations generated from thermal contraction is inadequate [78]. Miller and Humphreys [70] have examined the various strengthening mechanisms that may be occurring in a particle reinforced MMC, and suggested that the strengthening is due to a variety of mechanisms:

- Classical composite strengthening (load transfer).
- High dislocation density due to dislocation generation as a result of differences in CTE on cooling from high temperatures.
- Residual elastic stresses which are also caused by large difference of CTE between reinforcement and matrix. As Withers et al.(1987) [111], Levy et al.(1990) [47], and Arsenault and Taya (1987) [78] demonstrated, the effect of these residual stresses on the mechanical properties depends on the shape of particles. For whiskers aligned in the direction of testing, the residual stress is anisotropic, resulting in a net residual tensile stress in the fibre direction. Therefore the yield stress in compression

is expected to be higher than the yield stress in tension.

- Grain and subgrain strengthening. During thermomechanic processing, particle reinforced MMCs may recrystallise. For particles with a diameter greater than about 1 micron, recrystallisation may occur by particle stimulated nucleation [78]. The resultant grain size (from 1 to 10 microns) is often considerably finer than that found in an unreinforced alloy which will be given by:

$$D=d[(1-V_r)/V_r]^{1/3} \qquad .....(1.3.7)$$

where D is the grain size. According to the Hall-Petch equation ($\Delta\sigma_{gb}=K_y/D^{1/2}$, for aluminum $K_y=0.1\text{-}0.15MN/m^{3/2}$), the increment of the yield strength can be 50 MPa for a grain size of 10 μm and 150 MPa for 1 μm grains.

A subgrain structure is also often found in the matrix which may come from the thermomechanical processing or from the recovery of the residual dislocations. Its contribution to strengthening can not be ignored. The Hall-Petch relation can also be used to calculate the increment ($K_y=0.05MN/m^{3/2}$).

- Orowan strengthening. The amount of strengthening due to Orowan by-passing of the particles by the dislocations must also be considered, especially, when the reinforcement is smaller than 1 μm.

- Matrix and interfacial precipitation.

- Strengthening arising from constrained plastic flow and triaxiality in the ductile

matrix due to the presence of a brittle reinforcement [83].

- Work hardening. Usually, composites exhibit much greater rates of work hardening at low strains than their parent matrix alloys [79,112]. The work hardening of an MMCs will be influenced by residual dislocation structure. However, there are other factors that will increase the work hardening rate of the composite compared with that of the matrix alloy. First, in the early stages of deformation, load will be transferred from the matrix to the reinforcing phase by means of Orowan loops or some equivalent mechanism. The expected contribution to the strength due to the unrelaxed dislocation loops is given by:

$$\Delta\sigma = 4.5 G V_r \epsilon \quad \text{.....(1.3.8)}$$

where G is the elastic modulus and ϵ is the true strain. At higher strains the particle will contribute to work hardening due to the creation of geometrically necessary dislocations.

As pointed out by Humphreys [78], all the above contributions need to be taken into account. Their magnitude depends on the specific composites and the specific thermomechanical treatment, and they can not be added linearly.

Arsenault et al. [95] have emphasized that the most significant contribution to the strength of particle reinforced MMCs arise from the strengthening of the matrix, i.e.

the strengthening due to an increase in dislocation density generated by the difference in the CTEs of the matrix and the reinforcement. The relations between the dislocation density and SiC volume fraction and between the dislocation density and particle size are examined. They found that the dislocation density increased with increasing SiC volume fraction increasing, and decreased with increasing particle size. Predicted increases in yield strength are given in Tables 1.3 and 1.4. They pointed out that a good bond at the interface was necessary to produce a high dislocation density in the matrix. Taya et al. [96] suggested that another major contribution to the strengthening be the back stress which is the average internal stress in the matrix as a result of particle resisting the plastic flow of the matrix. They calculated the contribution of the back stress by the modified Eshelby's equivalent inclusion method for finite volume fractions of fillers. The prediction based on both Arsenault's model [95] and on Taya's model [96] seems correct for the composites used in their experiments. However, it is not known whether these models are still valid when they are used for another composites, which may be fabricated using different methods and have different matrix microstructure (e.g. grain size), different reinforcements and different nature of interfaces between matrix and reinforcement. Kamat et al. [85] suggested that in alumina particle reinforced Al composites, the initial yield depends on both shear lag and structural effects while subsequent flow is dominated by shear lag. Recently, Shi et al. [124] suggested that the matrix plasticity in a whisker reinforced SiC/Al composite be characterized by the expansion and interconnection of the thermally induced plastic zones under the external tensile load. The plastic zone

Table 1.3 Predicted Increase in Yield Strength of 20 Vol.% SiCp/1100 Al Matrix and Experimentally Measured Values as a Function of Particle Size

Particle size (μm)	$\Delta\sigma_d$(MPa)	$\Delta\sigma_{sg}$(MPa)	$\Delta\sigma_{rs}$(MPa)	$\Delta\sigma_{pd}$(MPa)	$\Delta\sigma_{ep}$(MPa)
0.5	126.6	131	0	257.6	153
9	99	69	17	151	88
70	79	20	17	82	69
250	59.7	0-13.8	17	42.7-56.5	26

Table 1.4 Predicted Increase in Yield Strength of 6061 Al Alloy/SiCw as a Function of Volume Fraction of SiC Whiskers

Volume (vol.%)	$\Delta\sigma_d$(MPa)	$\Delta\sigma_{sg}$(MPa)	$\Delta\sigma_{rs}$(MPa)	$\Delta\sigma_{pd}$(MPa)	$\Delta\sigma_{ep}$(MPa)
1	37.7	0	1.7	36	6.9
5	56.6	7	8.6	55	52
20	70	48.3	34.5	83.8	100

****

$\Delta\sigma_d$(MPa)----Predicted increase due to the increased dislocation density

$\Delta\sigma_{sg}$(MPa)---Predicted increase due to the reduced subgrain size

$\Delta\sigma_{rs}$(MPa)---Predicted average tensile residual stress

$\Delta\sigma_{pd}$(MPa)--- $\Delta\sigma_d + \Delta\sigma_{sg} - \Delta\sigma_{rs}$

$\Delta\sigma_{ep}$(MPa)---Increase of the yield stress obtained from experiments

****

expands initially in the zones with tensile residual stresses parallel to the external tensile axis (i.e. the longitudinal surfaces of the whiskers). It also indicated that the

strengthening was mainly the result of the thermally induced matrix work hardening at the tip of the whisker. Such strengthening accounts for 50% of the total composite strengthening as predicted by finite element methods (FEM).

The above review shows that several possible strengthening mechanisms and different models are used to explain strengthening of MMCs. The relative contributions of different mechanisms to the strengthening of composites, fabricated or processed by different methods or different conditions, are still unknown. An important problem is that the strengthening mechanism in MMCs may be different in different systems, because the properties of different matrixes and of different reinforcements are different; and also for each system, the interfacial nature and the geometry of reinforcements have to be taken into consideration. In order to better understand the contribution of the different strengthening mechanisms of MMCs, much more experimental data based on different alloys, different fabrication processes and different thermomechanical treatments are required.

1.3.2 Fracture Mechanisms

It has been found that the fracture of aluminum alloy matrix composites is often proceeded by a mechanism of ductile (dimpled) rupture of the matrix and the decohesion of the reinforcement/matrix interface or cleavage cracking of the SiC or Al_2O_3 reinforcements [62,63,67,71,76,77,85,94]. This mechanism can be broken down into

three stages: nucleation, growth and finally coalescence of voids to give total failure of the materials. A void will nucleate at the particle/matrix interface or within a cracked particle when the local stress exceeds the stress necessary for particle cracking [72,73,74]. Brown and Embury (1973) [113] suggested a model to explain the ductile fracture of the materials with low volume fraction of particles, which concentrates on the processes of void growth once voids have formed. The model assumes that void coalescence occurs when the void elongates along the tensile axis to a size equivalent to the initial intervoid spacing. This model concentrates on the amount of growth strain required before the voids reach the critical size for linkage. With increasing volume fraction of particles for a given mean particle size, the interparticle spacing decreases and the amount of growth strain required also decreases. Assuming that all the particles have a same size and are distributed uniformly, the particle volume fraction at which the growth strain becomes zero is calculated to be 16%. In real materials with random particle distributions, areas of local volume fraction greater than the mean value will be found, suggesting that the critical condition be reached in materials with even lower mean values of particle volume fraction than the 16% level. If the possibility of clustered microstructure is considered, an even more exaggerated effect might be expected. This has been borne out in the present study where fractography of the high volume fraction material has shown limited void growth and voids with a same size equal to the size of the associated particles [71]. It therefore appears that void nucleation is the critical stage in the fracture of MMCs [62,94].

Focusing on the void nucleation process, a number of microstructural factors must be considered [94]. The matrix yield strength and the work hardening behaviour are two important variables. The primary role of increasing the yield strength is to activate a greater number of potential nucleation sites by causing more particle/matrix interfaces to reach their decohesion stress or increasing the frequency of particle cracking. Work hardening behaviour has a similar effect on nucleation, higher work hardening resulting in a greater stress in the vicinity of a particle. This is in contrast to the role of work hardening in the void growth process, where higher work hardening levels restrict the growth of stable voids and increase strain to fracture and toughness. Another important variable is the bond strength between reinforcements and matrixes. It is generally agreed that the stronger this bond is, the greater resistance to void nucleation at the interface is. It is expected that as the bond strength increases, greater stress can be transferred to the particle prior to interface decohesion or particle cracking [2]. Deformation modelling of these composites by Christman et al.[83] has indicated that the flow properties of the matrix are likely to be significantly altered by the presence of the particles. This model indicates that the hydrostatic component of the stresses is significantly raised by particles, and the distribution of particles is an important factor in the model. Arsenault et al. [63] also pointed out that plastic deformation initiated in a clustered region because the stresses would be distributed in such a way that the clusters would bear more load than the rest of the matrix. It has been demonstrated experimentally that void nucleation occurs preferentially in the region where the local volume fraction of particles are high, due to the increased stress

concentration [61,62,64,94]. The distribution of particles will therefore greatly affect the tensile ductility of composites. As pointed out by many researchers [60,61,67,132], the ductility is significantly increased in extruded materials because extrusion reduces particle clustering. Increasing the volume fraction of the reinforcement will lead to a decrease of the fracture strain [67,71]. The question of particle size effects on void nucleation process continues to be controversial. Certain experiments have shown a particle size effect, while others have not [71,80,93]. Usually, in the case of decohesion-related nucleation (low interfacial strength), the particle size effect is smaller than in the case of particle fracture related nucleation. Particles of diameters greater than 8-10 μm show a greater tendency to crack, and this has been interpreted in terms of the increased chance of flaws occurring in larger particles [19,68,73,74,80,85,114]. Neither the dislocation pile-up model nor the shear lag model can satisfactorily explain cracking of SiC or Al_2O_3 particles in Al matrix composites, without considering the flaws inside the particles (the strength of single crystal SiC is about 2000 MPa) [76,80]. These models, however, are important to predict the concentration of stresses on the particles which have been indicated by the effects of the particle aspect ratio, matrix strength and the imposed strain on the fracture of the particles [68,80,107]. Thus, the intrinsic strength of the reinforcing particles could be an important parameter in determining composite ductility [19]. Stacking faults, dislocations, microcracks and a rough particle surface caused by the particle producing process or attack of the particles by matrix during composite fabrication are typical flaws expected in the particles [59,77]. Mummery and Derby [71] found that there is a change in fracture mechanism

from decohesion to particle cracking when the size of SiC particles is larger than 10 μm. They also indicated that for the lower volume fraction material (5 vol.%), the strain to failure increases with increasing particle size, whereas the opposite trend is observed at the higher volume fraction (e.g. 20 vol.%), because for the high volume fraction composites, the nucleation event dominates the total fracture process owing to the limited growth strain and for the low volume fraction materials, the void growth will determine the fracture process. Introducing a SiO_2 layer on the surface of the SiC particles by high temperature oxidizing or CVD (chemical vapour deposition) will decrease the attack of particle by molten Al [2,6]. At the same time, it should be noticed that the influence of the oxide layer on the mechanical properties is complex. Some studies reported that the interface strength was reduced by the oxide layer because spinel was formed at the interface as a result of interfacial reactions [2,125]. The UTS of the composite was reduced and the ductility was increased [2]. Knowles et al.[125] indicated that oxidation of the SiC lead to a reduction in fatigue crack growth resistance at higher values of stress intensity range. Le Petitcorps et al.[127] found that with an increase of the thickness of SiO_2 layer, the interfacial shear strength decreased for high temperature oxidized SiC, increased for CVD oxidized SiC in composites of SiC/(Al-7Si-0.6Mg). Johnston et al.[126] found that the shear strength of Al(Mg)/Al_2O_3 interface was greater than or equal to the shear strength of the matrix alloys, and increased with increasing Mg content in the matrix alloy (from 1wt% to 4.8wt% Mg). The interfacial reaction products (spinel or MgO) did not decrease the interfacial shear strength. Cho et al.[130] observed that the strength of the Al(4%Mg)/spinel interface

was stronger than that of Al(4%Mg)/Al_2O_3 interface.

Having determined that void nucleation is promoted in regions of high volume fraction of particles, we will ask if the concentration of particles is higher on the fracture surface than in the bulk material. Different answers were given by different studies [76,77,114]. You [76] found that the average number of particles on a given length of the fracture is comparable to that on a random line of the same length on a polished metallographic sample. Similar results were obtained by comparing the area fraction of particles on the fracture surface to that on the polished surface. Different heat treatment procedures did not affect the results apparently (2124/20%SiC composites, as-extruded, treated by naturally aged and overaged conditions). Roebuck [77] found that the fracture path passed through a similar number of particles as that on the polished surface, in 6061Al/SiC composites. Flom and Arsenault [114], in studying the fracture of 1100Al/SiC composites (made by powder metallurgy, extruded and hot rolled), found that there were more SiC particles along fracture path than that along other paths. They concluded that the crack follows the SiC particles. The results of Lloyd [80], show that for the same composite (6061Al/SiCp 10-20 vol.%, 6-10 μm in diameter), the concentration of the SiC particles on the fracture surfaces is different for different heat treatments. There is a higher density of particles on the fracture surface of aged samples, but in solution treated samples, the density is comparable to that in the matrix. Lloyd [80] also indicated that the fracture initiates in the particle clusters, by particle cracking and/or decohesion of the matrix between particles, and final fracture

is achieved by fracture through the matrix between clusters. The failure process appears to be controlled by the large triaxial stress intensification exerted on the matrix between particles in the cluster as a results of the constraint of the surrounding elastic particles. For particles separated by a matrix layer of a quarter of the particle diameter, stresses three times higher than the flow stress is generated in the layer of the matrix. You, Thompson et al. [76] proposed a fracture mechanism in which the matrix fails first, followed by fracturing or decohesion of the particles. In other words, cracking of the reinforcement or decohersion of the matrix/particle interface occurs, but only as a result of matrix failure. The dominant failure mechanism is failure in the matrix. The reinforcing particles contribute to the failure process primarily by imposing high levels of constraint on the matrix deformation and by raising the stress in the matrix to a level significantly greater than that normally associated with matrix failure. The proposed mechanism describes failure as occurring through the matrix, not specifically avoiding the particles nor specifically linking them. The factors influencing the yield and tensile strength of SiC/Al composites have been studied by Mcdanels [67]. He pointed out that the Al matrix used for the SiC/Al composites was the most important factor affecting yield strength and ultimate tensile strength of those composites. The results show that SiC/Al composites, with higher matrix strength such as 2024/2124 or 7075 Al, have higher strengths but lower ductility.

Different strengthening and fracture mechanisms have been reviewed above. We notice that most of the proposed mechanisms are based on only one or few composites.

It is particularly difficult to find reliable published experimental data for the mechanical properties of the metal matrix composites. Because the quality of the material is so variable, mainly due to processing problems, supposedly identical composites often have widely different properties [78]. As processing and production control improve, the properties of the composites will undoubtedly improve. The composite with a 5083 Al matrix reinforced by SiC whiskers (20 vol.%), studied by Mcdanels [67], failed in a brittle manner, with an ultimate tensile strength of about 380 MPa and a failure strain of about 1%. The reason might be that the addition of SiC reinforcement to the solid solution strengthening matrix probably overstrained the lattice, and thus the alloy no longer had sufficient strain energy remaining to gain its potential strength and ductility. So far, few experimental data are available in the literature for the composites with the 5083 Al matrix.

1.3.3 The Portevin-Le Chatelier Behaviour in Aluminum Alloys

In Al-Mg alloys, 'jerky flow' is often observed on the stress-strain curves [140-144]. The discontinuous yielding observed during serrated flow is known as the Portevin-Le Chatelier (PLC) effect. Both the micro- and macroscopic concepts of this effect have been discussed in many studies on monolithic alloys.

The serration appearance in the stress-strain curves is usually associated with conditions for which the strain rate sensitivity of the flow stress becomes negative [140].

The microscopic reason for negative strain rate sensitivity is dynamic strain ageing (DSA) which is believed to arise from the interaction between diffusing solutes and mobile dislocations [142,143]. Gliding dislocations are temporarily held up by obstacles, e.g. forest dislocations. Solute atmospheres form on forest dislocations and then drain by pipe diffusion from the forest dislocations to mobile dislocations [142,144,150] (some models also assume that atmospheres are formed on (mobile) dislocations by bulk diffusion during the waiting time). Since DSA is thermally activated, it occurs only within a certain range of temperatures T and strain rates $\dot{\epsilon}$. The shape and amplitude of the serration curve are affected not only by the amount of strain, strain rate and temperature during deformation, but also by the composition and the grain size of the alloys [145,146]. This phenomenon is observed at both room temperature and higher temperatures (e.g. 250-300°C [143]). In Al-Mg matrix composites, introduction of the reinforcements into the matrix often causes differences in dislocation structure and in other microstructure features. However, a study of the PLC effect in metal matrix composites has not been reported to our knowledge.

1.3.4 Deformation at High Temperatures

The mechanical behaviour of MMCs at elevated temperatures is of interest for two reasons. First, many composites are produced as billets, which are subsequently mechanically processed, e.g. forging or extrusion. As their low temperature ductility is limited, mechanical working at elevated temperatures is necessary. Second, some

composites are of interest for creep resistant structure applications, and therefore an understanding of the high temperature properties is required.

Usually, as pointed out by Humphreys [78] the flow stress of the MMCs falls with increasing temperature, although generally not as rapidly as that of the matrix alloy. There is then frequently a rapid decrease of the flow stress in the temperature range 200-300°C to a reasonably constant level and a decrease in work hardening rate. At temperatures around 500°C, the flow stress of the composite may fall below that of the matrix alloy, and the strain rate sensitivity may increase. These effects have been attributed to the onset of grain boundary sliding in fine grained composites. The total ductility usually increases with increasing temperature. The evidence of intergranular failure was found at 500°C in 2124/SiCp composites. The work hardening rate of the composite is high at low temperatures due to the accumulation of glide dislocations at particles. At high temperatures, it is possible for dislocations accumulating at the particles to climb and if the rate of climb around particles is greater than the rate of dislocation accumulation, there will be no build-up of stresses at particles, work hardening rate will be low and no fracture induced by high local stresses. As shown by Almas & Humphreys (1988) [115], for a given particle diameter and at a certain strain rate, there is a critical temperature below which the stresses will accumulate at the particles. This information can be used to predict the conditions under which a particulate MMCs may be hot worked. Composite containing large particles will be more difficult to work.

1.3.4.1 Extrusion of MMCs

Many whisker or particle reinforced MMCs are thermomechanically processed by extrusion [60,61,67,94], because it can improve the microstructure and ductility of composites. Osman & Lewandowski et al. [61] extruded a composite of 2083 Al/SiCp (15 vol.%, 16 μm) in different conditions, and showed the effects of the extrusion on the microstructure and mechanical properties of the composite. Two extrusion ratios (8:1, 20:1) were used, and the extrusion temperature was 441°C. The experimental results indicated that extrusion could reduce particle clustering, but produced particle alignment along the extrusion direction. Further improvement in particle distribution and some reduction in particle size (particle cracking) are observed with higher extrusion ratios. The strength properties are not significantly affected by deformation processing, and the materials with a greater degree of deformation imposed during processing have higher elongation values for a given matrix condition. One of the important reason is the reduction of particle clustering by extrusion. Brusethaug et al. [60] compared the grain structure of the extruded composites (A356/SiCp, 15 vol.%, 20 μm) with the extruded unreinforced materials. For the reinforced materials the grain structure after extrusion was equiaxed, recrystallized (cooled in air) and less sensitive to the extrusion temperature. They indicated that the SiC particles thus seemed to have a great influence on the recrystallization kinetics. The typical grain size was 40-50 μm. Cho et al. [130] obtained a very fine grain structure (smaller than 0.18 μm) in Al(4 wt% Mg)/Al_2O_3(5 vol.%, 10.5 μm) and Al(4 wt% Mg)/spinel materials fabricated by

PM and then extruded at 380°C with a extrusion ratio of 36:1. Tensile properties were 676 MPa (UTS), 3.5 % (elongation) in the composites with Al_2O_3 reinforcement, and they were 741 MPa (UTS), 4.5 % (elongation) in those with spinel reinforcement. By hot rolling at 430°C, the materials had lower UTS (443 MPa) and higher elongation (8 %) values. Nakagawa and Gungor [132] found that extrusion not only increased the tensile elongation, but also increased the yield strength and UTS of the composites.

The effect of Mg concentration on the dynamic recrystallization of Al-Mg alloys during thermomechanical processing has been studied by Sheppard et al. [65,66]. The alloys with 2-3 wt% Mg are only softened by dynamic recovery. The structure of the extruded 5% Mg alloy is partially recrystallized, but the 7% Mg alloy extrudate is almost completely recrystallized for similar deformation conditions (extrusion temperature was 375°C, extrusion ratio was 40:1 and speed was 3.1 mm/s). This is because the high solute content hinders the motion of dislocations and because recrystallization nuclei are formed when a large number of dislocations cluster at obstacles formed by other dislocations or at insoluble particles producing tangles of dislocations which eventually lead to the limit of recovery and the establishment of a high angle boundary. The recrystallized grains are also prevented from rapid growth by those particles. McQueen et al. [86] found that dynamic recrystallization could take place in 5083 Al alloy at 400-500°C deformed in torsion. The grain size was about 10-18 μm. Insoluble particles in the alloy (>0.6 μm) were believed to enhance the nucleation of recrystallized grains. 5083 Al matrix composites have about 4 wt% Mg.

It is expected that a large number of reinforcing particles will have a great effect on the extrusion behaviour of this composite. However, a detailed study of the role of the particle reinforcement on the extrued microstructure of the 5083 Al matrix composites has not been carried out yet and the relation between the microstructure and mechanical properties is not clear.

1.3.4.2 Superplasticity in Whisker and Particle Reinforced MMCs

There are two established types of superplastic behaviour in polycrystalline solids. The first type is known as fine-structure superplasticity (FSS). The second type is known as internal stress superplasticity (ISS). In the case of FSS materials, a strain-rate-sensitivity exponent (m) equal to or larger than 0.3 can usually be found and the materials deform principally by a grain boundary sliding mechanism accommodated by slip or diffusion flow [97]. In the case of the ISS materials, however, the strain-rate-sensitivity exponent is usually unity, i.e. they exhibit Newtonian-viscous flow. For example, Wu & Sherby (1984) [116] found that thermal cycling of Al/SiC composites resulted in superplastic behaviour. Internal stresses are developed at the interfaces between the matrix and reinforcements during thermal cycling. These internal stresses will relax by plastic deformation in the matrix to the value of the local interfacial yield stress of the materials. It is this remaining local internal yield stress that contributes to the low applied external stress, and results in macroscopic deformation along the direction of the applied force. For the composites deformed at higher temperatures, the

cavities are usually easily formed and the growth rate of these cavities is much higher than in unreinforced materials [99]. Because large particles often inhibit grain boundary sliding, most of the composites can only be deformed superplastically in temperature ranges near or above their matrix solidus temperatures [100,102,103]. L'Esperance et al. [101] proposed that the presence of a liquid phase or a low melting point region resulting from solute segregation at the whisker/matrix interface will enhance interfacial sliding and contribute to for the high strain rate superplasticity (HSRS). A fine grain size is a necessary but insufficient condition for the observed HSRS phenomena in these composites.

The superimposition of a hydrostatic pressure during superplastic flow for the composites, especially for the particle reinforced composites results in a virtual elimination of cavitation and very good superplasticity characteristics [99,103]. Superplastic deformation of the composites reinforced by whiskers have been widely studied [98], but there are few studies which have been performed for composites reinforced by particles, especially those with particles larger than 10 μm. The 5083 Al alloy has exhibited 700% elongation when deformed at 550°C and at a strain rate of 2.8×10^{-3}/s [97]. Similar results were reported by Iwasaki et al. [104]. The deformation behaviour of the 5083 Al matrix composites reinforced by SiC or Al_2O_3 particles (> 10 μm) at high temperature is still not known.

CHAPTER 2

INTERFACIAL PHENOMENA IN ALUMINUM MATRIX COMPOSITES

Introduction

As discussed in chapter 1, the interface between reinforcement and matrix in composites plays an important role in the mechanical properties of the composites. Chemical reactions between the reinforcement and matrix, segregation of solute elements and the formation of new phases or precipitates at interfaces are often observed. Moreover, due to the large difference between the thermal expansion coefficient of reinforcements such as SiC and Al_2O_3 and that of an aluminum matrix, there is usually a large residual stress in the matrix. This residual stress will affect the deformation and fatigue behaviour of the composites.

In this chapter, interfacial reaction mechanisms between different particles such as as-received SiC, oxidized SiC or Al_2O_3 particles, and a 5083 aluminum matrix are discussed extensively in sections 2.1 to 2.3. Both thermodynamic and kinetic factors are taken into consideration. The protective role of a SiO_2 layer and the newly formed MgO

or $MgAl_2O_4$ polycrystalline layer on the particle surfaces are investigated. Composites were fabricated using the compocasting method; some of them were remelted at 800 °C for different times. Scanning electron microscopy (SEM), transmission electron microscopy (TEM), energy dispersive X-ray spectrometry (EDS) and parallel electron energy loss spectrometry (PEELS) were used to characterize the interfacial reaction products. In section 2.4, the segregation of Mg and Cu at interfaces are determined using a deconvolution technique which can improve the spatial resolution of X-ray analysis without increasing the statistical error. Segregation of Mg and Cu at the interfaces between Si_3N_4 whiskers and a 2124 aluminum alloy were observed. As discussed in section 2.5, the residual stresses in an aluminum matrix were determined using a convergent beam electron diffraction technique (CBED) with transmission electron microscopy. The CBED technique allows us to determine the residual stress and stress state in an area as small as 50 nm. In the following chapter, the nature of the interfaces will be related to the deformation and fracture behaviours of the composites.

2.1 Interfacial Reactions in Al-Mg (5083)/SiCp Composites during Fabrication and Remelting

W.M. Zhong*, G. L'Espérance* and M. Suéry**

* Ecole Polytechnique de Montréal, Centre de Caractérisation Microscopique des Matériaux $(CM)^2$, Case Postale 6079, Succ. "A", Montréal, Québec, Canada H3C 3A7

**Institut National Polytechnique de Grenoble, Génie Physique et Mécanique des Matériaux, GPM2, URA CNRS 793 ENSPG, B.P.46, 38402 St Martin d'Heres Cedex, France

Abstract

The interfaces of aluminum alloy composites (5083) reinforced by SiC particles (as-received, oxidized 3.04 wt% and 14.06 wt%) were studied. The composites were fabricated by compocasting and certain samples were also remelted at 800°C for 30 minutes. The reaction mechanisms between SiCp and liquid Al, and between the SiO_2 layer and Al(Mg) are discussed. The crystal boundaries of the MgO (or $MgAl_2O_4$) reaction products are believed to be the diffusion paths (or channels) during the interfacial reactions. A SiO_2 layer, formed by oxidation of the SiC particles prior to

their incorporation in the melt, plays an important role in preventing the SiCp from being attacked by the matrix. The interfacial reaction products are affected by both the alloy composition and the thickness of the initial SiO_2 layer.

1. Introduction

Interfacial reactions in metal matrix composites not only affect the interface strength, but also affect the age-hardening behaviour of the matrix [1, 2]. As reported previously, some interfacial reactions can improve the wettability of the solid reinforcement (e.g. SiC) by the liquid [3], but sometimes they will cause the reinforcement to be attacked, forming harmful reaction products (i.e. Al_4C_3) around the reinforcement [4-7]. Introducing an oxide layer (SiO_2) on the surface of SiC has been reported to play an important role in preventing SiC from being attacked by liquid Al, improving its wettability, and also improving the fracture strain of the composites [2,8,9]. Because the interface reaction in Al/SiC depends on several fabrication parameters, (for example, temperature, holding time, atmosphere, and chemical composition of both the aluminium matrix and the SiC reinforcement), the nature of the interface will change with fabrication procedure and composite system.

The reaction between molten Al and SiC particles in the temperature range from 675 to 900 °C has been investigated by many authors [6,10,11,12]. From both the

points of view of thermodynamics and kinetics, the reaction can take place to yield Al_4C_3 during fabrication by a molten metal route [6-12]. From the studies of Narciso et al. [8] and Viala et al. [12], the reaction has been found to proceed via a dissolution (of SiC) and re-nucleation (of Al_4C_3) process. As reported by Lloyd et al. [6,10] and Iseki et al. [13], the formation of Al_4C_3 is limited by increasing the Si content of molten Al.

A chemical interaction between molten Al and SiO_2 was observed by Narciso et al. [8] and Brondyke [14] at 700-900°C, forming Al_2O_3 and Si. The reaction rate was believed to be controlled by the diffusion of Al and Si through the newly formed Al_2O_3 layer. J.G. Legoux et al. [5,9] have extensively studied the reaction between the SiO_2 layer on SiCp and Al alloys (containing 0.3 wt%, 1 wt% and 5 wt% Mg). $MgAl_2O_4$ was found to be the reaction product in the materials with 0.3 wt% and 1 wt% Mg; whereas a mixture of $MgAl_2O_4$ - MgO fine crystals was the reaction products in the materials made with 5 wt% Mg. Metallic Al channels were shown to be the diffusion path through the oxide layer for incoming Mg and out-going Si. Stephenson et al. [15] found, experimentally, that the reaction tendency and kinetics of Mg and SiO_2 are several times higher than that of Al and SiO_2 at 670-800°C; however they did not discuss the diffusion paths. Jin and Lloyd [16], in studying the reaction between pure Al-Mg alloys and Al_2O_3 particles, found that the reaction rate decreased for higher Mg contents (>5 wt%) because of the small size of the reaction product formed ($MgAl_2O_4$).

In this work, the reaction mechanisms between SiC particles covered by a SiO_2

layer and a commercial alloy containing a large amount of Mg (5083 alloy) are investigated in detail. Of particular interest are the effects of the alloy composition, the fabrication parameters and the nature of SiC particles on the interfacial reaction. The role of the SiO_2 layer in protecting SiC in 5083/SiCp composites has also been investigated. The 5083 aluminium alloy is a solution hardening alloy. It has moderate strength and good corrosion resistance. It has a potential for superplastic deformation. The mechanical properties and the high temperature deformation behaviour of the composites have been reported elsewhere [17]. A study of the effects of the thermomechanical processing of the composites and the interfacial reactions on the strengthening and fracture mechanisms will also be reported elsewhere.

2. Experimental Procedures

A modified compocasting technique was used to fabricate the composites. The 5083-Al alloy was first heated to the semi-solid state in the temperature range from 600 to 640 °C. The reinforcing particles were then incorporated into the vigorously agitated alloy. Approximately 5 minutes were required to add all the particles. Finally, the alloy was completely remelted at 720°C for 5 minutes and solidified under a pressure of 100 MPa [2]. The particles used were either in an as-received condition (from PRESI, France) or in an artificially oxidized condition. Oxidation was carried out in air at 1100°C for two different times (about 1 hour and 12 hours) using a SiC crucible heated

with an induction furnace. The SiO_2 layer formed in this way was continuous and the amount of SiO_2 determined by wet chemical analysis, was 3.04 wt% and 14.06 wt% of the particle weight for oxidation times of 1 hour and 12 hours respectively. A total of 15 vol% of SiCp was used (with an average diameter of 13 μm). The remelting experiments were performed in an induction furnace using a small graphite crucible, under Ar atmosphere. The samples were reheated to 800°C and held for 30 minutes. The composition of the alloy used is: 4.1wt%Mg - 0.56wt%Mn -0.12wt%Cr - 0.19wt%Fe -0.15wt%Si - 0.04wt%Cu - 0.02wt%Ti-(balance) Al.

All the internal acronyms used in this article were designated to indicate the state of the particles prior to their incorporation into the composites and the state of the composites (i.e. as-cast or remelted). For example, sample AOX14 means that the sample was as-cast (A) and the particles were oxidized (OX) 14 wt% and sample ROX14 means that the same composite was remelted (R).

Scanning electron microscopes (SEM, JEOL-840 and JEOL-820) and transmission electron microscopes (TEM, CM30-PHILIPS and JEOL-2000FX) electron microscopes were used. The interface microstructure was examined by using bright field images (BF), dark field images (DF), selected area diffraction (SAD), microdiffraction, electron energy loss and energy dispersive X-ray spectroscopies (EELS, EDS). The TEM thin foils were prepared by ion milling at 15° with a voltage of 5 kV after mechanical polishing and dimpling.

3. Experimental Results

3.1 5083/SiCp composites (as-received SiCp, as-cast composites, (ARS))

Figures 1,2 are SEM micrographs showing the distribution of the SiC particles in the composites, and the interface between the SiC and the matrix. As shown in figure 1, the distribution of SiCp is macroscopically uniform. At a magnification of 3000 times, interface reaction products and porosity are not observed.

Figure 3(a) shows a TEM micrograph in which the SiC particle is not attacked by the matrix. Figure 3(b) is the corresponding EDS line profile at the matrix/SiCp interface. No Mg is found inside the SiC particle as shown by the curve which represents the true Mg concentration profile near the interface. The Mg apparently detected inside the SiC particle is caused by electron beam broadening as confirmed by a deconvolution technique in which electron beam broadening and the expected true Mg concentration profile (the solid curve in figure 3(b)) is convoluted to yield the experimental profile [18]. $C_{apr.measured}$ and $C_{apr.calculated}$ represent the measured and the convoluted apparent Mg concentration. The Mg and O are found at high levels (as high as 17 wt% Mg) at the interface. Figure 4 is a higher magnification TEM micrograph which shows that fine MgO crystals as confirmed from the indexation of the SAD pattern, have formed near the SiC particle. The thickness of the MgO layer can be

larger than 50 nm but is typically in the 10 to 30 nm range. Occasionally, penetration of the matrix into a SiC particle along a crystal defect can be observed. A Cr, Mn, Fe rich phase such as $(Cr,Mn,Fe)_3SiAl_{12}$ is frequently found near the SiC particle. This phase is not associated with interfacial reactions but is a normal inclusion in 5083 aluminum alloy. Mg_2Si is also observed in the matrix and near SiC particles.

3.2 5080/SiCp composites (as-received SiCp, remelted at 800°C for 30 min, (RMS)).

After remelting of the composites, SiCp particles are attacked heavily (figure 5). From the SEM micrograph, we can see that a large number of Mg_2Si particles are formed in the matrix and around the SiC particles.

The TEM image, in figure 6(a), shows an attacked SiC particle where Al_4C_3 is formed. Figure 6(b) is a SAD pattern obtained from Al_4C_3. At some places, MgO crystals (see arrows in figures 7(a)), which may be formed during fabrication of the composites, are still found at the original interface of matrix/SiCp. Al_4C_3 is observed behind the MgO layer as a result of the attack of SiC during remelting. At the same time, Mg_2Si is found in the matrix near the MgO reaction zone. Figure 7(b) is the corresponding SAD (annular) pattern from MgO crystals. These results indicate that in as-cast materials, MgO is not formed at every matrix/SiCp interface, and that the oxide layer on the as-received SiC particles is not uniform. After remelting, Mg was not detected in the matrix using EDS.

3.3 5083/SiCp composites (SiCp oxidized 3.04 wt%, as-cast, (AOX3))

A reaction layer consisting mainly of fine MgO crystals is shown by TEM images in this sample (see figures 8(a)-(c)). The sizes of MgO particles are about 5 to 20 nm. As shown by the EDS line profile and the EDS spectrum (figures 9 (a)&(b)), Mg and O contents are high in the reaction zone. The thickness of the reaction zone is about 100-200 nm on the average. Inside the reaction zone, the SiCp boundary is clear and straight. There is no evidence of SiCp attack. Mg_2Si is found near the reaction zone in the matrix. $(Mn,Fe)Al_6$ and $(Cr,Mn,Fe)_3$ $SiAl_{12}$ are also found in the sample. There is about 2.5-3 wt% Mg remaining in the matrix measured using EDS.

3.4 5083/SiCp composites (SiCp oxidized 3.04 wt%, remelted at 800°C for 30 min, (ROX3))

After remelting, as shown in figures 10(a)&(b), most of the SiC particles still have clear, smooth boundaries indicating no attack by the matrix. Mg_2Si (dark phase) is found around the particles. A few particles with serrated boundaries can be seen; they were attacked at some places (see figure 11). As shown in figures 10&12, the matrix/SiCp interfaces are still rich in Mg and O. By TEM observation, the reaction zone around SiCp still consists of fine MgO crystals, as shown in figures 13(a)-(c). Figure 13(d) is an EELS spectrum obtained from the reaction zone, which shows a sharp Mg peak caused by the presence of MgO crystals as indicated from a comparison with

an EELS spectrum of a pure MgO crystal. Metallic Al present in the reaction zone is identified by the relatively smooth Al peak on the EELS spectrum [5]. Mg_2Si is also observed near the reaction zone in the matrix, identified by selected-area diffraction in TEM observation.

3.5 5083/SiCp composites (SiCp oxidized 14.06 wt%, as-cast, (AOX14))

X-ray maps in figure 14(a) reveal the presence of Mg, O and Al in the reaction zone. The interface reaction zone is also quite evident in the SEM image (figure 14(b)). Mg_2Si (D, dark phase) and some $(Cr,Mn,Fe)_3SiAl_{12}$ (B, bright phase) are found in the matrix near the SiCp. The thickness of the reaction zone is about 500-800 nm.

TEM micrographs (figures 15(a),(b)) show that the reaction layer consists mainly of fine MgO crystals, confirmed by the high intensity of the MgO diffraction rings. Diffraction spots, (111)Mg_2Si, (012)Al_2O_3, (111)$MgAl_2O_4$ and (100)SiO_2, also appear occasionally in the SAD patterns obtained by using different tilt angles, which can be used to unambiguously identify the presence of these phases in the reaction zone. Figure 16(a) shows an EDS line-profile at the matrix/SiCp interface, which illustrates the distribution of Mg, O and Al. Figure 16(b) is an EDS spectrum obtained from the reaction zone. The SiC particles have not been attacked at all. The Mg_2Si in the matrix and near the SiCp is a product of solidification. Si is produced by the reaction between SiO_2 and Mg or Al. In comparison to the AOX3 sample (with 3.04 wt% SiO_2 layer),

the reaction products are more complex in the reaction zone of the AOX14 sample (with 14.06 wt% SiO_2 layer). About 0.5-1 wt% Mg was measured remaining in the matrix.

3.6 5083/SiCp composites (SiCp oxidized 14.06 wt%, remelted at 800°C for 30 min, (ROX14))

In the ROX14 samples (with SiCp oxidized 14.06 wt%, remelted), the proportion of $MgAl_2O_4$ in the reaction zone has increased after remelting (see figure 17). Figure 17(b) shows a very strong (111) diffraction ring from $MgAl_2O_4$. Large Si and Mg_2Si phases (>1 μm) are found near the reaction zone in the matrix, as shown in figure 17(a). $MgAl_2O_4$ crystals, with a size in the range of 0.5 μm to 1 μm, are also found occasionally just outside the reaction zone (see figure 17(a) and the corresponding diffraction pattern in figure 17(c)). Figures 18(a)&(b) are the TEM BF and the DF images (obtained with the (111) spinel diffraction spots). The crystal size in the reaction zone appears slightly larger than that in as-cast composites. Figures 18(c)&(d) are the diffraction patterns obtained from pure MgO and $MgAl_2O_4$ standards respectively. Diffraction from $(111)_{spinel}$ with a d spacing of 0.466 nm and from $(220)_{spinel}$ with d=0.285 nm can be used to identify the presence of $MgAl_2O_4$. Figure 19 is the EDS line profile of Mg, O and Al at the matrix/SiCp interface. No Mg remains in the matrix after remelting.

As can be seen, the reaction products at the interfaces of the composites with the

3.04 wt% SiO_2 layer are different from those with the 14.06 wt% SiO_2 layer. In the latter case, a thicker SiO_2 layer increases the probability of $MgAl_2O_4$ formation.

4. Discussion

4.1 The Reaction Mechanism between liquid Al and SiC particles

The reaction between SiCp and liquid Al is believed to include several steps including the following [19,20]:

(a) Chemical reaction (dissolution) of SiCp with molten Al

(b) Diffusion of Si and C atoms away from the SiCp surface into the molten Al pool

(c) Formation of compounds when the Al and C concentrations or the Si and C concentrations exceed the values defined by equilibrium constants of Al_4C_3 or SiC

(d) Further precipitation of compounds on cooling due to a decrease in solubility

The dissolution kinetics of SiCp in Al have been suggested to be the rate determining step in the Al/SiC interfacial reaction during manufacture of composites [19]. As mentioned previously, increasing the amount of Si in the matrix can reduce the dissolution of SiC and prevent the formation of Al_4C_3 [6,11]. As shown by Lloyd [21], the reaction rate is very low in the fabrication temperature range from 650°C to 750°C (after holding for 2hs at 750°C, no attack was observed in the A356 (7 wt% Si) alloy).

Usually, 7 to 15 wt % of Si is necessary to prevent the reaction [6,11,12,19,21]. Since the matrix of the composites studied in this work contains only 0.15 wt% of Si, SiC is expected not to be stable in contact with the liquid Al. From our experimental results, we find that the dissolution of the SiCp is not uniform as shown from the preferentially attacked channels and the serrated morphology of the attacked SiC particles. The dissolution of the SiCp seems to be a preferential process (e.g. along crystal defects, or along some low index crystal planes).

Because the solubility of [C] in liquid Al is very low at temperatures from 660°C to 800°C, the threshold carbon activity values for Al_4C_3 formation are small. The carbon atoms that go into solution will react almost immediately with Al to form Al_4C_3 [22]. With the dissolution of SiC, the Al_4C_3 grows and Si will diffuse into the melt around the Al_4C_3. Therefore, at the beginning, the dissolution of the SiCp into the molten Al will control the Al/SiCp interface reaction. With increasing time, a layer of Al_4C_3 may form around the SiC particle, similar to the observation of Iseki [13]. The Al_4C_3 layer may act as a diffusion barrier for the diffusion of Si, C and Al, thus further reaction will be affected by the diffusion process although other diffusion paths, like crystal boundaries and defects, are also available.

4.2 Enrichment of Mg at the Al (Mg) Alloy/Reinforcement Interface

In many Al (Mg) matrix composites, segregation of Mg at the

matrix/reinforcement interface is frequently observed [2,9,23,24,25]. In 5083/SiCp as-cast materials, segregation of Mg is also found. This may have several causes. First, just as in Al-Mg alloys (Malis, 1982) [26], Mg can segregate at the grain boundaries and free-surfaces. This segregation is governed by thermodynamic factors related to the decrease of the grain boundary energy, interface energy or surface energy. For example, in a quenched sample, non-equilibrium segregation is established by vacancy drag of solutes as defects migrate to the sinks (grain boundaries) [26]. In composites, the interface of matrix/reinforcement is also a good sink for the solute atoms during rapid cooling.

Second, segregation of Mg is caused by the interfacial reaction of Mg with the SiO_2 layer on the SiCp surface, or with the oxygen trapped during the fabrication process, to form MgO or $MgAl_2O_4$ oxides [2,12,27]. These reactions can improve the wettability and form a diffusion barrier for reaction between liquid Al and SiCp [1,28].

Third, nucleation of the primary solid does not occur initially on the surface of the reinforcement during solidification. In the case of an alloy, the solid phase will avoid the reinforcement as it grows. Consequently, the last portion of the metal to solidify will be located close to or at the matrix/reinforcement interface with the solutes pushed to the interface by the liquid/solid front. Therefore, enrichment in the solutes (Mg) is observed near the interface [18,20,29].

4.3 Reaction Mechanism of the SiO_2 layer with Liquid Al-Mg Alloy

Reactions between Mg and SiO_2 layer can form MgO or $MgAl_2O_4$, MgO being formed more easily with high Mg content in matrix [5,9]. That is:

$$SiO_2 + 2Mg = 2MgO + Si \quad \ldots\ldots\ldots \quad (1)$$

$$2SiO_2 + Mg + 2Al = MgAl_2O_4 + 2Si \quad \ldots \quad (2)$$

After the first layer of MgO or spinel is formed, for the reaction to continue, Mg, Al and the released Si must diffuse through the reaction layer. As the bulk diffusion coefficients of these elements in oxides at temperatures of 700°C to 800°C are very small [9, 30] and since the reaction products are extremely fine crystals, crystal boundary diffusion must play an important role. Horvath [31] studied diffusion in nanocrystalline materials (crystal size about 10 nm). Owing to the enormous interface area in the material, the diffusion coefficient is many orders of magnitude higher than the lattice bulk diffusion coefficient. Bokstein [32] found that the grain boundary or phase boundary diffusion coefficient in Ti alloys is 5-6 orders of magnitude higher than that of its volume diffusion. Formation of $MgAl_2O_4$ from SiO_2 will cause a 27% volume contraction, and formation of MgO will also cause a 13.6% volume contraction. Due to this contraction, there will be gaps between the newly formed crystals or between the newly formed crystals and the rest of the SiO_2. Liquid Al and Mg infiltrate into these gaps and form so-called "diffusion channels" as Legoux, et al. [9] suggested. Released

Si will diffuse through these "channels" into the liquid and may form Mg_2Si with the Mg in matrix, that is:

$$Si + 2Mg = Mg_2Si \quad \ldots\ldots\ldots\ldots\ldots\ldots \quad (3)$$

The reaction between Mg (or Al) and SiO_2, during the fabrication of the composites, becomes kinetically possible because of the diffusion channels. However, our experimental results have shown that the attack of SiC by molten Al is decreased with increasing thickness of the SiO_2 layer during remelting. The reason is that the newly formed MgO or spinel crystals in the reaction zone decrease the effective exposed surface of the SiC particle to the molten Al and form a diffusion barrier for the incoming Al. In as-cast composites, the SiO_2 layer on SiC surface may also delay direct contact of molten Al with the SiC particles during incorporation, especially when the SiO_2 layer is thick. Of course, because of the large volume contraction in forming MgO (13.6%) or spinel (27%) crystals from SiO_2, the protecting role of the reaction zone should be less important compared to the reaction between Mg and Al_2O_3 particles [33]. The reaction between Mg and Al_2O_3 in which the protecting role of the newly formed MgO or spinel crystals is more pronounced because of the large volume expansion (30% for MgO and 15% for $MgAl_2O_4$) makes the diffusion channels become very narrow during the reaction [33]. It is quite possible that forming MgO in the reaction zone will better protect a SiC than forming $MgAl_2O_4$ does, owing to the smaller volume contraction in forming MgO crystals and the lower diffusivity in MgO crystal. Thus, SiC will be protected better

with a higher Mg content in the matrix because the probability of forming MgO increases with increasing Mg content, while the thickness of the SiO_2 layer is constant.

As discussed earlier, MgO is the main interfacial reaction product in the ROX3 sample (3.04 wt% oxidized, remelted), whereas $MgAl_2O_4$ is the main reaction product in the ROX14 sample (14.06 wt% oxidized, remelted) and MgO is the main reaction product in the as-cast composites (AOX3 and AOX14) reinforced by the two different particles. This difference can be explained as follows. Although both AOX14 and AOX3 (as-cast) materials have the same original Mg contents, the "dynamic" concentration in the matrix will be affected by the quantity of SiO_2 available on the surface of the particles. For the materials with a thicker SiO_2 layer, the Mg concentration at the beginning of the reaction will be quite different from that near the end of the reaction. It is known that MgO forms more readily with higher Mg contents as discussed previously [5,24,29,34]. In the AOX3 sample, because the SiO_2 layer is thin, the interfacial reaction consumes only a small amount of Mg (consuming about 1 wt% according to our measurements and 0.96 wt% as calculated from reactions (1) and (3)). In addition, the semi-solid processing during compocasting may increase the actual Mg content in the remaining liquid. Therefore, MgO is the main reaction product even at the end of the reaction period. During remelting (ROX3), the sources of oxygen are quite limited, so that further reaction is believed to be restricted. Finally, as reported by Mcleod in a study of the reaction between Mg and Al_2O_3 [34], MgO is more stable than $MgAl_2O_4$ when the Mg content is larger than 1.6 wt% at 800°C. For our material,

the remaining Mg content in the matrix is still as high as about 3 wt% after fabrication, so that the reaction products could be unchanged during remelting. Considering the AOX14 sample, because the SiO_2 layer is thicker, the interfacial reaction during fabrication will consume much more Mg (more than 3 wt% according to our measurements). The amount of Mg calculated based on reactions (1) and (3), however, indicates that there should be no Mg remaining in the matrix, if the interfacial reaction between SiO_2 and Mg went to completion and all of the released Si formed Mg_2Si after solidification. Thus, MgO can be formed at the beginning of the reaction, whereas with an increase of reaction time, the Mg level in the matrix will decrease significantly and some $MgAl_2O_4$ will be formed at interfaces. Since the liquid Mg content can be expected to be larger than the bulk Mg content during compocasting, as discussed previously and that the reaction between Mg and the SiO_2 layer is incomplete because of the short fabrication time, the amount of $MgAl_2O_4$ formed is limited during casting and MgO is the main reaction product. However, during remelting at 800°C, the matrix is completely melted, so that the Mg content in the liquid is the same as that in the bulk at that time (the remaining Mg content in the matrix is less than 1 wt% after fabrication). The interfacial reaction between Mg (Al) and SiO_2 during remelting will therefore mainly form $MgAl_2O_4$. In addition, in systems with a low Mg content, $MgAl_2O_4$ is more stable [34], so that some of the MgO initially formed could be transformed to $MgAl_2O_4$ during remelting. In order to understand more fully the relation between the amount of MgO (or $MgAl_2O_4$) formed as a result of the interfacial reaction and the thickness of the SiO_2 layer during fabrication, thermodynamic calculations were carried out for a given system

using the F*A*C*T Thermodynamic Database [35]. As shown in figure 20 and Table I, the possibility of forming $MgAl_2O_4$ increases with increasing thickness of the SiO_2 layer for a given alloy composition (assuming an uniform distribution of Mg). It therefore appears that a detailed discussion of interfacial reactions in composites requires consideration not only of the matrix composition but also of the type, volume fraction, and size of the reinforcement in addition to the thickness of coatings (if present).

Since MgO is expected to form first and $MgAl_2O_4$ later in AOX14 samples, the distribution of MgO and $MgAl_2O_4$ will not be uniform and there should be more MgO in the outer layer of the reaction zone and more $MgAl_2O_4$ in the inner layer of the reaction zone. However, because of the limited size of the objective aperture, it is not possible to select diffraction spots which originate uniquely from MgO or $MgAl_2O_4$ crystals so that TEM DF images, which uniquely consist of MgO crystals or $MgAl_2O_4$ crystals, could not be obtained to visualize their spatial distribution. In addition, because the reaction is controlled by a short-circuit diffusion, the reaction front will not necessarily move uniformly inside the reaction zone. Thus, in some areas, the reaction can occur deeply inside the reaction zone if the reaction in areas outside the reaction zone has not been completed. As a result, MgO and $MgAl_2O_4$ may form anywhere in the reaction zone.

Table I Relation Between the Reaction Products and the Amount of SiO_2

Products	**0.5**SiO_2 (R1)*	**1.0**SiO_2 (R2)	**3.0**SiO_2 (R3)
MgO	0.671	0.184	0.000
$MgAl_2O_4$	0.000	1.021	3.552
Mg_2Si	0.638	1.277	2.213
Si	0.000	0.000	0.592
SiO_2(rest)	0.000	0.000	0.000
Mg(rest)	3.149	2.832	1.860

* Calculations using the F*A*C*T Thermodynamic Database [35], at 700°C, 1 atm., in gram. R1, R2 and R3 indicate different reactions with different amounts of SiO_2.

$4Mg + 96Al + \mathbf{0.5}SiO_2 =$ .....(R1)
$4Mg + 96Al + \mathbf{1.0}SiO_2 =$ .....(R2)
$4Mg + 96Al + \mathbf{3.0}SiO_2 =$ .....(R3)

** In the AOX3 sample (with 3.04 wt% SiO_2), there is 0.65g SiO_2 per 100g of matrix which is similar to condition R1. In the AOX14 sample (with 14.06 wt% SiO_2), there is 2.94g SiO_2 per 100g of matrix which is similar to condition R3.

5. Conclusions

1) In the as-cast composite materials, there is no attack of SiCp by molten Al whether or not the SiCp has been artificially oxidized.

a. In as-cast composites reinforced with as-received SiCp, segregation of Mg at the

matrix/SiCp interface is observed. Some of the Mg forms fine MgO crystals at the matrix/SiCp interface with a thickness of about 20-30 nm.

b. In as-cast composites reinforced with 3.04 wt% oxidized SiCp (AOX3) or with 14.06 wt% oxidized SiCp (AOX14), a reaction layer consisting mainly of fine MgO crystals (5-20 nm) is found. This reaction layer has a straight, clear interface with the SiC particle and has an average thickness of 100-200 nm in the AOX3 sample and 500-800 nm in the AOX14 sample.

2) In remelted materials, different behaviours are found for different initial conditions of the SiCp.

a. In RMS materials (as-received SiCp, remelted), SiCp is attacked heavily. MgO crystals formed during fabrication remain at the original interface position.

b. In ROX3 material (3.04 wt% oxidized SiCp, remelted), MgO is still the main reaction product in the reaction zone. In ROX14 materials (14.06 wt% oxidized SiCp, remelted), the proportion of $MgAl_2O_4$ is increased at the interfaces. The type of reaction product formed is related to the dynamic concentration of Mg in the matrix. Attack of SiCp in ROX3 materials is observed only on some SiCp and the attack is slight. In ROX14 materials, the attack of SiCp is not observed. Attack of SiC by molten Al is decreased with increasing thickness of the SiO_2 layer. Mg_2Si, Si and $(Cr,Mn,Fe)_3SiAl_{12}$ are found in the matrix near the SiC particles.

3) The newly formed MgO (or spinel) crystal boundaries are believed to be the

diffusion paths (or channels) for the interfacial reactions to proceed. Higher Mg concentrations in the matrix will result in a denser MgO reaction zone which may protect the SiC particles better than the $MgAl_2O_4$ reaction zone.

Acknowledgments

The authors gratefully acknowledge the NATO International Scientific Exchange Programme (Grant no. CRG 900950) and the National Science and Engineering Council of Canada (NSERC, strategic grants) for financially supporting this project. They also thank E. Goiffon, L. Salvo and J.J. Blandin for the preparation of the composite materials. Thermodynamic calculations were performed with the help of P. Wu and J. Wu.

Reference

1. L. Salvo, M. Suéry, J.G. Legoux, G. L'Espérance, Mater. Sci. and Eng. A 135(1991), P.129

2. H. Ribes, R.Da. Silva, M. Suéry, T. Bretheau, Mater. Sci. and Tech., July(1990), Vol.6, P.621

3. F. Delannay, L. Froyen and A. Deruyttere, J. of Mater. Sci. 22(1987), P.1

4. C. Marumo, J.A. Pask, J. of Mater. Sci. 12(1977), P.223

5. J.G. Legoux, H. Ribes, G. L'Espérance and M. Suéry, Proc. of Interface in Metal-Ceramics Composites(1989), Anaheim, edited by R.Y. Lin, R.J. Arsenault, G.P. Martin and S.G. Fisman, The Minerals, Metals and Materials Society, 1989, p.187

6. D.J. Lloyd, H. Lagace, A. McLeod and P.L. Morris, Mater. Sci. and Eng. A107(1989), P.73

7. F.H. Samuel, H. Liu and A.M. Samuel, Metall. Trans. A, 24A(1993), P.1631

8. J. Narciso, C. Garcia-Cordovilla and E. Louis, Mater. Sci. and Eng., B15(1992), P.148

9. J.G. Legoux, G. L'Espérance, L. Salvo, M. Suéry, Proc. of Fabrication of Particulates Reinforced Metal Composites (1990), Montréal, edited by J. Masounave and F.G. Hamel, ASM, Metals Park, Ohio, 1990, P.31

10. D.J. Lloyd and I. Jin, Metall. Trans. A, 19A(1988), P.3107

11. C.A. Handwerker, J.W. Cahn and J.R. Manning, Mater. Sci. and Eng., A126(1990), P.173

12. J.C. Viala, P. Fortier, J. Bouix, J. of Mater. Sci., 25(3), 1990, P.1842

13. T. Iseki, T. Kameda, T. Maruyama, J. of Mater. Sci., 19(1984), P.1692

14. K.J. Brondyke, J. Am. Ceram. Soc. Vol.36, No.5(1953), P.171

15. T. Stephenson, Y. Le Petitcorps, J.M. Quenisset, Mater. Sci. Eng. Vol.135A(1991), p.101

16. I. Jin, D,J. Lloyd, Proc. of 2nd International Conference on Cast Metal Matrix Composites, Tuscaloosa, USA, Oct., 1993, edited by D.M. Stefanescu and S. Sen, American Foundrymen's Society, Illinois, 1994, P.288

17. E. Goiffon, W. Zhong, J.J. Blandin, M. Suery, G. L'Esperance, Proc. of 2nd International Conference on Cast Metal Matrix Composites, Tuscaloosa, USA, Oct., 1993, edited by D.M. Stefanescu and S. Sen, ibid 16, P.316-325

18. W.M. Zhong, G. L'Esperance, The True Composition Profile Obtained by Graphical Deconvolution Technique in AEM/STEM, University of Montreal, Canada, Unpublished research, 1993.

19. R.Y. Lin and K. Kannikeswaran, Proc. of Interfaces in Metal-Ceramics Composites(1989), edited by R.Y. Lin, R.J. Arsenault, Anaheim, P.153

20. K. Kannikeswaran and R.Y. Lin, J. of Metal, 9(1987), ibid 5, P.17

21. D.J. Lloyd, B. Chamberlain, Interfaces in Metal-Ceramics Composites, edited by R.Y. Lin, R.J. Arsenault(1989), Anaheim, ibid 5, P.263

22. G. Selvaduray, R. Hickman, D. Quinn, D. Richard and D. Rowland, Interfaces in Metal-Ceramics Composites, edited by R.Y. Lin, R.J. Arsenault(1989), Anaheim, ibid 5, P.271

23. M. Strangewood, C.A. Hippley, J.J. Lewandowski, Scripta Metall., Vol.24(1990), P.1483

24. A. Munitz, M. Metzger and R. Mehrabian, Metall. Trans A, Vol.10 A, 10(1979), P.1491

25. M. Fishkis. J. of Mater. Sci. 261(1991), P.2651

26. T. Malis, M.C. Chaturvedi, J. of Mater. Sci. 17(1982), P.1479

27. L.M. Dignard-Bailey, T.F. Malis, J.D. Boyd and J.D. Embury, CIM Proc., Advanced Structure Materials, 9(1988), P.87

28. A. Mortensen, Mater. Sci. and Eng., A 135(1991), P.1

29. A. Mortensen, J.A. Cornie, M.C. Flemings, J. of Metals, 2(1988), P.12

30. B. Hallestedt, Z.K. Liu and J. Agren, Mater. Sci. and Eng., A 129(1990), P.135

31. J. Horváth, Defect and Diffusion Forum, Vol.66-69(1989), P.207

32. B.S. Bokstein, Defect and Diffusion Forum Vol.66-69(1989), P.631

33. W.M. Zhong, G. L'Esperance, M.Suéry, Interfacial Reactions in Al-Mg (5083)/Al_2O_3p During Fabrication and Remelting, University of Montreal, Canada, Unpublished research, 1993.

34. A.D. Mcleod, Proc. of Fabrication of Particulates Reinforced Metal Composites(1990), Montréal, edited by J. Masounave and F.G. Hamel, ibid 9, P.18

35. F*A*C*T thermodynamic Database, CRCT, Ecole Polytechnique, Montreal, Canada, 1993

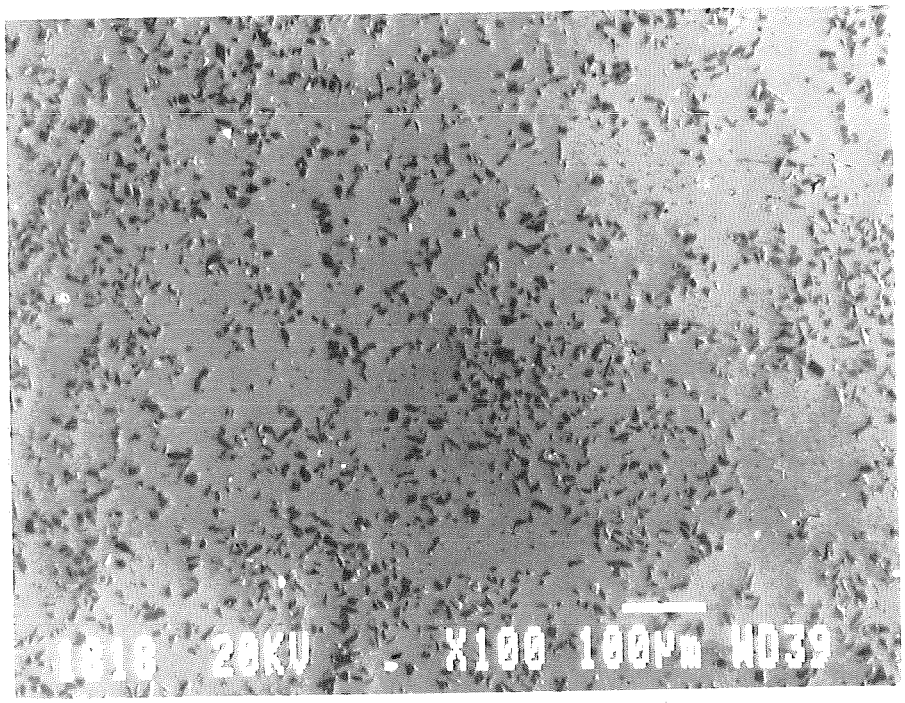

Figure 1 Distribution of SiCp (ARS, 5083/SiCp, as-cast)

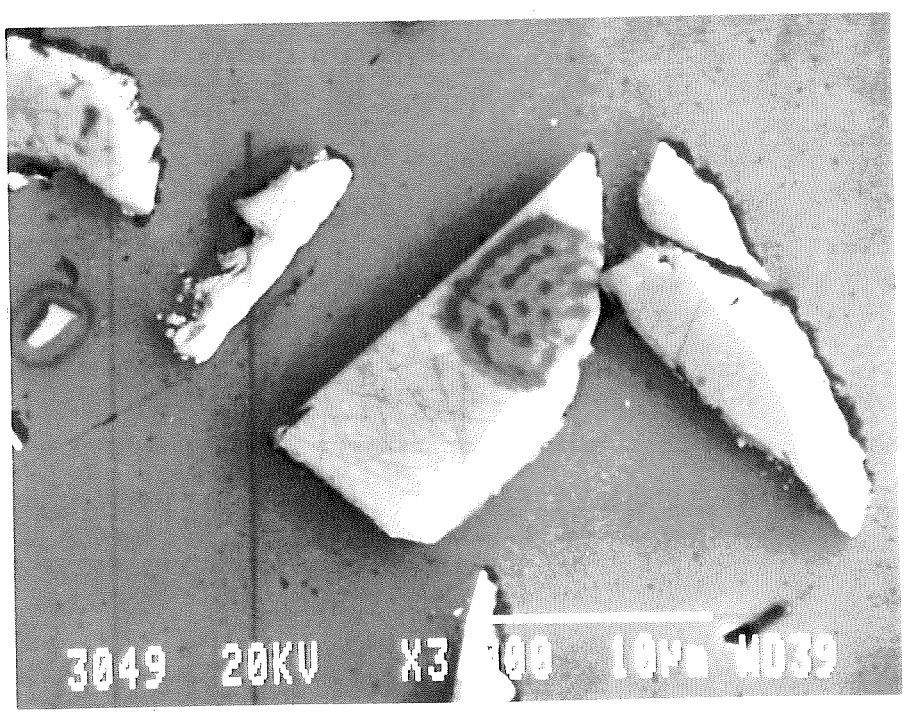

Figure 2 SiCp boundary is clear, no reaction product is seen at the interface (ARS)

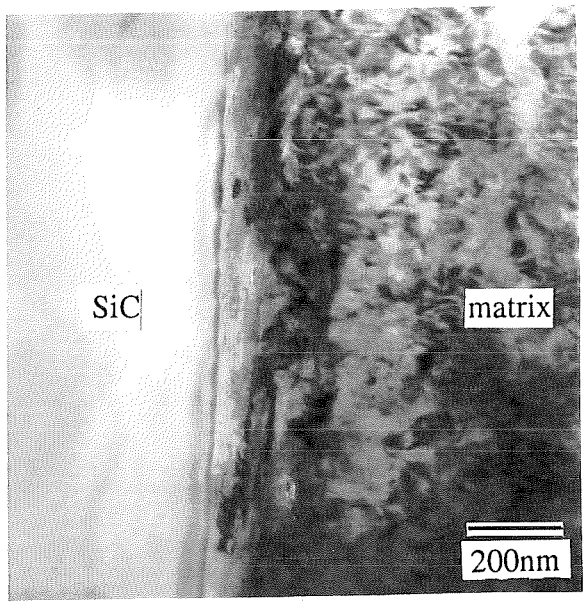

Figure 3(a) TEM image of the interface of matrix/SiCp (ARS)

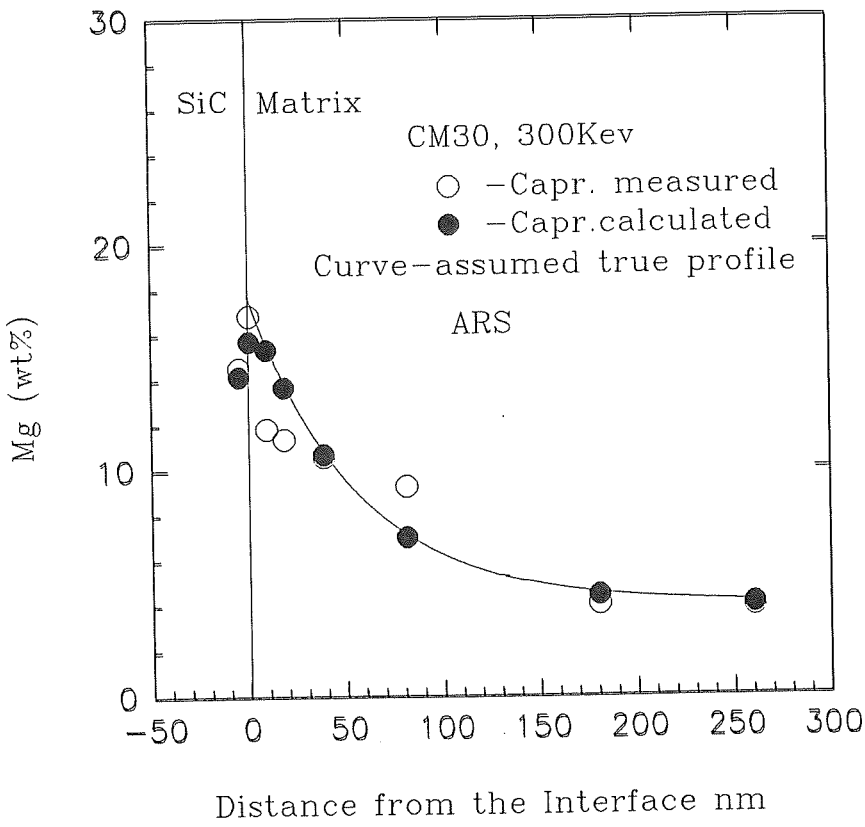

Figure 3(b) EDS line-profile at matrix/SiCp interface (ARS)

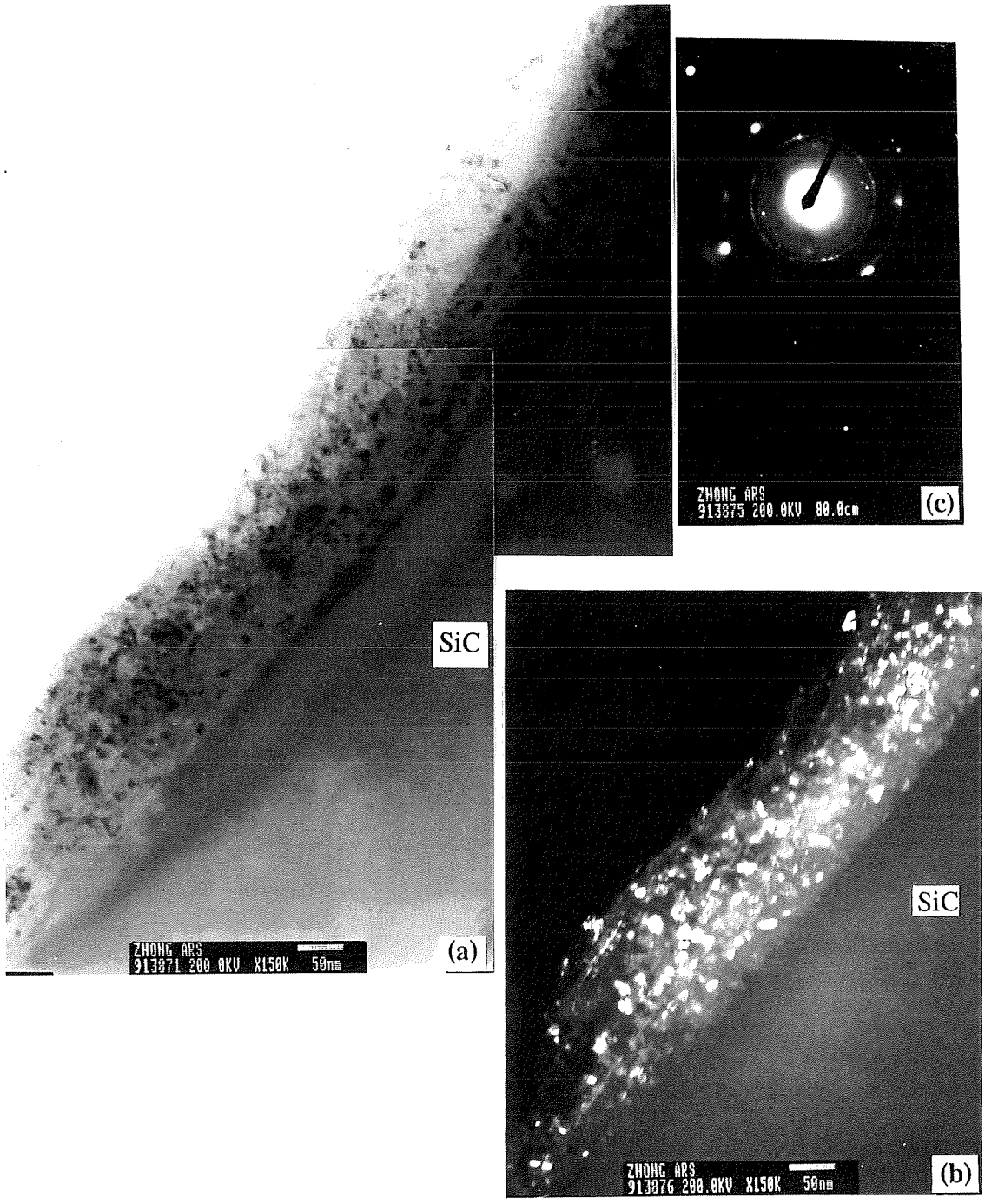

Figure 4 Small MgO crystals are observed at the interface, (a) TEM BF image, (b) DF image, (c) SAD pattern from reaction zone (MgO size 5-10 nm, ARS)

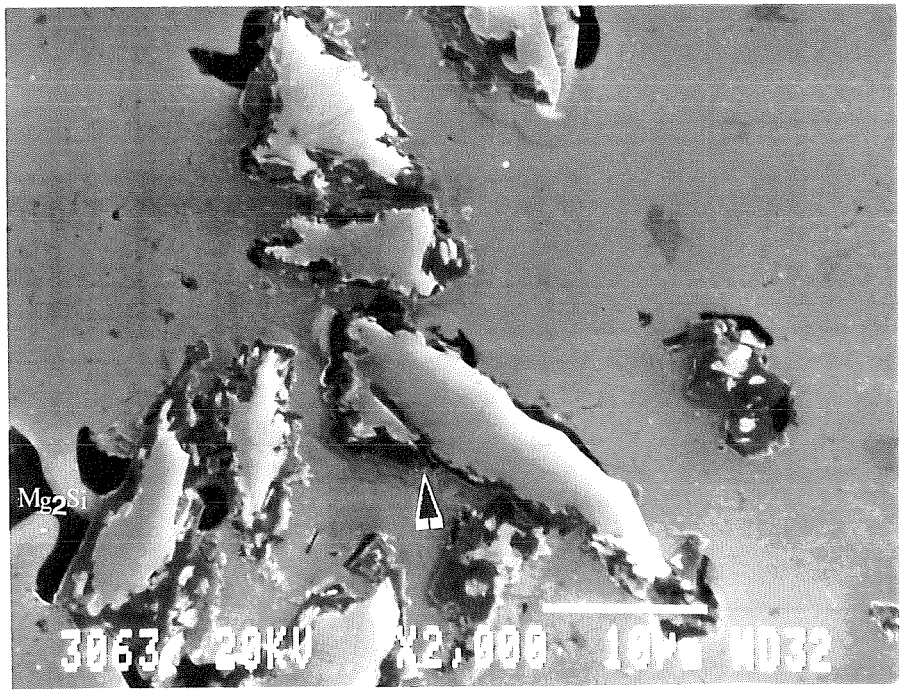

Figure 5 SiCp attacked by matrix (RMS, 5083/SiCp, remelted at 800°C for 30 min.)

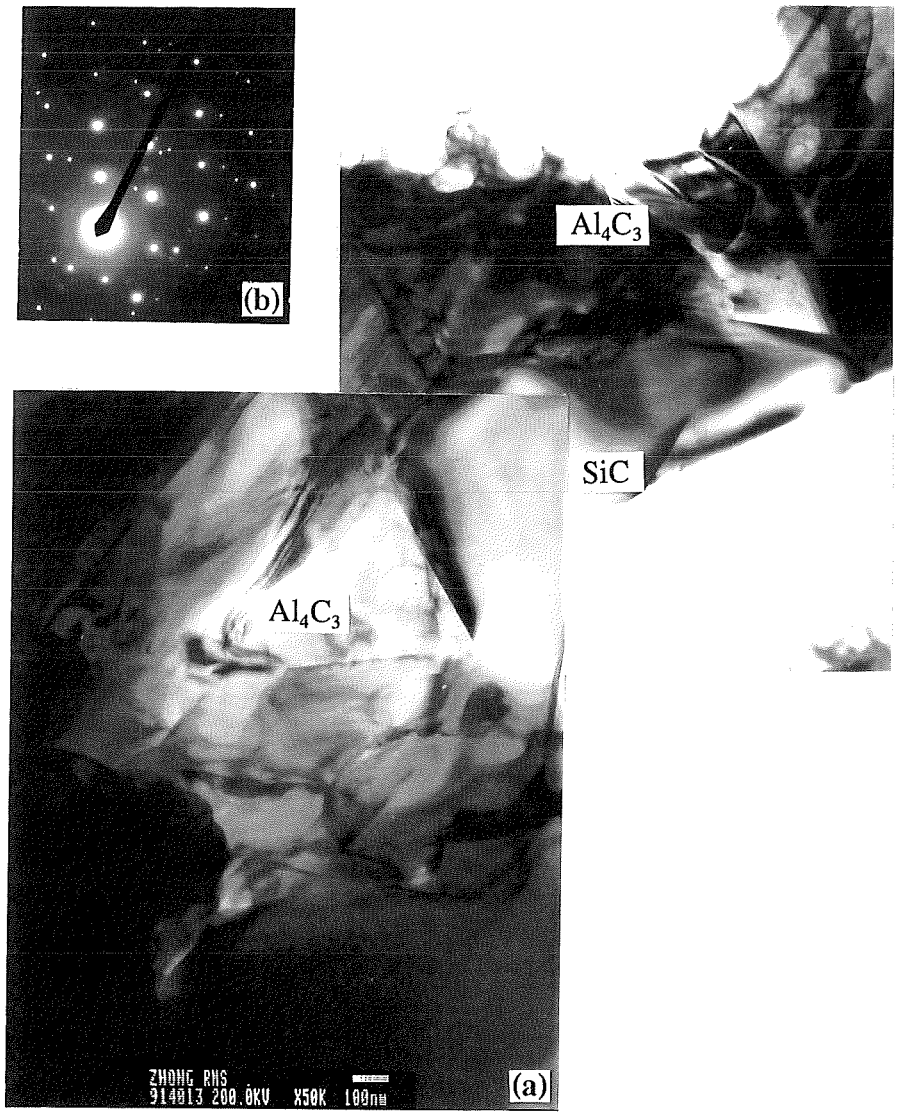

Figure 6(a) TEM BF image, the morphology of the attacked SiCp (RMS),
(b) SAD patterns of B[210]Al_4C_3

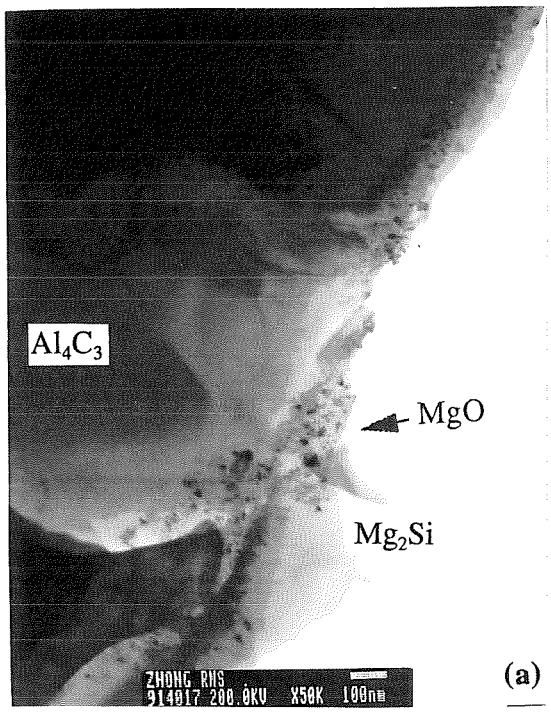

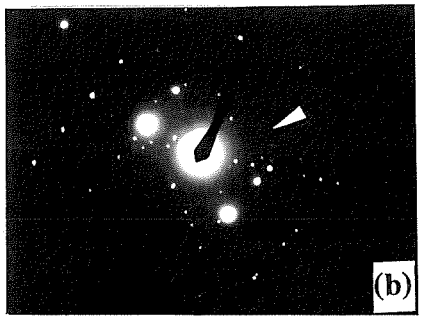

Figure 7(a) MgO crystals are observed at the original interface in front of Al_4C_3 (RMS),
(b) SAD pattern of MgO polycrystal

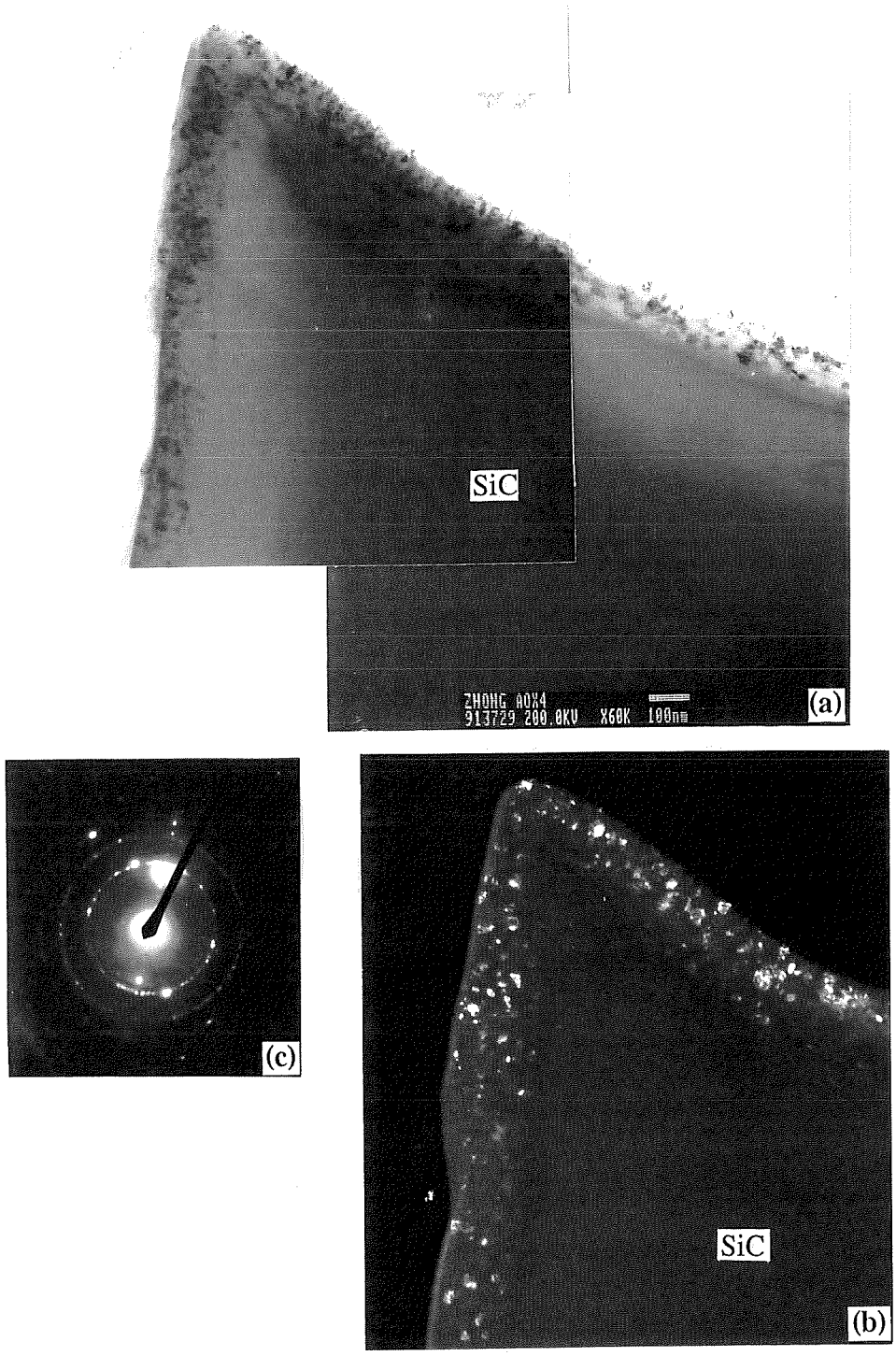

Figure 8 **(a)** TEM BF image, **(b)** DF image by (111)MgO, **(c)** SAD pattern of MgO obtained from the reaction zone (AOX3)

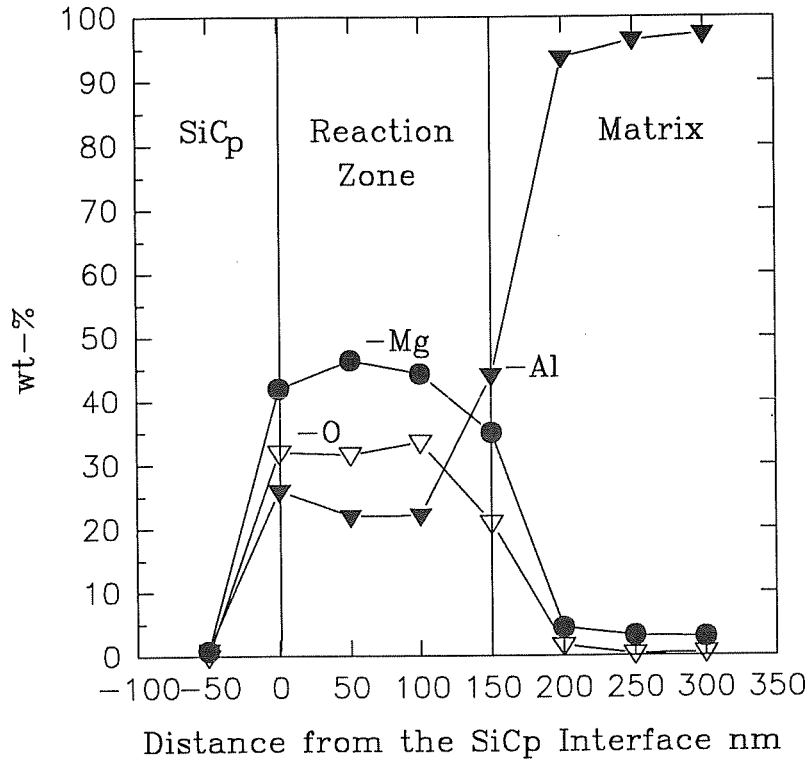

(a)

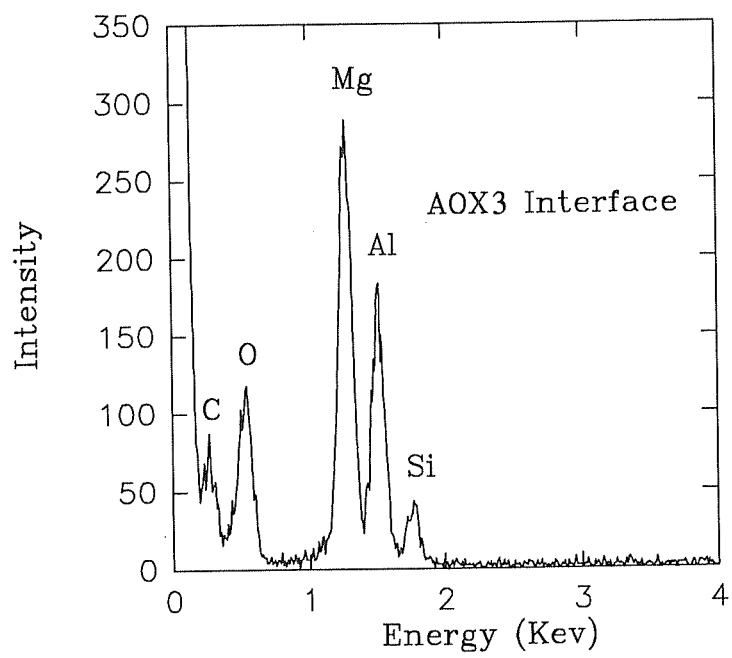

(b)

Figure 9(a) EDS line profile for AOX3
(b) EDS spectrum in the reaction zone

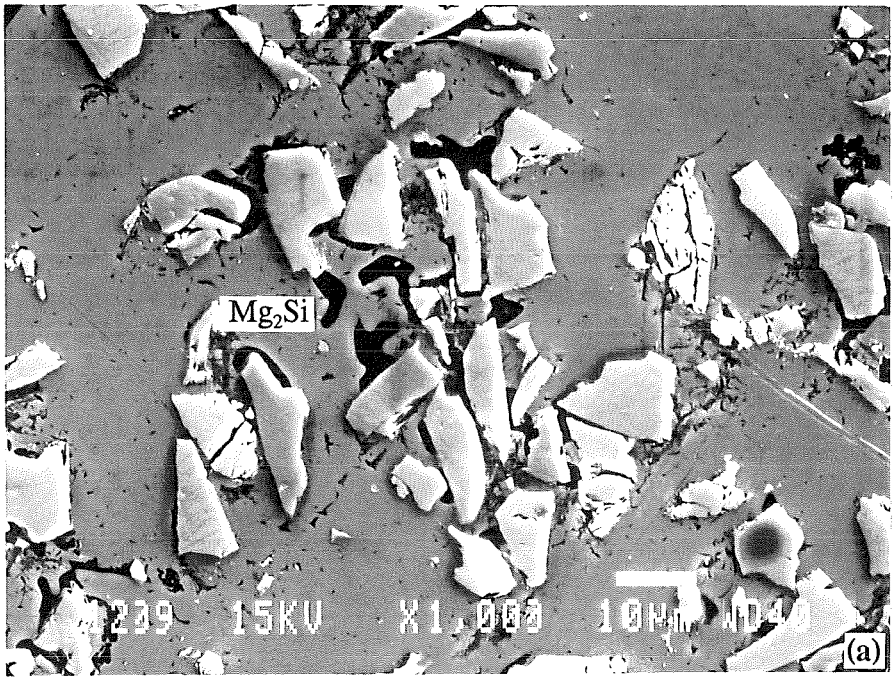

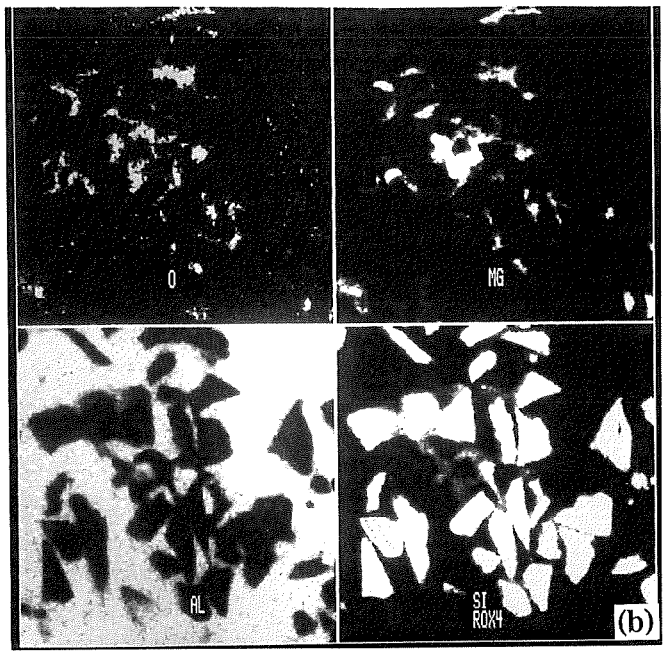

Figure 10(a),(b) SEM X-ray maps of the interfaces enriched in Mg and O (ROX3)

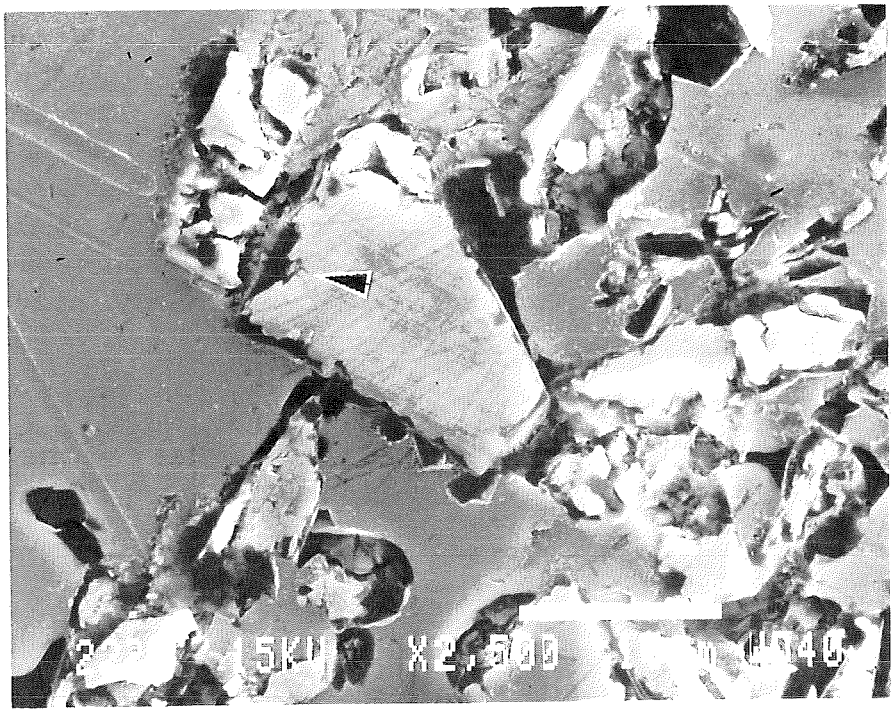

Figure 11 After remelting, some particles are attacked (ROX3)

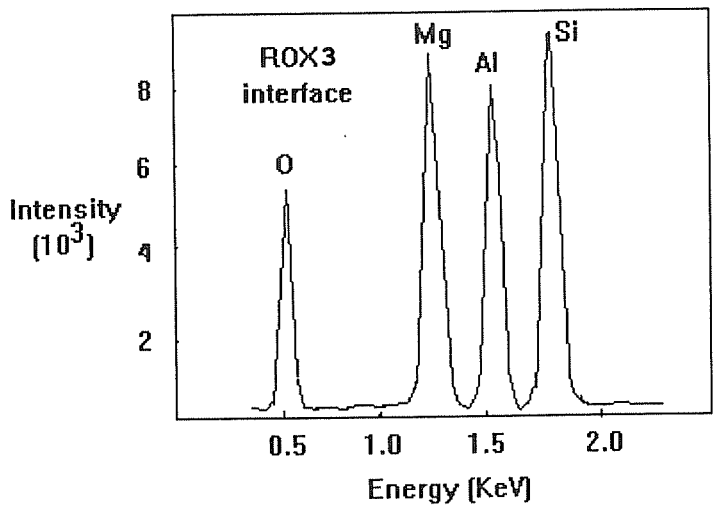

Figure 12 EDS spectrum obtained from matrix/SiCp interface (ROX3)

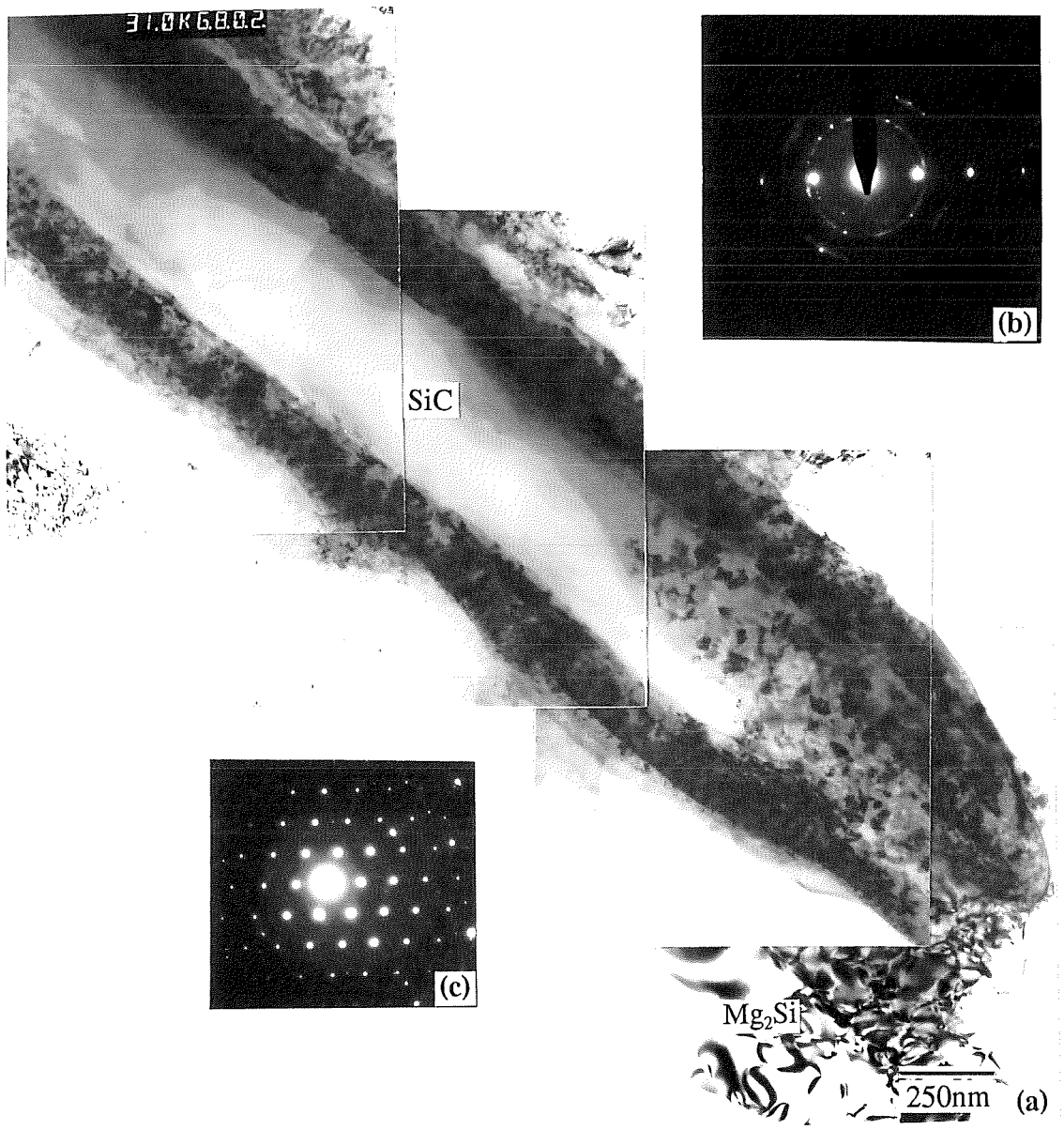

Figure 13(a) TEM BF image of ROX3, **(b)** SAD pattern of MgO, **(c)** Mg_2Si is found near SiCp, B[110]Mg_2Si

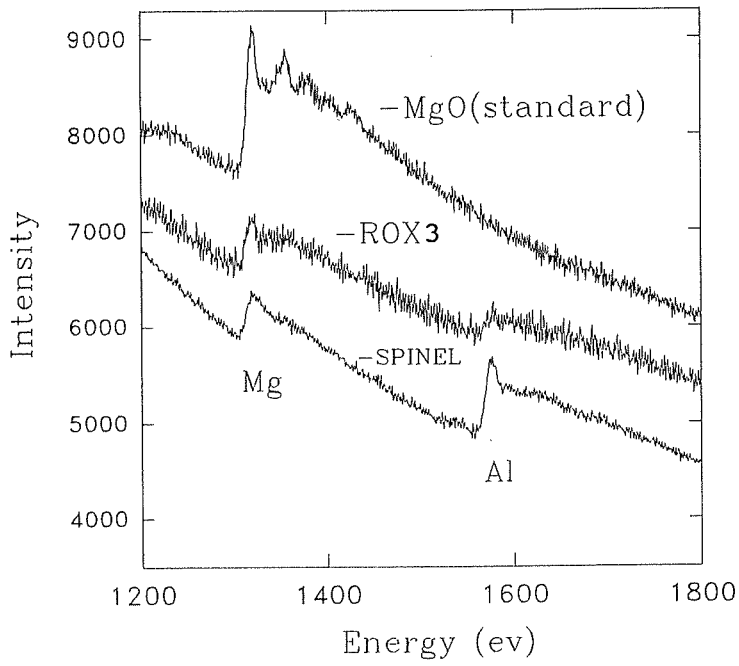

Figure 13(d) PEELS spectra obtained from the reaction zone (ROX3), pure spinel and MgO standards

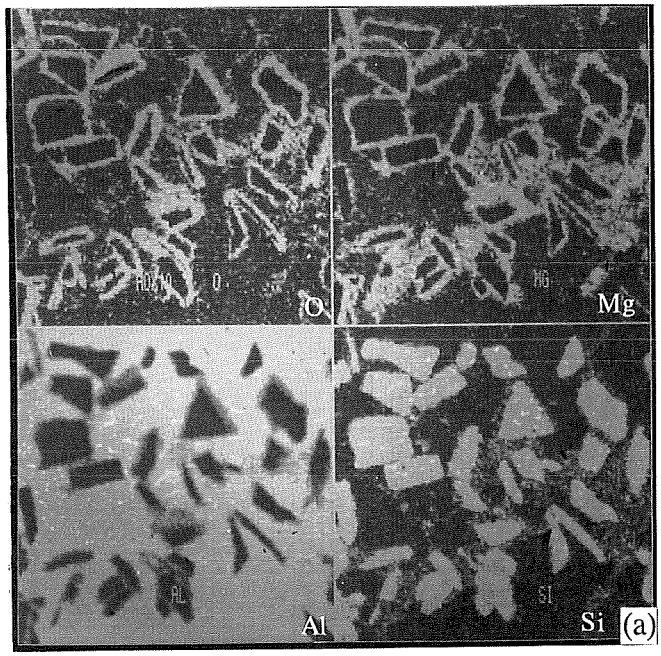

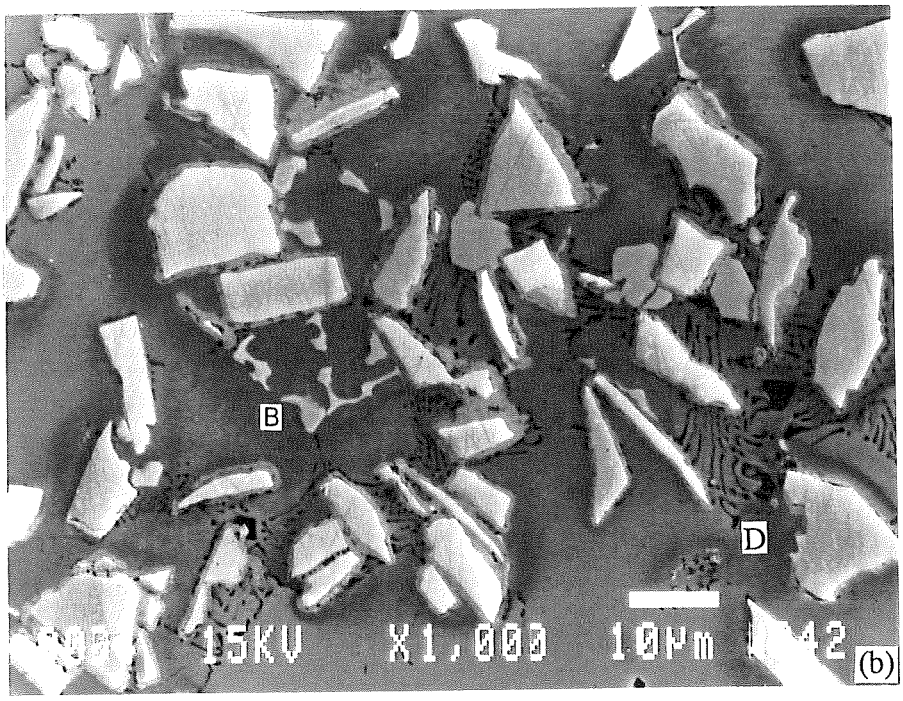

Figure 14 **(a)** SEM X-ray maps showing the segregation of Mg, O at the interfaces, **(b)** $(Cr,Mn,Fe)_3\ SiAl_{12}$ (B) and Mg_2Si (D) found in the matrix and near SiCp (AOX14)

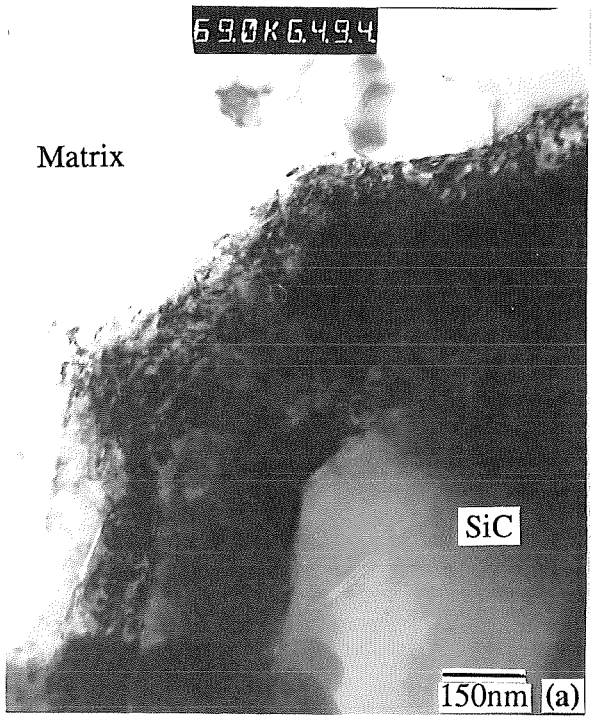

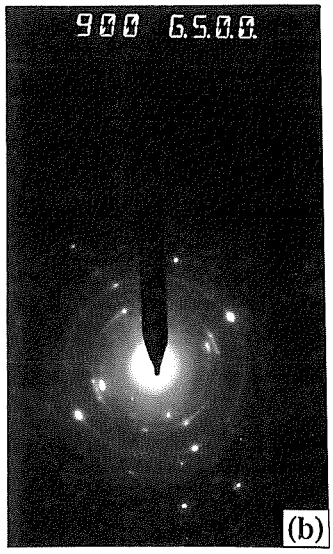

Figure 15 **(a)** TEM BF image of the interface (AOX14),
(b) SAD pattern with strong MgO rings

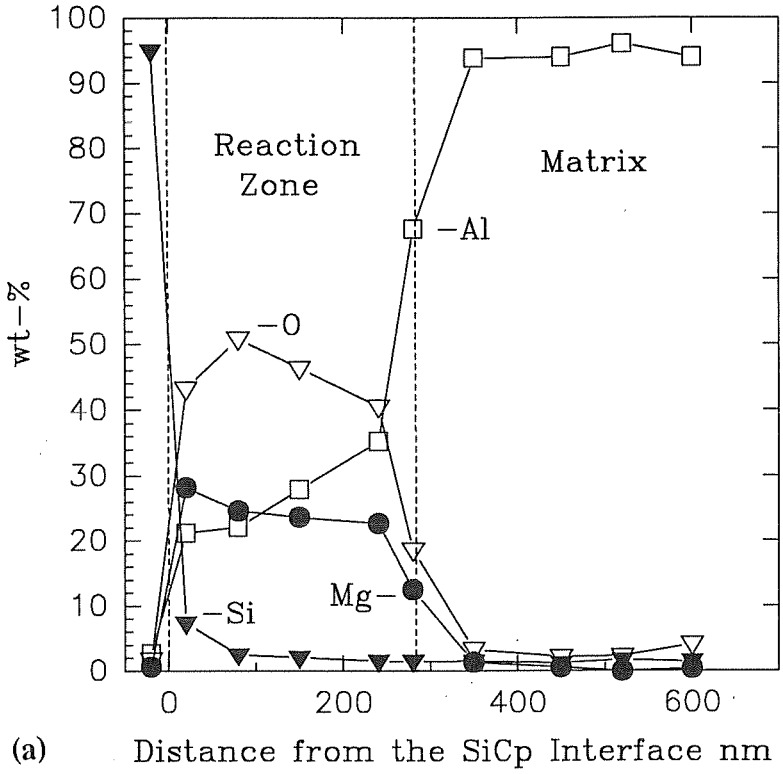

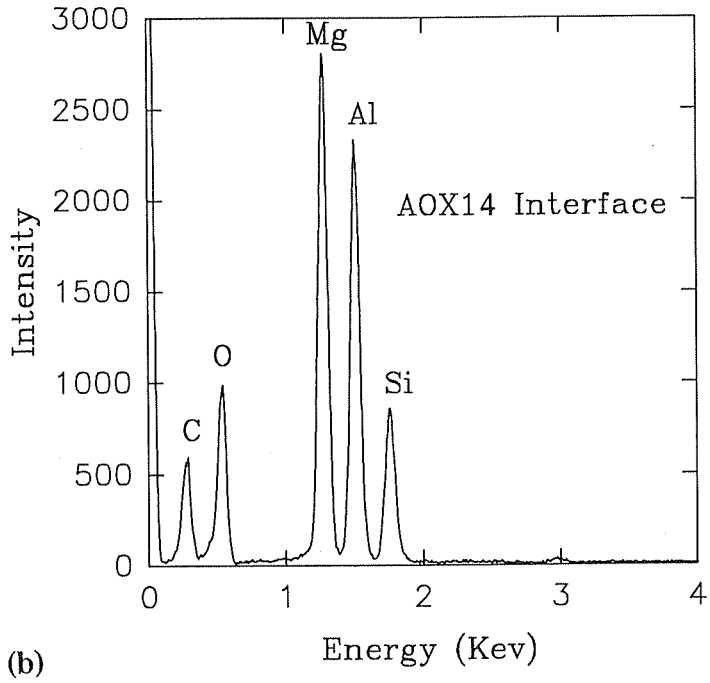

Figure 16 (a) EDS concentration profile for AOX14
(b) EDS spectrum in reaction zone

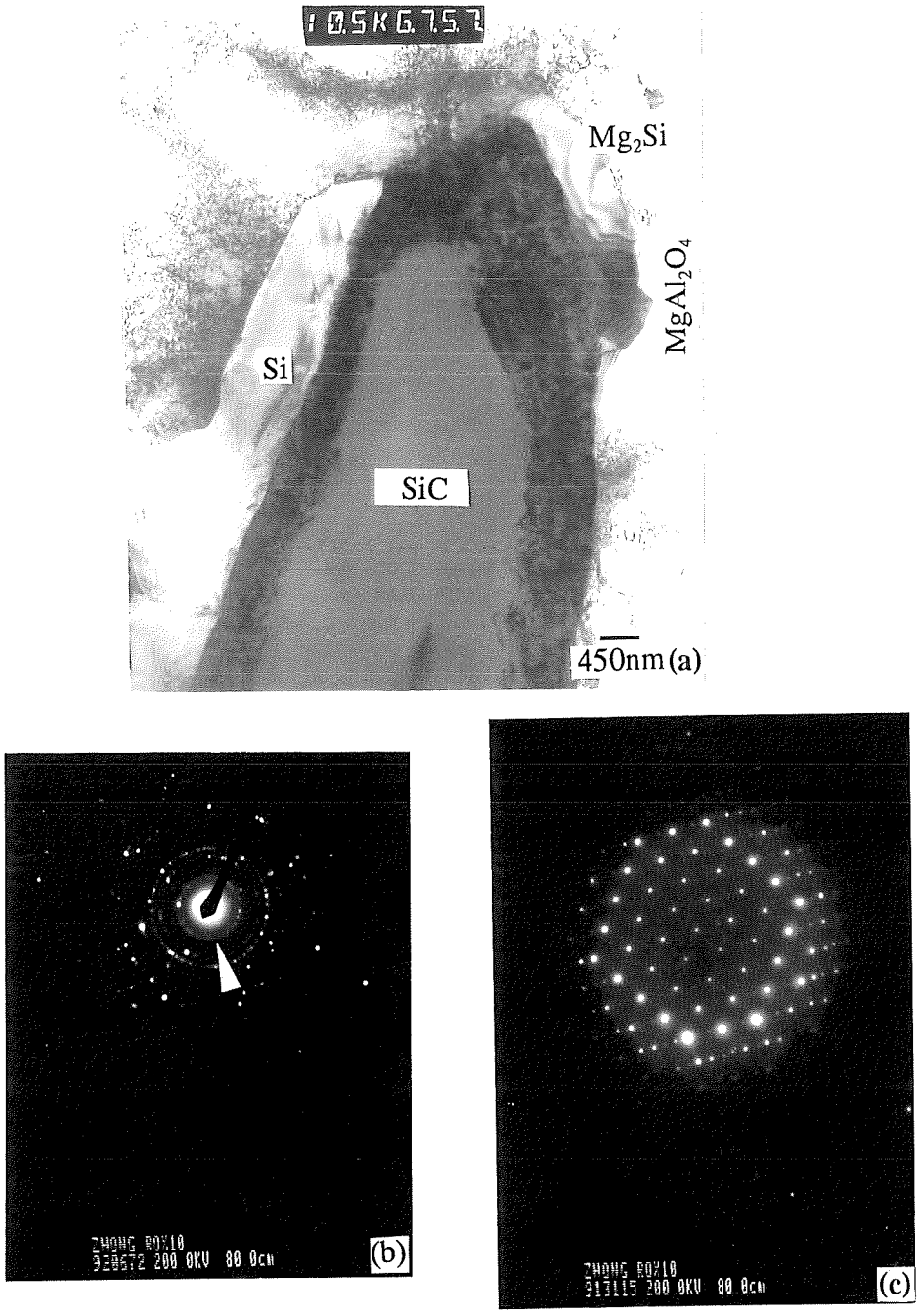

Figure 17(a) TEM BF image, Si, Mg_2Si and $MgAl_2O_4$ observed near the reaction zone in the matrix, **(b)** SAD pattern from the reaction zone indicating very strong (111)spinel diffraction, **(c)** SAD pattern of B[110]$MgAl_2O_4$ (ROX14)

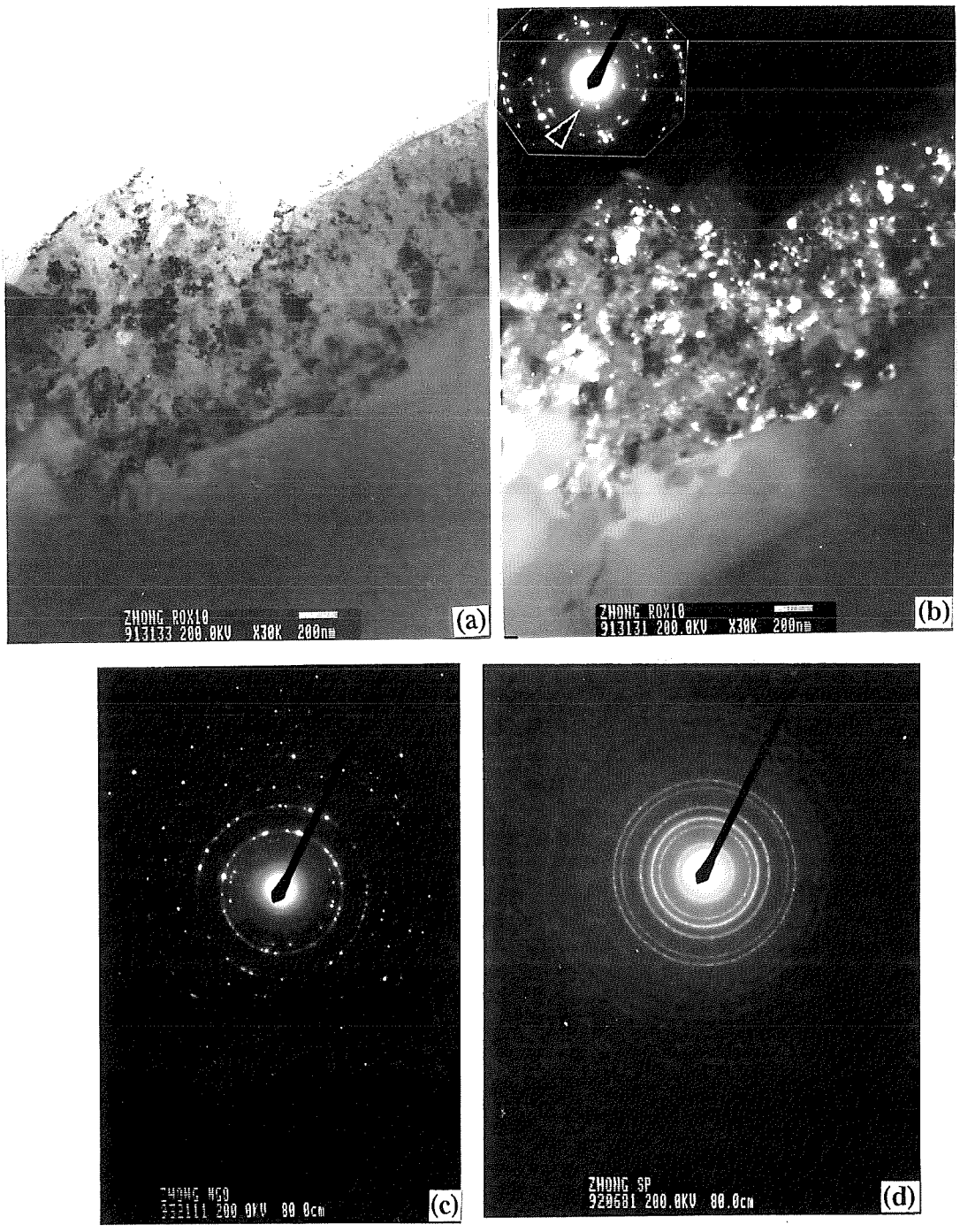

Figure 18(a) TEM BF image of the reaction zone around SiCp, **(b)** DF image by (111)sp (ROX14), **(c)** diffraction pattern of pure MgO, **(d)** diffraction pattern of pure $MgAl_2O_4$

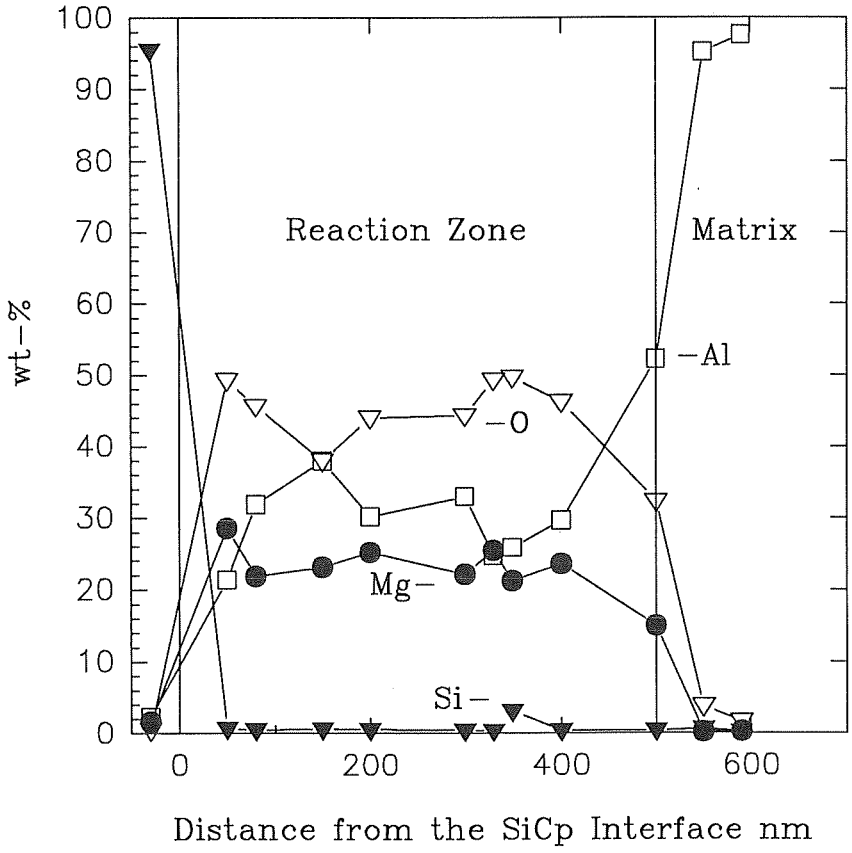

Figure 19 EDS profile at matrix/SiCp interface (ROX14)

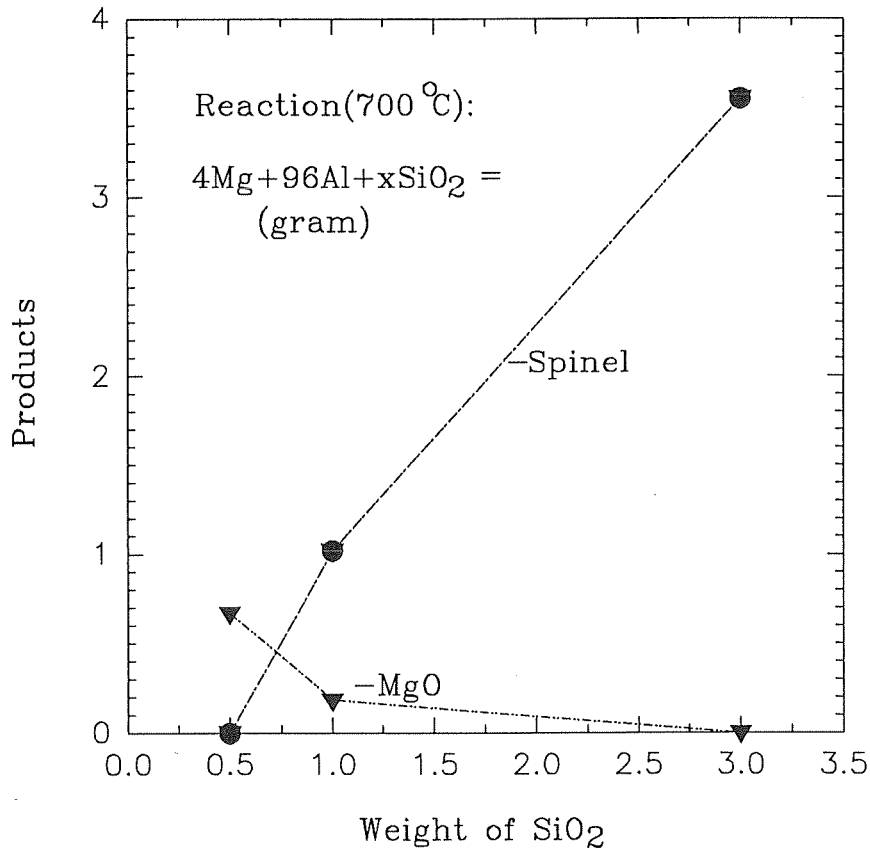

Figure 20 Effect of SiO_2 on the interfacial reaction products

2.2 Interfacial Reactions in Al-Mg (5083)/Al_2O_3p Composites During Fabrication and Remelting

W.M. Zhong*, G. L'Espérance* and M. Suéry**

* Ecole Polytechnique de Montréal, Centre de Caractérisation Microscopique des Matériaux $(CM)^2$, Case Postale 6079, Succ. "A", Montréal, Québec, Canada H3C 3A7

**Institut National Polytechnique de Grenoble, Génie Physique et Mécanique des Matériaux, GPM2, URA CNRS 793 ENSPG, B.P.46, 38402 St Martin d'Heres Cedex, France

Abstract

The interface reactions between α-Al_2O_3 particles and 5083 Al-Mg alloy during fabrication by compocasting and subsequent remelting at 800°C for 30 minutes have been studied using analytical transmission electron microscopy (TEM) and scanning electron microscopy (SEM). Experimental results show that MgO is the main reaction compound produced by the reaction: $3Mg(l) + Al_2O_3(s) = 3MgO(s) + 2Al(l)$. The MgO crystals formed by interfacial reaction are very small (about 5-20 nm in diameter) and the reaction zone is about 50-80 nm wide for as-cast materials and about 100-150 nm after

remelting. The reaction kinetics is controlled by seepage of Mg and release of Al(l) along the newly formed $MgAl_2O_4$ or MgO grain boundaries. Because of the large volume expansion during the formation of MgO from the reaction between Mg(l) and Al_2O_3, and because of the low diffusivity in MgO crystals, the reaction rate is very low.

1. Introduction

One of the requirements for a strong composite is a strong interfacial bond to permit load to be transferred from the matrix to the fibres or particles. Since the wettability between Al and Al_2O_3 is poor at temperatures below 900°C (Munitz et al. 1979 [1]), several procedures have been used to manufacture such composites. C.G. Levi et al.(1978) [2] used a process in which chopped Al_2O_3 fibres were added to vigorously agitated, partially solid metal slurries of Al-Mg or Al-Cu-Mg alloys. They found that incorporation, wetting and bonding of the fibres could be achieved by this technique and that agitation and additions of alloying elements such as Mg, Cu, etc. were essential. They concluded that bonding was achieved through the formation of a $MgAl_2O_4$ or $CuAl_2O_4$ (spinel) layer by the reaction between the fibres and the Mg or Cu in the liquid Al. P.K. Ghosh et al. (1990) [3], B.F. Quigley et al. (1982) [4] and M. Fishkis (1991) [5] have confirmed that $MgAl_2O_4$ was the main reaction product at the interface of Al-alloys/Al_2O_3 composites for Mg content lower than 4 wt%, but when the Mg content was greater than 4 wt%, MgO was found to be present (B.C. Pai, S. Ray

(1976) [6], Taftϕ et al. [7]). The possible reactions in such a system are:

$$Mg(l) + 2Al(l) + 2O_2 = MgAl_2O_4(s) \quad (1)$$

$$Mg(l) + 4/3\ Al_2O_3(s) = MgAl_2O_4(s) + 2/3Al(l) \quad (2)$$

$$MgO(s) + Al_2O_3(s) = MgAl_2O_4(s) \quad (3)$$

$$2Al(l) + 3/2\ O_2 = Al_2O_3(s) \quad (4)$$

$$2Mg(l) + O_2 = 2MgO(s) \quad (5)$$

$$3Mg(l) + Al_2O_3(s) = 3MgO(s) + 2Al(l) \quad (6)$$

As pointed out by Levi et al., reaction (6) is unlikely when the Mg content is less than 4 wt%, although the preceding reactions are all thermodynamically possible in the temperature range from 650~900°C. Reaction (3) is also unlikely because it occurs in the solid state. Both reactions (1) and (2) will contribute to the formation of $MgAl_2O_4$ at the interface in their systems. However, A.D. Mcleod (1990) [8] gave a stability diagram for the MgO-$MgAl_2O_4$ equilibrium. According to this diagram, the Mg concentration necessary for the formation of MgO is only about 1 wt% at 680°C , whereas at 800°C, it is about 1.6 wt% Mg. Cappleman et al. (1985) [9], did not find any interface reaction product in σ-Al_2O_3 fibres/Al-(9.5~11 wt%)Mg interfaces, owing to the short mixing time used (less than 1 min.) during fabrication. Y.Le. Petitcorps et al. (1991) [10], R. Molins et al. (1991) [11] studied the Saffil Al_2O_3 fibre (with 3%-4% SiO_2)/Al-Mg (Mg from 0.3~2.2 wt%) system. They suggested that the formation of MgO and $MgAl_2O_4$ arise from the following reactions:

$$SiO_2(s) + 2Mg(l) = 2MgO(s) + Si(s) \quad (7)$$

$$Mg(l) + 2Al(l) + 2SiO_2(s) = MgAl_2O_4 + 2Si(s) \quad (8)$$

The reaction between Mg and Al_2O_3 was not emphasized. B. Hallstedt et.al. (1990) [12] calculated the reaction kinetics in the Mg-Al_2O_3 system and concluded that the reaction between Mg(l) and $Al_2O_3(s)$ is impossible during fabrication of the composites because the interdiffusion of Mg^{2+} or Al^{3+} through the newly formed MgO or $MgAl_2O_4$ layer is very slow (D_{Al}^{MgO} is about $\sim 3x10^{-16}cm^2/s$, $D_{Al}^{sp} \sim 2x10^{-14}cm^2/s$, at 727°C). M. Pfeifer et al. (1990) [13] studied the interface reaction in the system α-alumina fibres/magnesium alloy (ZE41A) in the temperature range from 710 to 715°C. A reaction layer of MgO, with an average width of 100 nm, was found. The size of the MgO particles was found to range from about 10 nm to 100 nm. It was proposed that the growth of the reaction zone was controlled by a "seepage" mechanism involving infiltration of liquid magnesium between MgO crystals. Jin and Lloyd [14] found that the interfacial reaction rate decreased with the increase of the Mg concentration in Al-Mg/Al_2O_3 system and that the reaction product was $MgAl_2O_4$ even though the Mg content was as high as 7 wt%.

From the reported works, it is evident that the interfacial reactions are different in the various systems investigated. This could be caused by the different fabrication conditions, alloy compositions or volume fractions of the reinforcing materials (they change the relative composition of the matrix) which were used by the various

investigators. The reaction mechanism between commercial Al-4.1 wt% Mg (5083) alloy and Al_2O_3 particles is still not clear. Therefore, the interfacial reaction kinetics in the Al-Mg (5083) alloy/Al_2O_3p composites fabricated by compocasting will be presented. The protective role of the interfacial reaction products during remelting experiments will also be discussed. 5083 Al alloy, the matrix alloy, is a solid solution hardening alloy. It has moderate strength and good corrosion resistance, weldability, and superplasticity [15]. A study of the room temperature and the high temperature deformation behaviour of the composites, and the effects of the interfacial reaction on the mechanical properties will be published elsewhere.

2. Experimental Procedures

The α-Al_2O_3 particles used in this study were obtained from Elektroschmelzwerk Kempten Gmbh, Germany and the chemical composition was 99.4% Al_2O_3, 0.05% SiO_2, 0.03% Fe_2O_3 and 0.4% Na_2O. Their average size was about 13 μm diameter and a volume fraction of 10% was incorporated. The Al_2O_3 particles were single crystals. The composition of the 5083 alloy is 4.10Mg-0.56Mn-0.12Cr-0.19Fe-0.15Si-0.04Cu-0.02Ti-Al (balance) wt%. Composites were fabricated using the compocasting technique. Al_2O_3 particles were added to a semi-solid slurry in the temperature range of about 600-640°C. The slurry was agitated and reheated rapidly to about 720°C for casting (5 min.). The mould was preheated to 300°C. During solidification, a pressure of 100 MPa was

applied. In order to study the influence of a high temperature remelting treatment of the composites, as-fabricated composites were remelted and held at 800°C for about 30 min. in argon. The interface reaction was studied by scanning electron microscopy (SEM) coupled to a Link X-ray analysis system and by transmission electron microscopy (TEM). A CM30 Philips analytical transmission electron microscope equipped with energy dispersive X-ray spectrometer (EDS) and parallel electron energy loss spectrometer (PEELS, Gatan 601) and a JEOL 2000-FX TEM coupled to a Link EDS system were used. The samples for TEM observation were prepared by mechanical polishing, dimpling, and ion beam thinning (5 kV, at a tilt angle of 12-15°).

3. Results and Discussion

3.1 As-cast materials (ARO)

An SEM micrograph of the as-cast composites (ARO) is shown in Fig.1. The distribution of Al_2O_3 particles is macroscopically uniform, and the particles appear intimately bonded to the matrix. No porosity or shrinkage voids are observed at the interfaces or in the matrix. No reaction product is found at the interface by SEM. Mg_2Si, $(Cr,Mn,Fe)_3SiAl_{12}$ phases are found in the matrix, the usual phases in the 5083 alloy [16].

In TEM micrographs, interface reaction products are clearly seen (Fig.2(a)-(b)). The fine particles (with a size of 5-20 nm) are identified as MgO crystals from their selected area diffraction (SAD) patterns (see Fig.2(c)). Fig.2(b) is a TEM dark field (DF) image which shows MgO crystals inside the Al_2O_3 particles. The contour of the original Al (Mg)/Al_2O_3p interface can still be seen. The width of the reaction zone can be evaluated to be 50 nm to 80 nm. Fig.2 (d),(e) show the serrated morphology of the boundary of an Al_2O_3 particle which may have been caused by the separation of MgO crystals from the particle. Fig.2 (f) shows an interface where a MgO crystal protrudes out from an Al_2O_3 particle. Fig.2(f) also indicates that the MgO crystal is formed inside the Al_2O_3 particle and grows out from the particle. The results of EDS analyses show the high concentration of Mg and O in the interface reaction zone (see Fig.3).

3.2 Remelted materials (RMO)

In figure 4, the SEM image shows that the particles still have smooth and straight boundaries after remelting. In TEM micrographs, the interface reaction zone seems to be wider than that in the as-cast samples (Fig.5(a)&(b)). The width is now about 100-150 nm on the average; at some interfaces, it rises to several hundred nanometers (see Fig.5(a)&(b)). $MgAl_{26}O_{40}$ (tetragonal structure) and $MgAl_2O_4$ are found occasionally in the reaction zone in addition to large amounts of fine MgO crystals (Fig.5(c)&(e)). Fig.5(d)&(f) are the corresponding SAD patterns. Fig.6 (a) shows a reaction zone from which a streak-like diffraction pattern of the α-Al_2O_3 crystal is obtained (Fig.6(b)). The

EDS results show that the Mg content is still high in the reaction zone (accompanied by a large concentration of oxygen, see Fig.7). By assuming that all the Mg exists as MgO in the reaction zone and that the rest of the oxygen are attributed to Al_2O_3, the amount of metallic Al can be obtained after satisfying the requirement for oxygen to form MgO and Al_2O_3. For example, at the position of the largest Mg content measured (about 8% Mg, see Fig.7), the amounts of MgO, Al_2O_3 and metallic Al are about 14 wt%, 58 wt% and 28 wt% respectively. At a position located 80 nm inside the Al_2O_3, only 8 wt% MgO exists, the amount of Al_2O_3 is 85 wt% and the amount of metallic Al is 7 wt%. Therefore the MgO reaction zone is not a continuous layer and metallic Al and particularly Al_2O_3 exist in the reaction zone. Of course, the quantitative EDS composition profiles may be affected by several factors such as a large absorption, a relatively large uncertainty for the K_{AB}-factors needed to quantify analysis involving light elements, broadening of the incident electron beam in the sample, the position of the interface analyzed in relation to the X-ray detector and possibly the contribution of the nearby matrix and of the Al_2O_3 particle. Fig.8 shows EELS spectra obtained from the reaction zone and from pure $MgAl_2O_4$ and MgO crystals. The near edge fine structure of an EELS spectrum can be used to identify the bonding state of the element giving rise to the absorption edge in the spectrum [17]. Thus, a comparison of the sharp Mg edge obtained from the reaction zone to that of the pure MgO standard spectrum shows the existence of MgO in the reaction zone. In fact, MgO is found to be the main reaction product in this system. One of the reasons, as discussed previously, is that it is easier to form MgO thermodynamically when the Mg content in the matrix is larger than 4 wt%

[2,6,7]. From thermodynamic calculations carried out using the F*A*C*T Thermodynamic Database [18], we found that the relative amount of the reaction products changed with the amount of Al_2O_3 which actually took part in the reaction for a given Mg content (e.g. 4 wt%). The possibility to form MgO increases with the decrease of the amount of Al_2O_3 particles for our alloy system. As it will be discussed later, the reaction between Mg (Al) and Al_2O_3 is very slow. So, it can be assumed that only a small part of the Al_2O_3 particles is involved in the interfacial reaction because of the relatively short reaction time. For example, in our system, if only the outer layer of the Al_2O_3 particles (200 nm thickness, about 2% of the particles) takes part in the reaction, MgO will be the reaction product from our thermodynamic calculations. In our samples, the thickness of the reaction zone is about 50 to 150 nm. In addition, the Mg content in the remaining liquid Al in the semi-solid system during compocasting will be higher than the nominal composition (4.1 wt%). Therefore, the formation of MgO will be highly promoted. However, with the increase of reaction time, the possibility of developing $MgAl_2O_4$ will increase because the remaining Mg content in the matrix will decrease. An extreme situation would occur when the Al_2O_3 particles would be entirely consumed during the reaction. In this case, our thermodynamic calculations show that the final reaction product would be $MgAl_2O_4$ instead of MgO because of the small amount of Mg that would remain in the matrix.

3.3 Reaction Mechanism

The experimental results here show that the reaction between Mg and Al_2O_3 occurred in the as-cast samples (ARO), and became more pronounced in the as-remelted samples (RMO). Reaction (6) must have been involved in the interface reaction. The reaction between Mg(l) and Al_2O_3 does not form a perfect MgO or $MgAl_2O_4$ layer (with a thickness less than a few namometers) which would prevent further reaction, as Hallstedt et al. [12] suggested. Instead, it forms fine MgO crystals in the reaction zone, similar to the observations of M. Pfeifer et al.(1990) [13] and J. Taftϕ et al. (1988) [7]. The reaction was explained by a Mg "seepage" mechanism. The reaction zone nucleation starts as the Mg in liquid aluminum first comes into contact with the alumina grains. The MgO grains nucleate and grow along the edges of the alumina grains. MgO nucleation occurs further into the original alumina grains as molten Mg seeps in between already nucleated and growing MgO grains and reacts with the Al_2O_3 at the pre-existing reaction zone/Al_2O_3 interface. This seepage process continues until the MgO grains close to the matrix/reaction zone interface have grown large enough to close off the seepage spaces between these grains, or until the Al matrix has solidified. This mechanism can explain the limited thickness of the reaction zone. However, if the reaction time is long enough and there is sufficient Mg present in the matrix, it is expected that the reaction will continue until all of the Al_2O_3 particles have been consumed. As shown by B.C. Pai et al. (1976) [6], the reaction can continue into the centre of a 80 μm diameter Al_2O_3 particle without stopping, in the temperature range of 720 to 790°C. The Al released from the reaction must diffuse in the opposite direction for the reaction to continue although this has not been experimentally confirmed.

Usually, in reactions between liquid metals (such as Mg or Al) and oxides (such as Al_2O_3 or SiO_2) the diffusion of O^{-2} is neglected because of its large ionic size and its low diffusivity [12] (the ion diameter ratios of Mg^{+2}, Al^{+3} and Si^{+4} to O^{-2} are 0.47, 0.34 and 0.28 respectively [19]). Only the interdiffusion of the Al^{+3} and the Mg^{+2} cations between the O^{-2} "frame" is considered in the reactions [19]. Here, α-Al_2O_3 has a R3C structure. The oxygens are approximately in a hexagonal close-packed form, with the aluminum ions filling two-thirds of the octahedral interstices in the structure. The spinel structure ($MgAl_2O_4$, Fd3m) consists of an essentially cubic close-packed array of oxygen ions with metal cations occupying one-eighth of the tetrahedral interstices (the Mg^{+2}) and one half of the octahedral interstices (the Al^{+3}). A unit cell has 32 O^{-2}, 8 Mg^{+2} and 16 Al^{+3} ions. The MgO structure (Fm3m) consists of a cubic close-packing of O^{-2} ions with the smaller Mg^{+2} ions occupying the octahedral sites of the O^{-2} array. All of the interstices are occupied by Mg^{+2} ions. During any structure change, the condition of the neutralization of the charge around an anion in an ionic structure should be satisfied [19]. A series of diagrams is used to describe the reaction mechanism step by step, and to explain the reaction kinetics of the Mg(l) and Al_2O_3 (see Fig.9). As we know, the reaction between Mg(l) and Al_2O_3 is a thermodynamically favorable oxidation-reduction process which involves the interdiffusion of Al^{+3} and Mg^{+2} ions. When Mg^{+2} ions get into the interstitial sites of the Al_2O_3 and replace the Al^{+3} ions, the positions of the O^{-2} must be re-adjusted in order to retain electrical neutrality and to decrease the lattice distortion energy; thus, the crystal structure is changed. These processes are driven by the chemical potential of the reaction. The spinel is the intermediate reaction product and

it would be the final reaction product without sufficient Mg. For example, spinel can be in the form of $xMgO\text{-}yAl_2O_3$. When x=1 and y=13, the form of the spinel is $MgAl_{26}O_{40}$. When x=1 and y=1, it is $MgAl_2O_4$ (stoichiometric spinel). When x=1 and y=0, it is MgO. The x-y relation of the spinel ensures the static electrical neutralization in the oxides.

The MgO (or $MgAl_2O_4$) crystals in the reaction zone are usually quite fine. From reactions (2) and (6), one can calculate the volume expansion. This is about 30% for MgO and 15% for $MgAl_2O_4$. Because of the large volume change, the newly formed phase (MgO or spinel) will break its bond with the original Al_2O_3 particle at an early stage and form very fine isolated crystals with their new phase boundaries. On the other hand, the growth of MgO or spinel crystals is limited by the low diffusivity in the oxides and scarce oxygen. Because of the relatively lower volume expansion in forming spinel, the newly formed spinel may break its bond with the original Al_2O_3 particle later than the MgO does and, therefore, develop a relatively large crystal size. A relatively larger diffusivity in $MgAl_2O_4$ than in MgO may also make $MgAl_2O_4$ grow faster [12]. The size of MgO or spinel crystals is also affected by their nucleation rates. With a high Mg content, the nucleation rate is high. Concerning the growth of the nuclei at the interface, Mg and O in the liquids (if present) should uniformly diffuse to the newly formed MgO nuclei. This will contribute to an uniform growth of the MgO nuclei. Eventually, the growth of the newly formed crystals will be limited by their impingement on each other. This is supported by the observations of I. Jin and Lloyd [14] who found that the reaction

product was finer with higher Mg content. The Al released by reaction (6) or (2) should be in the liquid state in the given temperature range (700 to 800°C). At the beginning, released Al can go directly into the liquid, but as the reaction goes further into the Al_2O_3p, it will travel along the newly formed spinel or MgO phase boundaries to reach the melt, because of the difficulty of diffusing through the MgO or spinel crystals (B. Hallstedt et al. (1990) [12]). The phase boundaries and grain boundaries are the diffusion channels not only for released Al but also for the incoming Mg solute. Because the size of the MgO or spinel crystals is very small (5 nm ~ 20 nm), the contribution of the phase or the grain boundary diffusion will be very important [20-22]. J. Horvath (1989)[21] also found that in nanocrystalline materials (with a crystal size of about 10 nm), the diffusion coefficient is many orders of magnitude higher than that for lattice diffusion due to the very large interface area in these materials. In our case, the assumption that the diffusion coefficient is several orders of magnitude larger than the lattice diffusion coefficient therefore seems reasonable (an increase of 4 to 6 orders of magnitude is necessary to explain the reaction zone thickness observed in our experiments as estimated using Hallstedt's calculations [12]). With the reaction continuing, some MgO crystals will be pushed out by other MgO crystals growing from the original alumina particle because of the volume expansion as seen in Fig.2 (d)-(f) and Fig.9(c)-(d).

As shown by SAD pattern obtained from the reaction zone (Fig.6(b)), the diffraction spots of the α-Al_2O_3 have a streak-like appearance. This means that the lattice

may be distorted or that fine Al_2O_3 crystals may exist in the reaction zone, caused by the fragmentation of the Al_2O_3 particle during reaction. The defects in the crystal are increased as the reaction continues, because the volume change will induce stresses inside the Al_2O_3 particles [6]. These defects will also contribute to the diffusion process. It is believed that the reaction will not terminate with increasing time for the given temperature although the reaction rate may decrease with time, and that the reaction kinetics will increase with increasing reaction temperature.

The reaction between Mg(l) and Al_2O_3 in Al-Mg (5083)/Al_2O_3p composites has been confirmed by our results, although it must be emphasized that the reaction rate is very low. The large volume expansion in forming MgO (30%) or $MgAl_2O_4$ (15%) will make the diffusion channels between the newly formed crystals very narrow and contribute to a low reaction rate. It is interesting at this stage to compare our results to those obtained in other systems in order to compare the relative protective role of different reinforcements and reaction products. Thus, in the case of Al-Mg/SiCp composites in which Mg(l) reacts with the SiO_2 layer formed on the surface of artificially oxidized SiC particles prior to their incorporation [17,23], the formation of MgO and $MgAl_2O_4$ crystals leads to a volume contraction of 13.6% and 27% respectively. This must be an important factor accounting for the much larger rate of the reaction between Mg(l) and SiO_2 than that between Mg(l) and Al_2O_3 [12,17,23]. A reaction zone (mainly consisting of MgO crystals, size 5 to 20 nm) with a thickness of 500 nm was observed in as-cast Al-Mg (5083)/SiCp composites (the particles were artificially oxidized to 14.06

wt%) [23].

In the Al-Mg/Al_2O_3 system, the reaction rate for forming MgO should be lower than that for forming spinel due to the larger volume expansion in forming MgO from Al_2O_3 and also due to the relatively lower diffusivity in MgO. Thus the reaction rate may decrease with increasing Mg content in the aluminum alloy since generally the possibility to obtain MgO increases with Mg content. Clearly several factors can contribute to the decrease of the interfacial reaction rate. These include a uniform and dense reaction zone resulting in narrow diffusion channels as we observed. In addition, however, it is expected that coarse or continuous reaction product will lead to reduced reaction rates as the diffusivity in the reaction zone should be reduced as a result of a decreased effective boundary area. It also seems logical, as discussed above, to consider the effect of the Al_2O_3 particle size on the reaction product and reaction rate because this would change the effective surface of contact between the particles and the liquid. The effect of Mg content on the interfacial reaction rate has been studied by Jin and Lloyd [14]. They found that for a composite with pure Al-Mg alloys and Al_2O_3 particles and melted at 720°C, the reaction rate reached a maximum over the Mg range of 1.0 to 2.5 wt% Mg. For Mg levels above 3 wt% the rate of reaction decreases, and it is essentially zero for an alloy with an initial composition of 7 wt% Mg. The reaction zone thickness was less than 100 nm with 7 wt% Mg and was about 600 nm with 2 wt% Mg for a mixing time of 2 hours. They indicated that the protective action of the reaction zone observed for higher Mg contents was the result of a continuous, fine grained film which

is formed for these Mg contents, as we would expect. For a 4 wt% alloy, the reaction product was identified as $MgAl_2O_4$ which is surprising since MgO should be the thermodynamically stable phase for this Mg content [2,6-8]. It is possible, however, that the reaction products are also affected by alloy compositions, different sources of Al_2O_3 and processing conditions.

In our experiments, some MgO and $MgAl_2O_4$ were found in the matrix near the Al_2O_3 particles, possibly as a result of the reaction of Mg with free oxygen dragged into the melt by the Al_2O_3 particles during fabrication (reaction (1) and (5)). Another possibility is that the MgO or $MgAl_2O_4$ particles formed inside the Al_2O_3 particle are released into the matrix as a result of stirring. Stirring also increases the reaction kinetics. Decomposition of the Al_2O_3, which can be a source of oxygen, may also occur. But it is expected that this would be very slow for the given temperature (Munitz 1979 [1]).

4. Conclusions

1) The interface reactions between α-Al_2O_3 particles and 5083 aluminum alloys in as-cast or in remelted composites have been studied. Fine MgO crystals are found to be the main reaction product. The width of the reaction zone can vary from about 50-80 nm in as-cast materials to about 100-150 nm in remelted materials.

2) The main reaction which accounts for the formation of MgO is: 3Mg (l) + Al_2O_3 (s) = 3MgO (s) + 2Al (l).

3) The kinetics is controlled by the seepage of Mg and the release of Al(l) along the newly formed spinel and MgO boundaries.

4) The reaction rate in the Al-Mg (5083)/Al_2O_3p system is very low because of the large volume expansion in forming MgO which makes the diffusion channels between the newly formed crystals very narrow. The reaction rate in forming MgO is believed to be lower than that in forming $MgAl_2O_4$ due to the larger volume expansion in forming MgO from Al_2O_3 and the relatively lower diffusivity in MgO crystal. Generally, several factors can decrease the interfacial reaction rate. These include a uniform and dense reaction zone which would result in narrow diffusion channels and a coarse or continuous reaction product, which would reduce the effective boundary area and therefore the effective diffusion.

Acknowledgments

The authors gratefully acknowledge the NATO International Scientific Exchange Programme (Grant no. CRG 900950) and the National Science and Engineering Research Council (NSERC) of Canada (strategic grants) for the financial support. They also thank E. Goiffon, L. Salvo and J.J. Blandin for the preparation of the composite materials. Thermodynamic calculations were performed with the help of P. Wu and J. Wu.

References

1. A. Munitz, M. Metzger, and R. Mehrabian, Metall. Trans. A, Vol.10A, 10(1979), pp.1491-1491

2. C.G. Levi, G.J. Abbaschian, R. Mehrabian, Metall. Trans. A, Vol. 9A, 5(1978), pp.697-711

3. P.K. Ghosh, S. Ray, Proc. of fabrication of particulates reinforced metal composites, edited by J. Masounave and F.G. Hamel (1990), Montreal, ASM, Metals Park, Ohio, 1990, pp.23-30

4. B.F. Quigley, G.J. Abbaschian, R. Wunderlin and R. Mehrabian, Metall. trans. A, Vol. 13A, 1(1982), pp.93-100

5. M. Fishkis, J. of Mater. Sci. 26(1991), pp.2651-2661

6. B.C. Pai, S. Ray, Mater. Sci. and Eng. 24(1976), pp.31-44

7. J. Taftϕ, K. Kristiansen, H. Westengen, A. Nygard, J.B. Borradaile, D.O. Karlsen, Proc, Conf. on Cast Reinforced Metal Matrix Composites, Chicago, Il, (1988), edited by S.G.Fishman, A.K. Dhingra, ASM, Metals Park, Ohio, 1988, pp.71-75

8. A.D. Mcleod, same with 3, pp.18-21

9. G.R. Cappleman, J.F. Watts, T.W. Clyne, J. of Mater. Sci. 20(1985), pp.2159-2168

10. Y. Le Petitcorps, J.M. Quenisset, G.Le Borgne, M. Barthole, Mater. Sci. and Eng. A 135(1991), pp.37-40

11. R. Molins, J.D. Bartout and Y. Bienvenu, Mater. Sci. and Eng. A 135(1991), pp.111-117

12. B. Hallstedt, Z.K. Liu and J. Ågren, Mater. Sci. and Eng. A 129(1990), pp.135-145

13. M. Pfeifer, J.M. Rigsbee, K.K. Chawla, J. of Mater. Sci. 25(1990), pp.1563-1567

14. D.J. Lloyd, I. Jin and G.C. Weatherly, Scripta Metall, vol.31, No.4(1994), pp.393-396

15. M. Mizuno and H. Nagaoka, International Metals Reviews, No.2(1979), pp.68

16. Metals handbook, 9th edition, vol.9(1979), pp.362

17. J.G. Legoux, G. L'Esperance, L. Salvo and M. Suery, Proc. of Fabrication of Particulate Reinforced Metal Composites, edited by J. Masounave and F.G. Hamel (1990), Montreal, ibid 3, pp.31

18. F*A*C*T thermodynamic database, CRCT, Ecole polytechnique, Montreal, Canada, 1993

19. F. Donald Bloss, Crystallography and Crystal Chemistry, 1971, pp.240-253

20. B.S. Bokstein, Defect and Diffusion Forum Vols. 66-69(1989), pp.631-648

21. Jenö Horváth, Defect and Diffusion Forum Vols. 66-69(1989), pp.207-228

22. P.A. Lessing, R.S.Gordon, J. of Mater. Sci. 12(1977), pp.2291-2302

23. W.M. Zhong, G. L'Esperance and M. Suery, Interfacial Reaction in 5083/SiCp Composites During Fabrication and Remelting, unpublished research, Ecole polytechnique, Montreal, Canada, 1993

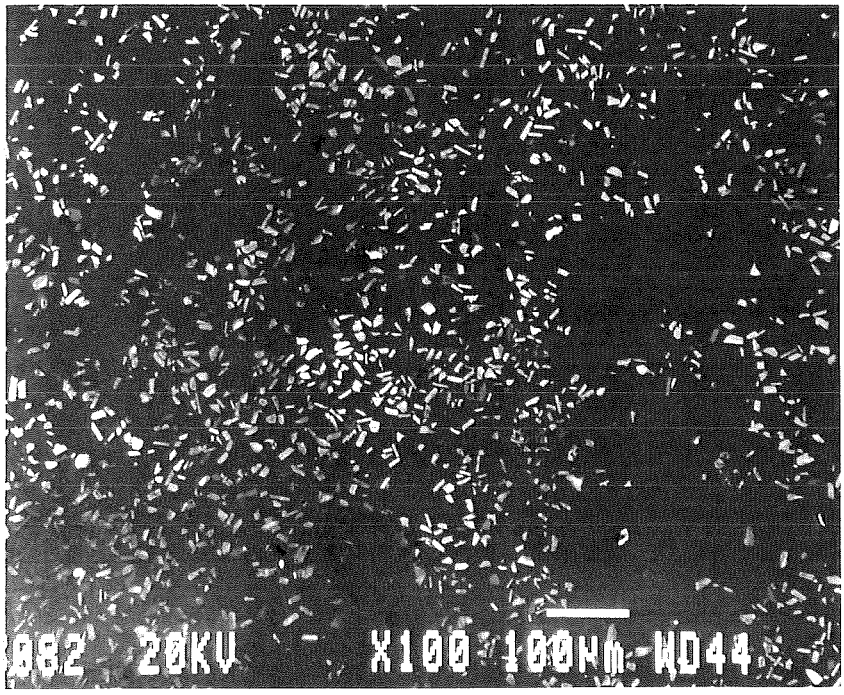

Figure 1 Distribution of Al_2O_3p (ARO, 5083/Al_2O_3, as-cast)

Figure 2 ARO (5083/Al_2O_3, as-cast)
a) BF images showing reaction zone inside Al_2O_3p
b) DF image by (200)&(111)MgO diffraction
c) SADP from reaction zone, showing strong MgO diffraction and weak (111)$MgAl_2O_4$ diffraction

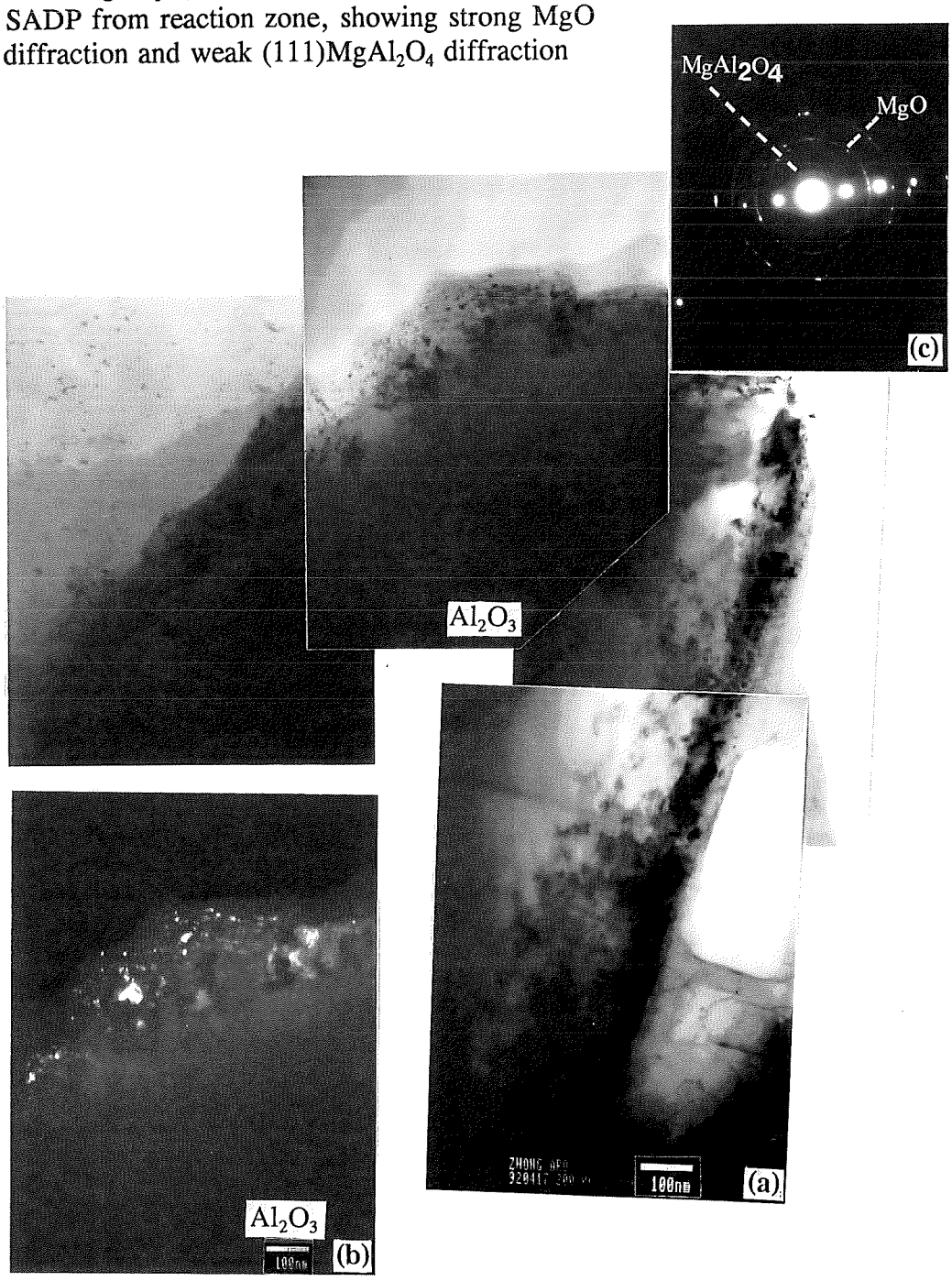

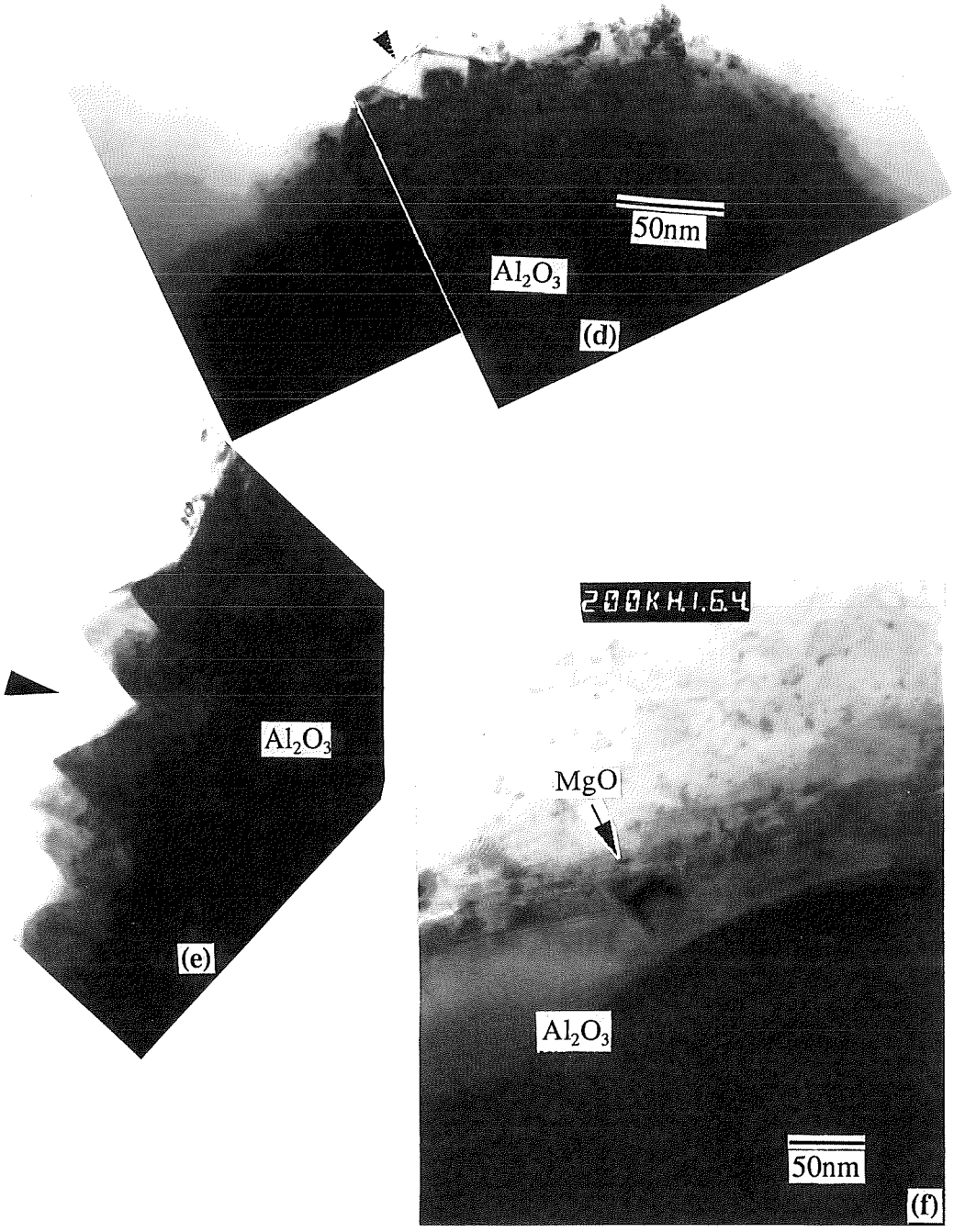

Figure 2 **(d),(e)** Serrated morphology at the boundary of Al_2O_3p
(f) a MgO crystal protruding out from the Al_2O_3p

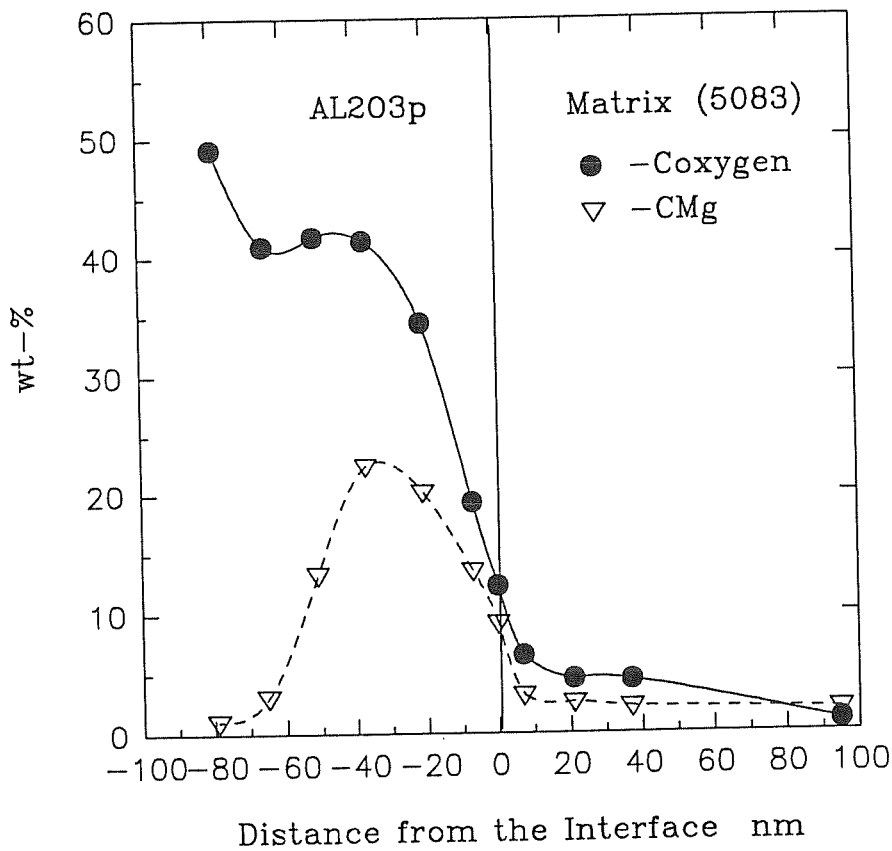

Figure 3 EDX concentration profile for ARO

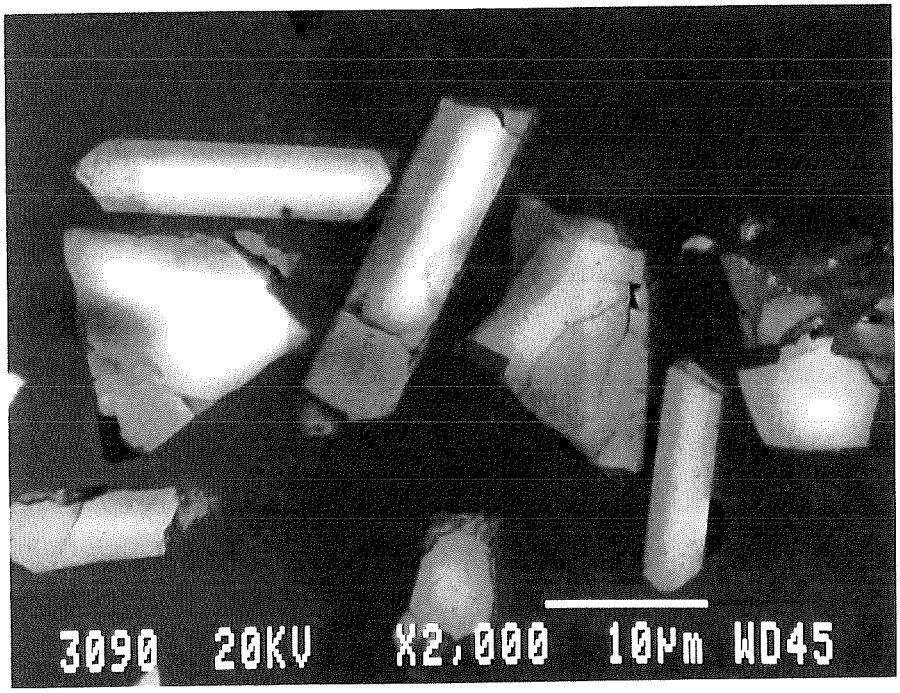

Figure 4 RMO (5083/Al_2O_3 - remelted) reaction layer still invisible by SEM.

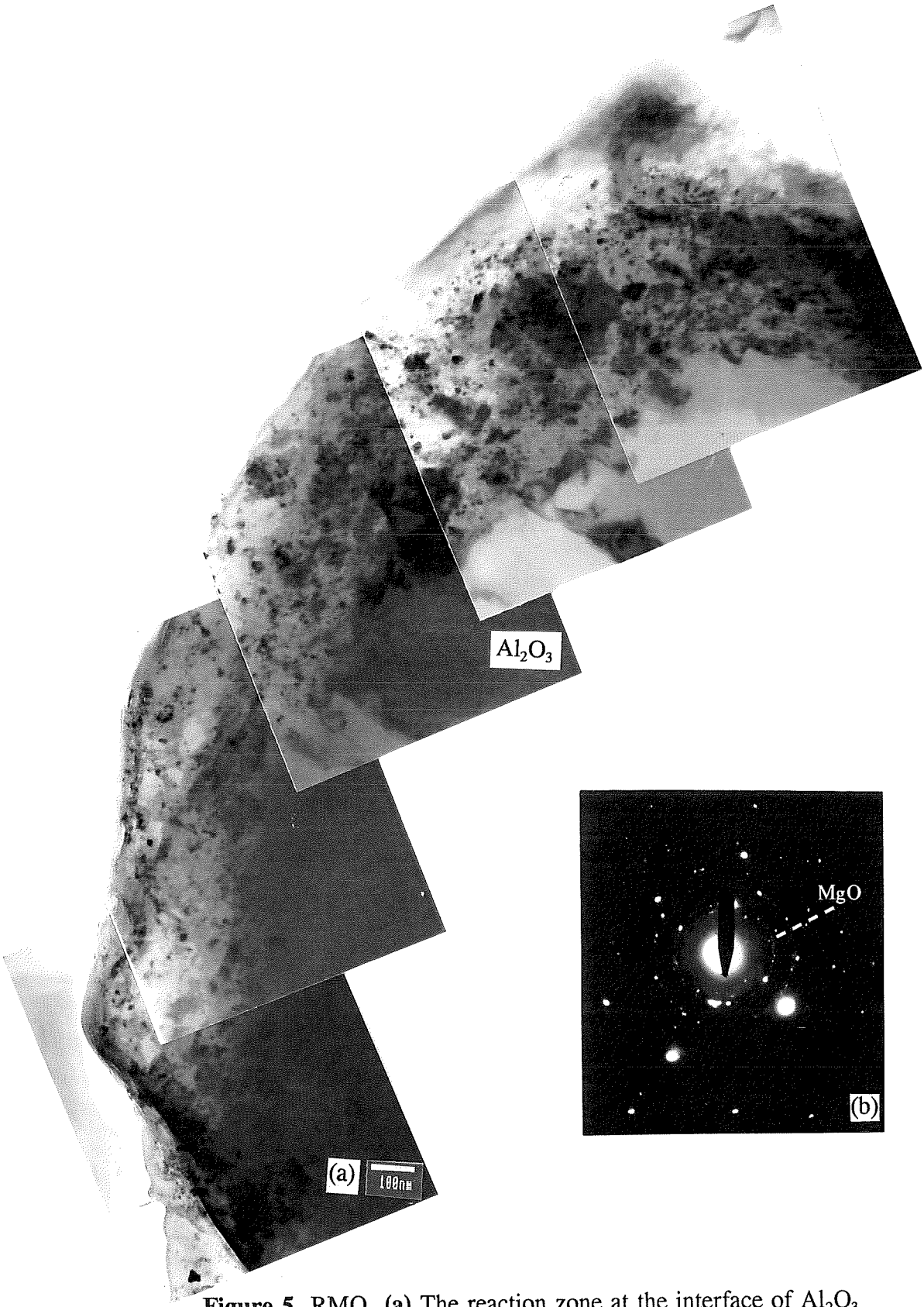

Figure 5 RMO, **(a)** The reaction zone at the interface of Al_2O_3 particle and **(b)** SAD pattern of MgO crystals

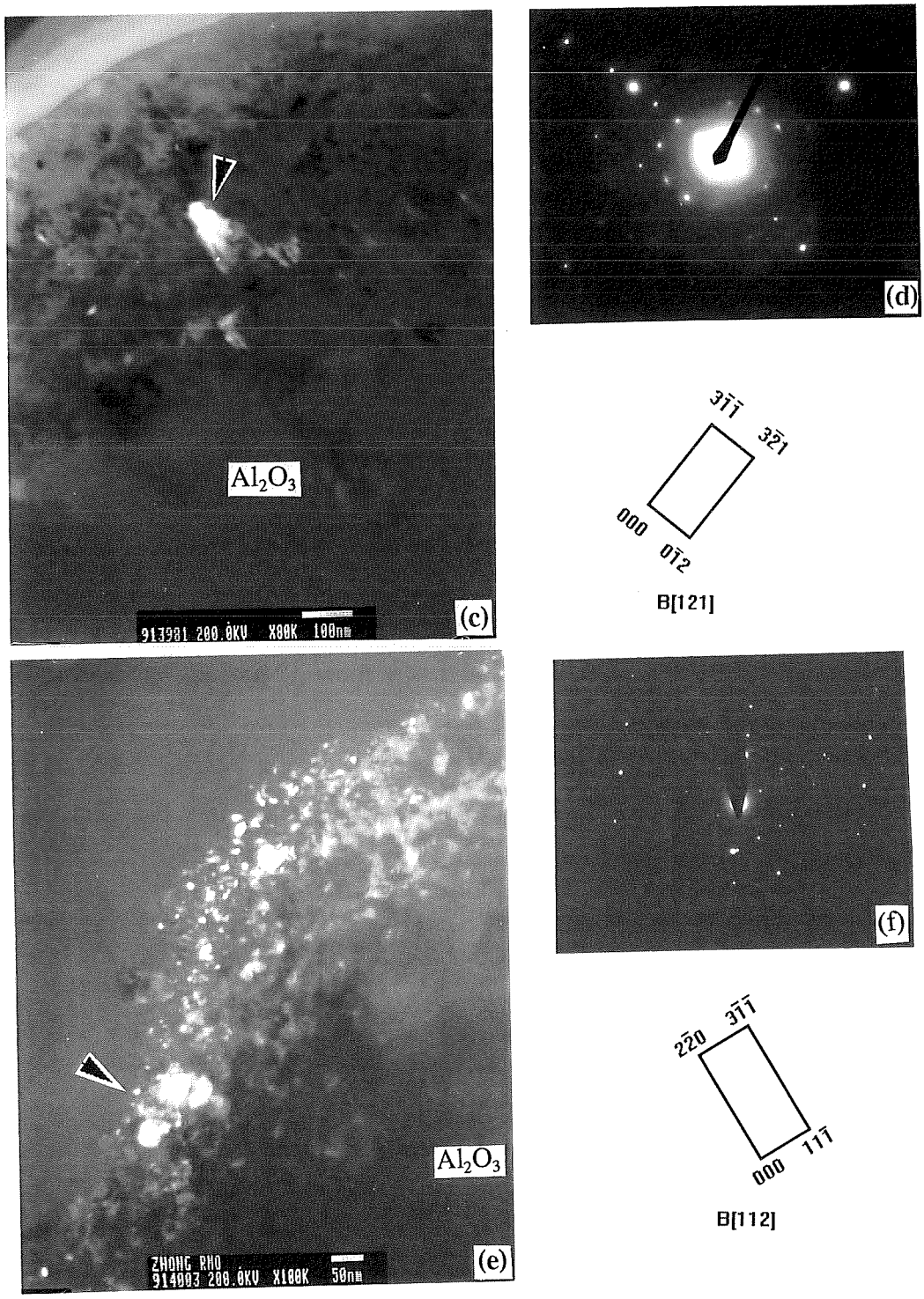

Figure 5 (c) DF image by (012)$MgAl_{26}O_{40}$, (d) SAD pattern of B [121]$MgAl_{26}O_{40}$ (e) DF image by (111)MgO, (f) SAD pattern of B [112]$MgAl_2O_4$

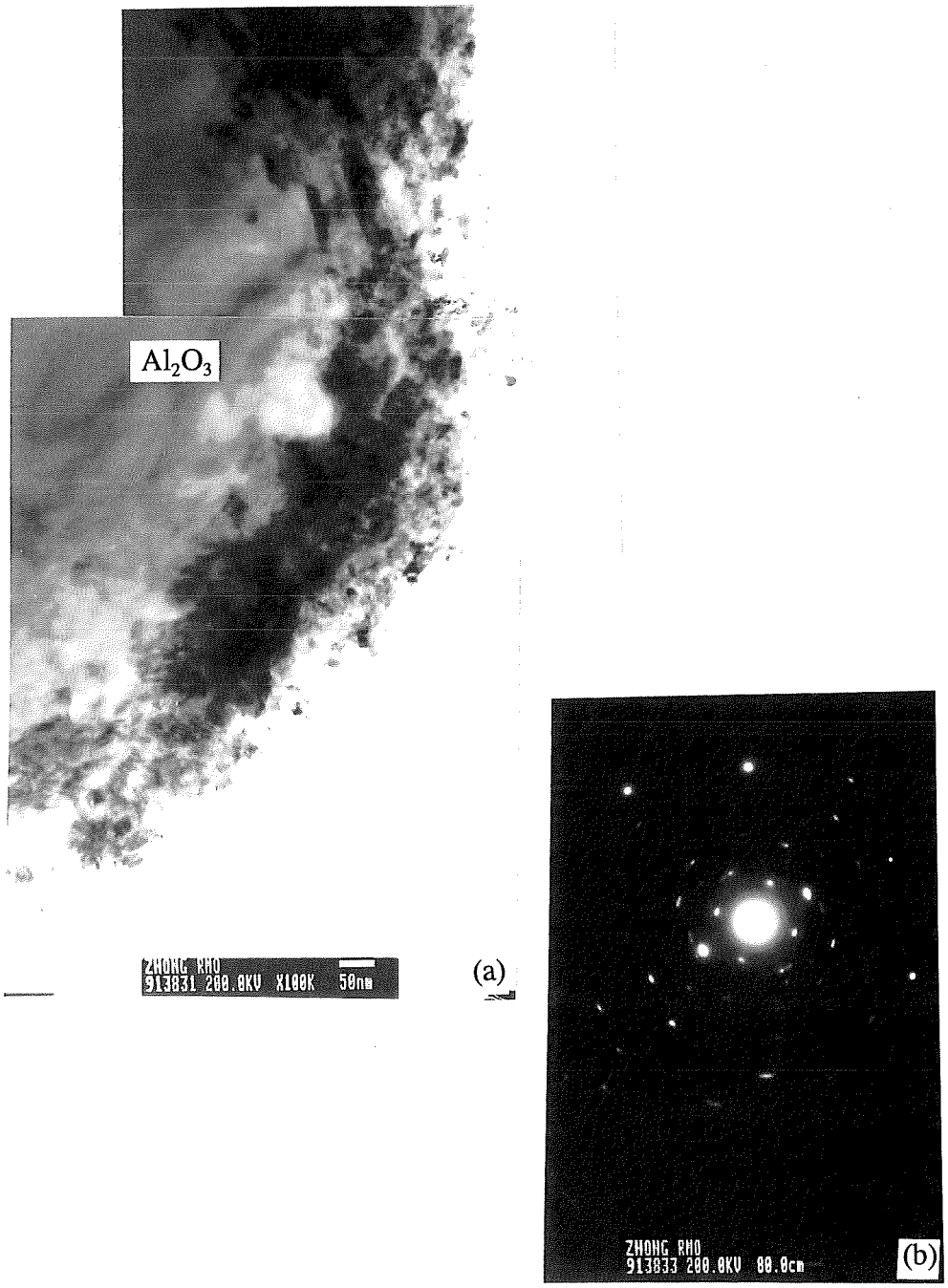

Figure 6 (a)(b) The interface of alumina/matrix and SAD pattern of B[2201]α-Al_2O_3

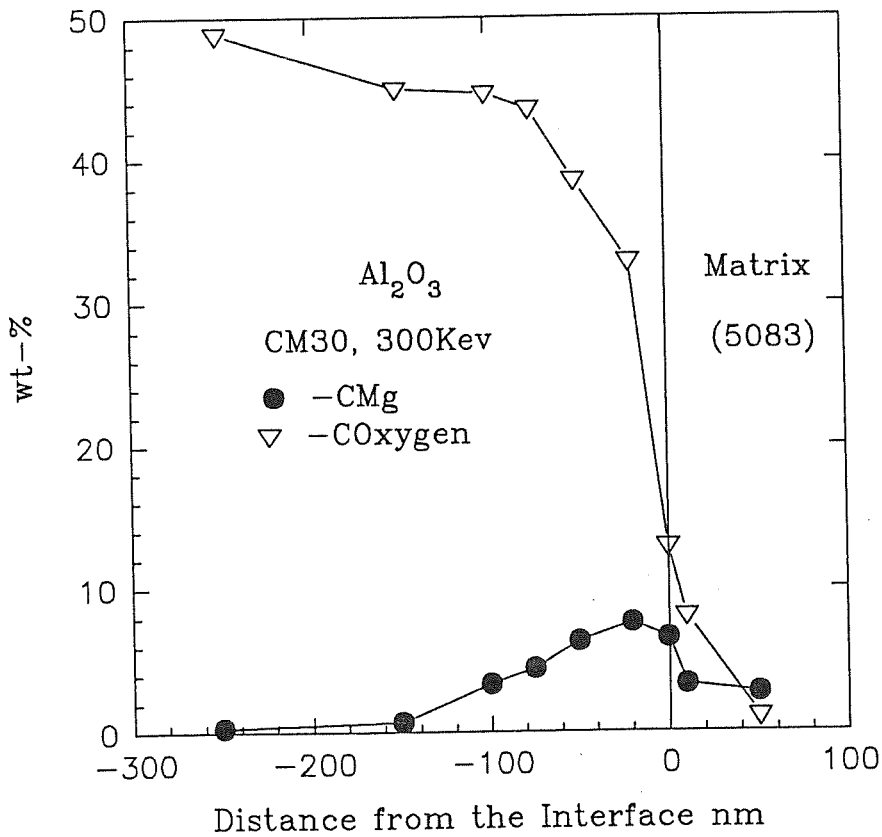

Figure 7 EDX concentration profile for RMO

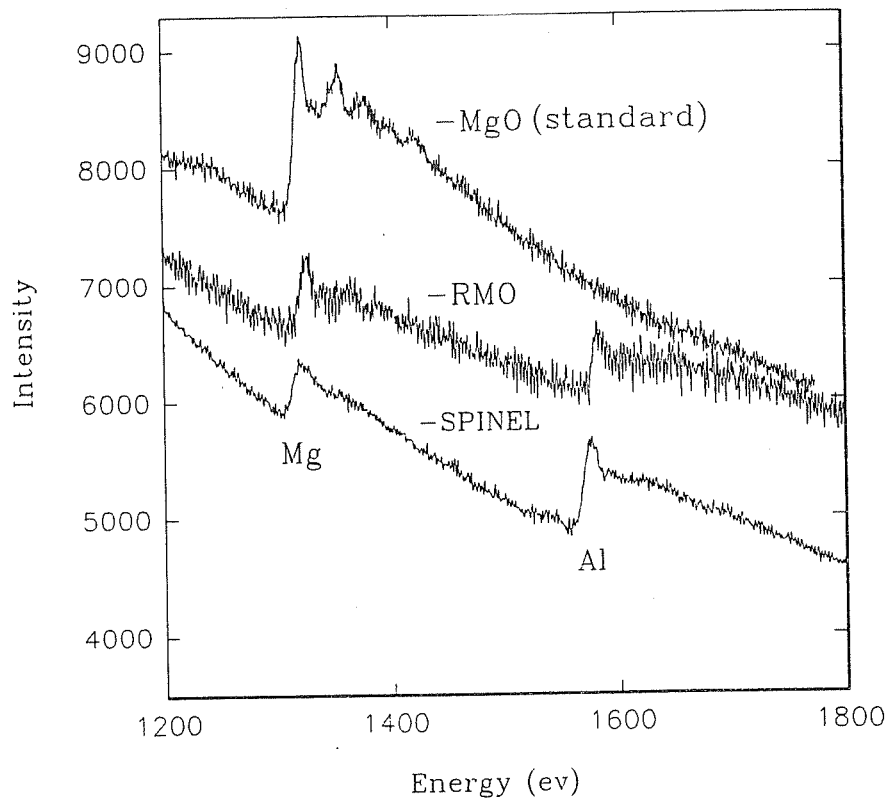

Figure 8 PEELS spectrum obtained from the reaction zone (RMO), pure standard $MgAl_2O_4$ (spinel) and pure MgO crystals.

(a) Mg solute comes to the surface of Al_2O_3 particle

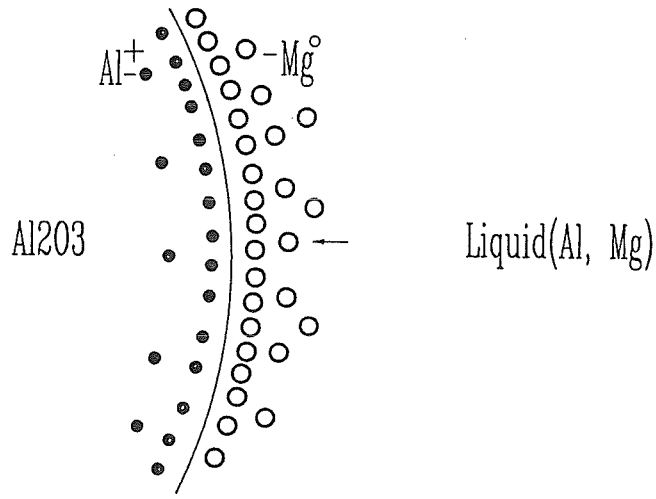

(b) The interdiffusion of Al^{+3} and Mg^{+2} on the surface of Al_2O_3 particle

$3(Mg° - 2e) \text{ --- } 3Mg^{+2}$

$2(Al^{+3} + 3e) \text{ --- } 2Al°$

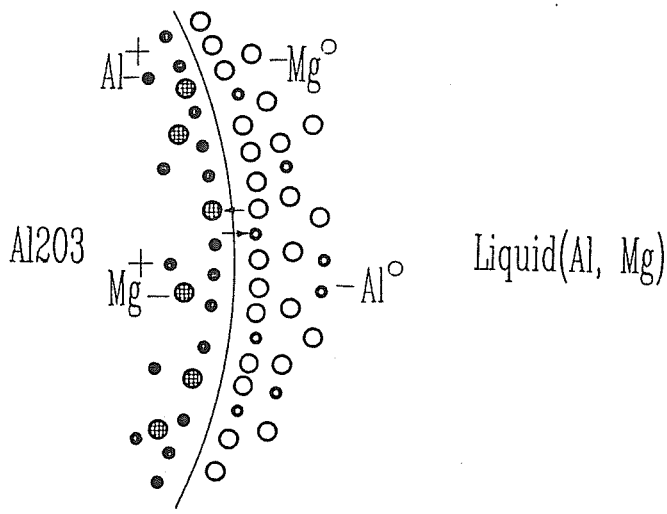

Figure 9 (a)&(b) The diagram for reaction mechanism of Al_2O_3p/Al(Mg) Alloy (at 680-800°C)

(c) MgO or spinel nucleates associated with a volume expansion, Mg,(Al) continue to enter or (leave) Al_2O_3 particle along the new phase or MgO crystal boundaries, interdiffusion of cations occurs at the new interface

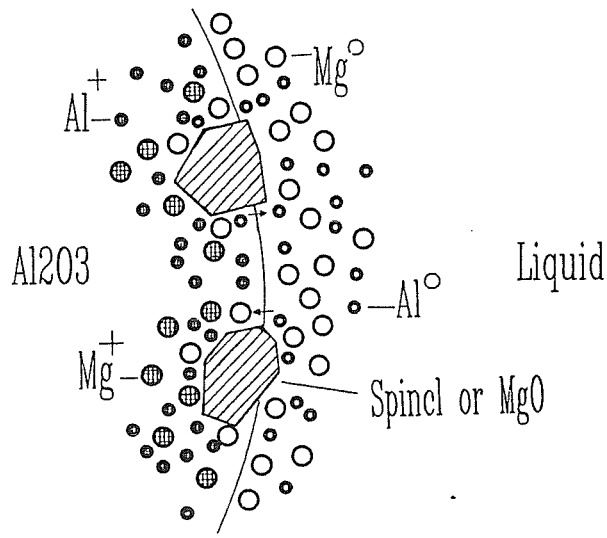

(d) With increasing time, new MgO or spinel crystals are nucleated further inside Al_2O_3 particle

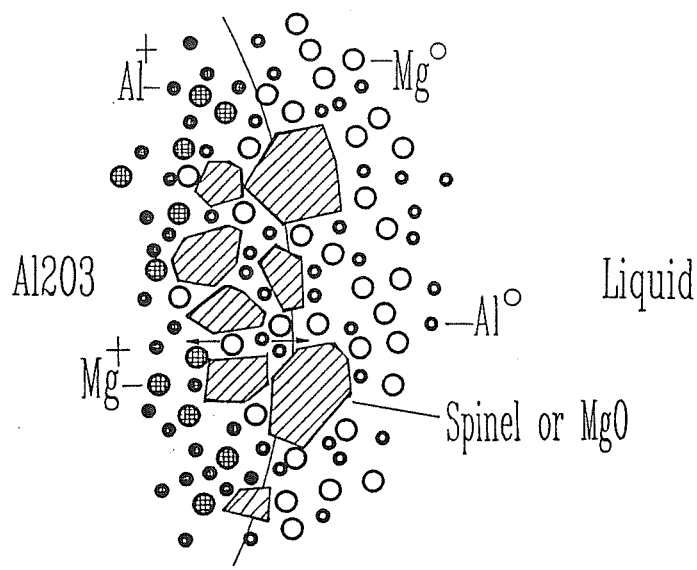

Figure 9 (c)&(d) The diagram for reaction mechanism of $Al_2O_3p/Al(Mg)$ Alloy (at 680-800°C)

2.3 Effect of Dynamic Mg Content on the Interfacial Reactions during Remelting of Al-Mg (5083)/Al_2O_3p Composites

G. L'Espérance*, W.M. Zhong* and M. Suéry**

* Centre de Caractérisation Microscopique des Matériaux $(CM)^2$, Ecole Polytechnique de Montréal, Case Postale 6079, Succ. "A", Montréal, Québec, Canada H3C 3A7

**Génie Physique et Mécanique des Matériaux, GPM2, Institut National Polytechnique de Grenoble, URA CNRS 793 ENSPG, B.P.46, 38402 St Martin d'Heres Cedex, France

Abstract

The interfacial reactions between α-Al_2O_3 particles and 5083 Al-Mg alloys during fabrication by compocasting and subsequent remelting at 800°C for 0.5 and 4 hours have been studied using analytical transmission electron microscopy (TEM) and scanning electron microscopy (SEM). It is found that the main reaction product is changed with increasing remelting time. MgO is the main reaction product after casting and after remelting for 0.5 hour. The MgO crystals formed by interfacial reaction are very small (about 5-20 nm in diameter) and the reaction zone is about 50-80 nm wide for as-cast

aterials and about 100-150 nm after remelting for 0.5 hour. However, after remelting for 4 hours, the interfacial reaction forms large $MgAl_2O_4$ crystals (about 1 μm) around the Al_2O_3 particle. The reaction products are controlled by the dynamic Mg content in the matrix.

1. Introduction

The interfacial reactions between Al-Mg matrix and Al_2O_3, during fabrication of composites, have been studied by many workers [1-14]. Generally, it is believed that Mg in the matrix will react with Al_2O_3 and form MgO or $MgAl_2O_4$. The possible reactions may be:

$$Mg(l) + 4/3\ Al_2O_3(s) = MgAl_2O_4(s) + 2/3Al(l) \ldots\ldots (1)$$

$$3Mg(l) + Al_2O_3(s) = 3MgO(s) + 2Al(l) \ldots\ldots\ldots\ldots\ldots (2)$$

As reported in previous studies, the interfacial reaction is mainly controlled by the Mg content in a matrix. For example, from the results of Levi et al. [2], Pai et al. [6], and Taftϕ et al. [7], it was found that the main reaction product at the interface of Al-Mg alloy/Al_2O_3 composites was $MgAl_2O_4$ for the alloys with Mg content smaller than 4 wt%, and MgO for the alloys with Mg content greater than 4 wt%. However, different results were shown by other studies. A.D. Mcleod [8] gave a stability diagram

for the MgO-$MgAl_2O_4$ equilibrium. According to this diagram, the Mg concentration necessary for the formation of MgO is only about 1 wt% at 680°C, whereas at 800°C, it is about 1.6 wt% Mg. Jin and Lloyd [14] found that the interfacial reaction rate decreased with the increase of Mg concentration in the Al-Mg/Al_2O_3 system and that the reaction product was $MgAl_2O_4$ even though the Mg content was as high as 7 wt%. B. Hallstedt et.al. [12] calculated the reaction kinetics in the Mg-Al_2O_3 system and concluded that the reaction between Mg(l) and Al_2O_3(s) is impossible during fabrication of the composites because the interdiffusion of Mg^{2+} or Al^{3+} through the newly formed MgO or $MgAl_2O_4$ layer is very slow. M. Pfeifer et al. [13] studied the interface reaction in the system α-alumina fibres/magnesium alloy (ZE41A) in the temperature range from 710 to 715°C. A reaction layer of MgO, with an average width of 100 nm, was found. In our previous studies [15], it was found that fine MgO crystals were the main reaction products during fabrication of Al-Mg (5083)/Al_2O_3p composites and during remelting at 800°C for 0.5 hour. $MgAl_2O_4$ would be the main reaction product with increasing reaction time as predicted from our thermodynamic calculations [15].

From the reported works, it is evident that the interfacial reaction products are associated with different fabrication conditions, alloy composition or purity of the reinforcing materials. Moreover, the reaction kinetics are a function of the reaction products formed, due to the different morphologies of the reaction products and volume expansion associated with the different reactions as discussed in [15,16]. It is therefore important to carefully study the factors which may influence the interfacial reaction

products formed. One of these factors is the composition of the Al-Mg Matrix, particularly its variation during processing. Thus, the Mg content of the alloy may change as a result of the occurence of interfacial reactions or due to the volatilisation of Mg when the alloy is held at high temperatures during fabrication or remelting. It follows that for a given starting alloy system, the reaction products formed could be a function of reaction times. This paper describes the results of a study to characterize the change of the reaction products formed as a function of remelting time in the case of the Al-Mg (5083) alloy/Al_2O_3p composite.

2. Experimental Procedures

The average size of α-Al_2O_3 particles used in this study was about 13 μm diameter (from ESK, Germany), and the volume fraction 10%. The composition of the 5083 alloy is 4.10Mg-0.56Mn-0.12Cr-0.19Fe-0.15Si-0.04Cu-0.02Ti-Al (balance) wt%. Composites were fabricated using the compocasting technique described in detail elsewhere [15]. Al_2O_3 particles were added to a semi-solid slurry in the temperature range of 600-640°C. The slurry was then agitated and reheated rapidly to about 720°C for casting (5min.). The mould was preheated to 300°C. During solidification, a pressure of 100 MPa was applied. In order to study the influence of a high temperature remelting treatment of the composites, as-fabricated composites were remelted and held at 800°C in argon for 0.5 and 4 hours. The interfacial reaction was studied by scanning

electron microscopy (SEM) coupled to a Link X-ray analysis system and by transmission electron microscopy (TEM). A CM30 Philips (300 kV) analytical transmission electron microscope equipped with EDS (energy dispersive X-ray spectrometer) and PEELS (parallel electron energy loss spectrometer, Gatan 601) and a JEOL2000-FX TEM coupled to a Link EDS system were used. The samples for TEM observation were prepared by mechanical polishing, dimpling, and ion beam thinning (5 kV, at a tilt angle of 12-15°).

3. Results and Discussion

There is a simple way to observe the interfacial reaction, using a piece of a freshly fractured sample. From the edge of a fractured particle and the surface of a decohered particle on the fracture surface, large reaction products may be characterized directly using scanning electron microscopy. Figure 1 is a SEM micrograph obtained from an as-cast sample, showing a particle with a clean, smooth and straight surface. Figures 2(a)&(b), obtained from a sample remelted at 800 °C for 4 hours, show many large crystals (about 1 μm) on the surface of a decohered Al_2O_3 particle. When viewed approximately normal to the fracture surface, the reaction zone thickness can be seen to be about 1.5 μm on average. Channels between these crystals can also been seen (arrow in figure 2(a)). An as-cast sample and a sample remelted at 800 °C for 0.5 hours were characterized using transmission electron microscopy. For the as-cast sample, fine MgO

crystals with a size of 5-20 nm are the main reaction product at interfaces. The width of the reaction zone can vary from about 50 to 80 nm. For the sample remelted for 0.5 hours, fine MgO crystals are still the main reaction product (see figure 3). The width of the reaction zone, however increases to about 100-150 nm. An interesting result obtained for the sample remelted for 4 hours was that all the reaction zone was now constuted of $MgAl_2O_4$ crystals as confirmed by TEM observations (figures 4(a)&(b)). The TEM micrograph in figure 4(b), shows a straight interface between $MgAl_2O_4$ and Al_2O_3. In additions, a crystal orientation relationship (see figure 5) between $MgAl_2O_4$ and Al_2O_3 was observed:

$$[1,-1,-2]\text{-}MgAl_2O_4//[001]\text{-}Al_2O_3$$

$$(311)\text{-}MgAl_2O_4//(-1,2,0)\text{-}Al_2O_3$$

$$(1,-1,1)\text{-}MgAl_2O_4//(110)\text{-}Al_2O_3$$

This orientation relationship is the same as that reported by Jin et. al. [14] in Al-Mg/Al_2O_3 composites. Mg is not detected by EDS in the matrix after remelting for 4 hours, indicating that the amount of Mg left in solution after remelting for 4 hours is less than 0.1 wt%, the detector limit.

From thermodynamic calculations carried out using the F*A*C*T database [17], we found that the relative amounts of the reaction products formed changed with the amount of Al_2O_3 which took part in the reaction for a given Mg content (e.g. 4 wt%). Table I shows the calculated amount of the different reaction products with different

amounts of Al_2O_3 taking place in the reaction.

Table I Calculated Amount of Reaction Products Formed with Different Amounts of Al_2O_3 Taking Place in the Reaction

Reaction Products	**0.5** Al_2O_3 (R1)* (gram)	**20** Al_2O_3 (R2)* (gram)
MgO	0.593	0.000
$MgAl_2O_4$	0.000	20.929
Mg(rest)	3.646	0.428

* Calculations using F*A*C*T database [17], at 700°C and 1 atm. (O partial pressure of oxygen is $5x10^{-5}$). R1 and R2 indicate the reactions with different amounts of Al_2O_3.

$$4Mg + 96Al + \mathbf{0.5}Al_2O_3 = \quad .....(R1)$$
$$4Mg + 96Al + \mathbf{20}Al_2O_3 = \quad .....(R2)$$

Thus, the possibility of forming MgO increases with the decrease of the amount of Al_2O_3 particles for our alloy system. As discussed in a previous paper [15], the reaction between Mg (Al) and Al_2O_3 is very slow. It can then be assumed that only a small part of the Al_2O_3 particles is involved in the interfacial reaction because of the relatively short reaction time during fabrication. For example, in our system, if only the outer layer of an Al_2O_3 particle (200 nm thickness, about 2 wt% of the particle) takes part in the reaction, the conditions to be used for thermodynamic calculations are similar

to reaction (R1) (Table I). Therefore, MgO will be the reaction product according to the calculations. In our samples, the thickness of the reaction zone is about 50 to 150 nm. Therefore, the interface reaction should lead to the formation of MgO. However, with an increase in reaction time, the possibility of forming $MgAl_2O_4$ will increase because the amount of Mg remaining in the matrix will decrease. An extreme situation would occur when the Al_2O_3 particles would be entirely consumed during the reaction. In this case, our thermodynamic calculations show that the final reaction product would be $MgAl_2O_4$ instead of MgO because of the small amount of Mg (about 0.4 wt%) that would remain in the matrix. In fact, after remelting for 4 hours, $MgAl_2O_4$ is the only reaction product observed. This is because Mg is largely consumed (no Mg was detected by EDS after the remelting experiment) by both interfacial reactions and may also partially volatilize as pointed out above. With the decrease in Mg content in the matrix during remelting, $MgAl_2O_4$ is formed and previously formed MgO crystals can be transformed into $MgAl_2O_4$ because, with low Mg contents, $MgAl_2O_4$ is thermodynamically more stable than MgO [8,18].

The formation of $MgAl_2O_4$ with high Mg contents was reported in other studies [14,18]. For example, Weirauch [18] also found that the reaction between Al-6 wt% Mg and sapphire-Al_2O_3 and between Al-3 wt% Mg and MgO formed $MgAl_2O_4$ after the sample was held at 800°C for 24 hours. These results are in agreement with those reported here. The loss of Mg caused by volatilisation was also quantified by Weirauch. For a Al-3 wt% Mg system, after holding at 800°C for 1 hour, the amount of Mg

remaining in the matrix was only about 1 wt% (the argon flowing rate was 1 litre/min.). Thus, the volatility of Mg and the furnace atmosphere should be taken into consideration when discussing the instantaneous Mg content during the reaction. On the other hand, Jin and Lloyd [14] found that $MgAl_2O_4$ was formed after holding at 720°C for 2 hours, even when the Mg content was as high as 7 wt% in the Al-Mg alloy. However, their results indicated that very little Mg was lost (less than 0.2 wt%) during the remelting. A possible explanation for the difference is that different types or sources of Al_2O_3 particles were used. Furthermore, the composites used in their study were fabricated by a die-casting process. In our case, using the semi-solid compocasting method could lead to increase of Mg content in the remaining liquid [15,16].

4. Conclusions

The interfacial reactions between α-Al_2O_3 particles and 5083 aluminium alloys in as-cast composites and in composites remelted for 0.5 hours and 4 hours were studied. Fine MgO crystals (5-20 nm) are found to be the main reaction product for the as-cast composites and composites remelted for 0.5 hour. The width of the reaction zone can vary from about 50-80 nm in as-cast composites to about 100-150 nm in composites held at 800°C for 0.5 hour. After remelting at 800°C for 4 hours, the reaction product is large $MgAl_2O_4$ crystals (about 0.5 to 1 μm) and the thickness of the reaction zone is about 1.5 μm. The reaction product, MgO, is gradually replaced by $MgAl_2O_4$ with

increasing remelting time due to the decreasing Mg content in the matrix.

Acknowledgements

The authors gratefully acknowledge the NATO International Scientific Exchange Programme (Grant no. CRG 900950) and the National Science and Engineering Research Council (NSERC) of Canada (strategic grants) for the financial support. They also thank E. Goiffon, L. Salvo and J.J. Blandin for their preparation of the composite materials. Thermodynamic calculations were performed with the help of P. Wu and J. Wu.

References

1. A. Munitz, M. Metzger, and R. Mehrabian, Metall. Trans. A10(1979), P.1491

2. C.G. Levi, G.J. Abbaschian, R. Mehrabian, Metall. Trans. A, Vol. 9A, 5(1978), P.697

3. P.K. Ghosh, S. Ray, Proc. of fabrication of particulates reinforced metal composites, edited by J. Masounave et.al..(1990), Montreal, P.23

4. B.F. Quigley, G.J. Abbaschian, R. Wunderlin and R. Mehrabian, Metall. trans. A, Vol. 13A, 1(1982), P.93

5. M. Fishkis, J. of Mater. Sci. 26(1991), P.2651

6. B.C. Pai, S. Ray, Mater. Sci. and Eng. 24(1976), P.31

7. J. Taftϕ, K. Kristiansen, H. Westengen, A. Nygard, J.B. Borradaile, D.O. Karlsen, Proc, Conf. on Cast Reinforced Metal Matrix Composites, Chicago, Il, (1988), edited by S.G.Fishman, A.K. Dhingra, P.71

8. A.D. Mcleod, same with 3, P.18

9. G.R. Cappleman, J.F. Watts, T.W. Clyne, J. of Mater. Sci. 20(1985), P.2159

10. Y. Lepetitcorps, J.M. Quenisset, G.Le Borgne, M. Barthole, Mater. Sci. and Eng. A 135(1991), P.37

11. R. Molins, J.D. Bartout and Y. Bienvenu, Mater. Sci. and Eng. A 135(1991), P.111

12. B. Hallstedt, Z.K. Liu and J. Ågren, Mater. Sci. and Eng. A 129(1990), P.135

13. M. Pfeifer, J.M. Rigsbee, K.K. Chawla, J. of Mater. Sci. 25(1990), P.1563

14. I. Jin, D.J. Lloyd, 2nd International Conference on Cast Metal Matrix Composites, Tuscaloosa, USA, Oct. 1993. P.236

15. W.M. Zhong, G. L'Esperance and M. Suery, Interfacial Reaction in 5083/Al_2O_3p Composites During Fabrication and Remelting, received by Metal. Trans. A, 1994

16. W.M. Zhong, G. L'Esperance and M. Suery, Interfacial Reaction in 5083/SiCp Composites During Fabrication and Remelting, received by Metal. Trans. A, 1994

17. F*A*C*T thermodynamic database, CRCT, Ecole polytechnique, Montreal, Canada, 1993

18. D.A. Weirauch, Jr., J. Mater. Res. 3(4), Jul./Aug. (1988), P.729

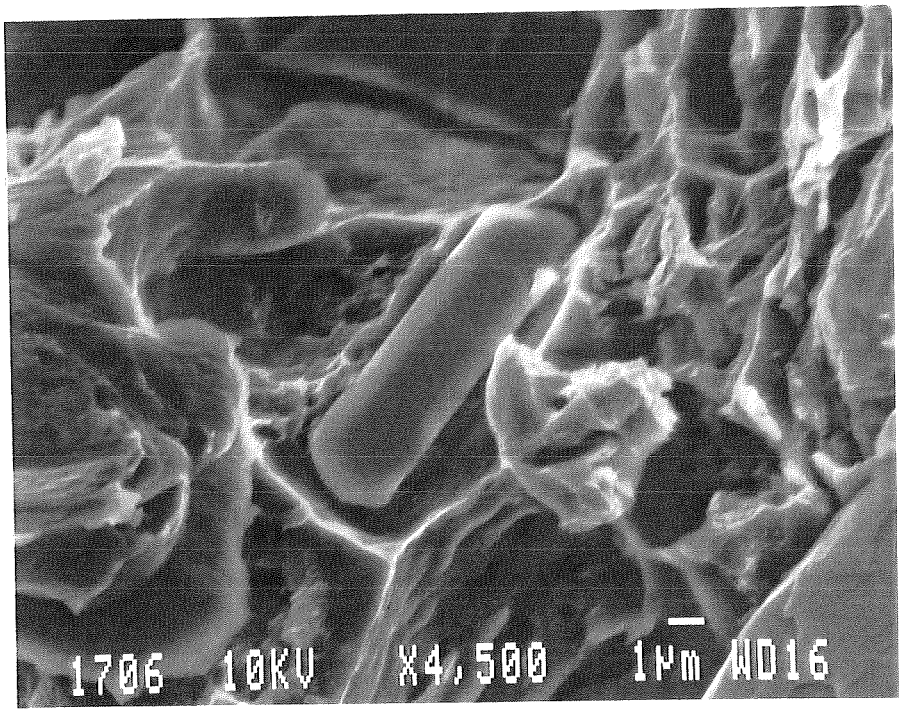

Figure 1 Fracture surface of the as-cast composite showing an Al_2O_3 particle with a clean surface (5083/Al_2O_3, as-cast)

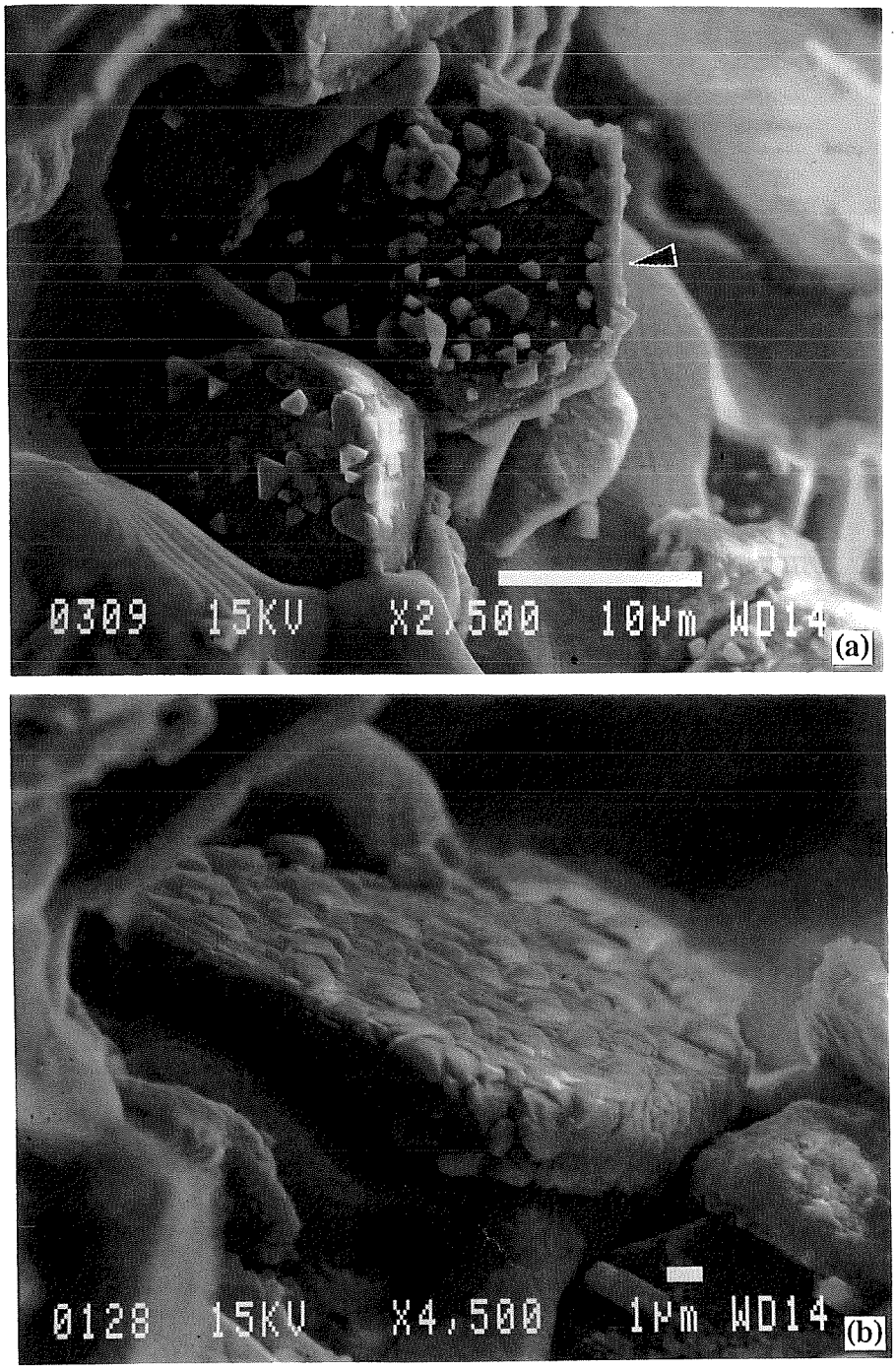

Figure 2(a),(b) SEM images showing $MgAl_2O_4$ crystals on the surface of decohered Al_2O_3 particles (remelting at 800°C for 4 hours)

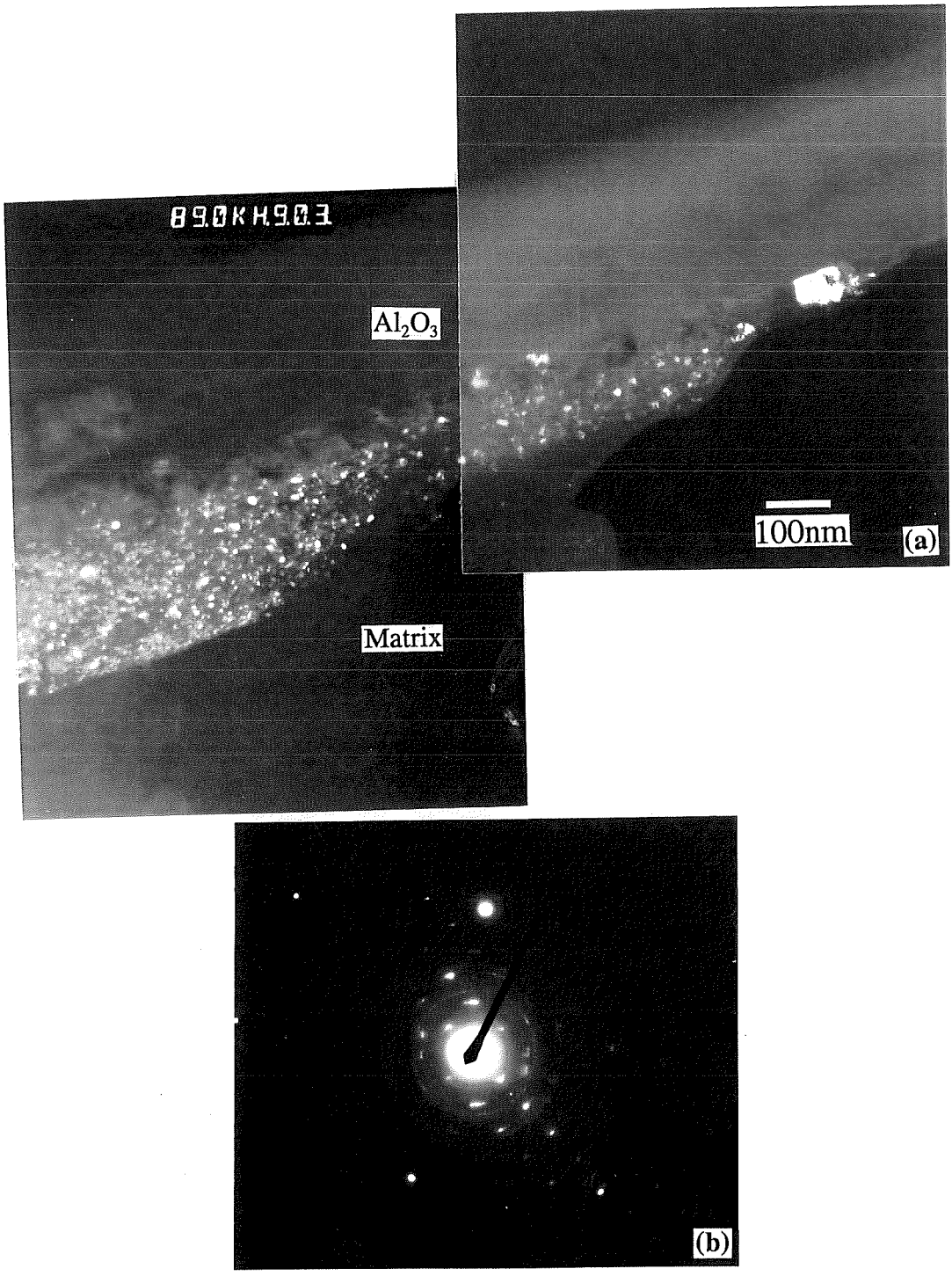

Figure 3(a) Dark field TEM micrograph showing many fine MgO crystals at an interface (5083/Al_2O_3, remelting at 800°C for 0.5 hours)
(b) SAD pattern obtained from reaction zone, showing strong MgO diffraction

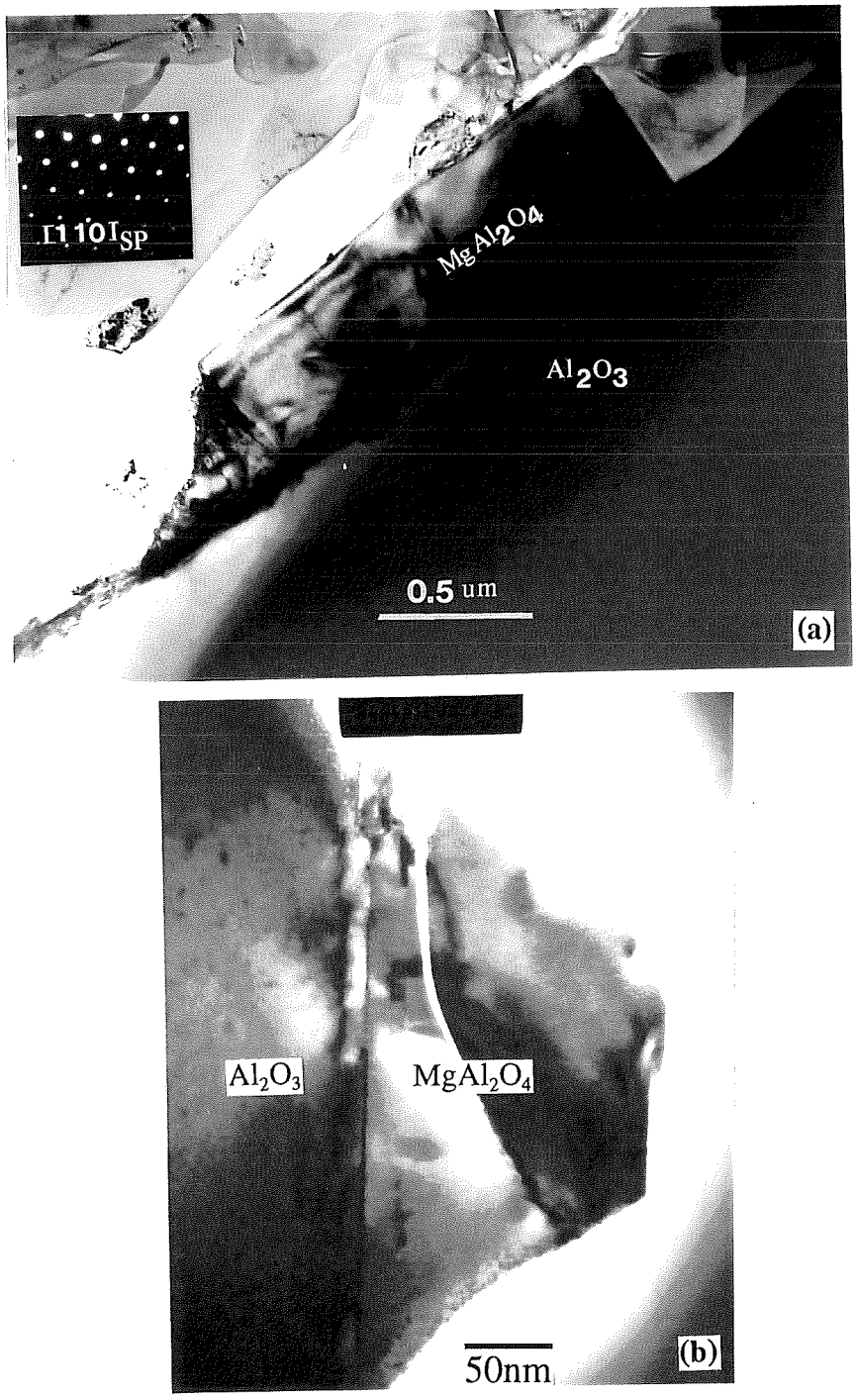

Figure 4(a),(b) TEM micrographs showing the large $MgAl_2O_4$ crystals at the interfaces ($5083/Al_2O_3$, remelting at 800°C for 4 hours)

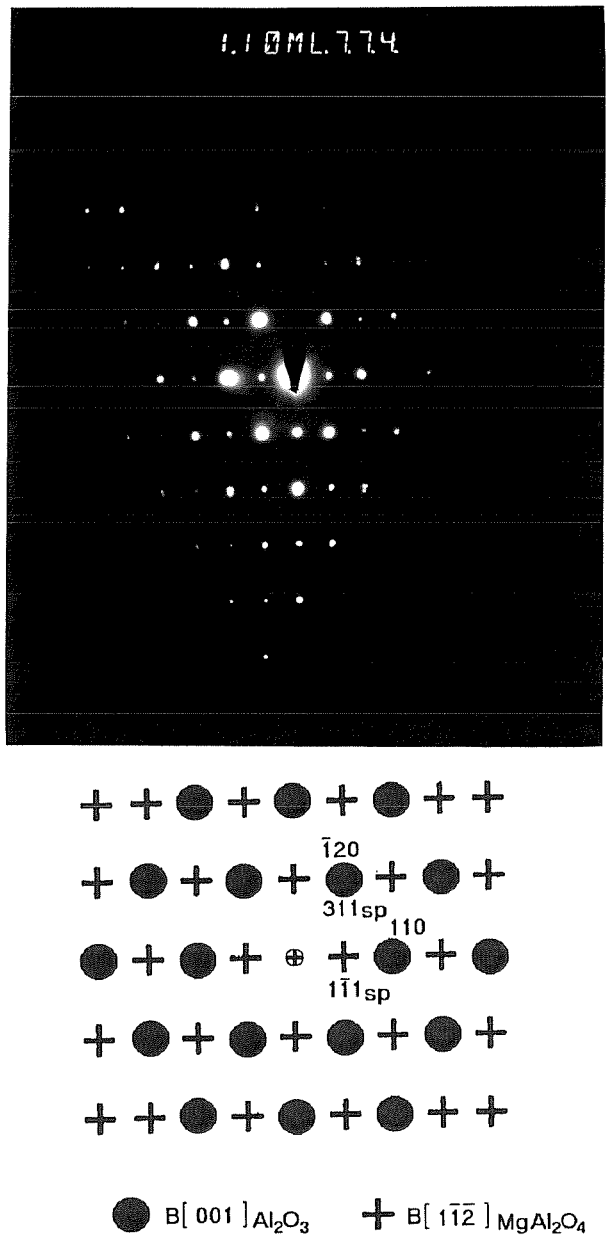

Figure 5 (a) SAD patterns and (b) computer simulated patterns, showing [1,-1,-2]-$MgAl_2O_4$//[001]-Al_2O_3 with (311)-$MgAl_2O_4$//(-1,2,0)-Al_2O_3 and (1,-1,1)-$MgAl_2O_4$//(110)-Al_2O_3

2.4 True Composition Profiles Obtained by a Graphical Deconvolution Technique Using Analytical Transmission Electron Microscopy (AEM/STEM)

W.M. Zhong G. L'Esperance

Centre de Caracterisation Microscopique des Materiaux $(CM)^2$,

Ecole Polytechnique de Montreal, University de Montreal, Canada, H3C 3A7

Abstract

Segregation of solute elements such as Mg and Cu at the interfaces between reinforcements and matrices of composites was studied using an analytical transmission electron microscope (TEM, Philips, CM30) coupled with a Link energy dispersive X-ray spectrometer. The composites used were Al-Cu-Mg (2124) alloy/Si_3N_4-whiskers and Al-Mg (5083) alloy/SiC-particles. In order to meet the need of high spatial resolution during microanalysis (often, < 50 nm), a graphical deconvolution technique was used to get true composition profiles at those interfaces. An assumed "true" composition profile with an exponential function shape was convoluted with the distribution of electron flux intensity within the total sampled region of the TEM foil. The convoluted results were compared with those measured apparent compositions. A true profile was obtained when the convoluted results coincided well with the measured apparent

concentrations by adjusting some constants in the function. A slab segregation profile is also discussed in this paper. The X-ray volume intersected by the assumed true composition profile was rated to the total X-ray volume during the convolution operation. The intersected volume was calculated by a numerical integration method. The total X-ray volume was calculated by using a single scattering model. With the help of a computer, the calculations were carried out within one minute and the sensitivity of convolution was smaller than 0.1 wt% or 1 nm.

1. Introduction

Segregation of solute elements such as Mg and Cu at grain boundaries or at the interfaces between reinforcements and matrix in composites, often affects the mechanical properties of the materials tremendously [1,2]. For example, segregation of Mg solute at the interfaces is believed to be one of the important contributions to the high strain rate superplasticity observed in Al-Cu-Mg (2124)/Si_3N_4-whisker composites, as reported by L'Esperance et al. [1]. Nowadays, spatial resolution of microanalysis systems is very high (usually about 10-50 nm in STEM) [3], however, quantitative characterization is still limited by the inadequate spatial resolution during analysis. As we know, in equilibrium segregations, a segregation is often confined within a grain boundary with a profile width only 1-2 nm [4]. In composites, it is also interesting to see if the solute atoms have diffused into the reinforcements. Therefore, much higher spatial resolution in

microanalysis is greatly desired. Unfortunately, decreasing the electron probe size will decrease the total X-ray count and increase the statistical errors of the analyses. Thus, a graphical deconvolution technique has been developed to get the actual composition profile.

The spatial resolution of X-ray microanalysis on the scanning transmission electron microscope (STEM) is controlled by the elastic scattering of the incident electrons. The measured characteristic X-ray intensity, Ix', is a convolution of the distribution of electron flux intensity I(v) and the actual solute composition C(v) within the total sampled region of a TEM foil [4,5], that is:

$$Ix' = K\int_V I(V) * C(V)\, dV \ldots\ldots (1)$$

where K is a constant that describes the efficiency of X-ray generation, emission and detection for the particular element of interest.

Doig and Flewitt (1982) [4] developed an equation which describes the intensity distribution of the electron beam (I) as a function of radial distance (r) from the probe centre at any depth (t) of the specimen:

$$I(r,t) = \frac{Ie}{\pi(2\sigma^2+\beta t^3)} \exp\left(-\frac{r^2}{2\sigma^2+\beta t^3}\right) \ldots\ldots (2)$$

where Ie is the total incident electron current, σ is the standard deviation of the incident probe current distribution (a measure of the incident probe size),

$\beta=500(4E^2/E)(\rho/A)$ nm, E the energy of incident electrons.

If a composition profile is only a function of the distance (y) from the boundary between a reinforcement and a matrix or between two grains, following expression will be obtained [6]:

$$C'(y_i)=\int_0^t\int_{-y}^{+y}\int_{-x}^{+x} I(x,y,t)C(y-y_i)dxdydt \quad .....(3)$$

where, $C'(y_i)$ is the calculated (apparent) composition at position i. C(y) is the true composition profile. y_i is the distance between the centre of electron probe and the centre of the true composition profile. $C'(y_i)$ should be equal to the measured apparent composition, if assumed X-ray generation volume and "true" composition profile are correct.

There are several methods to determine C(y). First, a physically realistic functional form for C(y) can be assumed and inserted into equation (3), and the values of $C'(y_i)$ will be calculated and compared with the experimental (apparent) values. The defining coefficients in C(y) are then adjusted until the calculated values of $C'(y_i)$ provide a best fit to the experimental values. Second, direct deconvolution of the terms I(x,y,t) and $C(y-y_i)$ from the measured $C'(y_i)$ can be accomplished by Fourier analysis. With this method, it is unnecessary to assume a "true" composition profile (which is sometime impossible). Then, as Rapperport pointed out (1969) [7], the solution of the equation

often has very large error, when the noise of the input data is large. Also, the calculation of a Fourier transformation is very complicated. Third, as reported by A.D. Romig et al. (1987) [8], a simple graphical or numerical technique was used to convolute the X-ray generation function with an assumed true composition profile in order to calculate the observed (apparent) composition profile and to avoid the difficulty of the explicit deconvolution. This process simply involves integrating the area under an assumed composition profile intersected by a cross section of a X-ray generation volume at certain position and rating the result to the total area of the cross section of the X-ray generation volume. The ratios of the integrated areas will change as the electron beam is moved across the analyzed interface. Direct plot of the ratios v.s. the beam positions will determine the convoluted profile. This process is shown in Fig. 1. The X-ray generation volume can be determined by either the single scattering model or monte carlo simulation [5]. Fig. 2. shows the X-ray generation volume calculated by the single scattering model [9].

Measured X-ray intensities of a solute element can be plotted as a function of electron beam position in order to produce an experimentally obtained composition profile. The assumed profile can be of different forms based on different conditions. An error function profile can be used as the assumed true composition profile for the un-equilibrium segregation [4]. As for an equilibrium segregation, a slab model can be assumed [8]. In the slab model, in order to do the convolution by area ratios, the thickness of the slab must be very small relative to the diameter of the X-ray generation

volume [8,9]. If the thickness (δ) of the slab is larger than one third or fourth of the diameter of the X-ray generation volume, errors which come from this calculation must be significant. In order to increase the analysis precision, a new method is proposed in which the X-ray volume intersected by the assumed actual composition profile is directly rated to the total X-ray generation volume during the convolution operation. The intersected volume is calculated by a numerical integration method.

2. Physical Models and Calculations

2.1 Slab model

In equilibrium segregation, such as the segregation of Pb or Sn to grain boundaries in steels or the formation of glassy layers at the boundaries between sintered ceramic powder particles, the segregation profile is often assumed with a slab shape because of the small lateral extent (< 1-2 nm) and large concentration change (often near 100%)[5,8]. For simplicity, TEM foil is assumed to be initially normal to the incident electron beam. The X-ray generation volume (V_T^i) has the shape of a Frustum Cone (Fig 2). $V_I(y_i)$ is the intersected volume of the electron beam with the composition profile (i.e. the assumed slab). $C_{apr}(y_i)$ is the apparent composition at position i. C_{gb} is the true concentration of a solute element in the slab and C_m is the concentration of the solute element in the matrix. The apparent composition can be calculated as [9]:

$$C_{apr}(y_i) = \frac{V_I(y_i)\,C_{gb} + V_m(y_i)\,C_m}{V_T^i} \quad \ldots\ldots (4)$$

$$V_m(y_i) = V_T^i - V_I(y_i) \quad \ldots\ldots (5)$$

$$V_T^i = \left(\frac{\pi * t}{12}\right)(d_p^2 + d_p * B + B^2) \quad \ldots\ldots (6)$$

Where, d_p -diameter of the incident beam, B - diameter of the electron scattering volume;

$$B = (d_p^2 + b^2)^{\frac{1}{2}} \quad \ldots\ldots (7)$$

Here, b is the electron beam broadening which can be determined from the single scattering model as [10]:

$$b = 625\,(Z/E)\,(\rho/A)^{\frac{1}{2}}\,t^{\frac{3}{2}}\,(cm) \quad \ldots\ldots (8)$$

where, Z is the average atomic number. E is the incident beam energy in kV. ρ is the average density g/cm^2. A is the average atomic weight. t is the foil thickness in cm. The composition used in the calculations is the measured apparent composition.

As an approximation, $V_I(y_i)$ can be calculated by following formula [9]:

$$V_I(y_i) = \frac{\delta t}{2}(d_p + B) \ldots\ldots (9)$$

In order to decrease the calculation error as discussed above, $V_I(y_i)$ will be calculated using numerical integration. This is particularly necessary when the width of the slab is unknown, because the electron beam must intersect with the slab at least at two positions in order to determine C_{gb} and δ uniquely.

In an experiment, the specimen is often tilted to make the analyzed boundary or the interface parallel to both the electron beam and the axis of detector, and also to obtain a high take-off angle to prevent the absorption of X-ray by the foil. Therefore, the effective thickness of the foil is increased and the shape of the X-ray generation volume is changed to a frustum ellipse cone. The distortion of the X-ray generation volume caused by the tilting is ignored at the beginning and only the effective foil thickness is changed, i.e., $T = t/\cos\varphi$. φ is the tilting angle which is equal to the angle formed between direction of the electron beam and the normal of the foil. In general $\cos\varphi = \cos\varphi_x \cos\varphi_y$ [11], where φ_x and φ_y are the tilting angles along the x and y axes.

The surface equation of the X-ray generation volume is necessary to calculate $V_I(y_i)$ by integration. According to the single scattering model, the X-ray generation volume has a shape of frustum right cone, therefore when $x^2 + y^2 \geq (dp/2)^2$, its surface equation is given as:

$$Z = ctan(\alpha)\left(\frac{1}{2}B - \sqrt{x^2+y^2}\right) \ldots\ldots (10)$$

where

$$ctan(\alpha) = 2\frac{T}{B-d_p} \ldots\ldots (11)$$

When $x^2 + y^2 < (dp/2)^2$, the surface equation is Z=T. The total electron interaction volume is:

$$V_T^i = \int_0^T \pi\left[\frac{B}{2} - \frac{Z(B-d_p)}{2t}\right]^2 dZ \ldots\ldots (12)$$

$$i.e., V_T^i = \frac{\pi T}{12}\left[B^2 + d_p B + d_p^2\right] \ldots\ldots (13)$$

The intersected volume $V_I(y_i)$ must be calculated using different surface equations when the electron beam intersects at different positions with the slab. When the steep edges of the frustum cone intersect with the slab, that is, $(y_i-\delta/2) \geq r$ and $(y_i+\delta/2) \leq R$, or $(y_i-\delta/2) \geq -R$ and $(y_i+\delta/2) \leq -r$, ($R=B/2$, $r=d_p/2$), $V_I(y_i)$ is given as:

$$V_I(y_i) = \int_{y_i-\delta/2}^{y_i+\delta/2} dy \int_{x_1}^{x_2} Z dx \ldots\ldots (14)$$

where Z comes from equation (10), $x_{1,2} = \pm(R^2-y^2)^{1/2}$.

After integrating along x axis, we obtain:

$$V_I(y_i) = \int_{y_i-\frac{\delta}{2}}^{y_i+\frac{\delta}{2}} f(y)\,dy \ldots\ldots (15)$$

The integration is calculated by Newton's numerical method, where,

$$f(y) = \frac{2BT}{B-d_p}\sqrt{R^2-y^2} - \frac{2T}{B-d_p}\left(\sqrt{R^2-y^2}\,R + \frac{y^2}{2}\ln\left(\frac{R+\sqrt{R^2-y^2}}{y}\right)^2\right) \ldots\ldots (16)$$

When the slab intersects with the up bottom of the X-ray generation volume, that is $(y_i-\delta/2) > -r$, or $(y_i+\delta/2) < r$, the equations for both upper and lower bottoms of the frustum cone are necessary in order to calculate the $V_I(y_i)$, which are given as:

$$x = \pm(r^2-y^2)^{1/2} \ldots\ldots (Z=T)$$

$$\ldots\ldots (17)$$

$$x = \pm(R^2-y^2)^{1/2} \ldots\ldots (Z=0)$$

The area of one intersection is:

$$S_i = \frac{2\left(\sqrt{R^2-y^2}+\sqrt{r^2-y^2}\right)}{2}T \ldots\ldots (18)$$

Finally, the intersected volume is $V_I(y_i)$:

$$V_I(y_i) = \int S_i dy = \int_{y_i - \frac{\delta}{2}}^{y_i + \frac{\delta}{2}} f(y)\, dy \ldots\ldots (19)$$

The integration is also calculated by the numerical method. Here,

$$f(y) = (\sqrt{R^2 - y^2} + \sqrt{r^2 - y^2})\, T \ldots\ldots (20)$$

2.2 Exponential model

In the case of non-equilibrium segregation, such as solute depletion around interfaces where heterogeneous precipitation is occurring or segregation of solute atoms caused by vacancy-assisted diffusion during quench from high temperatures, the whole process has not yet reached thermodynamic equilibrium [5]. An exponential model is assumed as following [4]:

$$C(y) = C_0 \exp\left(-\frac{|\cdot y|}{A}\right) \ldots\ldots (21)$$

A is a constant which defines the spatial extent of the profile and C_0 is the assumed peak concentration (y=0). From equations (3) and (4), we can have a relation such as:

$$C_{apr}(y_i) = \frac{C_0}{V_T^i} \int_{-R}^{R} S_i \exp\left(-\frac{|y - y_i|}{A}\right) dy \ldots\ldots (22)$$

When y changes from -R to +R (i.e. from the left side of the cone to the right side of the cone), the integration (22) is calculated as:

$$C_{apr}(y_i) = \frac{C_0}{V_T^i}\left[\int_{-R}^{-r} f_1(y)\exp\left(-\frac{|y-y_i|}{A}\right)dy + \int_{-r}^{r} f_2(y)\exp\left(-\frac{|y-y_i|}{A}\right)dy + \int_{r}^{R} f_1(y)\exp\left(-\frac{|y-y_i|}{A}\right)dy\right] \quad \ldots\ldots (23)$$

where, $f_1(y)$ and $f_2(y)$ have the same form as in equations (16) and (20) respectively. 6th degree Newton's integration is used. Constants C_0 and A can be adjusted graphically by comparing the calculated apparent concentrations with the measured apparent concentrations at various positions until the calculated apparent concentrations $C_{apr}(y_i)$ fit the measured concentrations satisfactorily (more than two positions are required in order to determine the constants C_0 and A uniquely).

2.3 Distortion of the X-ray Generation Volume

Considering the distortion of the X-ray generation volume caused by tilting is necessary when the foil is tilted by a large angle. Fig.3 (a) shows the relationships among the normals of the foil (n_f), interface (n_s) and electron beam (B). After tilting, the normals of the interface and the foil surface are n'_s and n''_f respectively. φ_x is the angle formed when the foil is tilted from n_s to n'_s to make the interface parallel to the incident electron beam. It may also be necessary to rotate the foil in order to make the interface parallel to the detector (Fig.3 (b)). In order to obtain a large X-ray take-off angle, tilting along the y axis toward the detector is necessary, that is angle φ_y. The projection direction of n''_f on x-y plane is the long axis of the ellipse formed by the electron beam intersecting with the foil, with a φ_p angle to the y-tilt axis. In Fig.4, we can see the cross-sections of the electron interaction volumes with distortion (A'B'C'D') due to tilting the sample and without distortion (ABCD). Two cones with a same cone angle (α) can be obtained by extending from their edges (one by dash lines, other by solid lines). The heights of the cones are different, but the effective thickness of the foil (T) is the same in both situations, i.e., $T=t/\mathrm{Cos}\varphi$, t-the thickness of the foil and where the angle φ can be obtained by the relation of $\mathrm{Cos}\varphi=\mathrm{Cos}\varphi_x\mathrm{Cos}\varphi_y$. The distance between the centre of the large cone and the centre of the small cone (dash lines) is Δy. The angle φ_p (in Fig.3(b)) can be obtained by the relation $\mathrm{tg}\varphi_p=\mathrm{Sin}\varphi_y/\mathrm{Sin}\varphi_x$ [11]. Equations required for calculation of the X-ray generation volume and the intersected volume are given in the following. First, the surface equation of the large cone is given as (N is the

coordinate's origin as shown in Fig.4):

$$(H-Z)^2=(\frac{2T}{B-d_p})^2(x^2+y^2)\ldots\ldots(24)$$

where H is the height of the large cone and T is the effective foil thickness.

Second, the surface equations for the upper and lower foil surfaces of large cone are:

$$Z-ytg\varphi-R_p tg\varphi-T=0\ldots\ldots(25)$$

$$Z-ytg\varphi-R_p tg\varphi=0\ldots\ldots(26)$$

where $R_p=H\cdot tg(\alpha)$ and $ctan(\alpha)=2T/(B-d_p)$.

Finally, the equation of the cross section of the sample (plane SS' in fig.3(b)), which has a distance y_i from the interface, is given as:

$$y=-tg\varphi_p x+(y_i/Cos\varphi_p-\Delta y)\ldots\ldots(27)$$

where, $\Delta y=(1/2)\cdot d_p\cdot tg(\varphi)\cdot tg(\alpha)$.

Slab Segregation Model: If the segregation profile has a slab shape, the intersected volume formed between the electron beam and the profile can be calculated in two parts while the electron beam intersects with the interface at different positions. In the first part, $Y_p^1+\delta/2<y_i<Y_p^2-\delta/2$. Here, Y_p^1 and Y_p^2 are the tangent points between the

surfaces of the slab and the upper edge of the truncate cone (points P_1, P_2 in figure 3(b)), i.e. $(Y_B^2-Y_B^1)$ and $(Y_p^2-Y_p^1)$ are the distances between the two edges of the lower ellipse or the upper ellipse along the Y-tilt axis respectively. $V_I(y_i)$ is given as:

$$V_I(y_i) = \int_{y_i-\frac{\delta}{2}}^{y_i+\frac{\delta}{2}} S_i(y_j)\,dy_j \ldots\ldots (28)$$

$$S_i(y_j) = \frac{T}{2}\left[\sqrt{(X_2^L(y_j)-X_1^L(y_j))^2+(Y_2^L(y_j)-Y_1^L(y_j))^2+(Z_2^L(y_j)-Z_1^L(y_j))^2}+\right.$$

$$\left.+\sqrt{(X_2^u(y_j)-X_1^u(y_j))^2+(Y_2^u(y_j)-(Y_1^u(y_j))^2+(Z_2^u(y_j)-Z_1^u(y_j))^2}\right] \ldots\ldots (29)$$

Here, y_j is the distance from the j-th intersection to the centre of the electron beam. $X_{1,2}^{L,U}(y_j)$, $Y_{1,2}^{L,U}(y_j)$, $Z_{1,2}^{L,U}(y_j)$ can be obtained from equations (24) to (27).

In the second part, $Y_B^1+\delta/2 \leq y_i \leq Y_p^1-\delta/2$, $Y_p^2+\delta/2 \leq y_i \leq Y_B^2-\delta/2$, $Y_B^{1,2}$ are the tangent points between the surface of the slab and the lower edge of the truncate cone. The intersected volume between the X-ray volume and the profile is:

$$V_I(y_i) = \int_{y_i-\frac{\delta}{2}}^{y_i+\frac{\delta}{2}} S_i(y_j)\,dy_j \ldots\ldots (30)$$

where $S_i(y_j)$ is the area of the intersection, i.e.:

$$S_i(y_j) = \int_{x_1^L(y_j)}^{x_2^L(y_j)} Z(x, y_j)\, dx \ldots\ldots (31)$$

where $Z(x,y_j)$ is the distance between the lower bottom and the edge of the truncate cone; it can obtained by equations (27) and (32) as follows:

$$Z(x,y) = (H - ctg\alpha\sqrt{x^2+y^2}) - (ytg\varphi + R_p tg\varphi) \ldots\ldots (32)$$

The integrations will also be calculated by numerical method. The total X-ray generation volume can be calculated as [11]:

$$V_T^i = \frac{t}{3}(S^L + S^u + \sqrt{S^L S^u}) \ldots\ldots (33)$$

Here, S^L, S^u are the elliptical areas of the upper and the low surfaces of the foil intersected by the electron beam. The apparent concentration is calculated using equation (4).

Exponential Model: With the exponential model, the apparent concentration is calculated as:

$$C_{apr}(y_i) = \frac{C_0}{V_T^i}\int_{Y_B^1}^{Y_B^2} S_i(y_j)\exp\left(-\frac{|y_j - y_i|}{A}\right) dy_j \ldots\ldots (34)$$

While $Y_B^1 \leq y_j \leq Y_p^1$, $Y_p^2 \leq y_j \leq Y_B^2$ (see Figure 3 (b)), $S_i(y_j)$ is calculated by equation (31) and while $Y_p^1 < y_j < Y_p^2$, $S_i(y_j)$ is calculated by equation (29).

3. Experiment Results and Discussions

Two types of composite samples were analyzed, such as Al-Cu-Mg (2124)/Si_3N_4-whiskers (as-extruded) and Al-Mg (5083)/SiC-particles (as-cast). The chemical compositions are: (2124) 4.2Cu-1.48Mg-0.62Mn-Al (balance, wt%) and (5083) 4.1Mg-0.56Mn-0.12Cr-0.19Fe-0.15Si-Al (balance, wt%). It was found that Mg and Cu were the main alloy elements segregating at the interfaces of the reinforcements and the matrixes. As pointed out by G. L'Esperance et al. [1], segregation of Mg solute at the interface of 2124/Si_3N_4-whisky composite played an important role in its superplastical behaviour. Because the segregation extended only a small range, deconvolution technique must be used. In order to get segregation profiles of Mg or Cu elements, some special consideration must be given for these materials. We assumed that Mg and Cu did not diffuse into reinforcements and the assumed concentration profiles had an asymmetry exponential shape. That is:

$$C(y) = C_m + C_0 \exp\left(-\frac{y}{A}\right) \quad \ldots\ldots (35)$$

Here, C_m is the concentration in the matrix far away from the interface. C_0 is the peak of the concentration profile when C_m is zero. When $y<0$ (i.e. inside the reinforcement), $C_m=0$ and $C_0=0$; when $y=0$ (i.e. just on the boundary), $C(0)=C_m + C_0$.

First, distortion of X-ray generation volume caused by tilting is not considered. The integrations will be calculated in four parts with different boundary conditions as the electron beam is moved to different positions, as shown in fig.5(a) (fig.5(b) is for the distortion model). If y_i is the distance from the centre of electron beam to the boundary of the reinforcement, y_i is given a negative value inside the reinforcement (see Fig. 5(a)).

Part I, $y_i \geq R$, (again, $r = d_p/2$ and $R=B/2$):

$$C_{apr}(y_i) = \frac{1}{V_T^i}\left[\int_{-R}^{-r} f_1(y)\,C(y+y_i)\,dy + \int_{-r}^{r} f_2(y)\,C(y+y_i)\,dy + \int_{r}^{R} f_1(y)\,C(y+y_i)\,dy\right] \quad \ldots\ldots (36)$$

Here, $f_1(y)$ and $f_2(y)$ have the same forms as equations (16) and (20).

Part II, $r \leq y_i \leq R$, because $C(y+y_i)=0$ while $y+y_i<0$, so we have:

$$C_{apr}(y_i) = \frac{1}{V_T^{i,1}}\left[\int_{-y_i}^{-r} f_1(y)\,C(y+y_i)\,dy + \int_{-r}^{r} f_2(y)\,C(y+y_i)\,dy + \int_{r}^{R} f_1(y)\,C(y+y_i)\,dy\right] \quad \ldots\ldots (37)$$

Here,

$$V_T^{i,1}=V_T^i-\int_{-R}^{-y_i} f_1(y)\,C(y+y_i)\,dy$$

Part III, -r < y_i < r :

$$C_{apr}(y_i)=\frac{1}{V_T^{i,2}}\left[\int_{-y_i}^{r} f_2(y)\,C(y+y_i)\,dy+\int_{r}^{R} f_1(y)\,C(y+y_i)\,dy\right]\ldots\ldots(38)$$

Here,

$$V_T^{i,2}=V_T^i-\int_{-R}^{-r} f_1(y)\,dy-\int_{-r}^{-y_i} f_2(y)\,dy$$

Part IV, $y_i \leq$ -r :

$$C_{apr}=\frac{1}{V_T^{i,3}}\int_{-y_i}^{R} f_1(y)\,C(y+y_i)\,dy\ldots\ldots(39)$$

Here,

$$V_T^{i,3}=\int_{-y_i}^{R} f_1(y)\,dy$$

The 8-th degree of Newton's numerical integration was used to calculate the integration above.

The experiment was performed with a Link EDX system on a transmission electron microscope (Philips, CM30). The high voltages used were 200 and 300 kV. X-ray spectra were processed using the multiple linear least square method for stripping away the background and the partial overlap between the Mg, Al and Si peaks. The EDS system has an ultra-thin window. Experimentally sensitive factors K_{AB} were measured using pure $MgAl_2O_4$ crystal (K_{MgAl}=1.10, 1.18 at 200 and 300 kV individually; K_{OAl}=2.18 at 300 kV) and also calculated using the software of the Link system (RTS-2) for some elements (K_{MgAl}=1.05, K_{CuAl}=1.30, 200 kV). Absorption correction was also calculated using RTS-2 software. The thickness of TEM foil was measured using a two beam convergent beam diffraction technique. The probe diameter was measured on TEM micrographs by extrapolating the diameters obtained using different exposing times to get the diameter of "zero" exposing time. During the experiment, the interface was put to the position just parallel to both the detector and the electron beam. The calculated apparent concentrations were fitted graphically to the apparent concentrations obtained by experiment in order to determine the values of C_0 and A in equation (35), whereafter, the true concentration profile is obtained.

In order to study the effect of the distortion of the X-ray generation volume caused by tilting, the experiment results obtained by the no-distortion model were compared to that obtained using so-called distortion model. Equation (34) was used to calculate the apparent composition. The integrations were also calculated in four parts just as that carried out in calculations of the no-distortion model. Fig.5(b) shows the

geometry and the integration regions for the distortion model.

The experiment results and the deconvoluted "true" composition profiles are shown in figures 6 through 10. Fig. 6(a) is the EDS spectrum obtained from an interface between the 2124 Al alloy and a Si_3N_4w. Figures 6(b)&(c) are the Mg composition profiles calculated using the no-distortion model and the distortion model respectively. The difference between the Mg peak concentrations (C_0) calculated using distortion and no-distortion models is about 10% when X-tilt is 10° and Y-tilt is 20°. As well, the true Mg content at the interface (3.9 wt%) obtained from the deconvolution is much higher than the apparent content (2.6 wt%) obtained by direct measurement. This means that the Mg content at the interface is under-estimated from direct measurement due to the insufficient spatial resolution. Usually, the effect of distortion of the X-ray generation volume is mainly caused by the X-tilting (the axis is parallel to the interface and detector direction). The larger the tilting angle is, the larger the distortion of the X-ray volume becomes, thus the larger the difference. For example, in the same case, assuming that the tilting angle φ_x is 20°instead of 10°, the expected difference of C_0 values obtained by the distortion and by the no-distortion models could be 25% (i.e. C_0 = 4.3 wt% and with A = 14 nm). Generally, using higher accelerating voltages and thinner foils can decrease the effect of the volume distortion.

In order to evaluate the convolution sensitivity, we change the fitting constants C_0 from 3.5 to 3.6 wt% and A from 24 to 25 nm, the change of the calculated results

can be seen in figure 7. That is, a change of 0.1 wt% and 1 nm in the constants can be observed on the resulting graphs. In our experiment, the statistical errors of Mg and Cu X-ray counts at peak position are about 10%. Thus, the sensitivity of the fitting constants (about 3 %) is better than these error values. Figures 8 & 9 are two additional examples, showing the results obtained from interfaces where the Mg concentration is high and the Mg profile extends over a very short distance. The true Mg concentrations at the interfaces (16.5 wt% and 3.75 wt%, in figures 8 &9 respectively) are approximately two times higher than the measured apparent concentrations (6.5 wt% and 2.0 wt%). Again, this confirms that direct measurement will lead to a large under-estimation of Mg content at the interface, especially when the distribution profile is very sharp. In fact, for a given electron beam size, the smaller the extending distance of the profile is, the larger the difference between the measured apparent compositiom and the "true" composition.

As is well known, the melting point of an alloy changes with its composition. The effect of Mg and Cu segregation on the local melting point of aluminum alloys is estimated to be -6°C/at% Mg and -6.5/at% Cu individually [1]. Therefore, it is meaningful to get a more precise estimation on the Mg and Cu concentrations. It should be noted, however, that at some interfaces, part of Mg may be in the form of magnesium oxides or Al and Mg precipitates. In this case, whether or not the deconvolution technique can still be effectively used will depend on the size and distribution of these products. It is also possible that the composition profile may have an exponential shape

or may be a combination of the slab and the exponential models, that is, a combination of equilibrium and non-equilibrium segregation.

Finally, another example of the application of the deconvolution technique is in which distribution of Mg inside the SiC reiforcement in a composites of Al-Mg (5083)/SiC particles must be determined. Fig. 10(a) shows a TEM image of an analyzed interface. Fig. 10(b) shows that the calculated apparent Mg concentrations fit the measured concentrations very well with an average relative error less than 5%. This means that the assumed "true" concentration profile is correct and Mg does not diffuse into the SiC particle. The Mg detected inside the SiC particle actually is caused by electron beam broadening.

4. Conclusions

(1) A graphical deconvolution method has been used to determine the distribution of Mg and Cu at the interface between matrix and reinforcement. The ratios of the volumes intersected by the X-ray volume and the concentration profile to the total X-ray generation volume is used in the deconvolution. Mathematical derivations for different assumed concentration profiles such as a slab profile and an exponential profile have been carried out. The sensitivity of the method is as small as 0.1 wt% and 1 nm.

(2) In 2124 Al/Si_3N_4w composites, the true Mg and Cu distribution profiles confirmed by the deconvolution technique obey the following expression:

$$C(y) = C_m + C_0 \exp\left(-\frac{(y)}{A}\right)$$

It is found that there is about 5 to 16 wt% Mg, as well as 3.6 wt% Cu, segregated at the interface which may affect the deformation behaviour of the composites.

In 5083 Al/SiC composites, Mg can not diffuse into the SiC particles.

(3) The effect of distortion of the X-ray generation volume caused by tilting has been considered. The difference between the peak concentrations calculated using distortion and no-distortion models respectively can be as large as 10% when X-tilt is 10°. The effect of the distortion of X-ray generation volume is mainly caused by the X-tilt (the axis parallel to the interface).

References

1. G. L'Esperance, T. Imai, B. Hong, Superplasticity in Advanced Materials, edited by S. Hori, M. Tokizane, N. Turushiro, Japan, 1991, P.379

2. E. Goiffon, W.M. Zhong, J.J. Blandin, M. Suery, G. L'Esperance, Pro. of 2nd Inter. Conf. on Cast Metal Matrix Composites, Tuscaloosa, USA, Oct., 1990

3. J.R.Michael, D.B. Williams, J. Microscopy, Vol.147(1987), (3), P.289

4. P.Doig, P.E.J. Flewitt, Microbeam Analysis, (1982) P.72

5. D.B.Williams, A.D.Romig, Ultramicroscopy, Vol.30 (1989), P.38

6. J.R.Michael, D.B. Williams, C.F. Klein and R. Ayer, J. Microscopy, Vol.160(1990), (1), P.41

7. E.J.Rapperport, Advances in electronics and electron physics, (1969), P.6

8. A.D.Romig, Jr., M.J. Cieslak, Analysis electron microscopy (1987)

9. A.D.Romig, Jr., J.C. Lippold and M.J. Cieslak, Metall. trans. Vol.19A(1988), P.35

10. J.J.B.Reed, Ultramicroscopy, Vol.7(1982), P.405

11. J. Pachner, Handbook of Numerical Analysis Applications, McGraw-Hill Book Company, 1980

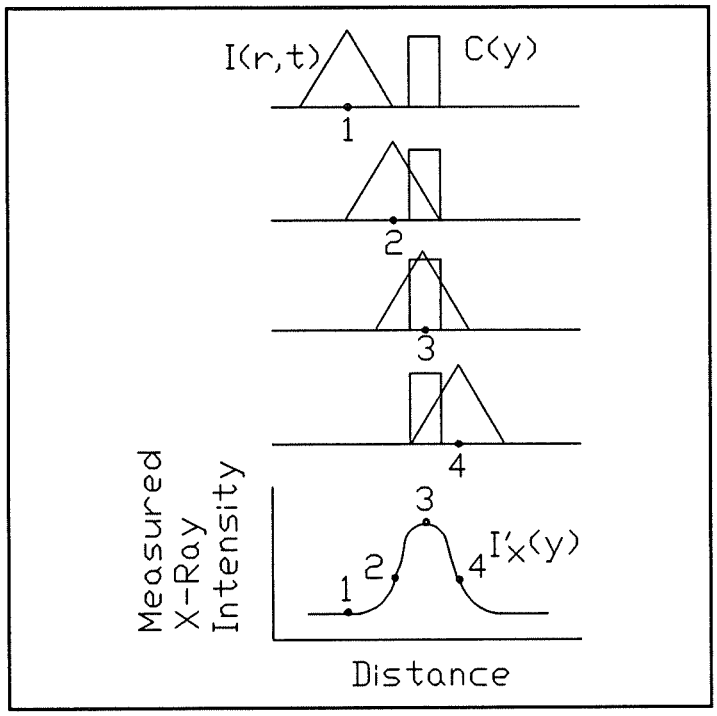

Fig. 1 The principle of convolution of the electron beam distribution I(r,t) in the thin foil and the segregation distribution (C(y), slab model). From the measured intensity profile $I'_x(y)$ and the calculated electron beam distribution, a "true" solute profile at the boundary can be determined (after Michael [6]).

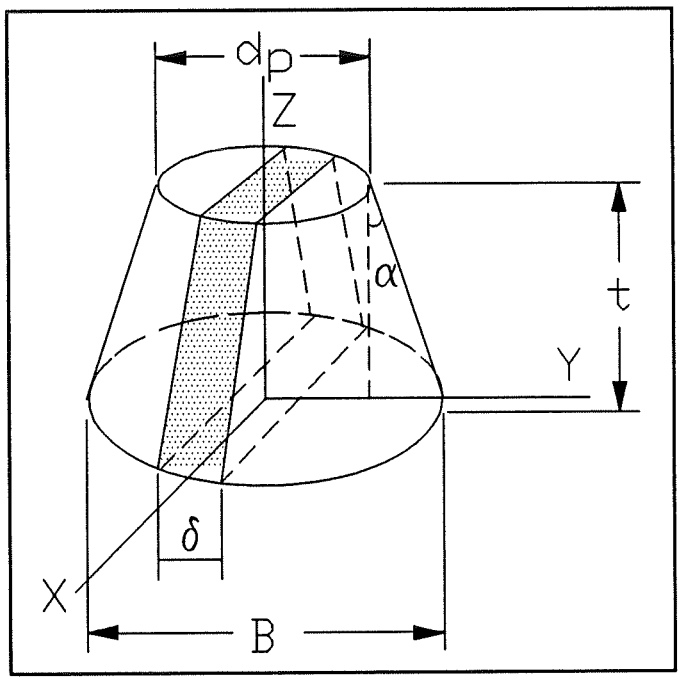

Fig. 2 Schematic representation of electron beam interaction with a grain boundary in a thin slab specimen. The volume of interaction is modeled as a frustum cone. d_p is the incident probe diameter. B is the diameter of the broadening exit electron beam (after Romig [9]).

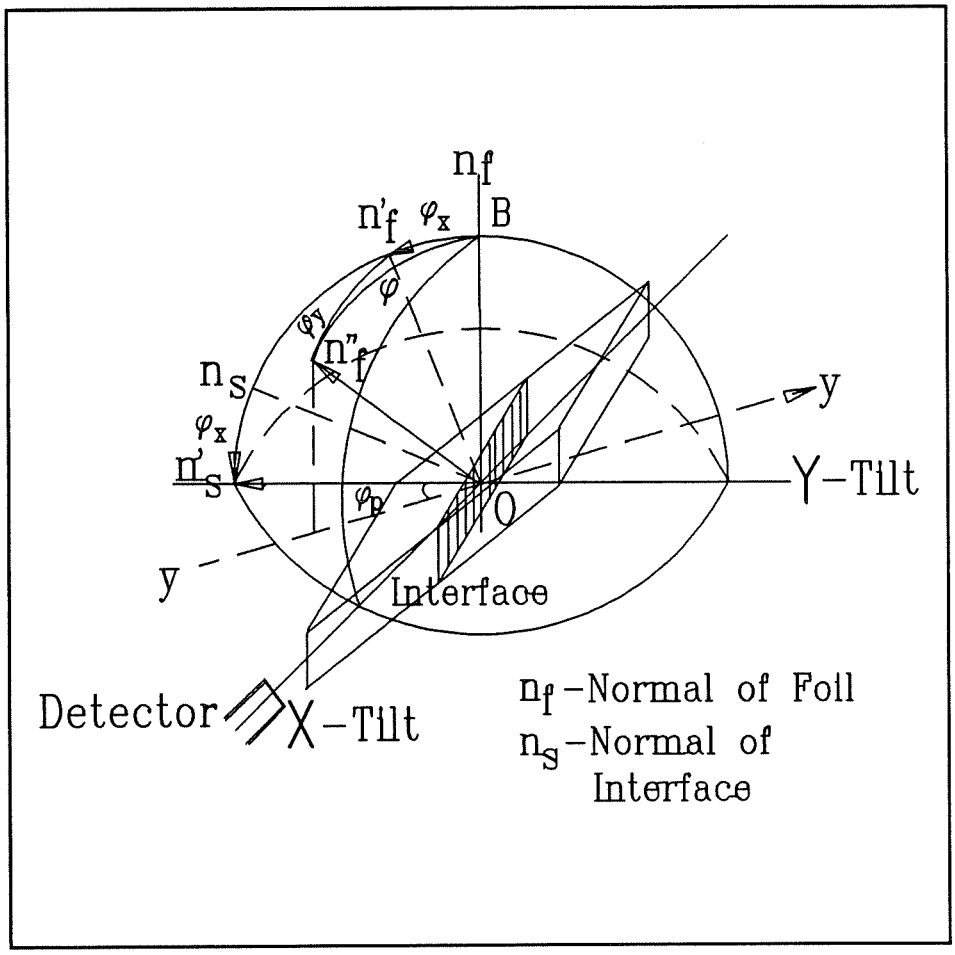

Fig. 3 (a) Relations among the normal of the foil n_f, the normal of the interface n_s and the direction of the electron beam B

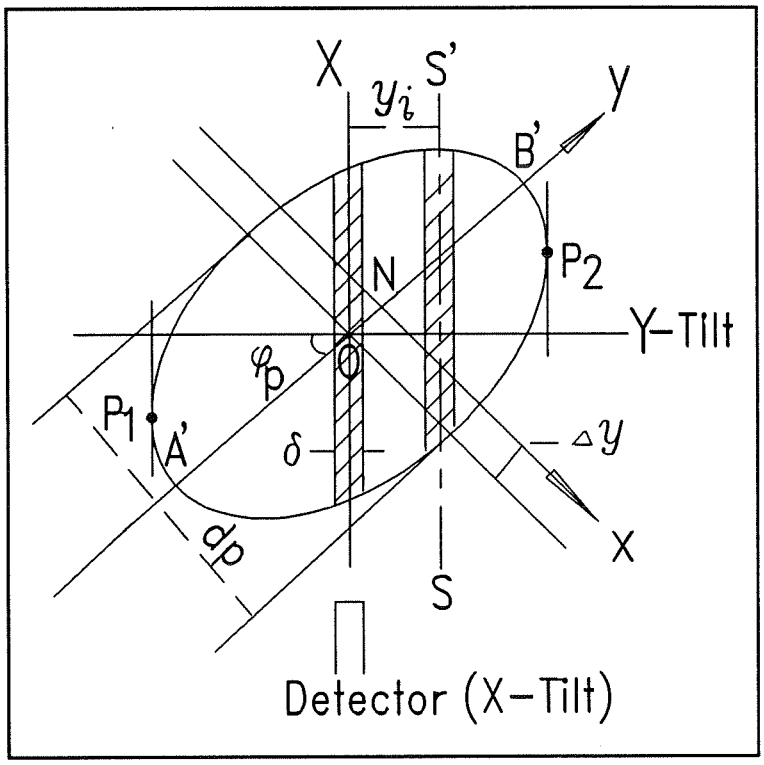

Fig. 3 (b) Intersection of the electron beam with the tilted foil surface and the interface

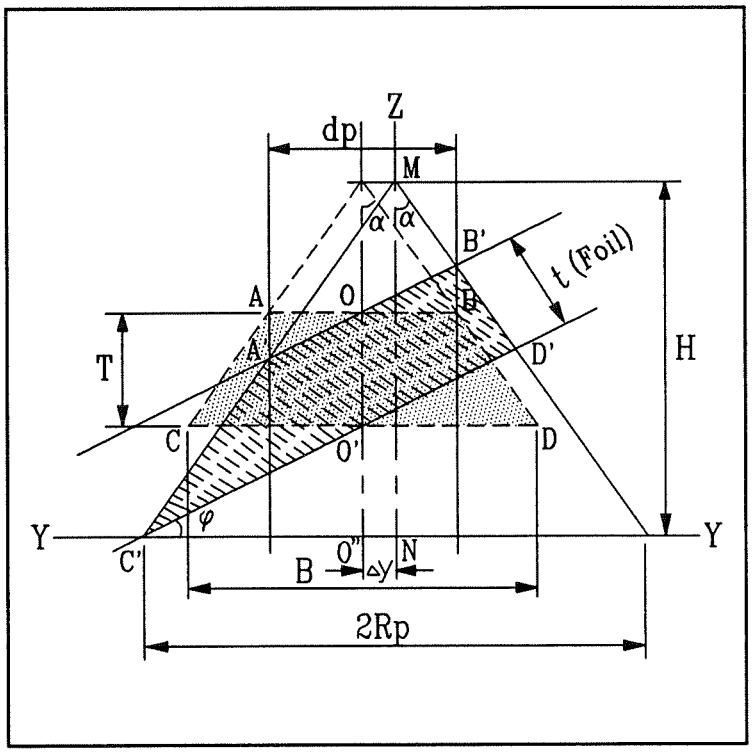

Fig. 4 Cross-section of the electron interaction volume in the thin foil,
ABCD is the cross-section without distortion,
A'B'C'D' is the cross-section with distortion, t=foil thickness

(a)

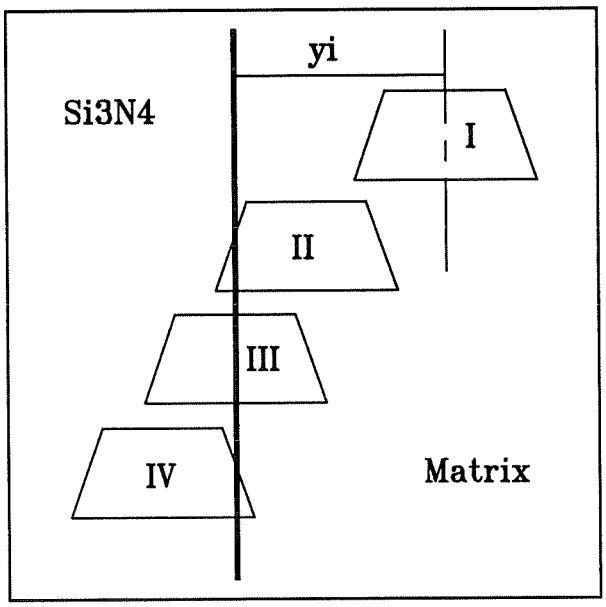

(b)

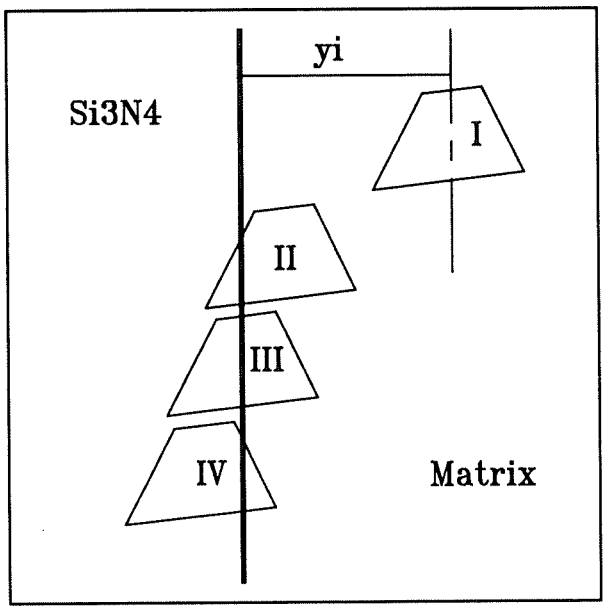

Fig. 5 Showing the four integration regions in both (a) no-distortion and (b) distortion models

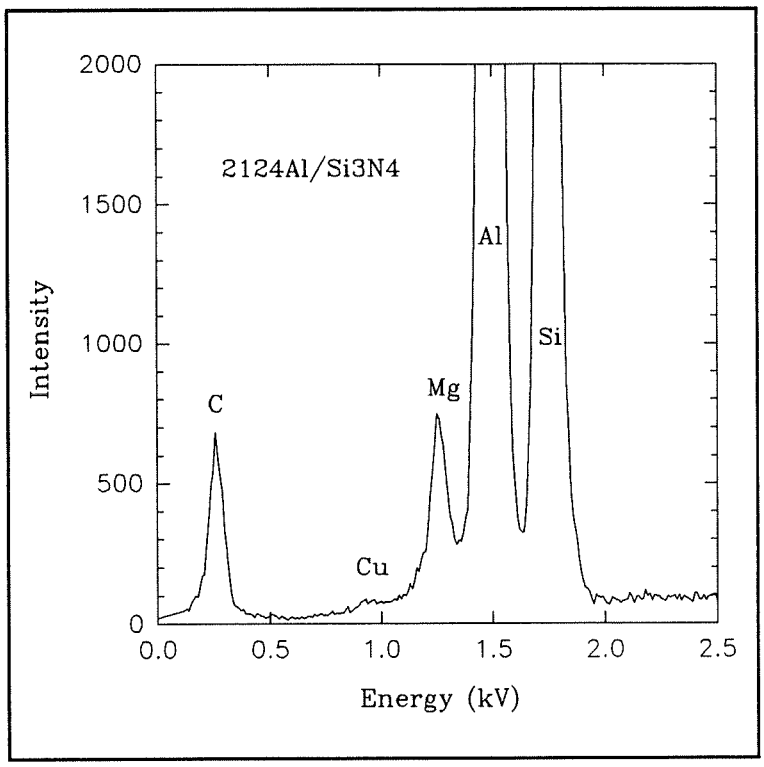

Fig. 6 (a) EDS spectrum obtained at the 2124Al/Si_3N_4 interface

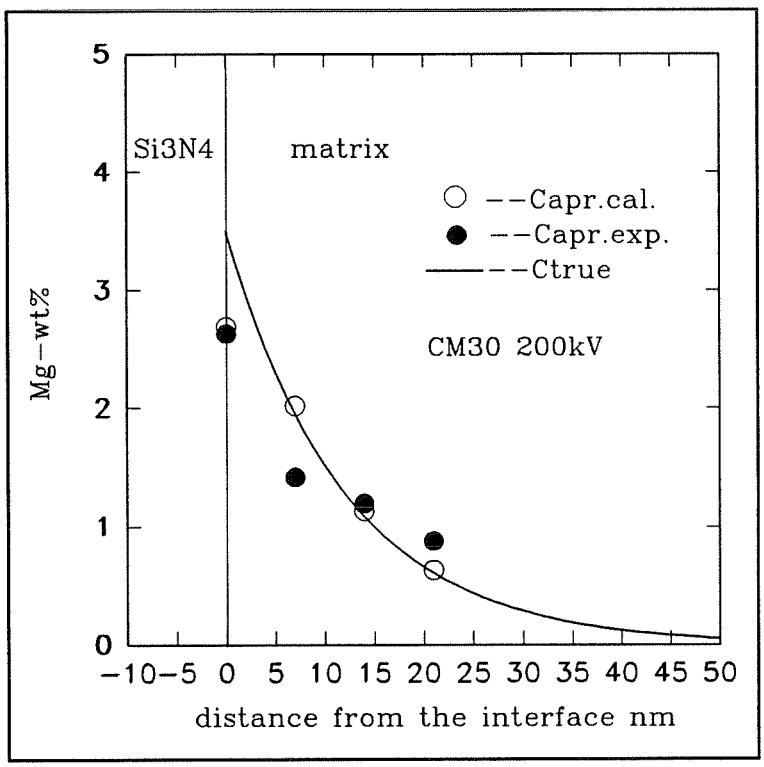

Fig. 6 (b) Mg concentration profile obtained by no-distortion model, C_0=3.5, A=12 nm, d_p=14 nm, X-tilt=10°, Y-tilt=20°, foil thickness=136 nm

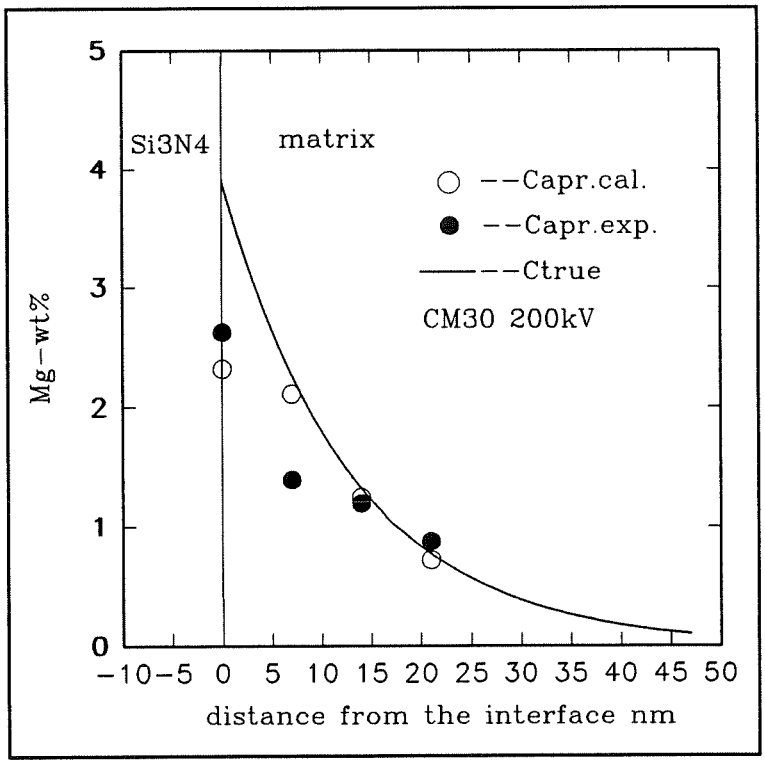

Fig. 6 (c) Mg concentration profile obtained by distortion model, C_0=3.9, A=13 nm

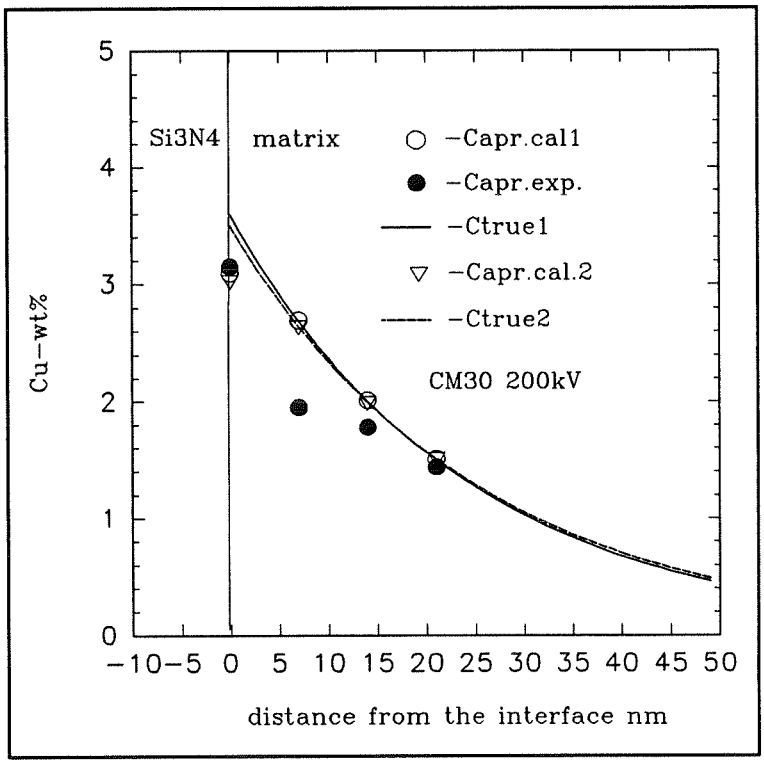

Fig. 7 Cu concentration profiles obtained by no-distortion model, showing the effect of C_0 and A

profile 1, C_0=3.6, A=24 nm; profile 2, C_0=3.5, A=25 nm

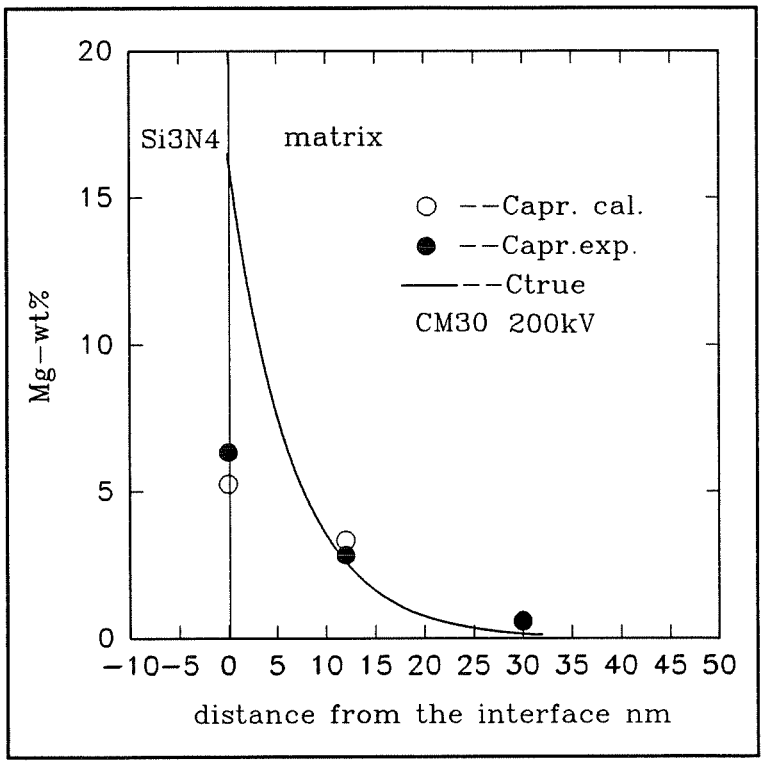

Fig. 8 A profile obtained from an interface with high Mg concentration, C_0=16.5, A=6.5 nm, X-tilt=5°, Y-tilt=20°, d_p=40 nm

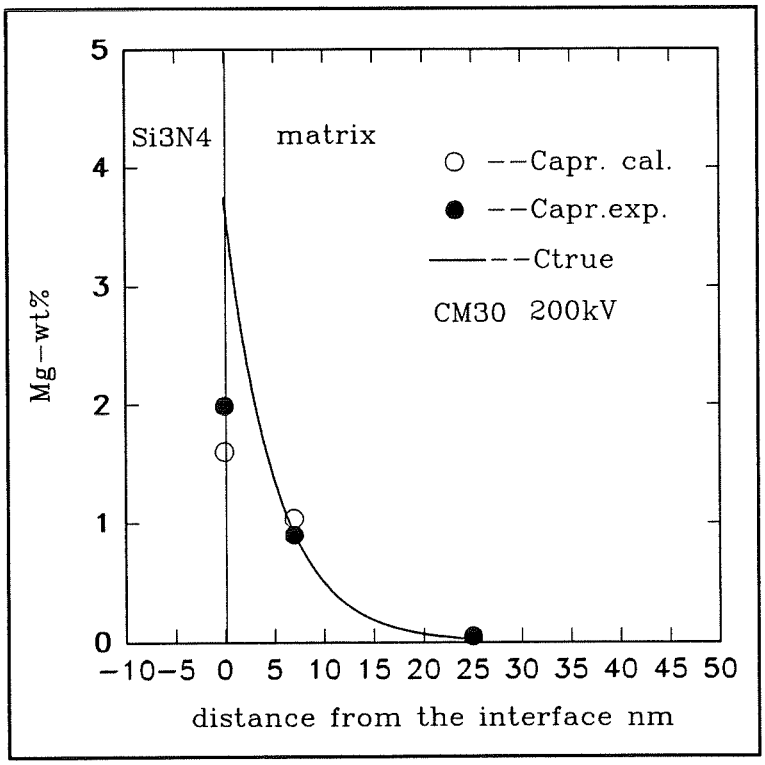

Fig. 9 Showing a narrowly extended Mg concentration profile

C_0=3.75, A=5 nm, d_p=20 nm

(a)

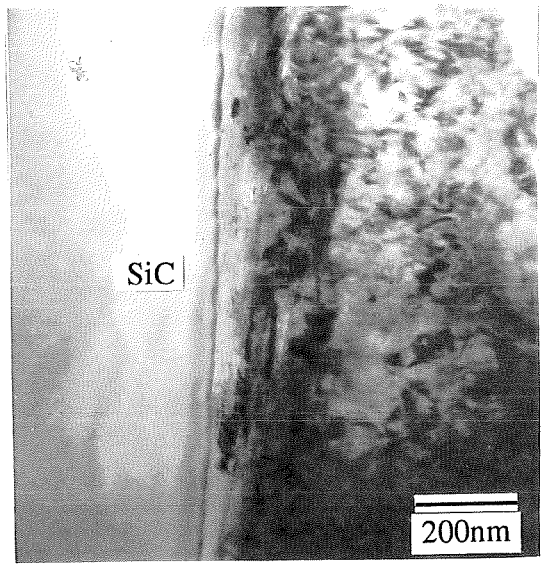

(b)

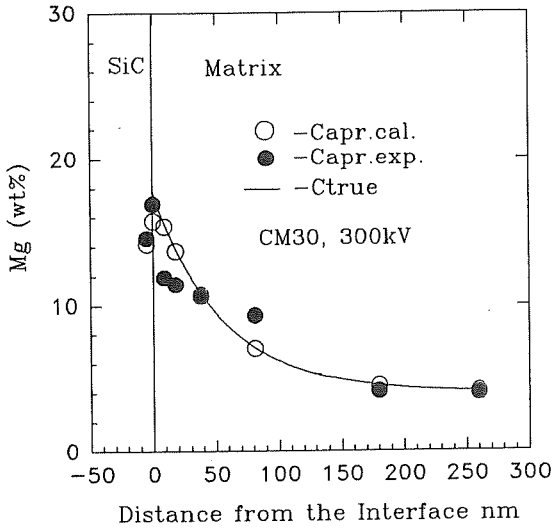

Fig. 10 (a) TEM BF image showing an analyzed interface (5083Al/SiCp)

(b) The convoluted "true" Mg profile (solid curve) obtained using no-distortion model, C_0=17.5, A=25 nm

* Capr.exp.-- measured apparent concentration

* Capr.cal.-- calculated apparent concentration

2.5 Determination of Residual Stresses and Stress State in Al-1%Mg/ SiCp Composites Using Convergent Beam Electron Diffraction Technique

W.M. Zhong*, G. L'Espérance* and M. Suéry**

* Ecole Polytechnique de Montréal, Centre de Caractérisation Microscopique des Matériaux (CM)^2, Case Postale 6079, Succ. "A", Montréal, Québec, Canada H3C 3A7

**Institut National Polytechnique de Grenoble, Génie Physique et Mécanique des Matériaux, GPM2, URA CNRS 793 ENSPG, B.P.46, 38402 St Martin d'Heres Cedex, France

Abstract

In SiC or Al_2O_3 reinforced Al matrix composites, the difference between thermal expansion coefficient of SiC or Al_2O_3 and that of the matrix leads to a misfit strain around the reinforcements when the composites are cooled from high temperatures. This may cause plastic deformation and elastic residual stresses in the matrix around the reinforcements. In this paper, a convergent beam electron diffraction technique (CBED) was used to determine the residual elastic strain around a SiC particle and the Hooke's

law was used to calculate the corresponding residual stresses. Mg segregation at the matrix/SiC particle interface was measured by energy dispersive X-ray spectrometry (EDS). Because the local Mg concentration could affect the measurement of lattice parameters, the Mg concentration was determined for each CBED analysis point and the contribution of the Mg segregation to the lattice parameters was subtracted. Moreover, the effect of the dislocations on the CBED results is also discussed. Our results show that the radial stress is compressive and the loop stresses are tensile around a particle. The effective stresses are near the yield stress of the matrix.

1. Introduction

In SiC or Al_2O_3 reinforced aluminum matrix composites, owing to the large difference (about 6:1) between the coefficient of the thermal expansion of the matrix and that of the reinforcements, a misfit strain between the SiC (or Al_2O_3) and the matrix is induced during the change of temperature such as during annealing, solution treatment or thermomechanical processing. This misfit strain will result in a large number of dislocations and a certain amount of residual elastic stresses near the reinforcement/matrix interface [1-3]. R.J. Arsenault and his co-workers [4] have observed in-situ the disappearance and re-generation of dislocations near a SiC particle while the thin foil was heated to 400°C, and then cooled to room temperature by using high voltage electron microscopy. The density of dislocations measured in-situ was

about $10^{13}/m^2$. A simple prismatic punching model was developed to account for the increase of the dislocation density due to the difference of coefficients of thermal expansion (CTE) between the matrix and the particles. Y. Flom et al. [5] measured the plastic strains and the extent of the plastic zone by directly observing the slip bands on a polished surface using interference microscopy. The combined plastic shear strains at Al/SiC interfaces were found to be about 1-1.3%. Prangnell et al. [3] found that the density and the orientation of the precipitates near SiC particles in 2014 Al alloy were affected by the residual stresses around these particles.

Most of the results of the evaluation of the residual stress were obtained by theoretical calculations [6-8]. When A. Levy (1990) [7] used an elastoplastic finite element analysis method to characterize the magnitude of the residual stresses in 5456/SiCw (20wt%) composites, he found that the longitudinal stress was compressive near the ends of the whisker and tensile near the middle. The results of C. Teodosiu et al. [8] also demonstrated that the radial residual stress was compressive and the loop stress tensile near a particle in a composite. As we know, almost all the theoretical models are based on some suppositions such as all particles with a shape of spheroid and a uniform distribution etc. [8-10], which are not the case in reality. On the other hand, several techniques can be used to determine experimentally the local residual stresses. For example, X-ray diffraction and neutron diffraction can be used [11,12], but the spatial resolution of these techniques is usually larger than several micrometers. Ashby-Brown contrast and Moirè fringe images in transmission electron microscopy

(TEM) can be used to determine the strain field around a small precipitate [13] and the stresses can then be calculated using certain relations. It can only be used, however, for the samples with particles with a radius smaller than the thickness of the TEM foil. Convergent beam electron diffraction (CBED) has also been used to measure the change in lattice parameters which result from residual strains in materials. The interest in this technique comes from the fact that the analysis area is defined by the incident probe (which usually can be as small as a few hundreds of Å) [14]. The limit of the measurement accuracy can be $\pm$ 0.0005 Å or $\pm$ 0.03° [15]. However, the interpretation of the CBED pattern is still difficult, since the change in the parameters caused by residual elastic stresses is often too small to produce an apparent shift of HOLZ lines which are used to determine the residual strain. Moreover, since the specimen used is a thin foil during the TEM observation, the relaxation of the residual stresses makes the interpretation of the stress state more difficult, and the misfit strain measured is usually different from that in bulk specimens [15,16]. Several studies have be carried out in this field [15,17]. For example, S.J. Rozeveld [15] measured the residual strains in Al-SiCw composite using the CBED technique. His results showed that the residual strains near the ends of whiskers approached the strain limit where the plastic deformation of the matrix will start. The magnitude and the sign of the residual stresses could not be established. Another important factor which we should take into consideration in study of composites is the segregation of solute atoms near interfaces such as the segregation of Mg in Al-Mg matrix composites [18]. This will result in an increase of the local lattice parameters. In this paper, optimal experimental parameters

to carry out measurements using CBED are suggested and the effect of Mg segregation and dislocations on the simulation of the HOLZ patterns are discussed. Finally, possible errors in using the CBED technique are presented.

2. Experimental Procedures

A kinematic model was used to simulate the HOLZ patterns in this study [19]. The accelerating voltage was calibrated using a foil of pure Si and using the same simulation program. Three models can be used to simulate HOLZ patterns: dynamic model, geometric model (or kinematic model) and geometric model combined with a first order dynamic correction [11,13,20,21]. Dynamic models can yield both the position and the intensity of the HOLZ lines. Purely kinematic simulating model have been widely used because of its simplicity and its sufficient precise [11,13]. The details of the kinematic model are given as the following.

In Fig. 1 (a)&(b) [11], g is the reflection under consideration. Then its projection into the plane of a diffraction pattern is (g-t), where t is the vector separating two reciprocal lattice layers, [u,v,w] is the index of a zone axis. A HOLZ line is perpendicular to the corresponding g vector, and its position is determined by $(2/\lambda)(\Theta-\Phi)$, where Θ is the Bragg angle and Φ the angle defining the radius of the FOLZ (first order laue zone) ring. V is the volume of a crystal cell. a, b and c are lattice

parameters. Θ and Φ can be calculated as followings:

$$\Theta=\lambda/2d_{hkl} \quad \text{.....(1)}$$

Where, $d_{hkl}=1/g_{hkl}$ .....(2)

$$g_{hkl}=ha^*_1+ka^*_2+la^*_3 \quad \text{.....(3)}$$

$$a^*_1=bc\sin\alpha/V \quad \text{.....(4)}$$

$$a^*_2=ac\sin\beta/V \quad \text{.....(5)}$$

$$a^*_3=ab\sin\gamma/V \quad \text{.....(6)}$$

$$V=abc(1-\cos^2\alpha-\cos^2\beta-\cos^2\gamma+2\cos\alpha\cos\beta\cos\gamma) \quad \text{.....(7)}$$

$$\Phi=t/(g^2_{hkl}-t^2) \quad \text{.....(8)}$$

Where, $t^2=1/(u^2a^2+v^2b^2+w^2c^2+2vwbc\cos\alpha+2wuac\cos\beta+2uvab\cos\gamma)^2$

.....(9)

The material used in this work was Al - 1%Mg alloy reinforced by block SiC particles of 13 μm average diameter with a volume fraction of about 10%. The composite was fabricated by a modified compocasting technique [18]. No chemical reaction and phase transformation were found in the area of CBED analysis near SiCp [22]. The specimen was heated to 525°C, kept for 5h and then quenched in water. The TEM thin foil was prepared by mechanical polishing (to about 250 μm thickness), mechanical dimpling (to about 25 μm) and ion thinning (to about 200 nm at 10° of ion gun tilt angle and 5 kV gun voltage). CBED patterns were obtained using JEOL-2000FX transmission electron microscopy. The probe diameter used here was about

50 nm. The nominal accelerating voltage Eo was 120 kV. A Link EDS system was used to identify the SiC particles and to determine the composition of the matrix. The concentration of Mg at each CBED analysis point was determined by an experimental K-factor method. The crystal orientation near the particle was determined by a select area diffraction technique (SAD) and the residual stresses were calculated using general Hook's formulas.

3. Results and Discussion

3.1 The Orientation of the Matrix near a SiCp

The analyzed interface and the electron diffraction pattern obtained near a SiC particle, with specimen stage at zero tilting, can be seen in figures 2 (a)-(d). The normal of the foil is near B[010] Al (about 5° deviation). The particle has a shape of lath (10 μm length, 2 μm width). The angle between the edge of the particle and the reflect vector g_{002} is about 40° to 45° (see Fig. 2(d)).

3.2 Determination of the Foil Thickness

As we know, it is necessary to know the foil thickness in both CBED measurement and EDS analysis. Generally, the ideal foil thickness should be in the

range of three to eight extinction distance in order to obtain a good quality of HOLZ patterns [14,20]. Thus, in our case, with the accelerating voltage of 120 kV, the "ideal" thickness is about 200 nm. The foil thickness can be measured by using a two-beam convergent-beam diffraction technique [22]. They are 208 nm, 182 nm and 201 nm at positions I, II and III respectively (see figure 2 (a)&(b)).

3.3 Stress State in the Thin Foil

In order to determine the stress state, we define the coordinations of the stresses in positions I and III as shown in Fig. 3, according to the crystal orientation relationship shown in figure 2 (c) (at position II, the coordinations are the same as those at I). For the sake of convenience, we assume that the radial stress is σ_x at each position. The strains of a crystal cell are projected onto the X and Y axes to calculate the strains along different axes (Z-axis is parallel to the normal of the foil).

3.4 Residual Elastica Strain near the SiC Particle

The true high voltage was calibrated using a pure Si foil, that is, 121.45 kV. This value and CBED patterns were used to determine the lattice parameters of an annealed Al-1%Mg alloy. The values of a,b and c are 4.0595, 4.0595, 4.0595 Å (see Fig. 4). These values agree with those obtained by Herve Ribers using a neutron diffraction method [24].

The experimental HOLZ patterns obtained at different positions around a SiC particle and the corresponding computer simulations are shown in figures 5-7. The zone axis used is [122]. Since larger indeces of the zone axis are associated with a larger elastic scattering of the incident electron and a larger Deby-Waller factor, a HOLZ pattern with a strong intensity can be obtained [19]. In our specimen, since the deformation of the matrix near the particle decreases the visibility of the HOLZ lines, it is necessary to select a diffraction zone axis with large indeces [14]. However, with the increase of the indeces of the zone axis, the number of HOLZ lines inside the diffraction disc will decrease. Then, in order to obtain a satisfactory simulation result, it needs to have more than six HOLZ lines inside the disc of a HOLZ pattern (because there are six simulation variables: a,b,c,α,γ,ß). The [122] zone axis is therefore one of the best compromises in selecting the zone axis because it has just six HOLZ lines inside the disc.

To get the "best" simulation, the position of the HOLZ lines, the angle between the HOLZ lines, the ratio of the height of the triangles intersected by the HOLZ lines and the symmetry of the HOLZ pattern should all be considered during the simulation. The relative changes of the lattice parameters at different analysis point are shown in Table 1. From these results, we can see that the changes of the lattice parameters at positions I and II are all positive compared with those of the matrix far from the particle. The strain along the **a** axis is the same as that along the **c** axis. At position II, the changes in the lattice parameters are smaller than those at position I. At position

III, the change is negative along **a** axis; whilst they are positive along the **b** and **c** axes. The strains along the **b** axis are smaller than those along the other two axes at every positions, indicating that **b** axis is parallel to the foil normal direction since it is expected that the stress along this direction is the smallest due to the larger stress relaxation [11,16]. The parameter α is also changed in different patterns which may be caused by some shear deformation.

3.5 Calculation of the Stresses by Hooke's Formulas

Because the anisotropy of the Al matrix is small, we can use general Hooke's formulas to calculate the magnitude of the stresses [25]:

$$\sigma_x = E * \frac{[\epsilon_x + \mu(-\epsilon_x + \epsilon_y + \epsilon_z)]}{(1-\mu-2\mu^2)}$$

$$\sigma_y = E * \frac{[\epsilon_y + \mu(\epsilon_x - \epsilon_y + \epsilon_z)]}{(1-\mu-2\mu^2)} \qquad \text{.....(10)}$$

$$\sigma_z = E * \frac{[\epsilon_z + \mu(\epsilon_x + \epsilon_y - \epsilon_z)]}{(1-\mu-2\mu^2)}$$

$$\tau_{xy} = \gamma_{xy} * G \qquad \tau_{yz} = \gamma_{yz} * G \qquad \tau_{xz} = \gamma_{xz} * G \qquad \text{.....(11)}$$

The stress volume element is shown in Fig. 3. The magnitude of a strain is the projection of a relative change of a lattice parameter to one of the stress coordinations. However, the orientation relationship between the stress axes and the crystal axes (**a**, **b** and **c**) in the foil is still uncertain. As discussed above, the strains along **b** axis are smaller than those along the other two axes at every positions, thus the direction of **b** axis is parallel to the foil normal direction (B[010] direction), that is the direction of Z axis in the stress coordinations. At positions I and II, since **a** equals to **c**, the directions of **a** and **c** can be chosen arbitrarily along the 002 or the 200 reflection vectors. As we know, usually the residual stress is compressive along the radial direction [7,8], therefore at position III, as the change of **a** is negative, it is believed that **a** axis is along the radial direction (direction X). Here, $\tau_{xz}=\tau_{yz}=0$, since the change of γ and β equals to zero.

In order to consider the effect of solute atoms on measured elastic strains, Mg distribution is determined using EDS X-ray analysis. Fig. 8 is the Mg concentration profile obtained using EDS analysis. Segregation of Mg near the SiC particle is observed. By using Hervè Ribes' relation between Mg concentration and lattice parameter (Fig. 9) [24], the increase of the lattice parameters caused by solid solution of Mg in the matrix can be subtracted from the strains measured by using CBED. Table II gives the strains and stresses obtained after removing the contribution of Mg segregation. As well, results obtained without considering the effect of Mg are given in the last row of the Table II, which give a stress of about 440 MPa (σ_i*) at position

I. This is much larger than the yield strength of the alloy (less than 150 MPa in annealing state) [25]. Therefore, it is very important to consider the effect of Mg solute. The effective stress at each position is calculated by Van Mises yield criterion [26], as:

$$\sigma i = \left(\frac{1}{\sqrt{2}}\right)\sqrt{(\sigma_x-\sigma_y)^2+(\sigma_y-\sigma_z)^2+(\sigma_z-\sigma_x)^2+6(\tau_{xy}^2+\tau_{yz}^2+\tau_{zx}^2)} \quad \ldots\ldots (12)$$

Where, Young's Modulus E is 68.2 GP, Shear Modulus G is 25.9 GP and poisson's ratio μ is 0.34 [25]. As calculated above, at positions I, II and III, the stresses are all tensile in directions Y and Z (loop stress), and are compressive in direction X (radial direction). σ_z (parallel to the foil normal) is only about one third of σ_y, due to the larger stress relaxation along the direction [16]. Moreover, most of the stress relaxation usually takes place near the foil surface along z direction [16], that is, in the middle of the foil the stress relaxation is smaller. This may be the reason of widening of the HOLZ lines compared with those in the pattern obtained in the matrix far from the SiC particle (See figures 4 & 5) [27]. The effective stresses (σ_i) are near the yield limit of the matrix. The effective stress at position I σ_i(I) is larger than that at position II. It means that near SiCp the stress is larger. The results also show that the compressive stress at position III is larger than those at positions I and II. These results are similar to those obtained by A. Levy et al. [7] and Jarry et al. [28] using finite element analysis. However, compared with the results obtained by C. Teodosiu et al. [8], the

stress gradient obtained by our experiments is much larger, in another word, the stresses decrease more rapidly with the distance from the particle. This may also be caused by the stress relaxation, because the studied interface is only 400 nm from the hole of the foil. The stress relaxation may be the function of the distance from particle, i.e., stress relaxing less near the particle. Moreover, during explanation of the measured stresses, It should be noticed that the measurement errors can be about ± 15 MPa estimated from the measurement error of the residual strain (about 2/10000 Å) [15].

3.6 Errors in Using CBED Technique

Our results indicate that the CBED technique can be used to measure the elastic residual strains in Al-matrix around a SiC particle. Thus, residual stress distribution can be obtained. However, when we use these stress values, a caution should be given as mentioned above, because there are several factors which may promote the measurement errors during using the CBED technique.

A first factor is the dynamic effect caused by deformation of the specimen [14]. The large misfit strain between the matrix and SiC particles could be accommodated by plastic deformation, producing dislocations around SiCp [29,30]. Indeed, high dislocation density around SiCp is observed in our samples. Some HOLZ lines become wider and sometimes even split as shown in figure 10 when the electron probe is put just on a dislocation line, because the crystal reflection plane is bent by dislocations

[14,29]. The split of the HOLZ lines makes the determination of the positions of HOLZ lines more difficult. A second factor is the increase and the relaxation of the stresses during the preparation of the specimen. Thus, the stresses and the stress state will be different from those in the bulk specimen. In addition, stress relaxation is not uniform along the foil normal direction, therefore HOLZ lines can be widened and the simulation of HOLZ patterns will be more difficult. A third factor, as discussed in this paper, is the segregation of Mg near SiC particles which can lead to an additional lattice strain and an over-estimation of residual stresses. The segregation of Mg near SiC particles in Al-Mg matrix composite is affected by different heat processing conditions [30,31]. Therefore, it is necessary to know the local matrix composition before CBED measurement is carried out.

4. Conclusions

(1) CBED has been used to measure residual strains near SiC particles in Al-Mg matrix composites quenched from 525°C to room temperature. The elastic residual stresses are calculated by using Hooke's formulas. The results show that the stresses are tensile along the Y and Z directions (loop stress) and are compressive along the X direction (radial stress). That is, radial residual stresses (σ_x) are -31 MPa, -7.4 MPa and -77 MPa at positions I (close to the side of the particle), II (a little far away from the side of the particle) and III (near the corner of the particle) respectively; loop

stresses are 92 MPa (σ_y along the edge of the particle) and 21 MPa (σ_z along the foil normal) at position I, 63 MPa (σ_y) and 19 MPa (σ_z) at position II, and 45 MPa (σ_y) and 11 MPa (σ_z) at position III.

The effective stresses (σ_i) calculated by Von Mises yield criterion are near the yield limit of the matrix, that is, 108 MPa, 60 MPa and 130 MPa at positions I, II and III.

(2) [122] zone axis is believed to be one of the best compromises in selecting zone axis which allows to obtain a clear CBED pattern and a good computer simulation results.

(3) Segregation of Mg near the particles can lead to the estimated residual stresses several times larger than their true values. Thus, the contribution of the segregation of Mg solute to the measured lattice parameters obtained by using CBED must be removed.

Table 1 The Lattice Parameters Obtained from Simulating of HOLZ Lines

postion	I	II	III	IV
a	4.0658	4.0622	4.0538	4.0595
b	4.0650	4.0615	4.0615	4.0595
c	4.0658	4.0622	4.0622	4.0595
α	90.14	90.08	89.90	90
β	90	90	90	90
γ	90	90	90	90

*** a, b and c --- in Å α, β and γ --- in degree

Table 2 Residual Strains and Calculated Residual Stresses (σ-MPa)

Position	I	II	III
ϵ_x	-1.029×10^{-3}	-0.521×10^{-3}	-1.404×10^{-3}
ϵ_y	1.414×10^{-3}	0.875×10^{-3}	0.985×10^{-3}
ϵ_z	0	0	0.320×10^{-3}
γ_{yx}	2.443×10^{-3}	1.396×10^{-3}	1.745×10^{-3}
σ_x	-31	-7.4	-77
σ_y	92	63	45
σ_z	21	19	11
τ_{yx}	62	35	45
σ_i	108	60	130
σ_i*	442	276	130

*** At position I, the Mg content (C_{Mg}) is 2.3 wt%, the corresponding lattice parameter without stress is a_0=4.0650 Å; at position II, the C_{Mg} is 1.5 wt% and a_0=4.0615 Å; at position III, a_0=4.0595 Å. σ_i* is the effective stress obtained without removing the contribution of Mg solute.

Acknowledgements

The authors gratefully acknowledge the NATO International Scientific Exchange Programme (Grant no. CRG 900950) and the National Science and Engineering Research Council (NSERC) of Canada (strategic grants) for the financial support. They also thank L. Salvo and J.G. Legoux for the preparation of the composite materials.

References

1 M. Volgelsang, R.J. Arsenault and R.M. Fisher Met. Trans 17A (1986) P.379

2 P.B. Prangnell, W.M. Stobbs, Proc. 12th Symp. Mater. Sci., RISϕ, Denmark, (1991), P.603

3 P.B. Prangnell, T. Downes, W.M. Stobbs and P.J. Withers, Acta Metall. vol.42, No.10 (1994), P.3425

4 R.J. Arsenault, N. Shi, Mater. Sci. and Eng., vol.81(1986), P.175

5 Y. Flom, R.J. Arsenault, Mater. Sci. and Eng., vol.79(1985), P.151.

6 E.J. Lloyd, Research Report (1989) Alcan International Limited Kingston Reseauch and Development Centre

7 A. Levy and J.M. Papazian, Metal and Ceramic Matrix Composites Edited by R.B.Bhagat (1990) P.319

8 C. Teodosiu, H, Ribes and M. Suery, Proc. of International Conference, RISϕ (1988), P.485

9 J.D. Eshelby, Proc. of the Royal Soc. of London Series A. vol.241 (1957), P.376

10 Y. Takeo and M. Taya, Trans. ASME (1985) 52, P.806

11 A.J. Porter, R.C. Ecob and R.A. Ricks, J. of Microscopy, vol.129 (1983) P.327

12 L.C. Davis, J.E. Allison, Metall. Trans. A, vol.24A(1993), P.2487

13 P. Hirsch, A. Howie, R.B. Nicholson, D.W. Pashley, M.J. Whelan, Electron Microscopy of Thin Crystal (1967), New York

14 J.W. Steeds, Introduction to Analytical Electron Microscopy Edited by John, J. Hren, J.I. Goldstein, David C. Joy, (1979) New York

15 S.J. Rozeveld, Proc. of ICEM-XII, Electron Microscopy vol.2, (1990), Edited by L.D.Peachey, D.B.Williams, P.502

16 M.M.J. Treacy, Philosophical Magazine A, (1985) vol.51, No.3, P.389-417

17 Y. You, R. Wang, H. Zou, M.X. Dai, Scripta Metall. et Mater. vol.30(1994), No.7, P.885

18 W.M. Zhong, G. L'Esperance, True Composition Profiles Obtained by Graphical Deconvolution Technique Using Analysis Transmission Electron Microscopy, (to be published)

19 R.C. Ecob, M.P. Shaw, A.J. Porter, Phil. Mag., A44 (1981), P.1133

20 P.M. Jones, G.M. Rackham and J.W. Steeds, Proc, E. Sic. Lond. A. 354 (1977), P.197

21 E.G. Bithell and W.M. Stobbs, Journal of Microscopy, vol 153 (1989), P.39

22 J.G. Legoux, L. Salvo, H. Ribes, G. L'Esperance et M. Suery Interfaces in Metal-Ceramics Composites Edited by R.Y. Lin, R.J. Arsenault (1990) P.187

23 P.M. Kelly, A. Jostsons, R.G. Blake and J.G. Napier, Phys, State Solide (a) 31, (1975) P.771

24 Hervè Ribes, Doctor Thesis (1989), Institut National Polytechnique de

Grenoble, GPM2, France

25 Metal Handbook, A.S.M., Ninth Edition, vol.2 (1979)

26 Alexander Mandelson, Plasticity: Theory and Application (1968), New York

27 Personel communication with M.H. Loretto

28 Ph. Jarry, K. Toitot and B. Janin, Proc. of International Conf. on Residual stresses (1988), France, P.436

29 R.W. Carpenter, Acta Cryst (1982) A38, P.55-61

30 M. Strangwood, C.A. Hippsley and J.J. Lewandowski, Scripta Metallurgica, vol.24(1990), P.1483

31 V.N. Svechnikov, Diffusion Processes in Metals (1966) P.67-80

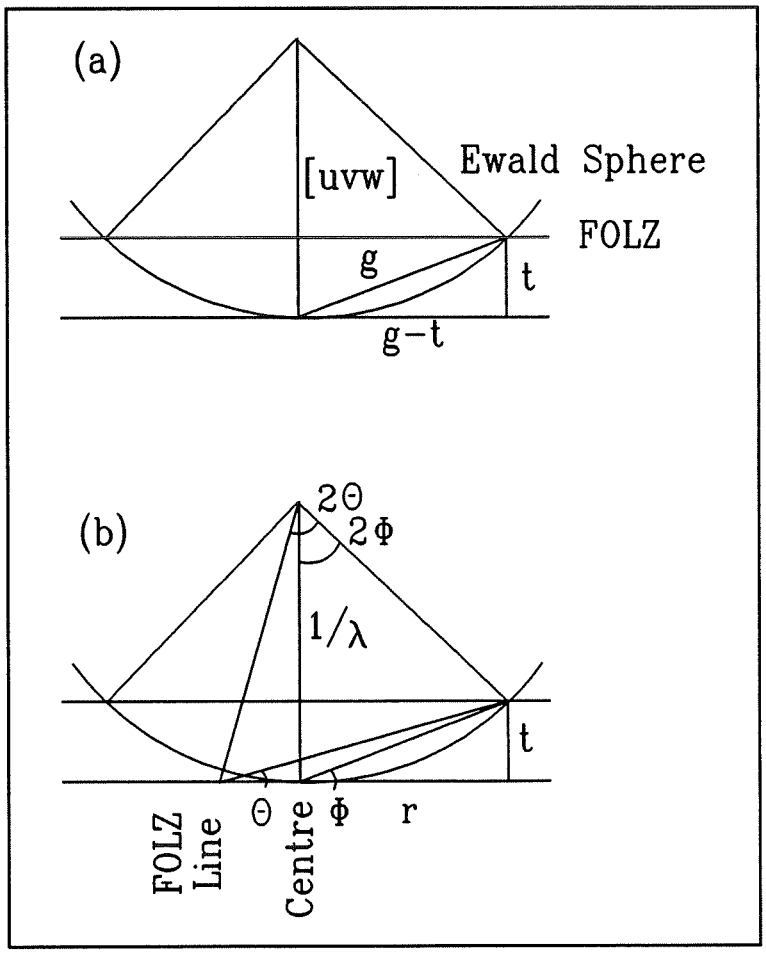

Figure 1 Schematic diagram of HOLZ line positions. (a) Section through reciprocal space showing the FOLZ, the projection (g-t) of reflection g onto the diffraction pattern. (b) Section through reciprocal space for [uvw] zone axis. 2ϕ defines the radius of the FOLZ ring. 2Θ, twice the Bragg angle, defines the angle between defect FOLZ lines.

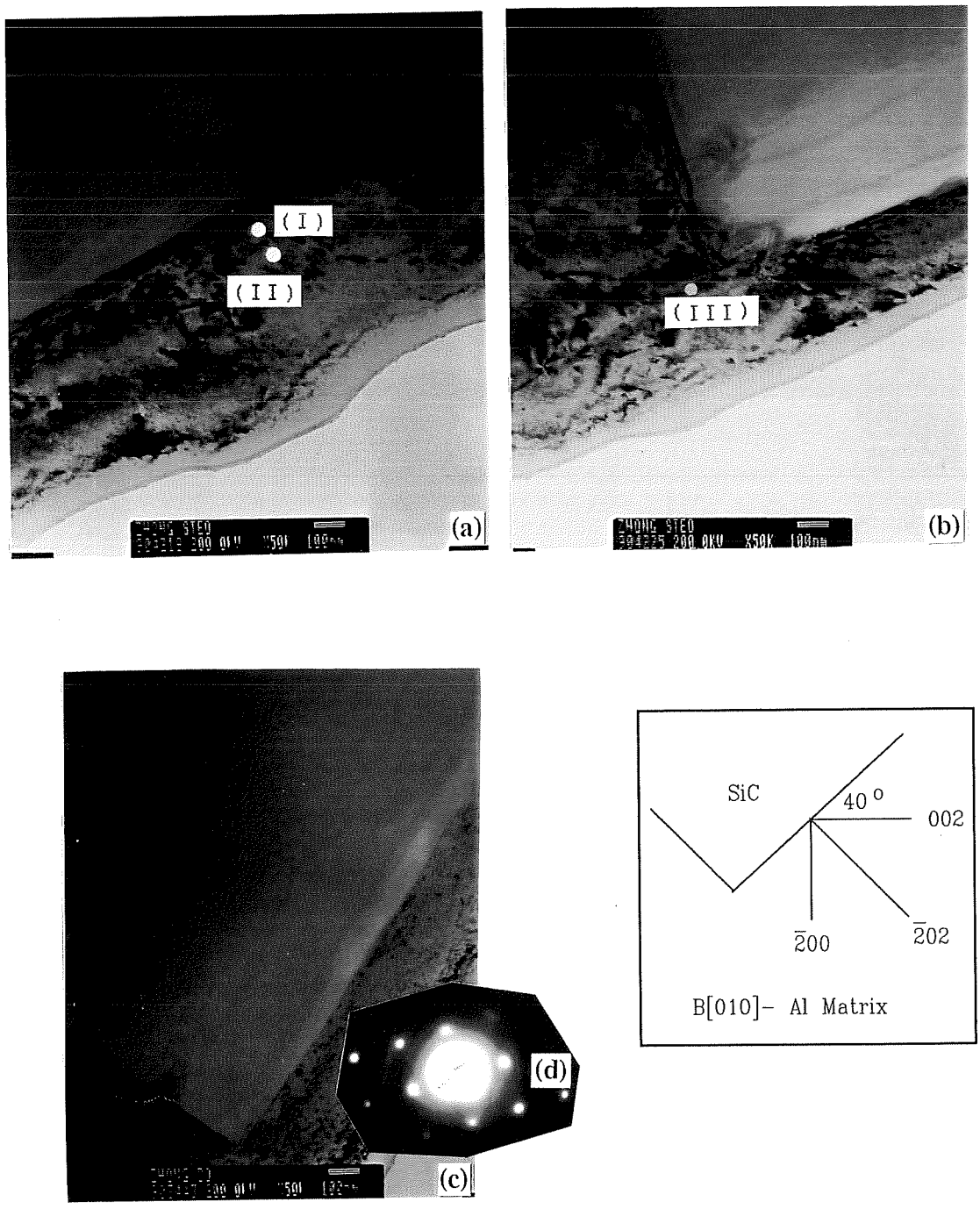

Figure 2 (a)-(c) TEM micrographs showing the studied interface,
(d) SAD pattern obtained at zero tilt, foil normal is B[010]

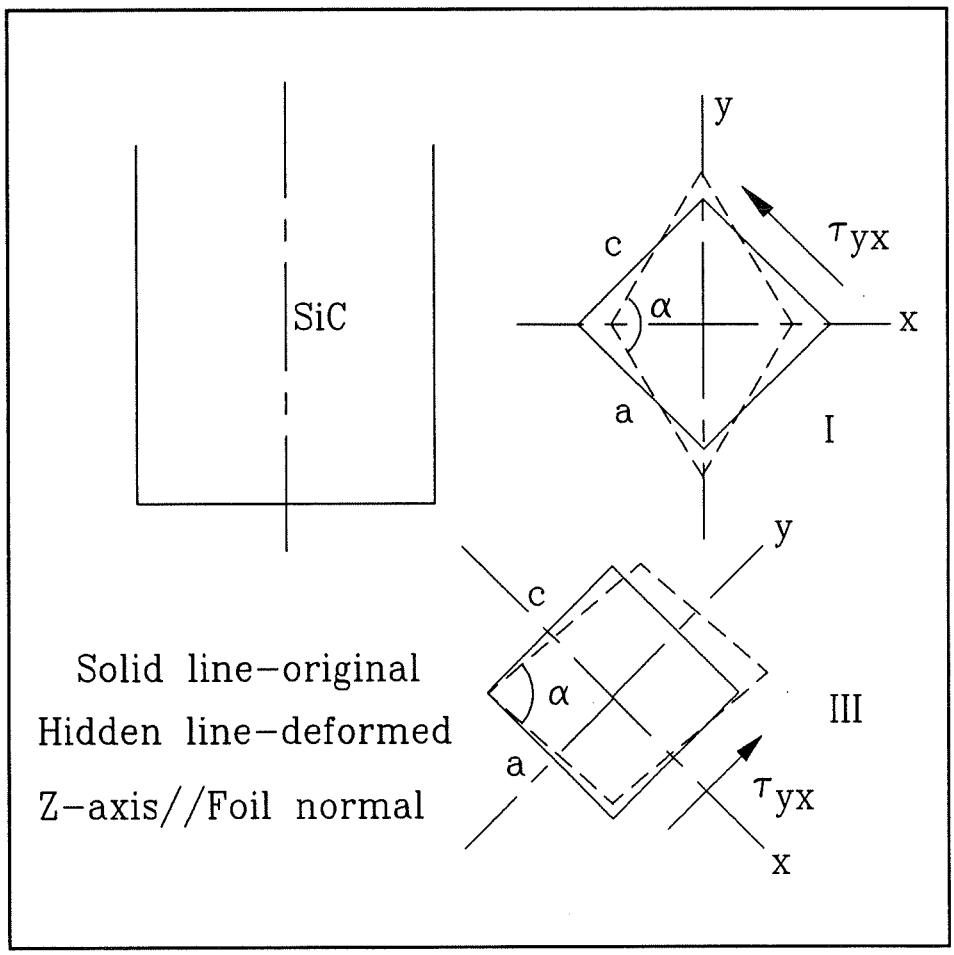

Figure 3 Schematic diagram of the stress volume element

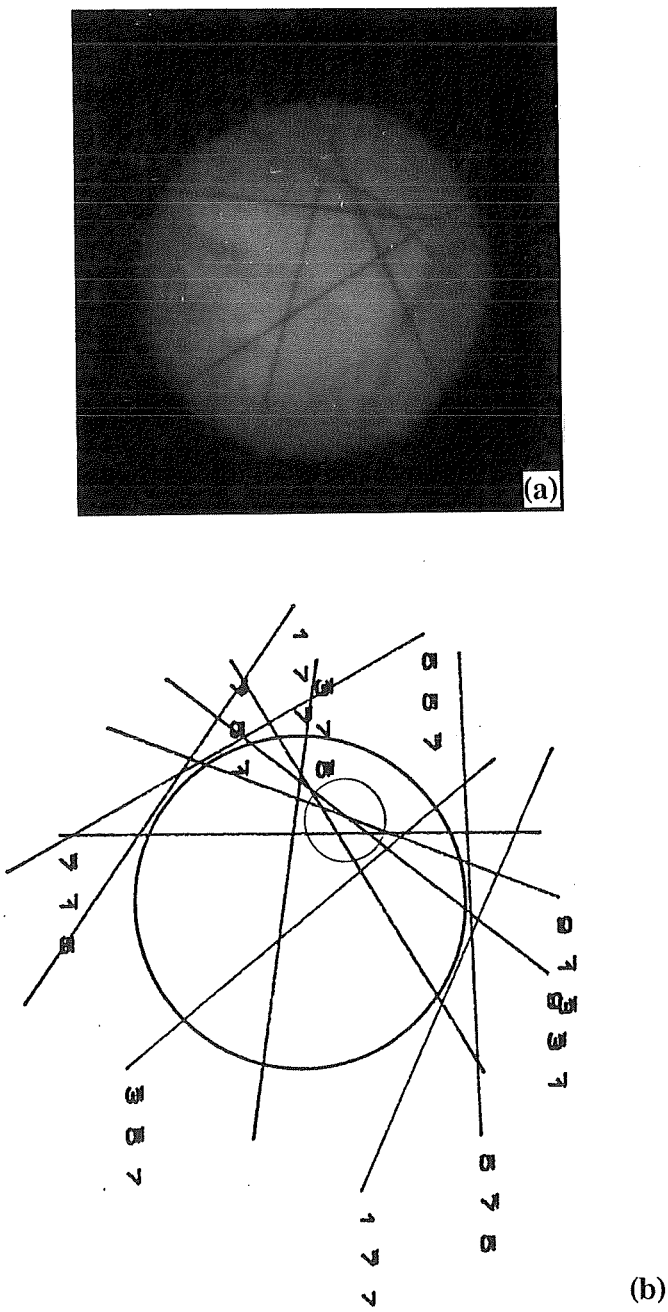

Figure 4 (a) HOLZ pattern obtained in the matrix far from SiC particle, (b) corresponding simulation pattern

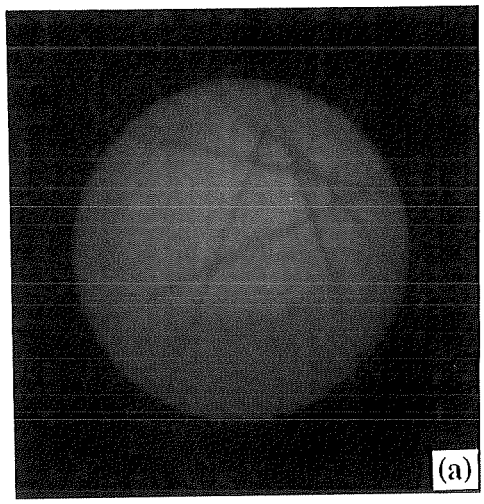

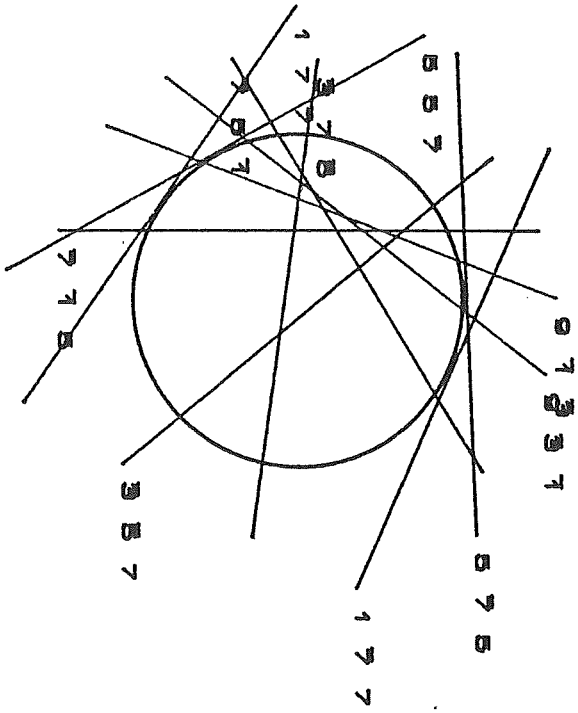

Figure 5 (a) HOLZ pattern obtained at position I,
(b) corresponding simulation pattern

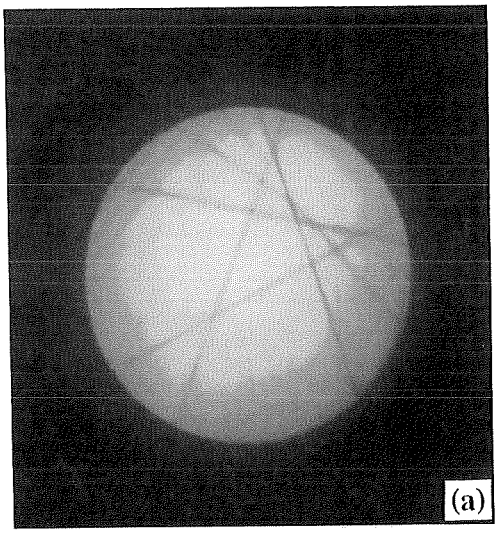

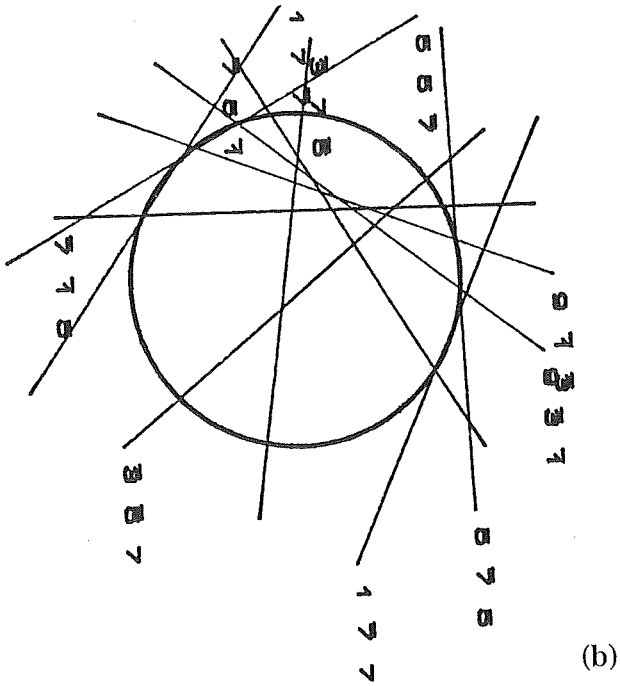

Figure 6 (a) HOLZ pattern obtained at position II,
(b) corresponding simulation pattern

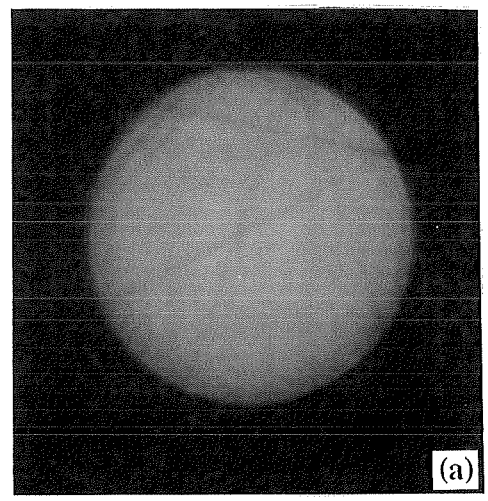

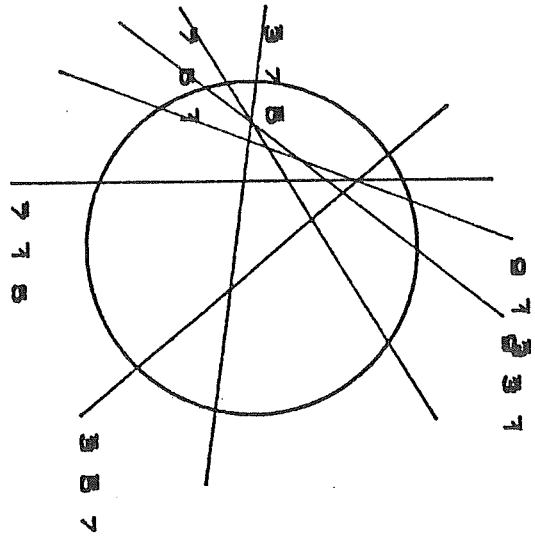

Figure 7 (a) HOLZ pattern obtained at position III,
(b) corresponding simulation pattern

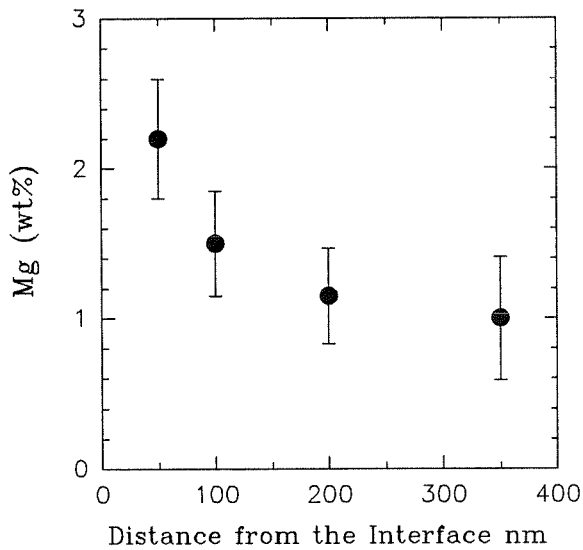

Figure 8 Mg concentration profile near the SiC particle (error bar indicating the statistical error)

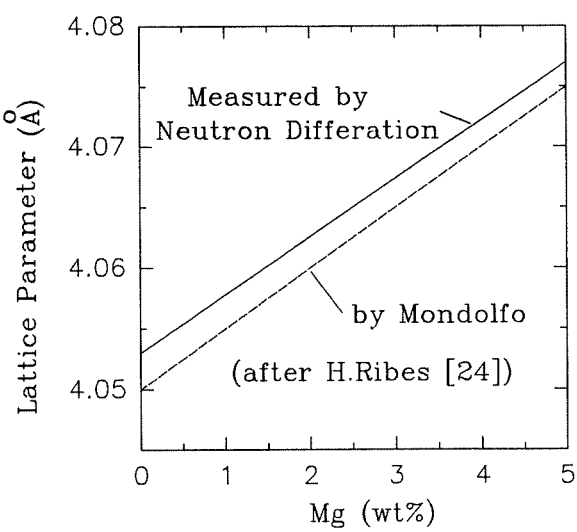

Figure 9 Relation between lattice parameter and Mg content in Al alloy

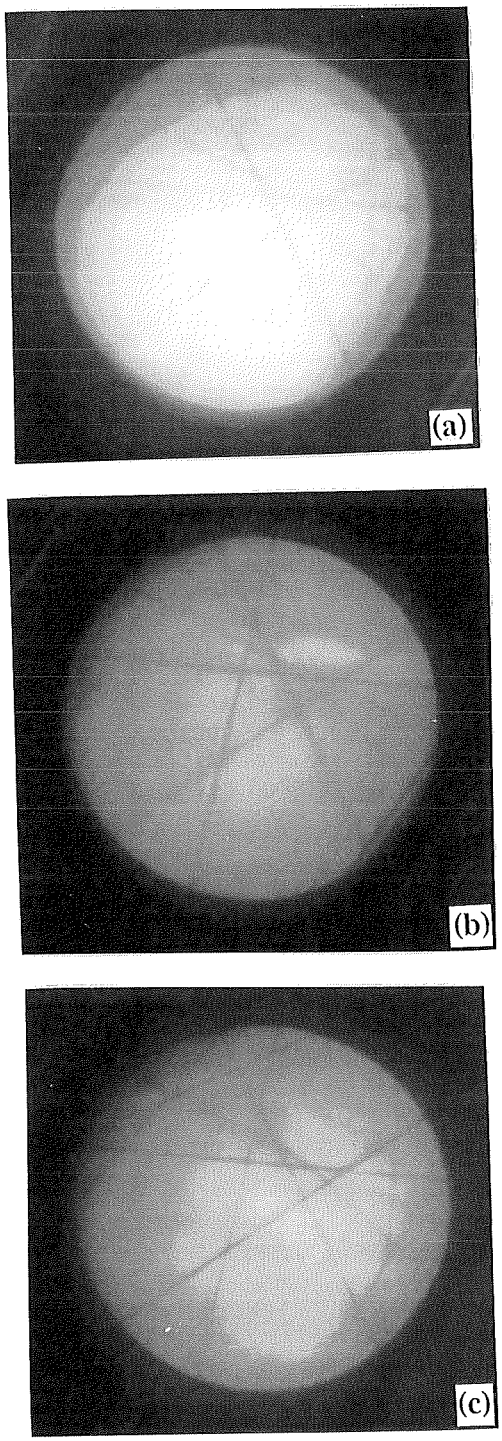

Figure 10 HOLZ patterns obtained individually at the position 0 nm (a), 50 nm (b), 100 nm (c) from the dislocation

2.6 Final Remarks on the Study of Interfaces in MMCs

This chapter, consisting of several papers, presented and discussed the nature of the interfaces between different particles and the aluminum matrices. In general, attack of SiC particles by liquid aluminum during fabrication is not observed. However, an interfacial reaction between the SiO_2 layer on the surface of the particles and the Mg in the matrix has occurred. The reaction between Al_2O_3 particles and the Mg in the 5083 aluminum matrix is very slow. As a result of interfacial reactions, a layer of fine MgO crystals with a size in the range of about 5-20 nm (and some $MgAl_2O_4$) is formed on the particles surface. The thickness of the reaction zone is about 30-50 nm for as-received SiC particles, 50-80 nm for Al_2O_3p and about 100-200 nm for the artificially oxidized SiCp (with 3.04wt% SiO_2). Since the interfacial reactions consume Mg, it is evident that the content of Mg in the matrix will vary with reinforcement type and reaction zone thickness. Segregation of Mg or Cu at the interfaces and large residual stresses in the matrix near the reinforcements have been found. The different nature of interfaces in different composites may cause a difference in the deformation and fracture behaviour of these composites. In the following chapter, the relationship between the nature of the interfaces and the deformation and fracture behaviour of the composites will be presented.

CHAPTER 3

DEFORMATION AND FRACTURE OF ALUMINUM MATRIX COMPOSITES

Introduction

In this chapter, the recrystallization behaviour of the composites during extrusion at high temperature and the deformation behaviour of the composites at different temperatures such as room temperature, 350°C and 550°C are presented. Strength mechanisms and fracture mechanisms for different composites deformed at various temperatures are discussed, and related to the interfacial nature of the composites reinforced by different particles. The deformation and fracture behaviour of the 5083 monolithic aluminum alloy and that of the as-cast composites are compared to that of extruded composites. Dynamic recovery in the 5083 monolithic aluminum alloy and dynamic recrystallization in different composites during the extrusion are discussed in section 3.1. The strengthening mechanisms of the composites deformed at various temperatures are presented in section 3.2. The section 3.3 presents the fractography and the fracture mechanisms of extruded and as-cast composites, and the monolithic aluminum alloy. Finally, the Portevin-Le Chatelier effect observed in tensile tests of the composites and of the 5083 aluminum alloy is presented. These four sections are

constituted of four papers, which have been accepted or submitted for publication.

3.1 Effect of Thermomechanical Processing on the Microstructure and Mechanical Properties of Al-Mg (5083)/SiCp and Al-Mg (5083)/Al_2O_3p Composites

Part I, Dynamic Recrystallization of the Composites

W.M. Zhong*, E. Goiffon**, G. L'Espérance*, M. Suéry** and J.J. Blandin**

* Ecole Polytechnique de Montréal, Centre de Caractérisation Microscopique des Matériaux $(CM)^2$, Case Postale 6079, Succ. "A", Montréal, Québec, Canada H3C 3A7

**Institut National Polytechnique de Grenoble, Génie Physique et Mécanique des Matériaux, GPM2, URA CNRS 793 ENSPG, B.P.46, 38402 St Martin d'Heres Cedex, France

Abstract

Three types of composites, reinforced by as-received SiC, artificially oxidized SiC or Al_2O_3 particles, were fabricated by a compocasting method and extruded at 480°C

with an extrusion ratio of 16:1. Extrusion of these composites causes large scale dynamic recrystallization resulting in a fine matrix microstructure. The extrusion increases not only the ultimate tensile strength (UTS), but also the elongation to fracture of the composites. In the first part of our series of three articles, the microstructure of as-cast composites, extruded composites and extruded monolithic 5083 aluminum alloy is studied. The effects of reinforcing particles and other parameters on the dynamic recrystallization behaviour of the composites are discussed.

1. Introduction

Many whisker or particle reinforced metal matrix composites are thermomechanically processed by extrusion, because it can improve their microstructure and ductility [1-4]. Extrusion can reduce particle clustering, make the distribution of the particles more uniform, although it can also cause particle alignment along the extrusion direction [2,5] and possibly fracture of whiskers and particles [2,6]. Further improvement in particle distribution and some reduction in particle size (particle cracking) have also been observed with large extrusion ratios (larger than 40:1) [1]. As reported by Brusethaug et al. [1], the strength (UTS) of extruded A356/SiCp composites is similar to that of as-cast composites, but the ductility is significantly increased. Osman et al. [2] reported that both UTS and yield strength were not significantly affected by extrusion in 2080/SiCp composites. Similar results were also obtained by Lloyd [7] in

A356/SiCp composites. Brusethaug et al. [1] compared the grain structure of extruded composites (A356/SiCp, 15 vol.%, 20 μm) with that of extruded unreinforced materials. For the reinforced materials, the extruded grain structure was an equiaxed, recrystallized structure (cooled in air) and relatively more independent of the extrusion temperature compared to the monolithic alloy. They indicated that SiC particles appeared to have a large influence on the recrystallization kinetics since the grain size in the extruded composites was 40-50 μm and that recrystallization of the extruded unreinforced alloys was not completed. L'Esperance et al. [8] reported that whiskers in 2124/Si_3N_4w composites could limit grain growth during superplastic deformation at high temperature. Cho et al. [9] obtained a very fine grain structure (smaller than 0.18 μm) in the Al-4 wt% Mg/Al_2O_3 (5 vol.%, 10.5 μm) and Al-4 wt% Mg/$MgAl_2O_4$ materials which were fabricated by powder metallurgy and then extruded at 380°C with an extrusion ratio of 36:1. Tensile properties were 676 MPa (UTS) and 3.5% (elongation) for the composites reinforced by Al_2O_3 particles, and 741 MPa (UTS) and 4.5% (elongation) for the composites reinforced by $MgAl_2O_4$ particles. The UTS was 662 MPa for the monolithic alloy. Nagwgawa and Gungor [10] found that extrusion not only increased the tensile elongation, but also increased the yield strength and UTS of 6061/Al_2O_3p (15 vol.%) composites.

The effect of Mg concentration on the dynamic recrystallization of Al-Mg alloy during thermomechanical processing has been studied by Sheppard et al. [11-12] and Hales and McNelley [13]. The structure of an extruded Al-5 wt% Mg alloy only

partially recrystallized when extruded at 450°C and with a ratio of 40:1 [11-12]. The recrystallized fraction increases with increasing solute content because Mg solute hinders the motion of dislocations and recovery becomes more difficult. When a large number of dislocations cluster at obstacles constituted by other dislocations or insoluble particles, to form tangles of dislocations, more energy is stored and more recrystallization nuclei are formed. McQueen et al. [14] found that dynamic recrystallization could take place in the 5083 Al alloy at 400-500°C deformed in torsion. The grain size was about 10-18 μm and the insoluble particles in the alloy (>0.6 μm) were believed to enhance nucleation of recrystallization.

The role of reinforcing particles on the extrusion microstructure of the 5083 Al matrix composites is still not well understood. In fact, no research on this type of composite, especially, when fabricated by compocasting was reported in the literature. The relationship between the microstructure and mechanical properties is also not clear. The aim of this work was therefore to study the effect of reinforcing particles and other parameters on the dynamic recrystallization behaviour of these composites during extrusion.

2. Experimental Procedures

2.1 Fabrication of the Composites

The composition of the 5083 matrix is given in table I. The 5083 Al alloy is a solid solution hardening and weldable alloy. It has moderate strength, good corrosion resistance and superplastic potential [15].

Table I Composition of the 5083 matrix alloy

	Mg	Mn	Cr	Fe	Si	Cu	Ti	Al
wt%	4.1	0.56	0.12	0.19	0.15	0.04	0.02	balance

A modified compocasting technique was used to fabricate the composites [16]. After incorporation of the particles into the vigorously agitated semi-solid alloy at temperatures ranging from 600 to 640°C, the material was completely remelted at 720°C for about 5 min. and then solidified under a pressure of 100 MPa in a steel mould. Three types of particles (all with a mean diameter of about 13 μm) were used to fabricate the composites: as-received SiC (from PRESI, France), oxidized SiC and Al_2O_3 (from ESK, German). The artificial oxidation was carried out in air at 1100°C. The amount of SiO_2 on the surface of the SiC particles was 3.04 wt% as measured by wet chemical analysis. 15 vol% particles were incorporated in the composites.

2.2 Thermomechanical Processing of the Composites

The ingots with an average diameter of 50 mm and a height of 100 mm were first homogenized at 450°C for 4 hours, then at 540°C for 12 hours and finally quenched in

water. The homogenized ingots were extruded at 480°C with an extrusion ratio of 16:1 and cooled in air. The final diameter of the extruded bars was 15 mm. Specimens for microstructural characterization were cut from the extruded bars in sections perpendicular and parallel to the extrusion direction. Grain size, dislocation structure and particle distribution of extruded composites were examined and compared with those of unreinforced extruded materials and as-cast composites.

2.3 Material Characterization

Scanning electron microscopy (SEM) and transmission electron microscopy (Philips CM30 and JEOL 2000FX) equipped with energy dispersive X-ray and electron energy loss spectrometers (EDS and EELS) were used. The samples for TEM observations were mechanically polished to 200 μm, then dimpled to 20-30 μm, and finally thinned by ion beam sputtering (5 kV at a tilt angle of 12-15°). Grain boundary misorientation was determined by convergent beam electron diffraction (CBED), selected-area diffraction (SAD) and Kikuchi patterns. Weak beam dark field imaging was used to study the dislocation structure in the matrix. Barker's reagent was used to etch samples for optical observation.

All acronyms used in our series of three papers were designated to indicate the state of the particles prior to their incorporation in the composites and the state of the composites (i.e. as-cast or extruded). For example, sample AOX3 means that the sample

was as-cast (A) and the particles were oxidized (OX) 3.04 wt % and sample AOX3E means that the same composite was extruded (E). A list for all the acronyms used can be found at the end of the paper.

3. Results and Discussion

3.1 Microstructure of As-cast Composites

As-cast composites have a dendritic microstructure with an average grain size of about 150 μm. Reinforcing particles are mainly distributed along the dendritic boundaries with some of them existing between the dendrite arms as shown in figures 1(a)&(b). A recovered structure was observed in the matrix by TEM (see figure 2), which is probably caused by the thermal stresses resulting from the difference of the thermal expansion coefficient of the matrix and that of the particles.

The nature of the interface between the matrix and different reinforcements was previously characterized [17,18]. This work showed that in as-cast composites with SiCp, attack of the reinforcement by liquid aluminum is not observed due to the short period of time (about 5 min.) at which the composite is at high temperature (720 °C) during fabrication. Because of the reaction between either Al_2O_3 particles or the SiO_2 layer on the surface of oxidized SiC particles with Mg from the matrix, fine MgO

crystals (5-20 nm) are formed at the interface between the matrix and the reinforcing particles. The thickness of the reaction zone is about 30-50 nm for as-received SiC particles (which were slightly oxidized during fabrication of particles), 50-80 nm for Al_2O_3p and increases to about 100-200 nm for artificially oxidized SiCp. Because the interfacial reactions consume Mg, the Mg content in the matrix decreases. The reaction between artificially oxidized SiCp and the matrix consumes more Mg (about 2.5 to 3 wt% Mg remain in the matrix), owing to the thicker reaction zone. About 3.6 to 3.9 wt% Mg remains in the composites reinforced by Al_2O_3 or by as-received SiC particles (for details see [17,18]). Additional interfacial reactions were not observed in the extruded composites because diffusion required for interfacial reactions to occur is slow in the solid state.

3.2 Microstructure of Extruded Monolithic Alloys

The 5083 aluminium alloy was extruded at 480°C with an extrusion ratio of 16:1. Some equiaxed recrystallized grains with an average size of 50 μm are observed in figure 3. TEM micrographs show that most parts of the sample exhibit a recovered structure and the misorientation between the subgrains is less than 3° (figures 4(a)&(b)). Many of the subgrains are elongated and contain a large density of dislocations and have poorly developed internal subboundaries. In addition, the size of the subgrains is not uniform. This is typical of a dynamically recovered structure [11,14]. Grains with large misorientations such as 19°, 30° and 40° are occasionally observed (see table II); they

are more easily found near large insoluble (Cr, Fe, Mn)-rich particles (about 1 μm) as shown in figure 5. This microstructure is similar to those observed by Sheppard et al.[11,12] and McQueen et al.[14]. According to the results of Sheppard et al., aluminum alloys with 2 or 3 wt% Mg recover dynamically during extrusion and recrystallise partially with 5 wt% Mg. Only when the Mg concentration rises to 7 wt% that the extrudate recrystallizes almost completely even though some alloying elements such as 0.8Mn, 0.17Fe and 0.12Cr (wt%) were added in all the alloys. Mg solute atoms are believed to hinder the motion of dislocations which limits recovery and increases the stored energy for recrystallization. Another explanation for the effect of Mg on the dynamic recrystallization is that Mg reduces the stacking fault energy [19], thus increasing the stacking fault width. The mobility of dislocations is limited and the driving force for dynamic recrystallization is increased. However, as suggested by both Sheppard et al. [11,12] and McQueen et al. [14], it is not obvious that Mg can reduce the stacking fault energy. Moreover, the methods used to estimate the changes in stacking fault energy are not believed to be sufficiently precise. In a comparison of the extruded microstructure of a super-pure Al-5Mg alloy (wt%) with that of a commercial Al-5Mg-0.8Mn alloy, only dynamic recovery is observed in the super-pure alloy. Conversely, in the commercial alloy, partial dynamic recrystallization occurs [11]. It appears that the large insoluble inclusions play a much more important role in promoting dynamic recrystallization in Al-Mg alloys [11,14]. In fact, even using the weak beam technique with an image resolution of 1.5 nm, generally used to evaluate the stacking-fault energy in many alloys with low stacking fault energy [19,20], we did not find any

evidence of extended dislocations or stacking faults in our materials. Moreover, in alloys with a much higher Mg content (e.g. 10 wt%), extended dislocations or stacking faults were not observed by Hales et al. [13]. Therefore, the effect of Mg solute on the stacking fault width does not seem very large and requires to be quantified more precisely. In our work, the Mg content in the 5083 Al alloy is about 4.1 wt%. Although our extrusion conditions are not exactly the same as those used by Sheppard et al. [11,12] and McQueen et al. [14], the alloy is still mainly softened by dynamic recovery. Only some large insoluble (Cr, Fe, Mn)-rich particles (about 0.6 - 1 μm) can induce nucleation of dynamic recrystallization although some of the newly formed grains in our samples may come from recrystallization during cooling in air from the extrusion temperature. This is because large inclusions can effectively resist local material flow, cause a large lattice distortion and produce a much higher stored energy to nucleate recrystallization [21].

3.3 Microstructure of Extruded Composites

The distribution of the particles as shown in figure 6(a) is much more uniform after extrusion, although alignment of the particles along the extrusion direction is observed. Some of the particles were cracked in the direction perpendicular to the extrusion direction (figure 6(b)). A large number of fine, equiaxed and highly misoriented (see Table II) grains are seen in the TEM micrographs in figures 7(a)&(b) (the average grain size is about 5 μm). These grains are not well developed and exhibit

a high dislocation density (see figure 8). The dislocation density in as-extruded composites ($4.9*10^{14}/m^2$) is twice that in as-cast composites ($2.4*10^{14}/m^2$) as estimated by measurements from TEM thin foils (the measurement error can be as large as 30%, see part II for details). Neither the grain size nor the dislocation density inside the grains is uniform. The grain size varies from 1 μm to 10 μm. Some grain boundaries (or subboundaries in a grain) show a serrated appearance as shown in figure 9(a) (arrows A&B) and figure 10, which may be caused by strain-induced boundary migration (SIBM) [19]. Subboundaries or dislocation walls are also observed inside grains (see figures 7 & 9). All these observations indicate that dynamic recrystallization has occurred during extrusion.

Near particles, some grains or subgrains are smaller than 1 μm (see figures 11(a)&(b)). In the matrix, a recovered substructure is also occasionally found (figure 9(a)), although most of the matrix has recrystallized. Small (Fe, Mn)-rich particles (about 0.1-0.2 μm) are observed inside the grains and at the grain boundaries (figures 9(a)&(b), arrows C&D). The movement of the grain boundaries may be pinned by these small particles [12]. In comparison with the results obtained from the monolithic alloy (see figures 3 & 5), reinforcing particles in composites strongly enhance the rate of dynamic recrystallization in the matrix and produce fine recrystallized grains during extrusion. The large reinforcing particles, such as large inclusions, impede metal flow and localize deformation. The mobility of the dislocations is also affected. Thus, there will be more stored energy and more favourable nucleation sites for recrystallization

[21]. Besides nucleating near SiCp, recrystallization may nucleate at the junction of grain boundaries (see arrowed grain in figure 12). This small newly formed grain shows only few dislocations. This may be explained by either static recrystallization during cooling from the extrusion temperature or dynamic recrystallization at the end of extrusion. Large insoluble (Cr, Fe, Mn) rich particles can still cause nucleation. The recrystallized grains are also prevented from rapid growth by these particles.

Table II Misorientations between Different Regions Obtained from TEM Thin Foils

Sample	Figure No.	Regions	Misorientation (°)
5083E	Figure 5	1&2 1&3 2&3 3&4	30 30 40 19
AOX3E	Figure 7	1&2 1&3 1&4 2&4 2&5 3&4 4&5	30 12 14 27 45 19 27
AOX3E	Figure 10	1&2	19
ARSE	Figure 11	1&4 2&5	32 19

Although, as discussed above, the relatively lower Mg concentration in the matrix of the composite reinforced by oxidized SiC particles (3.04 wt% SiO_2, AOX3E) caused

by the thicker reaction zone may decrease the recrystallized fraction [11,12], there is no obvious difference in the microstructure of the composites reinforced with different particles. This is because the effect of the variation of matrix composition (about 0.7-0.8 wt% difference) is small and the recrystallization is mainly controlled by the reinforcing particles. Another possibility is the relatively large error associated with our limited number of measurements made for each sample and the large variation of grain size observed in a given sample.

The effect of particles on recrystallization of composites can be evaluated quantitatively. Humphreys et al. [21,22], suggested a relation to calculate the recrystallized grain size (D), assuming that each reinforcing particle nucleates one grain:

$$D = d_p[(1-V_f)/V_f]^{1/3} \ldots\ldots (1)$$

Here, d_p is the particle diameter and V_f is the volume fraction of the particles. For composites with an average particle size of 13 μm and a volume fraction of 15 vol%, the calculated grain size is 23 μm. In our samples, several grains are usually found around each particle and the average grain size is only about 5 μm, indicating that one particle nucleates several grains. This may be caused by the different nature of the reinforcing particles, the different matrix composition and hot-working conditions in our work. Thus, relation (1) may underestimate the nucleation rate in our case.

Other factors which may affect the nucleation of recrystallization are the matrix composition and extrusion conditions, including extrusion temperature, extrusion ratio and extrusion rate. As discussed above, high Mg contents may promote dynamic recrystallization and nucleation near the reinforcing particles. Further work is necessary in order to optimize these conditions for the 5083 aluminum matrix composites studied here.

4. Conclusions

5083 aluminum matrix composites, reinforced by as-received SiC, artificially oxidized SiC or Al_2O_3 particles, were extruded at 480°C with an extrusion ratio of 16:1. The main results of the work can be summarized as follows.

1) In as-cast composites, a partially recovered structure was observed inside the dendritic grains. This may be caused by the thermal stresses resulting from the difference between the thermal expansion coefficient of the matrix and that of the particles.

2) The microstructure in the extruded monolithic 5083 aluminum alloy is characterized by a recovered structure. Occasional recrystallization is induced by the large insoluble particles in the alloy. The average grain size of the extruded alloy is about 50 μm.

3) Large scale dynamic recrystallization is observed in all the extruded composites studied with an average grain size of about 5 μm. Reinforcing particles enhance the nucleation of recrystallization.

4) The composites reinforced by different particles have a similar matrix microstructure. The different interfacial reactions observed in the various as-cast composites have no apparent effect on the recrystallization behaviour. The interface in as-extruded composites was found to be similar to that in the as-cast composites.

List of Acronyms

ARS - 5083/SiCp, as-cast with as-received SiC particles

AOX3 - 5083/SiCp, as-cast with artificially oxidized SiC particles

ARO - 5083/Al_2O_3p, as-cast with Al_2O_3p particles

5083E - extruded 5083 Al alloy

ARSE - extruded ARS composite

AOX3E - extruded AOX3 composite

AROE - extruded ARO composite

References

1. S. Brusethaug, O. Reiso, W. Ruch, Proc. of Fabrication of Particulate Reinforced Metal Composites(1990), Montréal, edited by J.Masounave and F.G.Hamel, p.173

2. T.M. Osman, J.J. Lewandowski, W.H. Hunt Jr., Proc. of Fabrication of Particulate Reinforced Metal Composites(1990), Montréal, edited by J.Masounave and F.G.Hamel, p209

3. D.L. Mcdanels, Metall. Trans. A, vol.16, No.6(1985), p.1105

4. W.H. Hunt Jr., O. Richmond, R.D. Young, Proc. ICCM6, vol.2(1987), p.2.209

5. D.L. Davidson, Metall. Trans. A, vol.22(1991), p.113

6. Y.L. Lin, N. Hansen, D.J. Jensen, H. Lilholt, P. Nielsen, N.J. Fei, Advances in Powder Metallurgy, vol.3(1989), p.461

7. D.J. Lloyd, Metal Matrix Composites-Processing, Microstructure and Properties, Proc. 12th. Risϕ Symp., Denmark(1991), p.81

8. G. L'Esperance, T. Imai and B. Hong, Superplasticity in Advanced Materials, edited by S. Hori, M. Tokizane and N. Furushiro, Japan, 1991, p.379

9. J.S. Cho, S.I. Kwun, Scripta Metall. et Mater., vol.27(1992), p.789

10. A.H. Nakagawa, M.N. Gungor, Fundamental Relations between Microstructure and Mechanical Properties of MMCs, eds. P.K. Liaw, 1990, p.127

11. T. Sheppard, N.C. Parson and M.A. Zaidi, Metal Sci. vol.17, No.10(1983),

p.481

12. T. Sheppard, M.G. Tutcher, Metal Sci. vol.14, No.12(1980), p.579

13. S.J. Hales, T.R. McNelley, Acta. Metall. vol.36(1988), p.1229

14. H.J. McQueen, E. Evangelista, J. Bowles, G. Crawford, Metal Sci. vol.18, No.8(1984), p.395

15. Metal Handbook, A.S.M., 9th Edition, vol.2(1979)

16. H.Ribes, R.D.Silva, M.Suéry, T.Bretheau, Mater. Sci. and Tech., July(1990), Vol.6, p.621

17. W.M. Zhong, G. L'Esperance, M. Suery, "Interfacial Reactions in 5083/SiCp Composites During Fabrication and Remelting", (accepted for publication in Met. Trans.)

18. W.M. Zhong, G. L'Esperance, M. Suery, "Interfacial Reactions in 5083/Al_2O_3p Composites During Fabrication and Remelting", (accepted for publication in Met. Trans.)

19. A.R. Jones, Grain Boundary Structure and Kinetics, American Socciety for Metals, 1980, p.373

20. K. Gardner, R. Grimes, Mater. Sci., vol.13(1979), p.216

21. F.J. Humphreys, Proc. 9th. Risφ Symp, ed. S.I. Anderson, H. Lilholt, and D. B. Pederson, Denmark(1988), p.51

22. W.S. Miller, F.J. Humphreys, Scripta Metall. et Mater, vol.25(1991), p.33

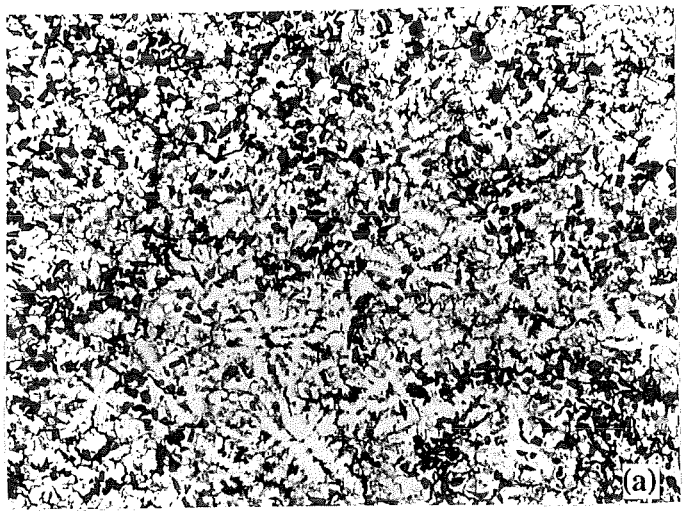

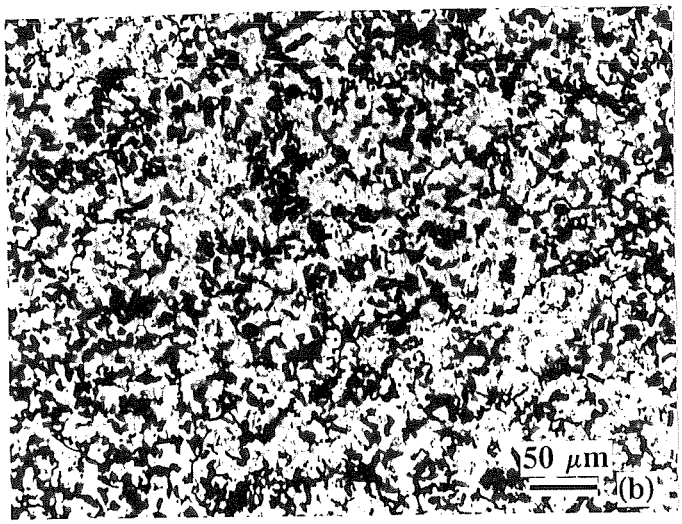

Figure 1 Optical Micrographs, **(a)** As-cast 5083/SiCp (ARS), **(b)** As-cast 5083/SiCp (oxidized 3.04%, AOX3). Samples Etched in Kelly's Reagent

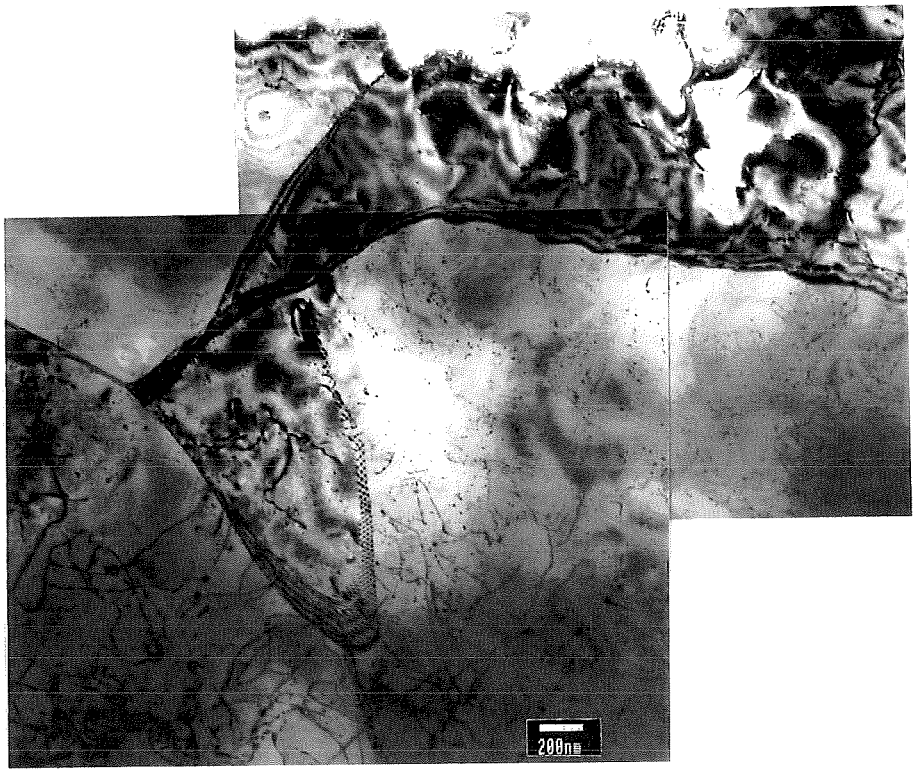

Figure 2 TEM BF Images of Subboundaries in As-cast Composites (ARS)

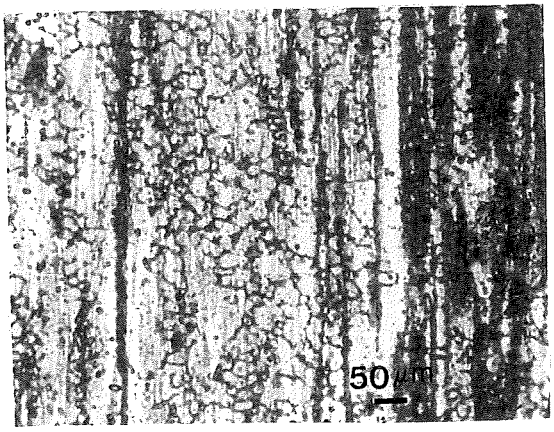

Figure 3 Microstructure of Extruded 5083Al Alloy (5083E, SEM)

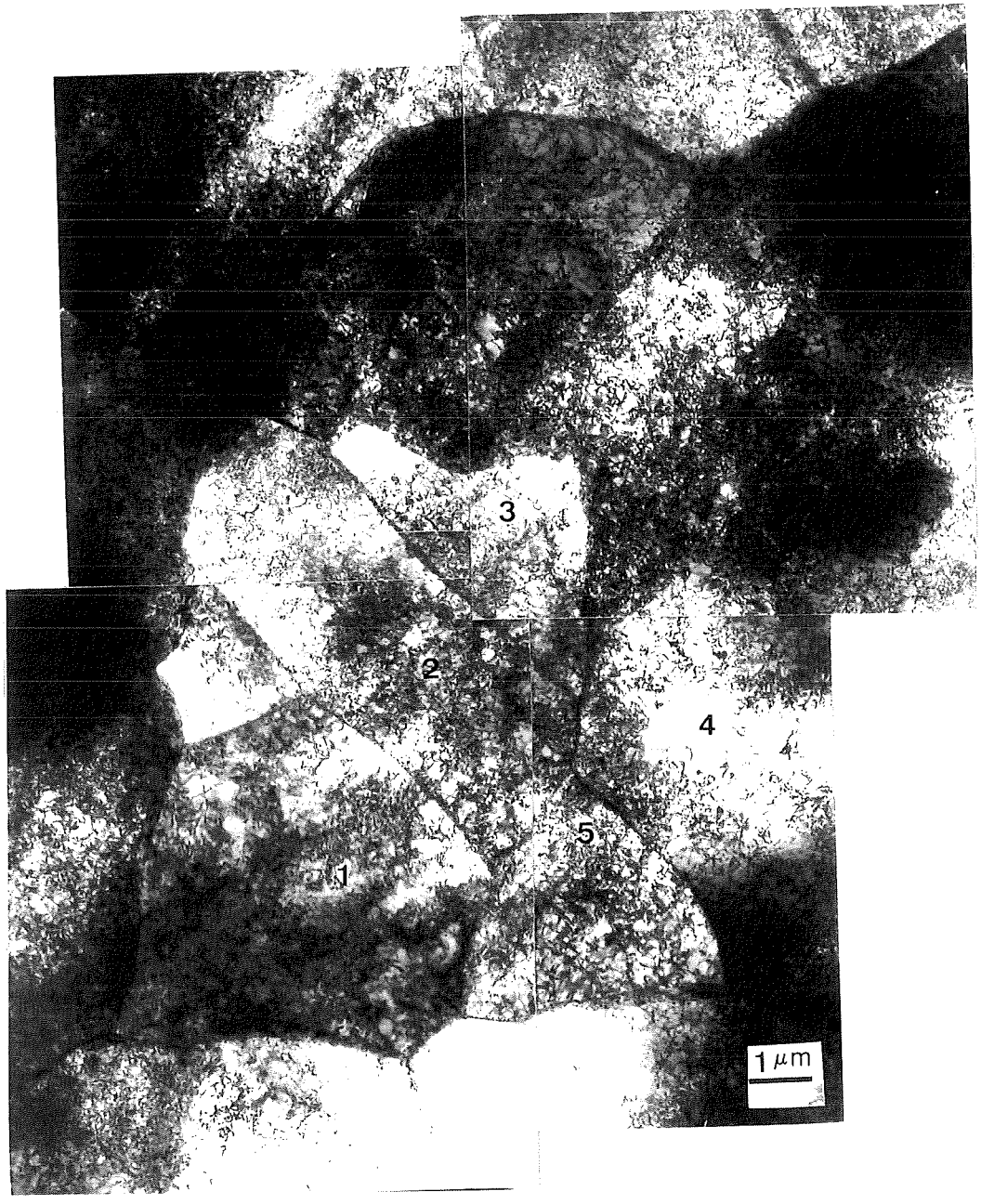

Figure 4 (a) TEM Image Showing the Subgrains in Extruded 5083Al Alloy (5083E)

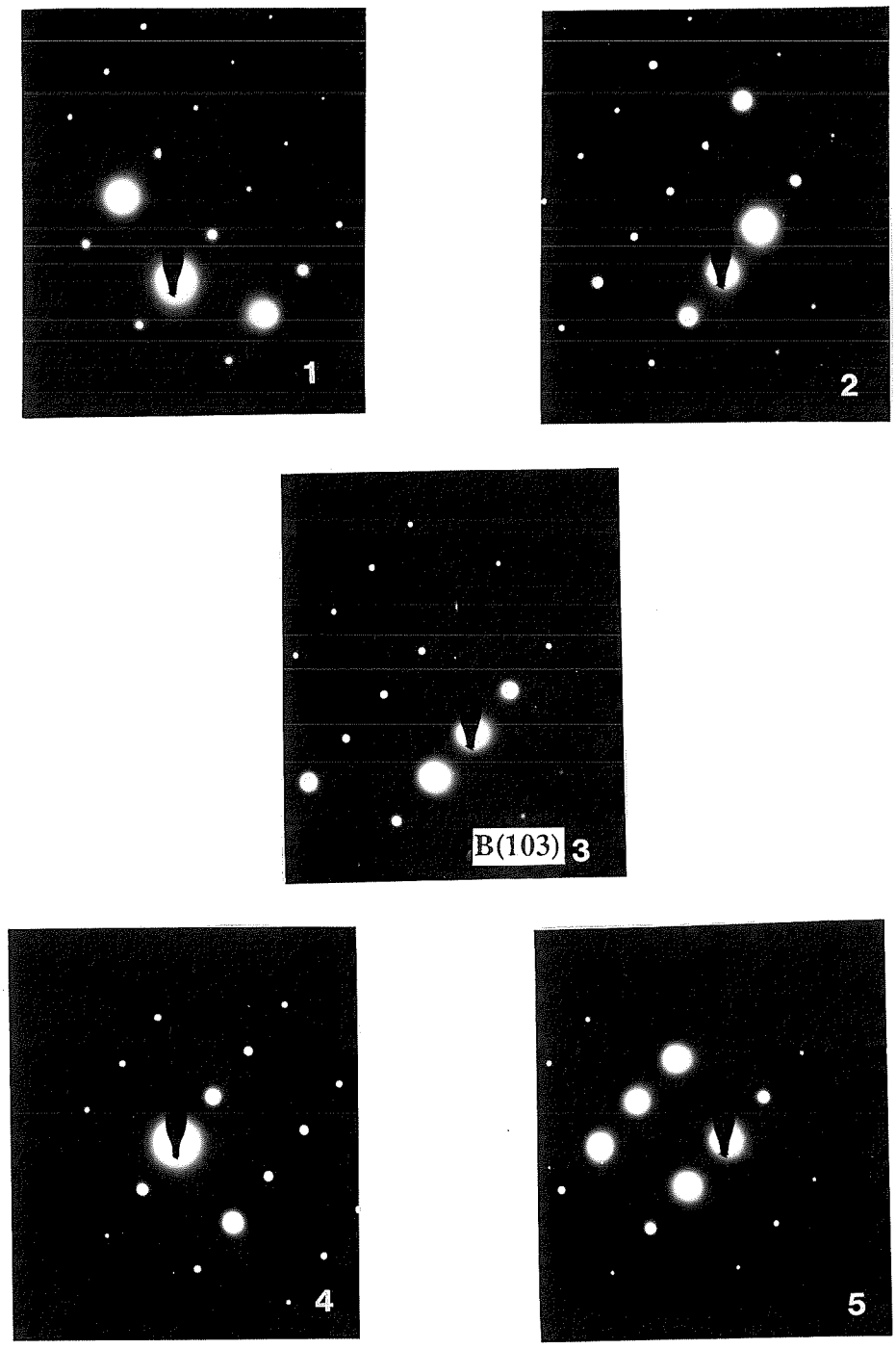

Figure 4 (b) Corresponding SAD Patterns Obtained From the Different Regions Shown in Figure 4(a)

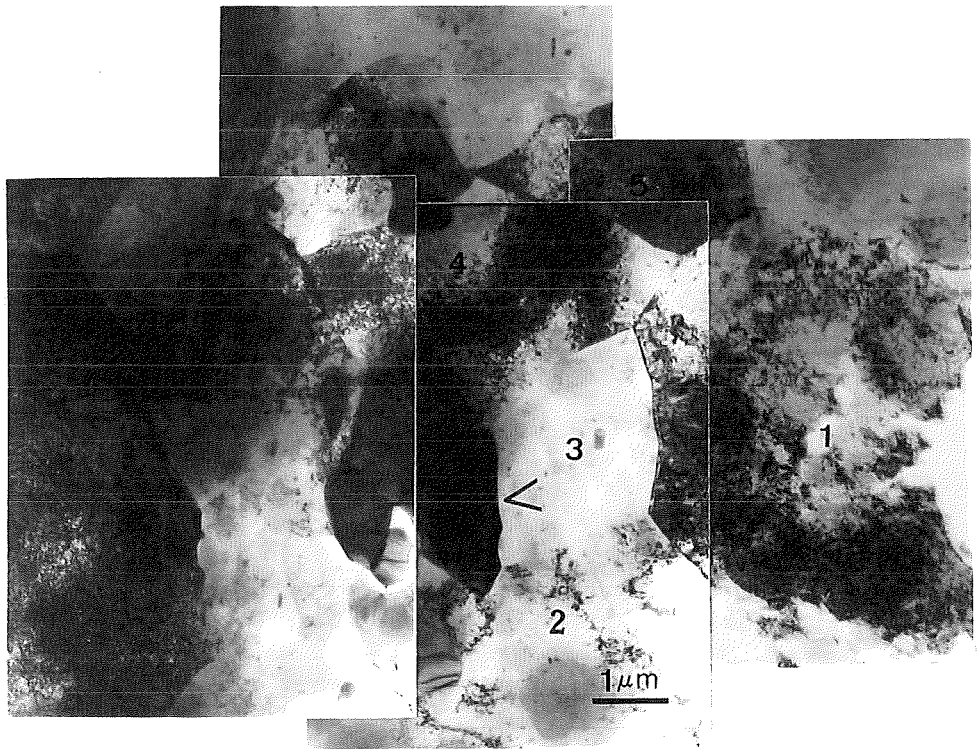

Figure 5(a) Recrystallized Structure Formed Near Large Insoluble Inclusions (arrow) in Extruded Monolithic Alloys (5083E)

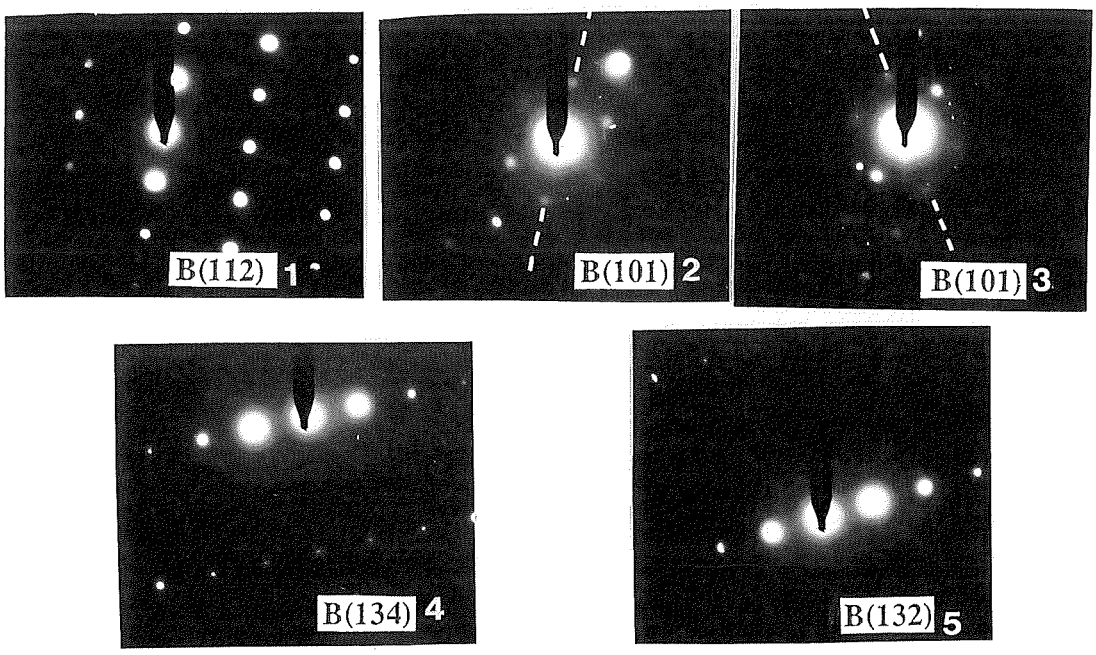

Figure 5(b) Corresponding SAD Patterns

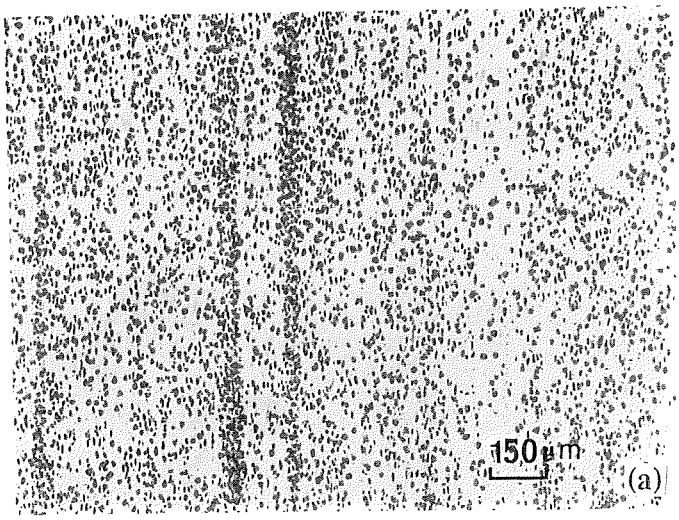

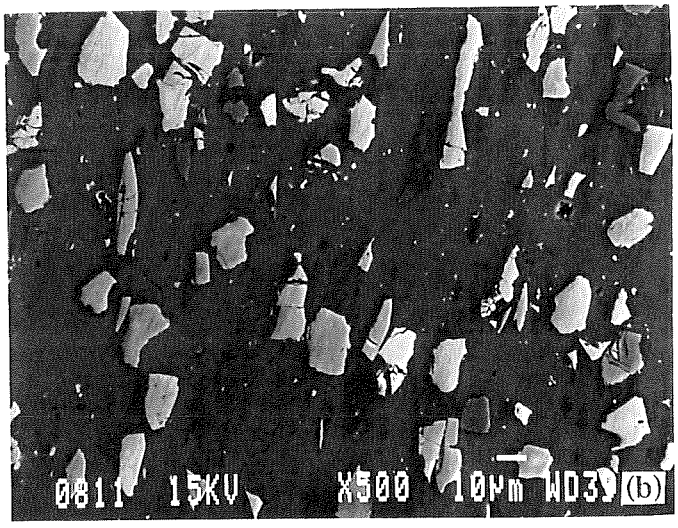

Figure 6 (a) Distribution of Particles after Extrusion (longitudinal section)
(b) Cracked Reinforcing Particles after Extrusion (extruded 5083/SiCp, ARSE)

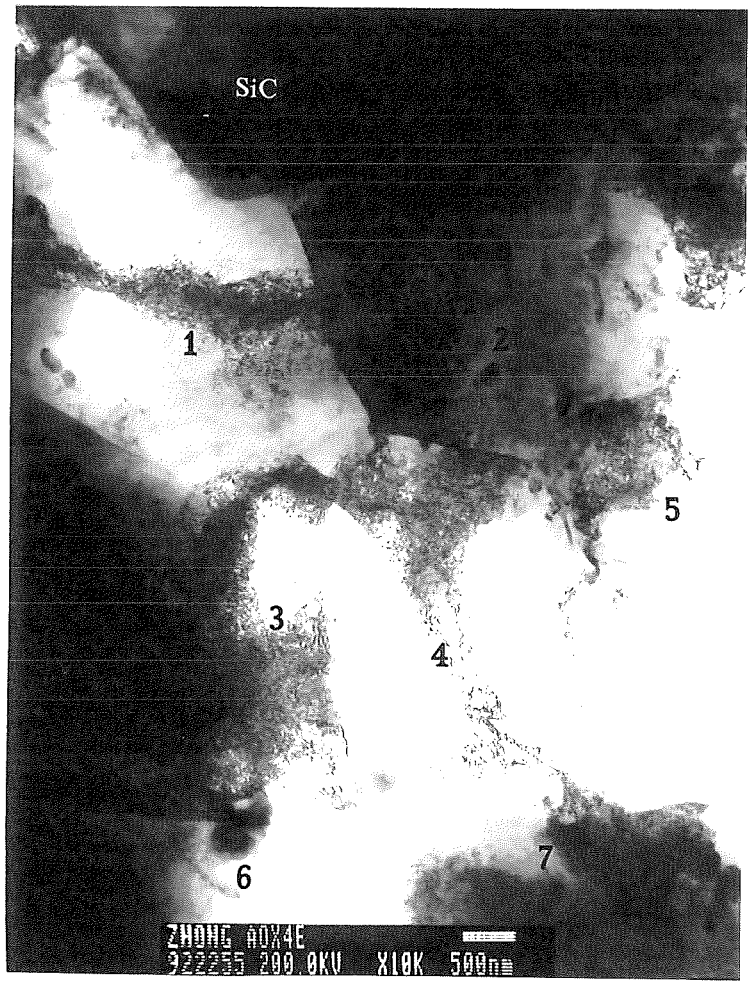

Figure 7 (a) Equiaxed Structure Near a SiC Particle in an Extruded Composite (AOX3E)

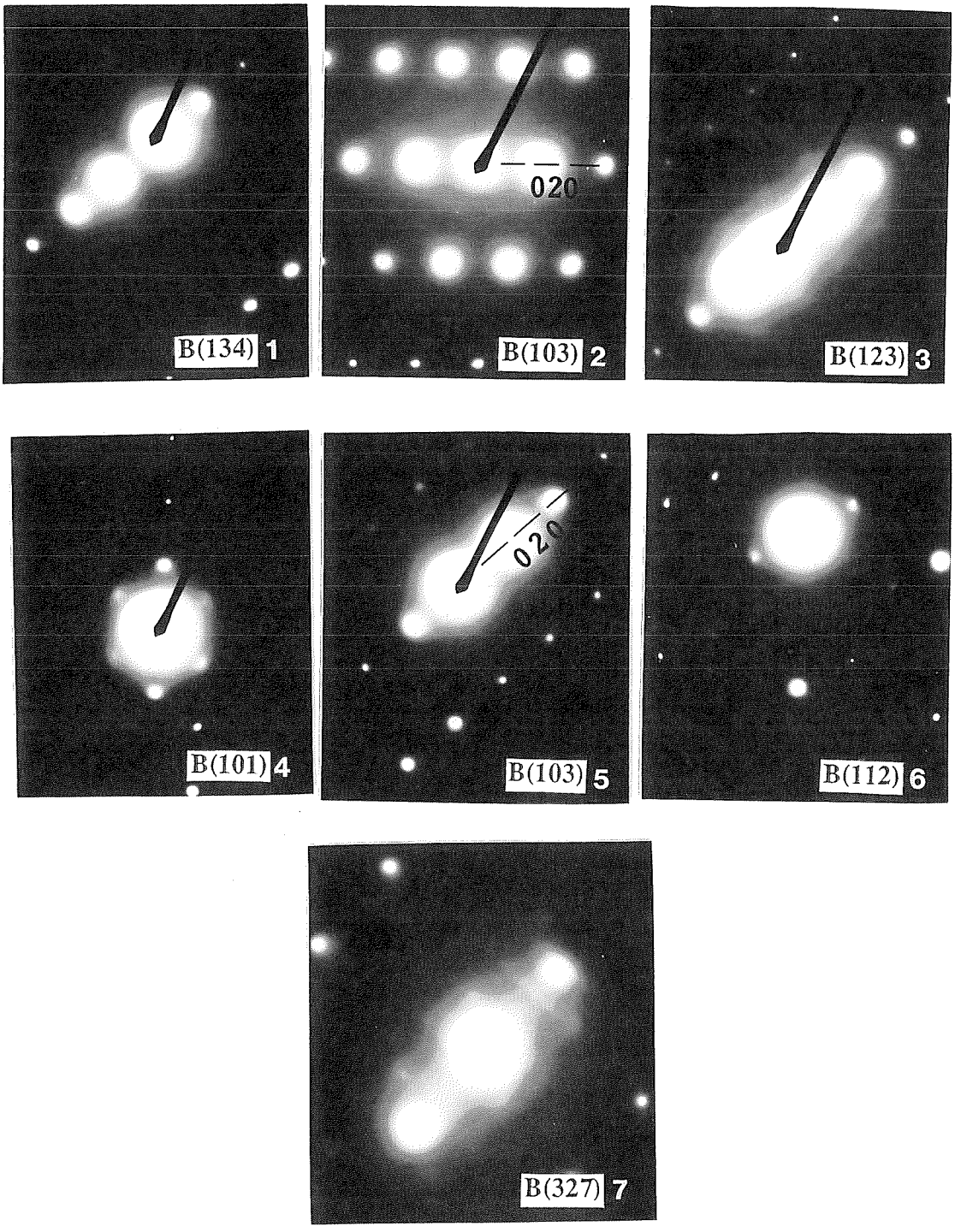

Figure 7 (b) Corresponding SAD Patterns (AOX3E)

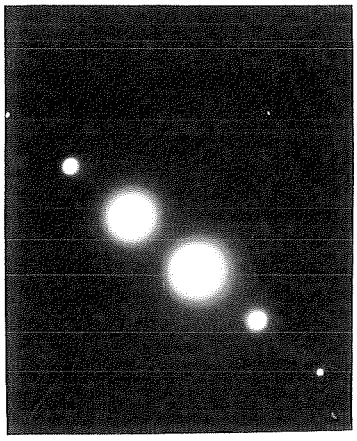

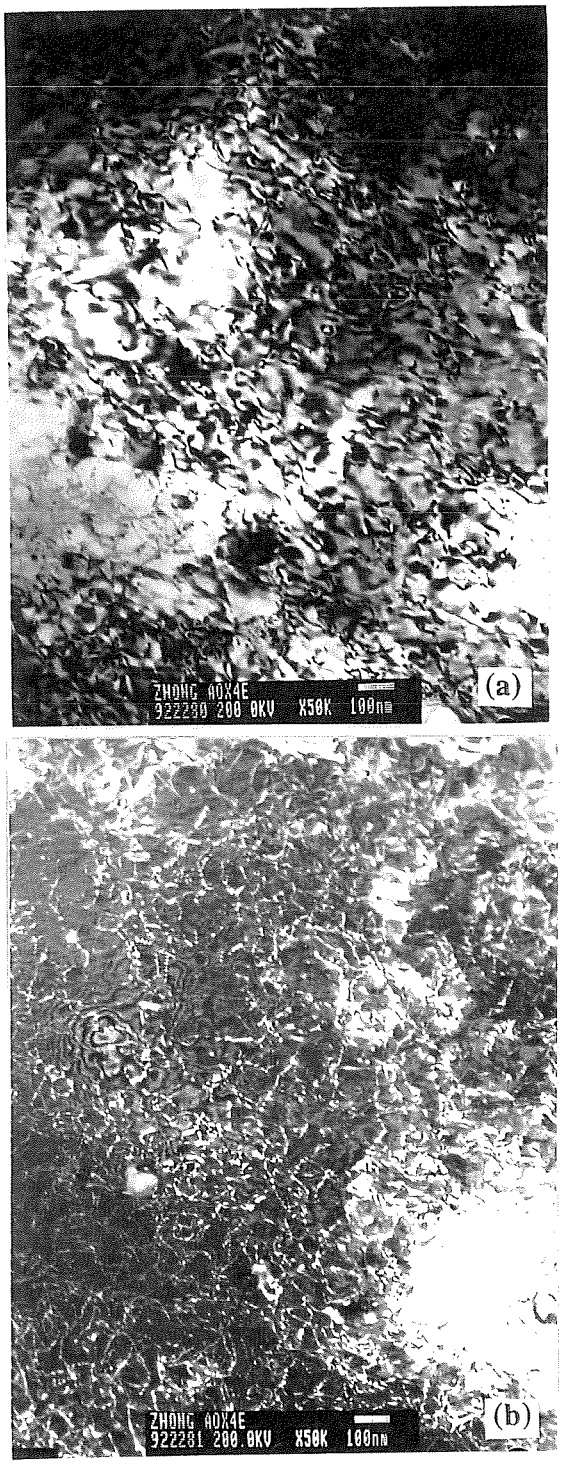

Figure 8 (a) TEM Bright Field (BF) Image of Dislocations in an Extruded Composite, (b) Weak Beam DF Image (g_{111},g/3g) (AOX3E)

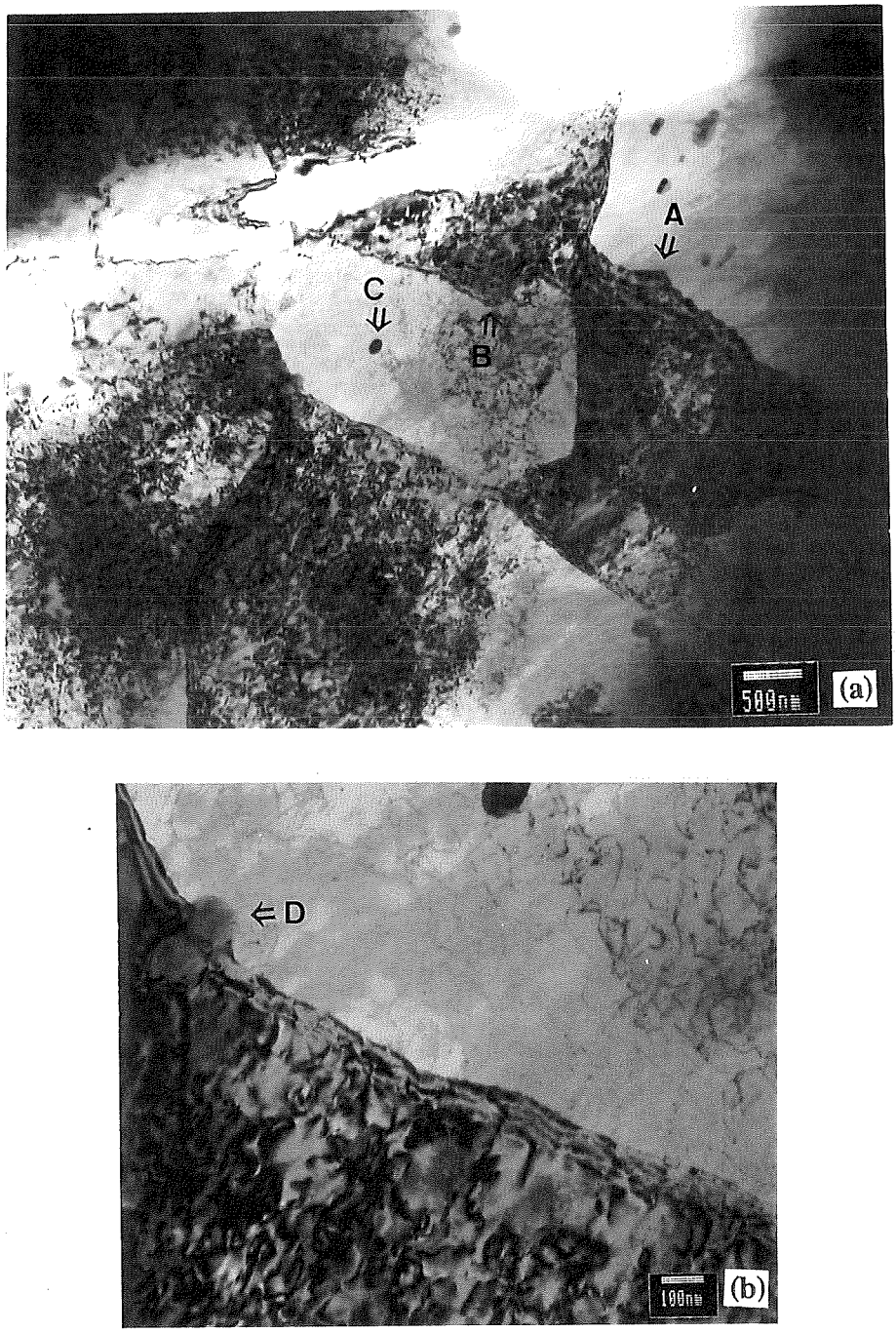

Figure 9 (a) Elongated Structure in Extruded Composites (AOX3E), (b) A Boundary Observed at Higher Magnification (arrows A&B showing serrated boundaries, C&D showing inclusions)

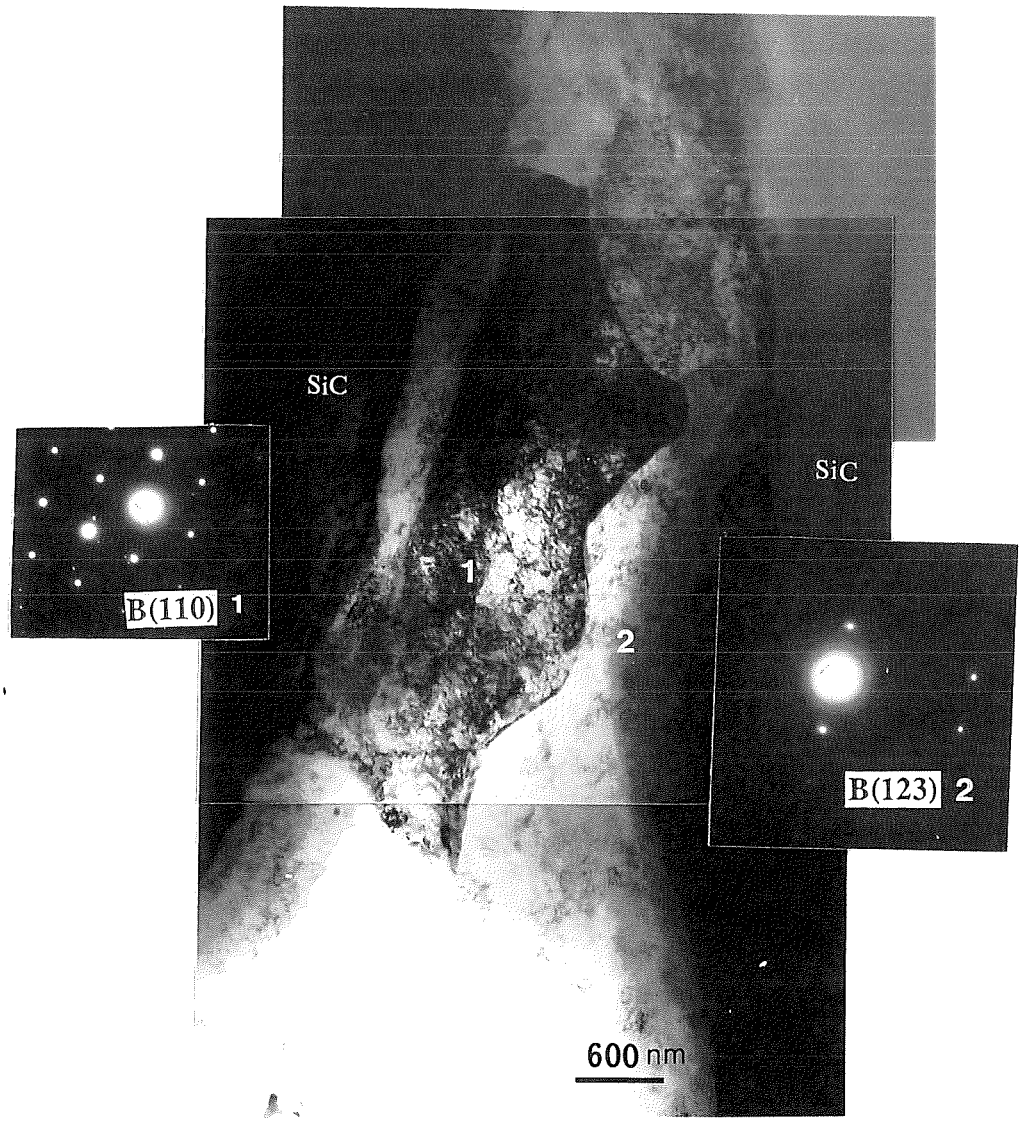

Figure 10 A Grain Formed Between Two SiC Particles with a Serrated Boundary in an Extruded Composite (AOX3E)

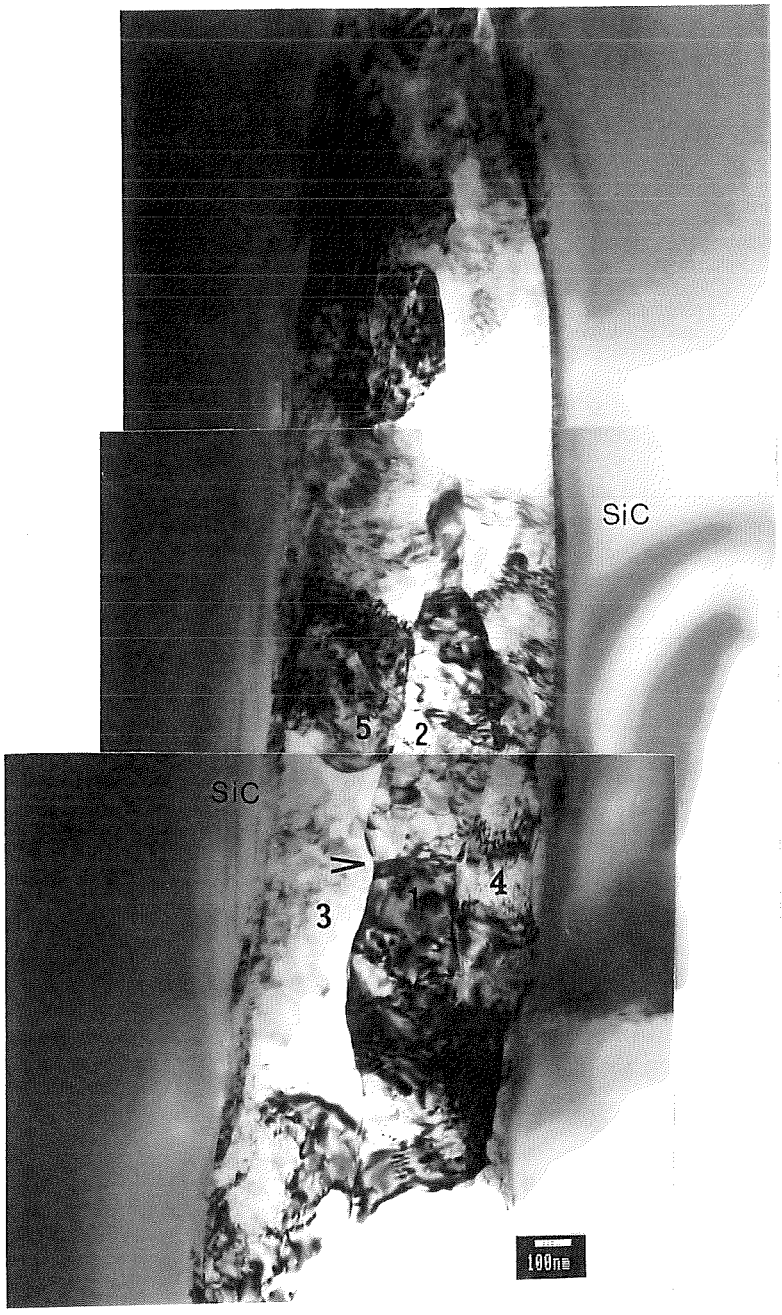

Figure 11 (a) TEM BF Image Showing Very Fine Structure (& Substructure) between Two Reinforcing Particles in an Extruded Composites (ARSE)

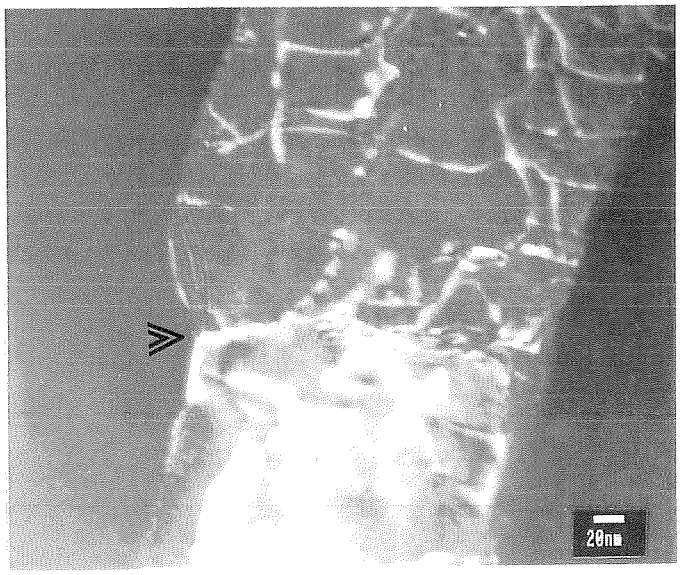

Figure 11 (b) DF Image Showing the Dislocation Structure in a Subboundary (ARSE)

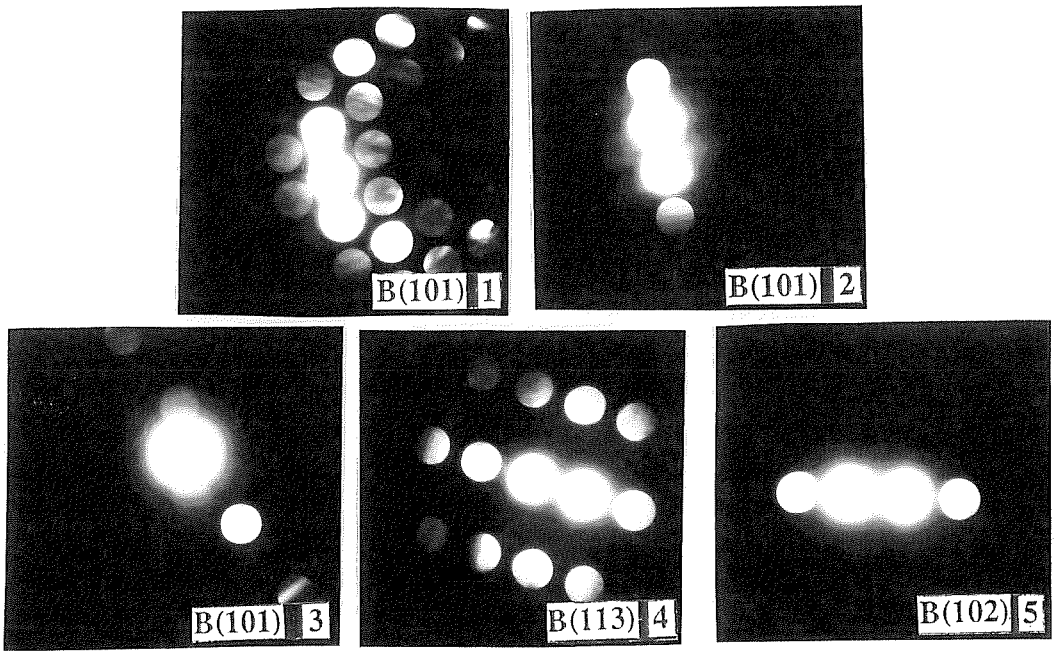

Figure 11 (c) Corresponding SAD Patterns from Areas Shown in Figure 11(a) (ARSE)

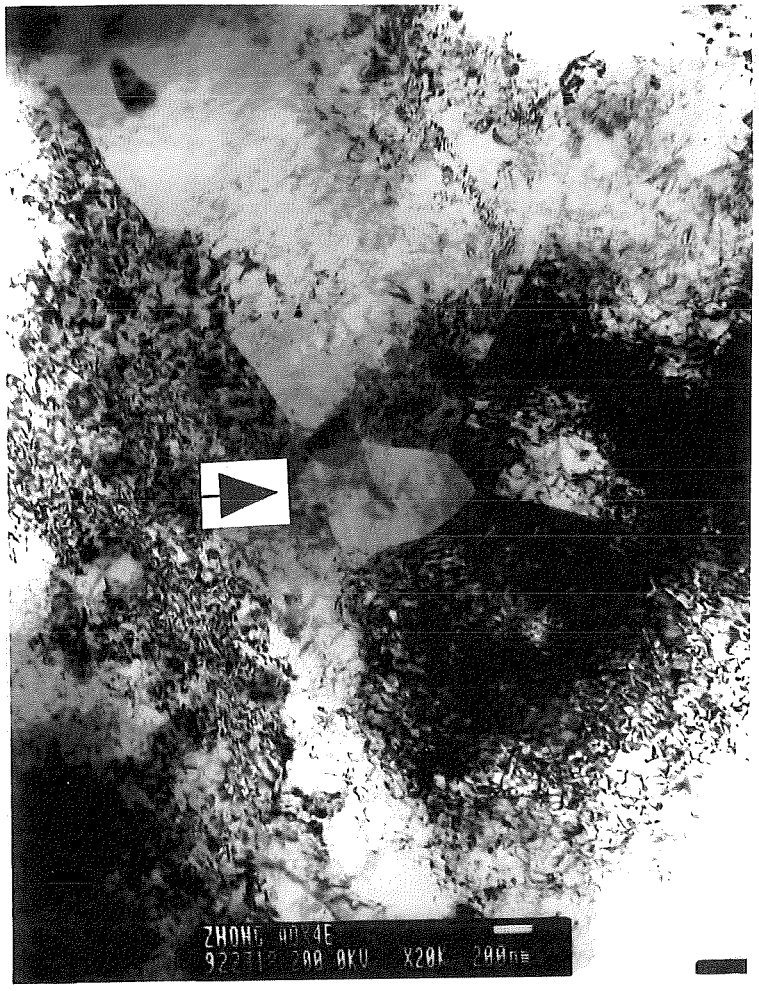

Figure 12 Recrystallization Nucleated at the Junction of Several Grains in an Extruded Composite (AOX3E)

3.2 Effect of Thermomechanical Processing on the Microstructure and Mechanical Properties of Al-Mg (5083)/SiCp and Al-Mg (5083)/Al_2O_3p Composites

Part II, Tensile Properties at different Temperatures

W.M. Zhong*, G. L'Espérance*, M. Suéry**

* Ecole Polytechnique de Montréal, Centre de Caractérisation Microscopique des Matériaux $(CM)^2$, Case Postale 6079, Succ. "A", Montréal, Québec, Canada H3C 3A7

**Institut National Polytechnique de Grenoble, Génie Physique et Mécanique des Matériaux, GPM2, URA CNRS 793 ENSPG, B.P.46, 38402 St Martin d'Heres Cedex, France

Abstract

In this paper, the second part of our three papers, the mechanical properties of as-cast and extruded composites and of the extruded monolithic 5083 aluminum alloy are discussed. Tensile tests were carried out at 25°C, 350°C and 550°C. The effects of extrusion on the properties of the composites were investigated. Three types of composites reinforced by as-received SiC particles, artificially oxidized SiC particles or

Al_2O_3 particles and deformed at different temperatures are examined. Extrusion increases both the UTS and the elongation to fracture. Whereas, artificial oxidation of SiC particles (with 3.04 wt% SiO_2) has the opposite effect. These properties are interpreted in terms of the various possible strengthening and fracture mechanisms as a function of temperature.

1. Introduction

As discussed in part I, extrusion of 5083 aluminum matrix composites causes a large scale dynamic recrystallization which produces a very fine microstructure (about 5 μm grain size in average). At the same time, it can reduce particle clustering although it may also cause particle alignment along the extrusion direction. Therefore, mechanical properties of the composites are affected. As reported previously, the ductility of extruded composites can be significantly increased in some cases, but the strength is similar to that of as-cast composites [1-3]. In other cases, not only the tensile elongation is increased, but also the yield strength and the UTS of the composites are increased [4,5]. Moreover, the composites used in different studies were fabricated by different methods or had different matrix compositions and reinforcements [6-9]. In fact, most of the previous studies related to the strengthening and the deformation of composites at both room and high temperatures have been mainly carried out on the age hardened Al alloys [6-21]. In contrast, 5083 Al-Mg alloy is a solid solution hardened alloy. It also

has a good corrosion resistance and weldability, and can be produced to exhibit superplastic behaviour. However, only a few studies were reported on this material [22], so that, it is of interest to study the deformation and fracture behaviour of this type of composites.

Strengthening mechanisms of composites have been studied extensively in recent years [6-9]. Several mechanisms and models have been suggested to explain the strength of metal matrix composites.

(1) Load transfer from the matrix to the particles [6].

(2) High dislocation densities produced on cooling from high temperatures due to the large difference between the coefficient of thermal expansion (CTE) of the matrix and that of the particles [8,23].

(3) Residual elastic stresses also caused by the large difference in the CTE [24,25].

(4) Grain and subgrain strengthening [7].

(5) Orowan strengthening [7].

(6) Matrix and interfacial precipitation [25,26].

(7) Strengthening arising from constrained plastic flow and triaxiality in the ductile matrix due to the presence of a brittle reinforcement (back stress) [9,27].

(8) Work hardening [7].

In this part, the second in this series of three papers, the mechanical properties of as-cast and extruded Al-Mg (5083)/SiCp and Al-Mg (5083)/Al_2O_3p composites and of the extruded monolithic 5083 aluminum alloy are compared. The fracture mechanisms of the different materials will be discussed in part III.

2. Experimental Procedures

The 5083 matrix composites were fabricated using a modified compocasting technique (the details were given in part I). The ingots were extruded at 480°C with an extrusion ratio of 16:1. Tensile tests were performed on as-cast and as-extruded materials at constant cross-head velocities at 25°C, 350°C and 550°C. An annealing treatment was not carried out prior to testing in order to investigate the effect of thermomechanical processing on the microstructure (see part I) and on the properties (this paper) of the materials. The initial strain rate was $1.6 \times 10^{-3} s^{-1}$ at 25°C and $1.2 \times 10^{-4} s^{-1}$ at 350°C and 550°C. The tensile samples had an initial 25 mm gauge length and a 4 mm diameter. Instron 1125 and Zwick 1474 tensile machines were used.

3. Results and Discussion

3.1 Mechanical Properties

The tensile properties obtained at various temperatures are given in figure 1 and Table I. For as-cast composites, both the UTS and the elongation to fracture are low. For example, the AOX3 composite with SiC oxidized to 3.04 wt% exhibits an UTS of 165 MPa and an elongation to fracture of about 0.3%. After the composite is extruded (AOX3E), its UTS increases to 360 MPa and the elongation to fracture increases to 8.1%. Thus, extrusion increases not only the strength of the composites, but also their elongation to fracture. This result is also obtained with the other composites, the extruded materials (ARSE and AROE) exhibiting high UTS (about 375-400 MPa) and large elongations to fracture (about 8.1-10.5% as an average of at least three samples). Extrusion also increases the microhardness of the composites as shown in figure 2. However, there is no difference in microhardness between the different extruded composites, because the microstructure of the extruded matrices are quite similar, as discussed in part I. The ductility of the extruded composites is better than that of the 5083/SiC_w composite studied by McDanels who obtained a value close to 1% with a UTS of about 380 MPa [22]. It is noticed that the tensile curves in figure 1 show a serrated appearance which may be associated with dynamic strain aging (DSA). Details of the DSA phenomenon in these composites will be discussed elsewhere [28].

Typical tensile curves in figure 1 also show that both the UTS and the elongation to fracture of the extruded 5083/SiCp composite (ARSE reinforced with as-received SiCp) are slightly higher than those of the extruded 5083/Al_2O_3p composite (AROE). One of the reasons may be that the strength of SiC particles is larger than that of Al_2O_3

particles (further discussion will be given in part III). The fracture strength (UTS) of the extruded composites is also larger than that of the extruded unreinforced materials (5083E) by 40-80 MPa.

With the artificially oxidized SiC particles, both the UTS and the elongation to fracture of the composites (AOX3E) are decreased compared to composites reinforced with as-received SiCp (ARSE). Several factors can contribute to this result. First is the nature of the interface between the matrix and the particles. As discussed in part I, the interface of the composites reinforced by different particles mainly consists of fine MgO crystals which were formed as a result of interfacial reactions during fabrication of the composites. The thickness of the MgO layer (or reaction zone) is different for the different reinforcing particles. It is about 30 nm, 50 nm and 150-200 nm thick for composites with as-received SiCp, Al_2O_3p and artificially oxidized SiCp respectively [29]. It thus appears that the relatively low properties of the AOX3E composite reinforced with artificially oxidized SiCp are related to the relatively thicker MgO reaction zone at the interface. It is also possible that a thicker reaction zone promotes decohesion between the particles and the matrix or that particles fracture more readily during deformation [30,31]. Second, since Mg is consumed by the interfacial reaction, the thicker reaction zone in the AOX3E composite will have consumed more Mg from the matrix, thereby reducing solute strengthening [29,31]. Third, Si released by the interfacial reaction forms many Mg_2Si particles in the matrix of AOX3E composites [29,30]. This can act as nucleation sites for micro-voids during deformation. Fourth, artificial oxidation

slightly reduces the effective volume of the reinforcements and may also result in relatively more flaws in the SiC particles due to thermal-cycling during oxidation. Thus, the SiC particles will crack more easily, micro-voids will nucleate at lower strains and the load transferred to the particles will be decreased. All these factors contribute to lower values of the UTS and elongation to fracture for extruded composites reinforced with artificially oxidized SiCp (AOX3E) compared to composites reinforced with as-received SiCp (ARSE).

It is noticed that although there is an obvious difference between the tensile strength of the ARSE composite and that of the AOX3E composite, the difference between the microhardness of ARSE and that of AOX3E composite is insignificant, since the microstructure of the different composites are quite similar as discussed above. Moreover, although solute strengthening in the AOX3E composite should be less because of the lower Mg content of the matrix, it is possible that Mg_2Si particles formed in the matrix of the composite compensated for the expected decrease of the microhardness.

The UTS of the composites decreases with increasing temperature (see Table I). At 350°C, it is about 40 MPa and only 6-7 MPa at 550°C, the difference between the tensile properties of the different composites being smaller at higher temperatures. The ductility of the composites increases at high temperatures. Indeed, the elongation to fracture is about 50% at both 350°C and 550°C. To understand the deformation behaviour of these composites, the strain-rate sensitivity parameter (m) was measured by

the strain rate jump method [32]. The maximum values of m for ARSE samples, obtained in the strain rate range from 1.1 to 1.9x $10^{-4}s^{-1}$ increase from 0.16 to 0.27 when the temperature increases from 350°C to 550°C (see figure 3). It is noticed that the elongation to fracture does not increase with increasing m values, when the temperature rises from 350°C to 550°C. There is also no obvious difference in m values for the composites reinforced by different particles. The values of m measured here are smaller than the value of 0.3, above which materials are considered to exhibit superplastic behaviour [32]. The large size of the reinforcing particles can lead to large stress concentrations in the matrix around the particles and impede grain boundary sliding. These effects facilitate cavitation in the composites and limit their ductility. In contrast, a maximum elongation of 250-300% and a maximum m value of about 0.5 were obtained for the hot rolled monolithic 5083 alloy deformed at 450°C and at a strain rate of about 10^{-3}-$10^{-4}s^{-1}$. Since the grain size in the monolithic alloy is slightly larger (about 10 μm) compared to that of the composites (about 5 μm), this implies that the reinforcing particles must play an important role in the deformation of the materials in addition to the grain size.

3.2 Contributions to the Strength of the Composites

The different mechanisms contributing to the strength of the composites can be estimated. Usually, several contributions must be considered to explain the observed strength of the composites [7]. In order to evaluate these contributions, the grain and the

subgrain size, and the density of dislocations were measured. The dislocation densities in the matrix and near SiC particles are given in Table II. The dislocation density increases with the volume fraction of the reinforcement and is higher near the particles. Extrusion increases the total dislocation density as would be expected for this type of material in the as-extruded condition. In addition, extrusion decreases the difference between the densities near the particles and away from the particles (ARSE). The grain size of the different materials is given in Table III. The average grain size is about 5 μm for extruded composites (ARSE) compared to about 150 μm for as-cast composites.

The contribution of the different mechanisms to the yield strength is shown in Tables IV&V. This contribution ($\Delta\sigma_i$) was calculated from the dislocation densities measured experimentally (ρ_a, Table IV), as well as from the dislocation densities calculated using the prismatic punching model (ρ_{ac}, Table V) [23]. The Hall-Petch relationship was used to calculate the contribution of the grain size ($\Delta\sigma_g$) and of the subgrain size ($\Delta\sigma_{sg}$) [7]. A modified shear lag model [6] was used to estimate the load transferred from the matrix to the reinforcement ($\Delta\sigma_{yn}$). The comparison between the extruded composite (ARSE) and the extruded monolithic alloy (5083E) shows that the contributions of the dislocations ($\Delta\sigma_d$) and of the fine grain size ($\Delta\sigma$g) are predominant, and that the contribution of the load transfer ($\Delta\sigma_{yn}$) is relatively small. Comparing between the extruded composite (ARSE) and the as-cast composite (ARS), the contribution of the small grain and subgrain sizes in the extruded composite is obvious together with that of the dislocation density. Table V shows that the calculated

dislocation densities are obviously identical for ARS and ARSE composites since the prismatic punching model does not account for the effect of extrusion. These values are much smaller than the experimental ones. This discrepancy may be attributed to errors associated with the measurements. As pointed out by Hirsh et al. [33], the dislocation density may be overestimated when measured using TEM thin foils. The error, however, is usually considered to be in the range from 20 to 40 % which is not sufficient to account for the differences observed here. The validity of the prismatic punching model could be another explanation. Indeed, Arsenault et al. [8,23] have shown that the model predicts the correct dislocation density only for small reinforcement, the prediction being largely underestimated for large reinforcement as in this case. Table IV then shows that the contribution of the load transfer to the yield strength of the composites is relatively small. However, our observations show that the particles with relatively large aspect ratios are fractured more frequently during the tensile tests and that the cracks are perpendicular to the tensile axis (see figure 4). According to the shear lag model, the load acting on the reinforcement increases with increasing aspect ratio, which implies that the contribution of the load transfer to the reinforcement can not be ignored. Moreover, the results calculated with the shear lag model [6] show that the maximum stress acting on the reinforcing particles is about 1280 MPa (σ_{pc}) for the extruded composites and it is slightly lower for as-cast composites (assuming that the particles which are cracked have an aspect ratio of L/d = 3:1). This stress is smaller than the general nominal strength (1800-2000 MPa [34]) of the SiC or Al_2O_3 particles. However, many particles (about 70%, see part III for details) were observed to be cracked on the fracture surface

of the extruded composites. This indicates that the shear lag model underestimates the load transferred or that most of the reinforcing particles have defects.

The properties of reinforcing particles may be affected by the roughness of the particle surface and internal defects. As illustrated by the SEM micrographs in figures 5 (a)&(b), the surface of the SiC particles consists of many steps probably formed during particle fabrication. From TEM images (figures 6 (a)&(b)) obtained at different tilts, a crack is observed passing through the reaction zone into an oxidized SiC particle. The area arrowed in figure 6(a) was seen at lower magnification as a groove on the surface of the particle which can act as a notch to initiate a crack. The crack propagates between the fine MgO crystals, indicating that the boundaries of MgO crystals are preferred sites for crack initiation. Cracks formed along twin boundaries can also be observed in figures 7 (a)&(b). Thus, poor surface quality and twins in the particles are important factors which decrease the strength of the particles. This may also be the reason for which the increase of the measured strength only due to reinforcing particles (about 50 - 100 MPa) is much smaller than that calculated in Tables IV (about 180 MPa when comparing $\Delta\sigma_t$ for ARSE and 5083E). In addition, the assumption that the different contributions to the yield strength may be linearly added may not be exact [7].

Alignment of the particles along the extrusion direction and some insoluble (Mn, Fe)-rich phases existing along the grain boundaries, inside the matrix and near the reinforcements, may cause stress concentrations and contribute to the local premature

yielding of the matrix and to a decrease of the strength and ductility. However, even though there are still differences between the theoretical values estimated and the experimental results, the above discussion clearly shows that the strength of the composites is not due to an unique mechanism, but that several mechanisms act simultaneously.

3.3 Deformation and Fracture At High Temperatures

At room temperature, the fracture of extruded composites is caused by ductile (dimple) fracture and 70-80% of the particles on the fracture surface are cracked (fracture at room temperature will be discussed in detail in part III). Fractographs of samples tested at 350°C show a fracture surface consisting of a mixture of dimple fracture (the dimples are associated with the reinforcement) and intergranular fracture (see figures 8-10). Tear ridges are observed in figure 8. As well, fine striations are observed on the wall of dimples as showed in figure 10. These could be an indication that the growth of the voids is still related to a dislocation deformation mechanism [31]. Particle fracture is not observed and damage occurs essentially at the interface between reinforcement and matrix (figure 10).

In order to precisely determine whether the crack propagates between the particle and the reaction zone (constituted of a layer of fine MgO crystals) or between the matrix and the reaction zone, EDS X-ray analysis was carried on the exposed surface of the

decohered SiC particles. As is well known, the X-ray emission depth increases with increasing accelerating voltage. However, if the distribution of the elements analyzed (Al, Mg and Si) is uniform along the electron beam direction, the relative X-ray intensity of these elements should not change significantly with increasing accelerating voltage for the given system. If, however, the content or relative X-ray intensity of the element (e.g. Mg) increases rapidly with decreasing accelerating voltage, Mg must be enriched on the surface of the analyzed sample. The results in figure 11 show that the X-ray intensities of Mg and O on the surface of a decohered SiC particle increase greatly and that of Si decreases, when the accelerating voltage decreases from 15 kV to 5 kV. A Mg and O rich layer therefore exists on the surface of the particle, indicating that decohesion occurred between the matrix and the reaction zone. The results of Auger electron spectrometry (AES) (figure 12) also show that the surface of a decohered Al_2O_3 particle is enriched in Mg and O. The thickness of this Mg and O enriched layer, estimated by Auger spectrometry, is approximately equal to the thickness of the interfacial reaction zone (50 to 100 nm) observed by TEM [29]. Moreover, as indicated directly from TEM (figure 13), decohesion has occurred at the interface between the reaction zone and the matrix in the AOX3E sample tested at 350°C.

The SEM image obtained from a longitudinal section (figure 14) indicates that the cavities which are often perpendicular to the tensile axis, are mainly formed at interfaces between the particle and the matrix. Coalescence of micro-voids is also observed. Observations of the fracture surfaces show that there are more particles on the fracture

surface of the sample deformed at high temperatures than that deformed at room temperature (see figure 15). Moreover, the number of particles on the fracture surface of the sample deformed at 350°C is higher than that of samples deformed at both room temperature and at 550°C. This implies that particle induced cavitation is important in the fracture of composites at 350°C and that the final failure tends to follow the particles. Cavities initiating at reinforcements and growing along the reinforcements rich region, when the composites are deformed at high temperatures, were also reported by Kwon et.al. [18]. Our observations on the distribution of damage in terms of cavities measured per unit length near the fracture surface of the tensile samples also show that the damage is more pronounced at a given distance from the fracture surface in the sample deformed at 350°C than that in samples deformed at 550°C and room temperature (see figure 16). In addition, damage is slightly less localised at 350°C and 550°C than it is at room temperature.

Fracture at 550°C is entirely caused by intergranular fracture and interfacial decohesion as shown in figure 17. Because the contribution from the intergranular fracture becomes larger, the number of particles on the fracture surface is lower than that at 350°C. It is observed that at a given distance from the fracture surface, the size of the cavities in the sample deformed at 550°C is much larger than that at 350°C, indicating more rapid growth of the microcavities at 550°C. Both fast growth of the microcavities and enhanced intergranular cavitation at 550°C may be responsible for the relatively lower ductility compared to the sample tested at 350°C (see table I). Some

matrix and small MgO crystals remain on the surface of the decohered particles (see figures 17 and 18), implying that the fracture also occurred at the interface between the reaction zone and the matrix. The cavities formed have a relatively round and smooth contour (figure 19) as a result of an increasing contribution from diffusion processes.

A final observation of interest is the presence of filaments on the surface of decohered particles (figure 18), or around grains on the fracture surface (figure 20 (a)). The filaments are elongated along the tensile direction. These filaments are Mg-rich as shown by the EDS analysis and the X-ray maps in figure 20 (b). Their origin is not entirely clear. It is possible, however, that they were caused by the deformation of some locally remelted matrix during tensile test (enrichment of Mg will locally decrease the melting point of the alloy).

4. Conclusions

(1) Extrusion increases both the tensile strength (UTS to about 400 MPa) and the elongation to fracture (to about 10%) of the particle reinforced 5083 matrix composites at room temperature. The microhardness of the composites also increases after extrusion. A number of different strengthening mechanisms contribute to the strength of the extruded composites. The fine grains produced as a result of extrusion play an important role in the strength of the composites.

(2) Increasing the reinforcement strength also increases both the UTS and the elongation to fracture of the extruded composites. Artificial oxidation of SiC particles (with 3.04 wt% SiO_2) prior to their incorporation reduces the UTS and the elongation to fracture of the composites. This is because the oxidation reduces the strength of the SiC particle and that of the matrix by reducing its Mg content. In addition, a thick reaction zone promotes decohesion at the reaction zone/matrix interface.

(3) At high temperatures, the UTS of the composites decreases and the elongation to fracture can be as large as 50%. The effect of different types of particles on the strength and the fracture behaviour of the composites is not significant. At 350°C, fracture of the composites is mainly caused by interfacial decohesion between the reaction zone around the particle and the matrix. Both dimple fracture and intergranular fracture of the matrix are observed. Particle associated cavitation plays a more important role in the fracture of composites at 350°C than that at both room temperature and at 550°C.

At 550°C, fracture is caused by intergranular fracture associated with cavitation and particle/matrix interfacial decohesion. At 550°C, grain boundary cavitation occurs much more easily, resulting in a smaller number of particles observed on the fracture surface compared to the composites deformed at 350°C. The formation of filaments during deformation may be associated with the occurrence of partial melting of the matrix as a result of local enrichment in Mg.

Acknowledgements

The authors gratefully acknowledge the NATO International Scientific Exchange Programme (Grant no. CRG 900950) and the National Science and Engineering Research Council (NSERC) of Canada (strategic grants) for financial support. They thank E. Goiffon who took part in some of the experiments and L. Salvo and J.J. Blandin for their help in preparation of the composite materials.

References

1. S. Brusethaug, O. Reiso, W. Ruch, Proc. of Fabrication of Particulate Reinforced Metal Composites(1990), Montréal, edited by J.Masounave and F.G.Hamel, p.173

2. T.M. Osman, J.J. Lewandowski, W.H. Hunt Jr., Proc. of Fabrication of Particulate Reinforced Metal Composites(1990), edited by J.Masounave and F.G.Hamel, p.209

3. D.J. Lloyd, Metal Matrix Composites-Processing, Microstructure and Properties, Risφ, (1991), p.81

4. J.S. Cho, S.I. Kwun, Scripta Metall. et Mater., vol.27(1992), p.789

5. A.H. Nakagawa, M.N. Gungor, Fundamental Relations between Microstructure and Mechanical Properties of MMCs, eds. P.K. Liaw, 1990, p.127

6. V.C. Nardone, K.M. Prewo, Scripta Metall., vol.20(1986), p.43

7. F.J. Humphreys, Proc. 9th. RISΦ Symp., ed. S.I. Anderson, H. Lilholt and O.B. Pederson, Roskilde, Denmark(1988), p.51

8. R.J. Arsenault, Proc. 9th. RISΦ Symp., ed. S.I. Anderson, H. Lilholt and O.B. Pederson, Roskilde, Denmark(1988), p.279

9. T. Christman, A. Needleman, S. Suresh, Acta Metall. Mater. vol.37, No.11(1989), p.3029

10. J. Llorca and P. Poza, Mater. Sci. and Eng., vol.185 A, (1994), p.25

11. P.B. Prangnell, T. Downes, W.M. Stobbs and P.J. Withers, Acta Metall. Mater. vol.42, No.10(1994), p.3425

12. S.F. Corbin and D.S. Wilkinson, Acta Metall. Mater. vol.42, No.4(1994), p.1319

13. S.F. Corbin and D.S. Wilkinson, Acta Metall. Mater. vol.42, No.4(1994), p.1329

14. P.E. McHugh, R.J. Asaro and C.F. Shih, Acta Metall. Mater. vol.41, No.5(1993), p.1461

15. G. Liu, Z. Zhang and J.K. Shang, Acta Metall. Mater. vol.41, No.5(1993), p.1461

16. T.W. Clyne and P.J. Withers, An Introduction to Metal Matrix Composites, Journal of Aerospace Eng. vol.208, No.1 (1994), p.68

17. T.M. Osman, J.J. Lewandowski, W.H. Hunt Jr., Proc. of Intrinsic and Extrinsic Fracture Mechanisms in Inorganic Composite Systems, TMS Annual Meeting,

Feb., 1995, Las Vegas, USA, editors: J.J. Lewandowski, W.H. Hunt Jr., Minerals Met. & Mat. Soc., p.103

18. D. Kwon, S. Lee and B.I. Roh, Metall. Trans. A, vol.24, No.5(1993), p.1125

19. S.J. Barnes, P.B. Prangnell, S.M. Roberts and P.J. Withers, Scripta Metall. & Mater., vol.33, No.2(1995), p.323

20. S.V. Nair, J.K. Tien and R.C. Bates, Int. Met. Rev., vol.30(1985), p.275

21. T.G. Nieh, K. Xia and T.G. Langdon, J. Eng. Mater. Tech., vol.(1988), p.77

22. D.L. McDanels, Metall. Trans. A, vol.16, No.6(1985), p.1105

23. R.J. Arsenault, N. Shi, Mater. Sci. and Eng., vol.81 A, (1986), p.175

24. P.J. Withers, D.J. Jensen, H. Lilholt, W.M. Stobbs, Proc. 6th. Int. Conf. on Composites (ICCM6), Elsevier Applied Sci., London and New York, vol.2(1987), p.255

25. A. Levy and J.M. Papazian Metal and Ceramic Matrix Composites Edited by R.B. Bhagat (1990), p.319

26. L. Salvo, M. Suéry, J.G. Legoux, G. L'Espérance, Mater. Sci. and Eng. A 135(1991), p.129

27. M. Taya, K.E. Lulay, D.J. Lloyd, Acta Metall. Mater. vol.39, No.1(1991), p.73

28. W.M. Zhong, G. L'Esperance, M. Suery, Portevin-Le Chatelier effect in an Al-Mg (5083) monolithic alloy and Al-Mg (5083)/particles reinforced composites,

unpublised work

29. W.M. Zhong, G. L'Esperance, M. Suery, Interfacial Reactions in Al-Mg (5083) alloy/SiCp Composites During Fabrication and Remelting, Metall. Trans. A, vol.26A, Oct.(1995), p. 2637

30. J.G. Legoux, G. L'Espérance, L. Salvo, M. Suéry, Proc. of Fabrication of Particulate Reinforced Metal Composites, ed. J. Masounave and F.G. Hamel, Montreal(1990), p.31

31. C. Milliere, M. Suery, Mater. Sci. and Tech. vol.4, No.1(1988), p.41

32. Deformation and Fracture Mechanics of Engineering Materials, Eds. R.W. Hertzberg, 1983, p.155

33. P.B. Hirsh, A. Howie, R.B. Nicholson, D.W. Pashley and M.J. Whelan, Electron Microscopy of Thin Crystal, London Butterworth, 1967, p.422

34. T.B. Shaffer, Plenum Press Handbooks of High Temperature Materials, Plenum Press, New York, 1964

Table I Properties of Composites Deformed at Different Temperatures

	T (°C)	$\dot{\epsilon}$ (s^{-1})	UTS(MPa)	$\sigma_{0.2}$(MPa)	ϵ(%)
5083O*	25		290	145	20
5083E	25	0.0016	320	165	14.4
AOX3	25	0.0016	165	160	0.3
ARSE	25	0.0016	400	240	10.5
AROE	25	0.0016	375	235	9.3
AOX3E	25	0.0016	360	225	8.1
ARSE	350	0.00012	40		51
AROE	350	0.00012	37		53
AOX3E	350	0.00012	43		50
ARSE	550	0.00012	6.7		50
AROE	550	0.00012	7.0		47
AOX3E	550	0.00012	6.4		44

* 5083O - annealed monolithic alloy, data from Metals Handbook 9th edition vol.2
5083E - extruded monolithic 5083 alloy
AOX3 - as-cast 5083/SiCp (oxidized 3.04 wt%)
ARSE - 5083/SiCp extruded
AROE - 5083/Al_2O_3p extruded
AOX3E - 5083/SiCp (oxidized 3.04 wt%) extruded

Table II Dislocation Densities in Different Composites

	ρ_p ($10^{14}/m^2$)	ρ_m ($10^{14}/m^2$)	ρ_p/ρ_m
ARS (10%SiC)	2.5	0.7	3.6
ARS (15%SiC)	3.3	1.5	2.2
ARSE (15%SiC)	5.6	4.3	1.3

ρ_m--Dislocation density in the matrix (more than 5 μm away from the particle).
ρ_p--Dislocation density near the SiC particle.

Table III Grain and Subgrain Size in the Different Materials

	Grain Size (μm)	Subgrain Size (μm)
5083E	50	10
ARS (15%SiC)	150	50
ARSE* (15%SiC)	5	2

* The grain size of AROE and AOX3E samples is similar to that of ARSE sample

Table IV Contribution of Different Mechanisms to the Yield Strength
(Results Based on Measured Dislocation Densities)

	ρ_a $10^{14}/m^2$	$\Delta\sigma_d$ (MPa)	$\Delta\sigma_{yn}$ (MPa)	$\Delta\sigma_g$ (MPa)	$\Delta\sigma_{sg}$ (MPa)	$\Delta\sigma_t$ (MPa)
5083E	1.4	89	0	21	16	126
ARS*	2.4	117	33	12	7	169
ARSE*	4.9	169	37	67	36	309

Table V Strength Based on Calculated Dislocation Densities
($\Delta\sigma_g$ and $\Delta\sigma_{sg}$ from table IV)

	ρ_{ac} $10^{12}/m^2$	$\Delta\sigma_d$ (MPa)	$\Delta\sigma_{yn}$ (MPa)	$\Delta\sigma_t$ (MPa)	σ_{pc} (MPa)
ARS	1.1	8	33	60	1160
ARSE	1.1	8	37	148	1280
AROE*	0.9	7	37	147	1280

* ARS, ARSE and AROE in tables IV and V have 15 vol.% of particles

ρ_a--Measured average dislocation density in the matrix.

ρ_{ac}-Dislocation density calculated from the prismatic punching model [8,23].

$$\rho_{ac} = [V_f B\epsilon/(1-V_f)bt]$$

$$\epsilon = \Delta CTE \Delta T/2$$

where, V_f - volume fraction of the reinforcement, B - 12 (constant), b - Burgers vector ($2.86*10^{-10}$m [7]), t - minimum dimension of the reinforcement ($13*10^{-6}$m), ΔCTE-

difference between the thermal expansion coefficient of the particle and that of the matrix, ($19.3*10^{-6}°C^{-1}$ for SiC and $15.3*10^{-6}°C^{-1}$ for Al_2O_3), ΔT- temperature change (200 °C [8])

$\Delta\sigma_d = \alpha\mu b\rho^{1/2}$, $\alpha=1$, $\mu=26.4$ GPa.

$\Delta\sigma_g = 150/D^{1/2}$, (Grain boundary strengthening, D in μm)

For the reason of simplicity, the same K factor was used for all the materials in the Hall-Petch relation.

$\Delta\sigma_{sg} = 50/D^{1/2}$, (Subgrain boundary strengthening).

$\Delta\sigma_{yn}$- Increase in yield stress calculated by modified shear lag model [6], supposing: L/d=3; strength of matrix $\sigma_{my}=145$ MPa for ARS, 165 MPa for ARSE and AROE samples (these are the strengths of the annealed and extruded monolithic alloys, see table I). Shear strength is the half of the yield strength. That is:

$$\Delta\sigma_{yn} = \sigma_{my}[0.5V_f(L/d + 2) + (1-V_f)] - \sigma_{my}$$

$$= 0.5\sigma_{my}V_fL/d$$

σ_{pc}- The maximum load acting on the particle [6],

$$\sigma_{pc} = \sigma_i(1+L/d)$$

$\sigma_i=\sigma_{UTS}=290$ MPa for as-cast composites and 320 MPa for extruded composites (using the UTS of the annealed and extruded 5083 alloy respectively, see table I), L/d=3.

$$\Delta\sigma_t = (\Delta\sigma_d + \Delta\sigma_g + \Delta\sigma_{sg} + \Delta\sigma_{yn})$$

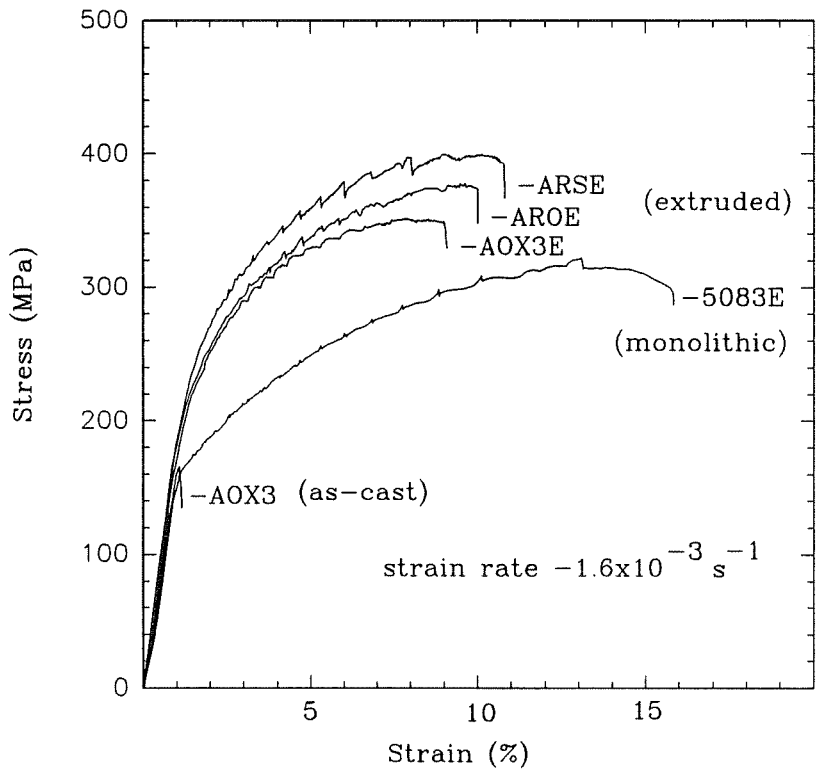

Fig. 1 Tensile Test Curves at Room Temperature

ARSE - 5083/SiCp, extruded
AROE - 5083/Al_2O_3p, extruded
AOX3E- 5083/SiCp (oxidized), extruded
5083E - Monolithic 5083 alloy, extruded
AOX3 - 5083/SiCp (oxidized), as-cast

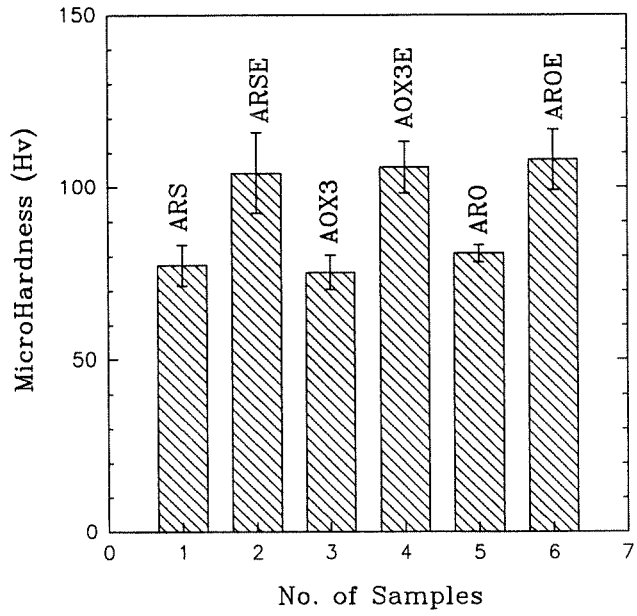

Fig. 2 Microhardness of the Extruded and the As-cast Composites

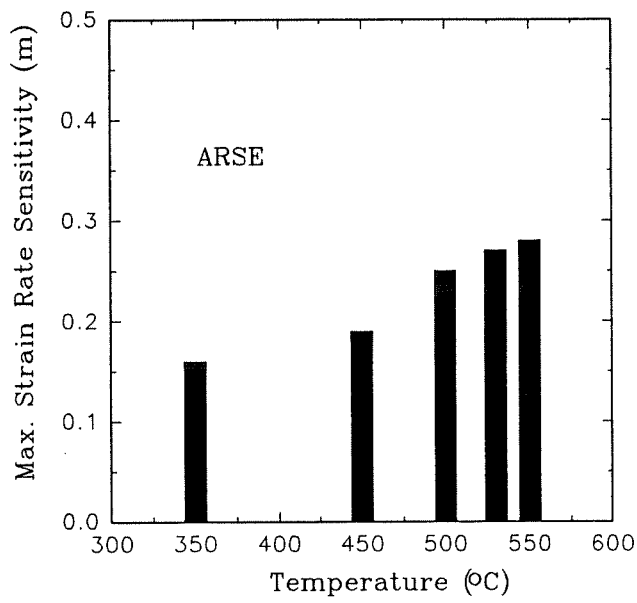

Fig. 3 Maximum Strain Rate Sensitivity Measured at Different Temperatures

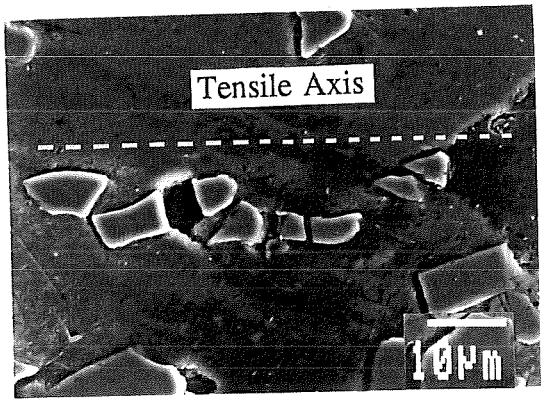

Fig. 4 SEM Micrograph of a Longitudinal Section (ARSE)

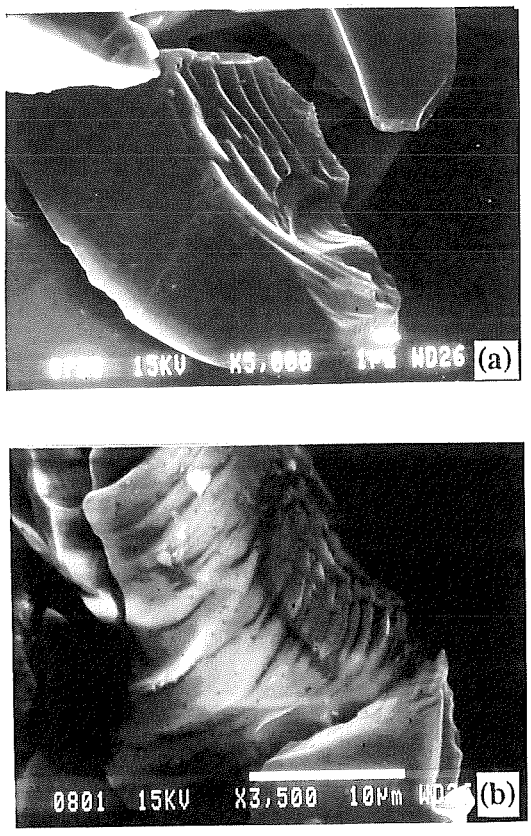

Fig. 5 (a),(b) SEM Micrographs Showing the Morphology of SiC Particles (before incorporation)

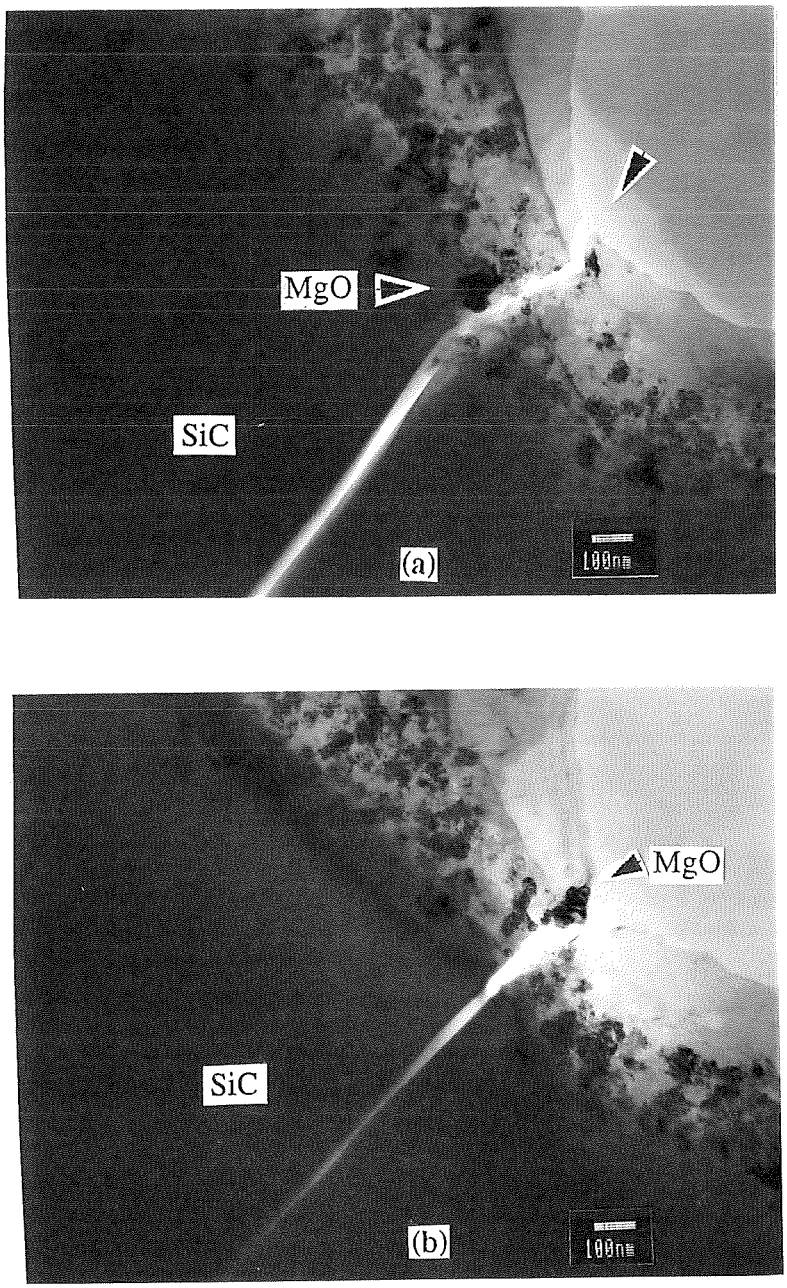

Fig. 6 (a), (b) TEM Images Obtained at Different Tilts Showing a Crack Passing between MgO Crystals in the Reaction Zone (AOX3E tested at room temperature)

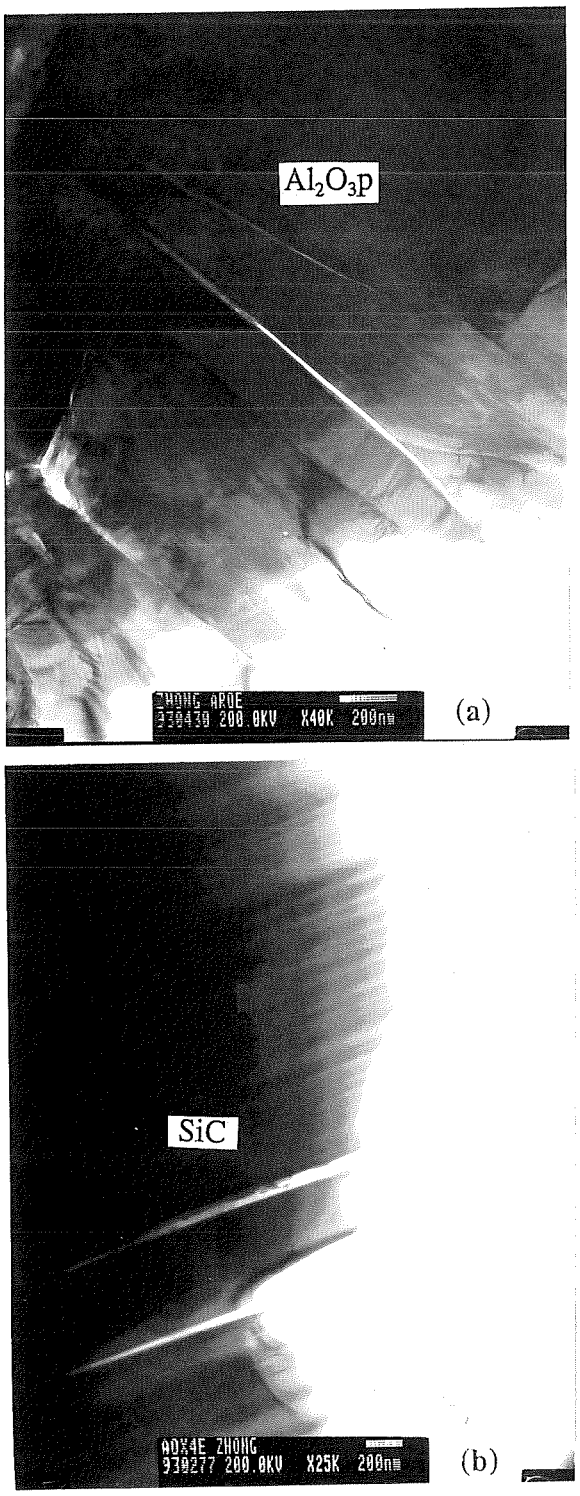

Fig. 7 (a),(b) Cracks Formed Along Twin Boundaries inside Particles

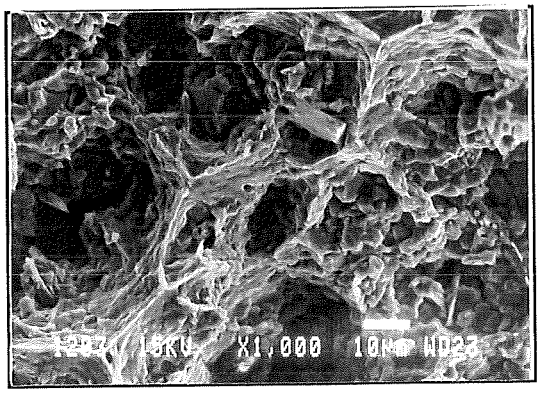

Fig. 8 Tear Ridges Observed on the Fracture Surface (ARSE tested at 350°C)

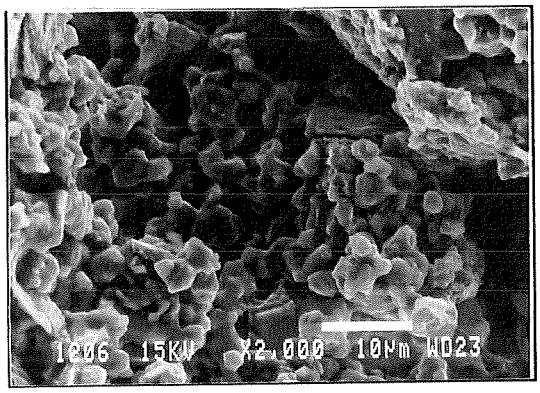

Fig. 9 Intergranular Fracture Observed (AOX3E tested at 350°C)

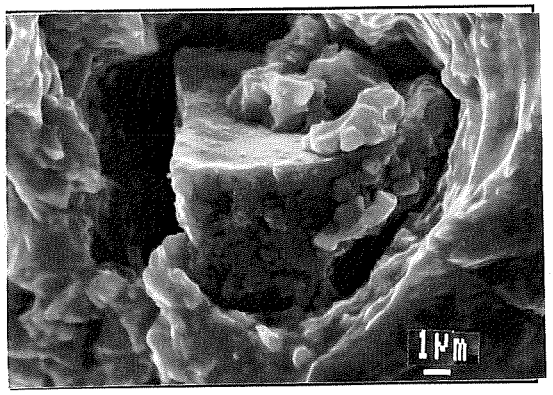

Fig. 10 Void Formed by Interface Decohesion (AOX3E tested at 350°C)

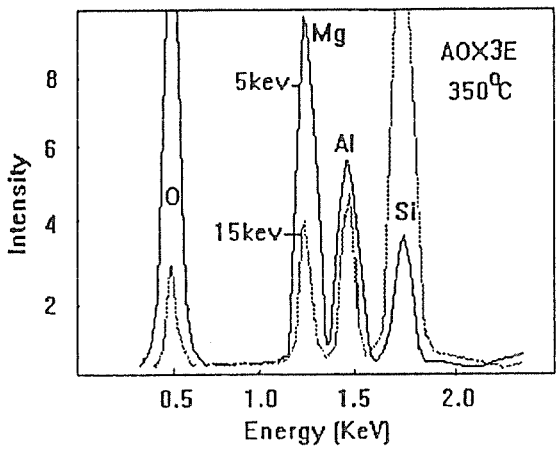

Fig. 11 X-ray Spectra Obtained from the Surface of a Decohered SiC Particle at Different Accelerating Voltages

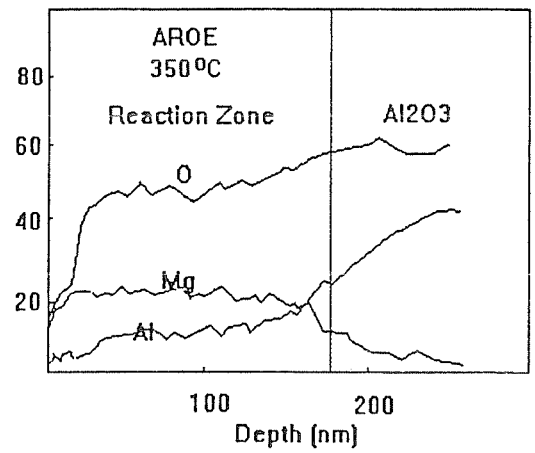

Fig. 12 Auger Depth Profile Obtained from the Surface of a Decohered Al_2O_3p Particle

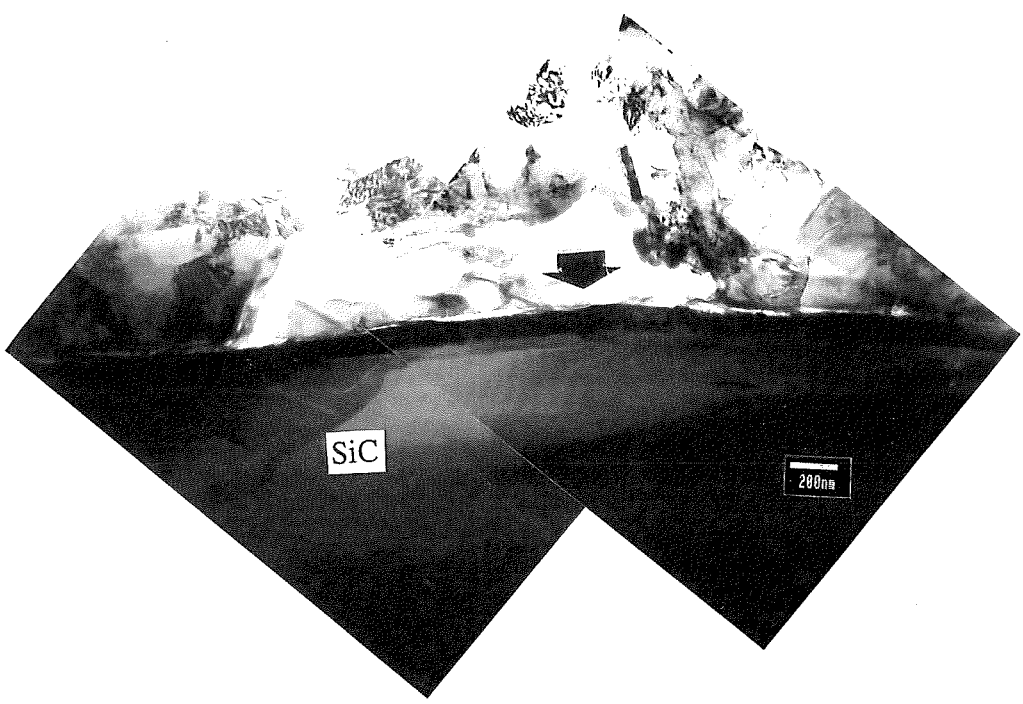

Fig. 13 TEM Image Illustrating that the Decohesion Occurs at the Matrix/Reaction Zone Interface (AOX3E tested at 350°C)

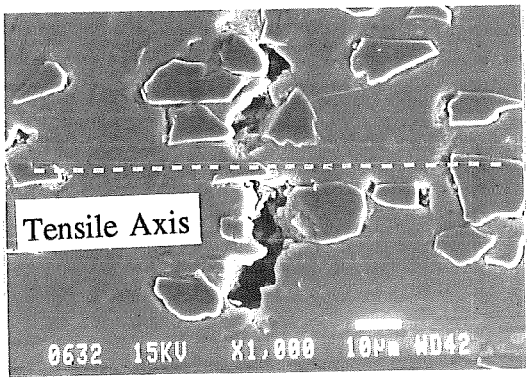

Fig. 14 Longitudinal Section Showing the Nucleation and Coalescence of Voids (ARSE, 350°C)

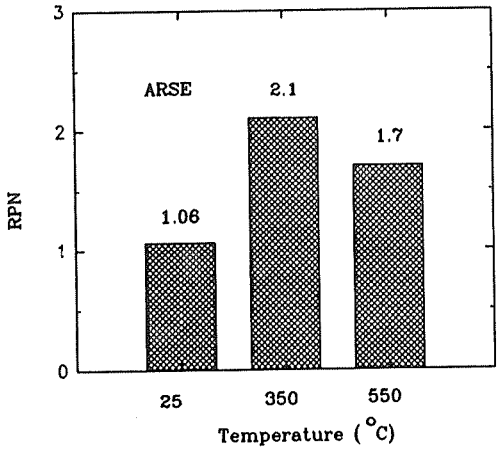

Fig. 15 Ratio of the Number of Particles on the Fracture Surface to that on Polished Surface

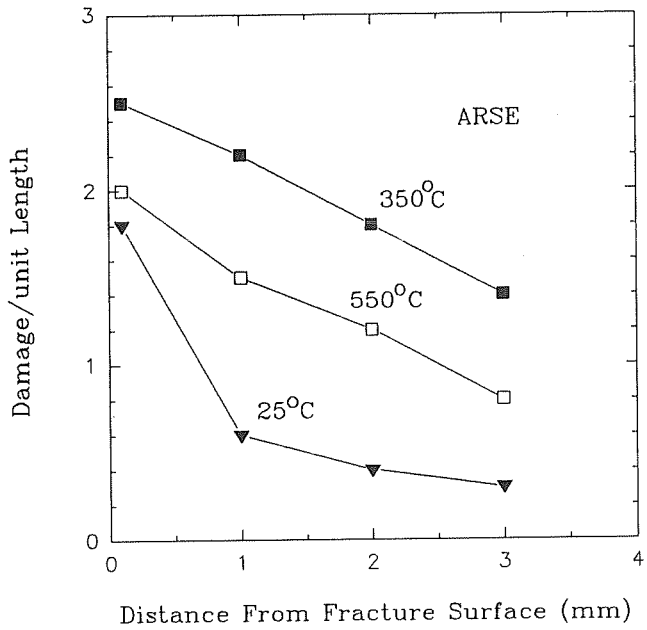

Fig. 16 Distribution of Damage at Different Temperatures

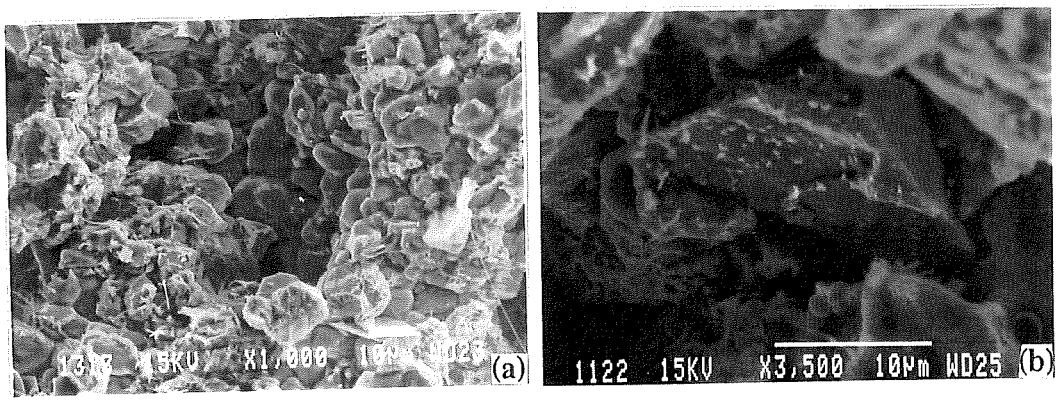

Fig. 17 (a),(b) Fracture Surface Observed after Testing at 550°C (ARSE)

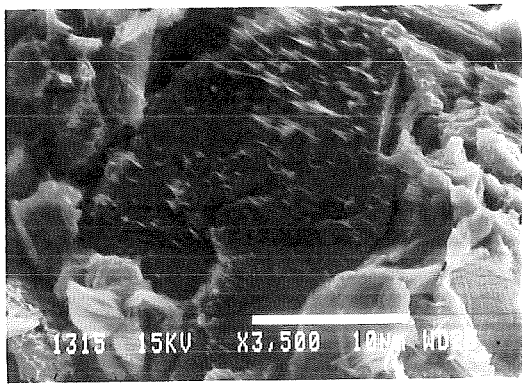

Fig. 18 Surface of Decohered Particle Observed on a Fracture Surface (550°C, ARSE)

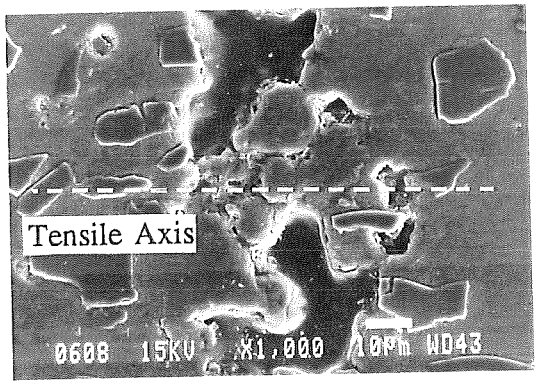

Fig. 19 Longitudinal Section of a ARSE Sample Tested at 550°C (1 mm from the fracture surface)

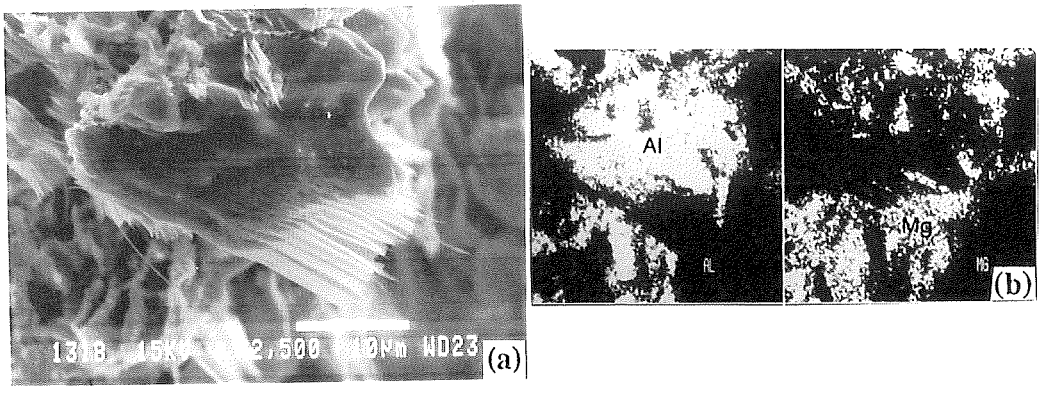

Fig. 20 **(a)** Fibres Observed on a Grain Surface of a Fractured Sample, **(b)** Corresponding X-ray Maps (ARSE tested at 550°C)

3.3 Effect of Thermomechanical Processing on the Microstructure and Mechanical Properties of Al-Mg (5083)/SiCp and Al-Mg (5083)/Al_2O_3p Composites

Part III, Fracture Mechanisms of the Composites

W.M. Zhong*, G. L'Espérance* and M. Suéry**

* Ecole Polytechnique de Montréal, Centre de Caractérisation Microscopique des Matériaux $(CM)^2$, Case Postale 6079, Succ. "A", Montréal, Québec, Canada H3C 3A7

**Institut National Polytechnique de Grenoble, Génie Physique et Mécanique des Matériaux, GPM2, URA CNRS 793 ENSPG, B.P.46, 38402 St Martin d'Heres Cedex, France

Abstract

In this paper, the last of three articles, the fracture mechanisms of as-cast composites, extruded composites and extruded monolithic 5083 aluminum alloy deformed in uniaxial tension are discussed. Dimple fracture is observed in both the monolithic 5083 aluminum alloy and the extruded composites, whereas, the fracture of the as-cast composites is mainly caused by decohesion at matrix/particle interfaces and crack propagation along dendrite boundaries. For extruded composites the fracture is mainly

nucleated by particle cracking and final failure occurs by shear coalescence of the small void sheets of matrix between the large reinforcing particles (or between clusters of particles). The large voids caused by fracture/decohesion of reinforcing particles induce localization of deformation in the matrix which accelerates the nucleation, growth and coalescence of the small voids in the matrix. Localization of deformation is one of the important factors which decrease the ductility of the composites. Three types of composites reinforced by SiC particles, artificially oxidized SiC particles prior to their incorporation and Al_2O_3 particles are examined. The effects of the interfacial reactions on the fracture of the composites are also presented.

1. Introduction

The fracture of aluminum matrix composites at room temperature often proceeds by a mechanism of ductile (dimple) rupture of the matrix and decohesion of the reinforcement/matrix interfaces or cleavage cracking of SiC or Al_2O_3 reinforcements [1-8]. This fracture mechanism can be divided into three stages [1-8,9]: nucleation, growth and finally coalescence of voids to give total failure of the materials. However, the controlling stage and the crack propagation path in the fracture of composites are different in different composites [1,5,6,8,10,11].

Extrusion of the 5083 aluminum matrix composites reinforced by SiC or Al_2O_3

particles causes a large scale dynamic recrystallization which produces a very fine microstructure (about 5 μm) and increases both the UTS and the elongation to fracture (see parts I & II). The UTS of the extruded composites is close to 400 MPa and the elongation to fracture is about 10%. The composites are mainly strengthened by mechanisms such as a high density of dislocations, a small grain and subgrain size and load transfer from the matrix to the reinforcements. For as-cast composites, the UTS is only about 165 MPa and the elongation to fracture is 0.3%. It is then of interest to investigate whether extrusion changes the fracture mechanism. Also, most of the studies on the fracture of composites were carried out for either pure Al or age hardening alloys [1,4,5,9]. The 5083 Al-Mg alloy is a solute hardening alloy with a medium strength, for which only very few reports are found with this alloy as the matrix of the composites [3,11,19]. In this paper, an effort has been made to understand the fracture mechanisms of 5083 matrix composites reinforced by different particles and fabricated by a compocasting method.

2. Experimental Procedures

The composites were fabricated by a modified compocasting technique (for details see part I). The ingots were extruded at 480°C with an extrusion ratio of 16:1. Tensile tests were performed at a constant cross-head velocity at 25°C. The initial strain rate was 1.6×10^{-3} s^{-1}. The size of the tensile samples was 25 mm gauge length and 4 mm

diameter. Longitudinal sections and fracture surfaces were examined using optical microscopy and scanning electron microscopy (SEM) coupled to an energy dispersive X-ray spectrometer (EDS). Matching pairs of SEM micrographs were obtained from the two fracture surfaces of each fractured sample in order to determine whether particles inside dimples were cracked or decohered. SEM stereo-pairs were obtained from both sides of the fracture surfaces by tilting the samples by about 6° to 7°. The stereo-pairs show the fracture steps and the depth of the dimples on the fracture surfaces. From the dimple depth observed on the stereo-matching pairs, the fracture strain could be estimated. The number of particles per unit length of fracture (NPF) was obtained by counting along the fracture surface on a longitudinal section. The number of particles per unit length of matrix (NPM) was also counted along a line at a certain distance from the fracture surface on the same section of the sample. The RNP is then defined as the ratio of the number of particles per unit length of fracture (NPF) to the number of particles per unit length of matrix (NPM). When the NPF was counted from only one side of the fractured samples, the total number of particles along the fracture path was calculated from:

$$\text{Total Number} = \text{Number of Cracked Particles} + 2 \times \text{Number of Decohered Particles}$$

assuming that the decohered particles were equally distributed on both sides of the fracture surface. The number of cracked and decohered particles was counted at the same time. The total path length counted for each material was about 10000 μm from

several sections.

3. Experimental Results

3.1 Fracture of Extruded composites

At low magnification, the fracture surfaces of the extruded samples are all approximately in a plane at 45° to the tensile axis (see Fig. 1(a)). A small amount of necking is observed near the fracture surface. There are also many micro-cracks on the surface of the tensile bar. A saw-tooth like morphology, indicating sites of crack nucleation on the surface [12], is observed at the edge of the fracture surface (see arrow in Fig. 1(a)). For the as-cast composites, the fracture surface is perpendicular to the tensile axis and necking and shear lips are not observed (see Fig. 1(b)). Figs 2(a) and 2(b) show the fracture surfaces of the extruded composites which appear to be very rough. Large cavities are observed which are crack nucleation sites (arrow in Fig. 2(a)). In the middle of the sample, there is a small fibrous zone which is approximately perpendicular to the tensile axis. Shear lips extend from this small fibrous zone along the direction of maximum shear stress to the two edges of the sample. As known, microvoids are likely to nucleate in the middle of the sample which may experience plane strain conditions and triaxial tensile stresses [12,13]. However, because clusters of particles can nucleate microvoids, other areas can also be nucleation sites (see arrow in

Fig. 2(b)). Striations on the fracture surface (see arrow 2 in Fig. 2(b)), which are approximately perpendicular to the main shear direction which is at about 45° to the tensile axis (dash line in the figure), are the result of many fine steps on the fracture surface which were observed at higher magnifications as discussed below.

Figs 3-5 are matching pairs and stereo-pairs obtained from the fracture surfaces of the extruded composites reinforced by different particles. As shown by these micrographs, the matrix of the composites is fractured by a ductile (dimple) mechanism. A large number of particles are cracked (see matching pairs). There are two types of dimples on the fracture surfaces. One of them is associated with cracked SiC or Al_2O_3 particles, with a size slightly larger than that of the reinforcing particles. Another type of dimple has a size typically smaller than 3 μm and is formed between the large reinforcing particles associated with the dimples. Insoluble (Fe, Mn)-rich inclusions are often found in the small dimples. By stereoscopy, it is observed that the fracture surfaces of the large reinforcing particles are usually very flat and perpendicular to the tensile axis. The fractured particles or the clusters of fractured particles form many small platforms on the fracture surface. The fine steps, as observed in Fig. 2(b), are caused by those platforms located at different height levels. The fractured matrix between two cracked particles or two platforms is often at about 45° to the tensile axis. Fig. 6 shows a schematic diagram of dimple formation. The large dimples have usually grown symmetrically (see arrows A in Figs 3&4), but the small dimples formed in the matrix between two platforms are elongated (Fig. 7) and point into opposite directions

on the two matched fracture surfaces (see arrows B in Figs 3 (a)&(b)). This indicates that the particles are fractured by cleavage and that the matrix is fractured by shear [12]. In addition, scratches are found in the matrix near cracked particles (see arrow C in Fig. 3(b)). The scratches are caused by dragging of the cracked particles over the fracture surfaces when the two parts of the fracture surfaces are sheared away. Some dimples are quite deep as shown in Fig. 8, in which many fine striations are observed on the surface of their walls. These striations are probably the result of dislocation slip steps formed by plastic deformation after that the voids were formed [13].

Decohesion between particles and matrix is also occasionally observed as shown in Fig. 9. In contrast, when composites are fractured at higher temperatures, all the particles are decohered as discussed in part II. Some matrix material is present on the surface of the decohered particles and was found to be rich in Mg and O by X-ray EDS analysis, suggesting that decohesion takes place between the reaction zone and the matrix. This is supported by the TEM micrograph shown in Fig. 10, in which a microvoid formed at the interface between the reaction zone (arrowed in the figure) and the matrix can be seen.

In longitudinal sections of the samples, near the fracture surfaces, cracking of the particles and decohesion at the particle/matrix interface are observed (see Fig. 11). The cracked particles usually have relatively large aspect ratios (L/d) and they are pulled apart when the voids are elongated by further deformation. It is noticed in Fig. 11 that

the growth of the voids near the fracture surface (arrowed) is quite limited. Some voids coalesce when the distance between two voids is small (see arrow A in Fig. 12) and the appearance of necking of the matrix between two voids can also be observed (arrow B). Fractured particles are also observed at a distance of 3 mm from the fracture surface. However, the distance between the two parts of a cracked particle is smaller than that for particles near the fracture surface, indicating that deformation is localized in the area near the fracture surface. Other features related to the fracture mechanism can also be observed on longitudinal sections. Fig. 13 shows the fractured matrix between two cracked particles at different height levels (particles P) which is consistent with the mechanism suggested in Fig. 6.

3.2 Fracture of the Extruded Monolithic Alloy and the As-cast Composites

Fig. 14 is a fractograph of the extruded monolithic 5083Al alloy. The dimples are associated with (Mn, Fe)-rich inclusions as analyzed by X-ray (EDS) spectrometry. The average dimple depth is shallower than that observed in the composites.

The fractographs of the as-cast composites are quite different from those of the extruded composites. Thus, about 90% of the particles are separated from the matrix by decohesion at the interface. Fig. 15 shows some decohered particles on the fracture surface. The dimples are very shallow. Many voids are formed in particle clusters (Fig. 16) and between dendrites (Fig. 17). Secondary cracks, which may propagate along the

dendrite boundaries, are also observed (Fig. 16). A void between dendrites, indicated by a round and smooth fracture surface in Fig. 17(a), may be formed by a lack of liquid during solidification. Fig. 17(b) shows the distribution of Al and Si in the void which confirms that the round and smooth area is the matrix. Some particles, however, are found around the void. Some cracks may also be related to the presence of oxide skins introduced into the melt during fabrication of the composites. Longitudinal sections of fractured as-cast composites show that the crack is formed preferentially at dendrite boundaries where a large number of particles are segregated (Fig. 18). Secondary cracks are observed to propagate parallel to the tensile axis (Fig. 19) or parallel to the fracture surface (Fig. 20).

In order to understand the role of reinforcing particles on the fracture of composites and to compare the fracture behaviour of different materials, some quantitative measurements were carried out. Fig. 21 shows that the number of particles on the fracture surface is comparable to that observed on polished sections for all the extruded composites, but it is much larger in as-cast composites. The amount of particles on the fracture surface is estimated by the number of particles per unit length of fracture as discussed above. This implies that the crack does not preferentially go through the particles in the extruded composites in contrast to the as-cast composites.

The extent of damage related to cracked and decohered particles was estimated to evaluate the efficiency of load transfer and the quality of the particles and that of the

interfaces. On the fracture surfaces of the extruded composites, about 70-80% of the particles are cracked (see Figs 22&23). Also, the total number of particles and the number of fractured particles on the fracture surfaces are almost the same for all extruded composites reinforced with different particles. The different reinforcing particles, with different strengths and reaction zone thicknesses do not lead to significant differences in the extent and nature of damage observed on the fracture surfaces of the composites. Fig. 22 also shows that the number of damaged particles decreases with increasing distance from the fracture surface. This result is similar to those of Lloyd [14] et al. and of Singh and Lewandowski [15], who also found that the cracked particles are concentrated on the fracture surface and that deformation is localized in the area near the fracture surface.

4 Discussion

4.1 Effects of the Oxidation of SiC Particles on the Fracture of Extruded Composites

Generally, as shown above, the effect of artificial oxidation of SiC particles on the characteristics of fracture is not obvious. It seems that, as indicated in Fig. 22 for extruded composites, the artificially oxidized SiC particles crack more readily than the as-received SiC particles for a given distance from the fracture surface. As discussed in

part II, artificial oxidation decreases the effective volume of the SiC particle and increases the number of flaws in the particle as a result of the thermal cycle during oxidation. The interfaces, consisting of many fine MgO crystals formed as a result of interfacial reactions [17,18], may also increase the surface friction of particles which will contribute to an increase in load transfer. In addition, in the composites with oxidized SiCp, the MgO reaction layer could be a nucleation site for particle cracking. It is noticed that although more oxidized SiC particles are cracked at a certain distance from the fracture surface, there is no obvious difference in the number of cracked SiC particles (or decohered particles) on the fracture surface of the different composites. The slightly larger number of decohered particles (about 5% difference between the as-received SiC and the oxidized SiC particles), observed on the fracture surface of the composites with oxidized SiC particles (AOX3E), is probably within the experimental errors of the measurements although it has been reported that oxidation of SiC particles increases the possibility for decohesion during fracture of composites [16]. As discussed in part II and [17,18], the interfacial reactions between the matrix and the particles during fabrication consume Mg from the matrix, leading to the formation of fine MgO crystals in the reaction zone. Artificial oxidation of SiC particles increases the thickness of the reaction zone, so that more Mg is consumed and the matrix strength decreases. Si released as a result of the interfacial reactions reacts with Mg in the matrix and forms Mg_2Si inclusions which are likely to be located near SiC particles [17]. These two factors should promote crack propagation around the SiC particles rather than through them. The fact that there is very little difference in the amount of cracked particles for composites with oxidized

particles and with as-received particles indicates that other microstructure features induced by extrusion dominate the fracture behaviour of these composites.

4.2 Effect of Extrusion on the Fracture of Composites

In as-cast composites, because the reinforcing particles are pushed by the solid/liquid front during solidification, the particles are segregated in the interdendritic regions where solidification occurs last [21]. The segregation of these particles at dendrite boundaries will restrict the flow of liquid before the composite is completely solidified and micro-cavities can therefore be formed in these regions (as shown in Figs 17&18). Even if a small amount of matrix exists between these segregated particles, it can not support the large stress concentrations caused by the particles [14] so that the matrix between the particles will fail after only a small amount of deformation and cavitation will occur. The interdendritic regions are weakened as a consequence of the large amount of cavities produced by solidification and deformation. Therefore, cracks mainly occur at the dendrite boundaries and a large number of decohered particles are observed on the fracture surface.

As shown in Fig. 23, only about 10% of the particles on the fracture surface of the as-cast composites are fractured, which is very low compared to the extruded composites (about 70-80%). Thus, extrusion increases the amount of cracked particles on the fracture surface. As discussed in parts I&II, extrusion increases the dislocation

density and decreases the grain and subgrain sizes. Therefore, the strength of the matrix is increased after extrusion and a larger load can be transferred to the particles before failure of the matrix occurs [20]. This will lead to a large number of cracked particles, as was also reported in references [14,19] in which the number of fractured particles increased with the strength of the matrix.

Extrusion significantly reduces the effect of segregation of particles. It leads to a more uniform particle distribution and the old dendrite boundaries are destroyed and new grain boundaries are formed as a result of recrystallization. These new grain boundaries are stronger than the original ones because defects and segregation of inclusions or reinforcing particles at the boundaries are largely eliminated. Large inclusions and oxidized skins are also broken into smaller ones and dispersed [22]. Cavities or microcracks formed during solidification are largely rewelded. All these changes decrease the stress concentration caused by the segregation of particles and inclusions, improve the matrix plastic flow and decrease the possibility of cavitation in the matrix during deformation.

4.3 Fracture Mechanisms

The above discussion has presented a different fracture behaviour for the as-cast and the extruded composites. In the as-cast composites, decohesion of the matrix/particle interfaces, cavities formed during solidification and cracking along the dendrite

boundaries are all void nucleation sites and fracture mainly occurs at the dendrite boundaries. Plastic deformation of the matrix is then very limited.

For the extruded composites, the matrix will work harden during deformation so that a larger load will be built on the particles. As shown in Fig. 24, the particles usually located in the region I and, especially, the ones with a large size or with a large aspect ratio (L/d) or located in a cluster will crack first (see particles A in the figure). This is supported by the fact that the triaxial tensile stresses [6,12] are possibly larger in the middle of the tensile sample, the number or size of flaws in particles increase with increasing particle size [14,23], larger loads can be transferred to particles with a larger aspect ratio [20] and that large stress concentrations occur inside clusters of particles [2,14,24]. When voids are formed as a result of particle cracking, the stress state in the matrix between these particles may be changed from plane strain to plane stress. Thus, stress concentrations are relaxed [13]. The matrix will undergo a shear deformation with further straining, resulting in unloading in this area [12]. As shown in Fig. 12, necking occurs between two cracked particles.

In another area (Region II in Fig. 24) of the same cross section, because the particles have not been cracked, matrix flow is still constrained by them and considerably more load will be supported by this area. Soon after the particles (particles B) in this area are cracked, is the matrix further deformed. This process causes localization of plastic deformation in a very small region (W). Because the maximum resolved shear

stress is in a plane oriented 45° to the tensile axis [12,13], the shear strain will mainly concentrate in this plane (arrowed in the figure) and the many small (Mn, Fe)-rich inclusions in the matrix can lead to the formation of a sheet of voids along the shear plane when deformation is larger than a critical value. When a critical number of particles are fractured in a certain cross section, the remainder of the section can not support the increasing load. Deformation will be further concentrated in this area (W). When the work hardening rate becomes smaller than the geometrical softening rate caused by void formation and necking, total unloading will occur. With further deformation, the small voids formed in the "shear sheet" eventually coalesce. Therefore, a shear step is formed by the matrix between two cracked particles (or cluster of particles) after the material is fractured (see Figs 6&13).

It can be concluded from the above discussion that the voids are first nucleated by cracking (and some decohesion) of the reinforcing particles, and that final failure is caused by the coalescence of the small voids in the matrix. Direct coalescence of large voids is observed only when the distance between two particles is very small (as illustrated in Fig. 12). In most cases, the growth of the large voids is limited compared to the particle size. The role of the large voids is mainly to introduce concentration of plastic deformation in the matrix. Localized deformation will accelerate nucleation, growth and coalescence of the small voids in the matrix. Thus, the total elongation to fracture is decreased, even though the local ductility of the matrix may be larger than that of the monolithic alloy because of the smaller grain size in the matrix of extruded

composites. The relatively shallow dimples on the fracture surface of the monolithic alloy can be explained by both a much more uniform deformation in the monolithic alloy and the small size of the inclusions in the materials. Usually the fracture strain increases with increasing dimple depth [6,12]. Thus, for the same amount of total elongation, the required plastic deformation near the fracture surface of the monolithic alloy can be smaller than that of composites. In other words, the total volume of the monolithic material involved in the deformation is larger than that of composites, because in composites, deformation is localized in a small region near the fracture surface.

From the fracture mechanism proposed here, several more of our observations can be explained. First, as discussed in part II, a decrease of the reinforcing particle strength, for example, by artificial oxidation of SiC particles or by using Al_2O_3 particles (their strength is lower than that of as-received SiC particles), causes a decrease of both the UTS and the elongation to fracture of the composites. This is because stronger particles may delay void nucleation by particle cracking (since the interfacial bond is also very strong) and decrease localized flow, leading to larger elongations to fracture. At the same time, the suppression of the nucleation of the large voids will increase the local constraint and allow additional work hardening of the matrix. As a result, the ultimate tensile strength of the composites increases. Thus, nucleation of voids at reinforcing particles appears to ultimately control the tensile strength and the ductility of the composites. Our results are similar to those of Mummery et al.[11] who studied the fracture of Al-5050 and Al-1070 matrix composites by acoustic emission. They found

that void nucleation occurs from the onset of plastic deformation and continues throughout the plastic regime. Suppression of void nucleation at the particles increased the ductility of the composites. They suggested that a critical number of fractured particles is required before failure.

Second, as discussed above, the number of particles on the fracture surface of extruded composites is comparable to that on polished surfaces. This can be explained as follows. After extrusion of the composites, the distribution of the particles becomes more uniform and the total number of particles should be similar in any cross section even though particle alignment may exist. In addition since the matrix is finally fractured by shearing along the "void sheet", the crack path can not deviate too much from the maximum shear plane in order to minimise the fracture energy. Fracture may still be nucleated at those sites with a larger density of particles during deformation. However, since the fracture path is confined by the plane of maximum shear stress, the average particle concentration on the fracture surface will not be very different from that observed in other areas.

The last aspect that needs to be addressed, is the relatively small fibrous zone observed on the fracture surface of the extruded composites. This is because the sample is mainly deformed by shear deformation or local shear deformation between the large voids [12,13]. Many fine fracture steps at approximately 45° to the tensile axis are formed by such local shear deformation. Thus, macroscopically, the fracture surface is

a plane at about 45° to the tensile axis. In as-cast composites however, the fracture surface is in the plane perpendicular to the tensile axis. This implies that extruded composites undergo a relatively larger shear deformation before fracture compared to that of as-cast composites and thus exhibit a better ductility [3,25].

5. Conclusions

Extrusion of the 5083 matrix composites reinforced by SiC and Al_2O_3 particles produces fine grains and subgrains in the matrix and increases both the strength and the elongation to fracture of the composites. The effect of extrusion on the mechanical properties is associated with a change of the fracture mechanisms of the extruded composites compared to the as-cast materials.

(1) In as-cast composites, decohesion of the matrix/particle interface, cavities formed during solidification and cracking along the dendrite boundaries are all sites of void nucleation. Segregation of the reinforcements at dendrite boundaries causes stress concentrations, which increase the probability of void nucleation. Because of the large number of void nucleation sites, premature fracture occurs in as-cast composites.

(2) In extruded composites, fracture of the reinforcing particles is the main source of void nucleation. Final failure occurs by shear coalescence of the small void sheets in

the matrix between the large reinforcing particles (or particle clusters). The large voids associated with the reinforcing particles induce localization of deformation in the matrix which accelerates the nucleation, growth and coalescence of the small voids in the matrix. Delaying the formation of the large voids will increase both the strength and the elongation to fracture of the composites.

(3) Factors which decrease the strength of particles or promote fracture of the particles such as artificially oxidizing SiCp particles prior to fabrication will accelerate void nucleation and decrease both the UTS and the elongation to fracture.

Acknowledgements

The authors gratefully acknowledge the NATO International Scientific Exchange Programme (Grant no. CRG 900950) and the National Science and Engineering Research Council (NSERC) of Canada (strategic grants) for financial support. They also thank E. Goiffon, L. Salvo and J.J. Blandin for the preparation of the composite materials. E. Goiffon was also involved in part of the fabrication and extrusion experiments.

References

1. D.L. Davidson, Metall. Trans. A, vol.22(1991), p.113

2. R.J. Arsenault, N. Shi, C.R. Feng and L. Wang, Mater. Sci. and Eng., A, vol.131(1991), p.55-68

3. D.L. Mcdanels, Metall. Trans. A, vol.16, No.6(1985), p.1105

4. P. Mummery, B. Derby, Mater. Sci. and Eng. A, vol.135(1991), p.221

5. C.P.You, A.W. Thompson and I.M. Bernstein, Scripta Metall., vol.21(1987), p.181

6. B. Roebuck, J. of Mater. Sci. Letters, vol.6(1987), p.1138

7. S.V. Kamat, J.P. Hirth, R. Mehrabian, Acta Metall. Mater. vol.37, No.3(1989), p.2395

8. W.H. Hunt Jr., O. Richmond, R.D. Young, Proc. ICCM6, edited by F.L. Mathews et al., Elsevier, Amsterdam, vol.2(1987), p.209

9. L.M. Brown, J.D. Embury, Proc. 3rd Int. Conf. on Strength of Metals and Alloys, London, (1973), p.164

10. Y. Flom, R.J. Arsenault, Proc. ICCM6, edited by F.L. Mathews et al., Elsevier, Amsterdam, vol.2(1987), p.189

11. P.M. Mummery, B. Derby, C.B. Scruby, Acta Metall. Mater., vol.41, No.5(1993), p.1431

12. Deformation and Fracture Mechanics of Engineering Materials, Eds. R.W. Hertzberg, 1983, p.155

13. Elementary Engineering Fracture Mechanics, by David Broek, fourth edition, 1987

14. D.J. Lloyd, Acta Metall. Mater. vol.39, No.2(1991), p.59

15. P.M. Singh and J. Lewandowski, Metall. Trans. A, vol.24A(1993), p.2531

16. H. Ribes, R.D. Silva, M. Suery, T. Bretheau, Mater. Sci. and Tech., July(1990), vol.6, p.621

17. W.M. Zhong, G. L'Esperance, M. Suery, Interfacial reactions in Al-Mg (5083)/SiCp composites during fabrication and remelting, accepted for publication in Metall. Trans.

18. W.M. Zhong, G. L'Esperance, M. Suery, Interfacial reactions in Al-Mg (5083)/Al_2O_3p composites during fabrication and remelting, accepted for publication in Metall. Trans.

19. J.G. Legoux, Ph.D. Thesis, Ecole polytechnique, Montreal, Canada(1991)

20. V.C. Nardone, K.M. Prewo, Scripta Metall., vol.20(1986), p.43

21. I. Jin, D.J. Lloyd, Proc. of Fabrication of Particle Reinforced Metal Composites (1990), Montreal, Canada, edited by J. Masounave and F.G. Hamel

22. E. Goiffon, W.M. Zhong, J.J. Blandin, M. Suery, G. L'Esperance, Proc. of 2nd Inter. Conf. on Cast Metal Matrix Composites, Oct.(1993), Tuscaloosa, USA, p.316

23. J. Gurland, Acta Metall., vol.20(1972), p.735

24. T. Christman, A. Needleman, S. Suresh, Acta Metall. Mater. vol.37, No.11(1989), p.3029

25. Metal Handbook A.S.M., 9th Edition, vol.12(1979), p.91

List of Acronyms

5083E - extruded monolithic alloy

AOX3 - 5083/SiCp (oxidized 3.04 wt%) as-cast

ARSE - 5083/SiCp extruded

AROE - 5083/Al_2O_3p extruded

AOX3E - 5083/SiCp (oxidized 3.04 wt%) extruded

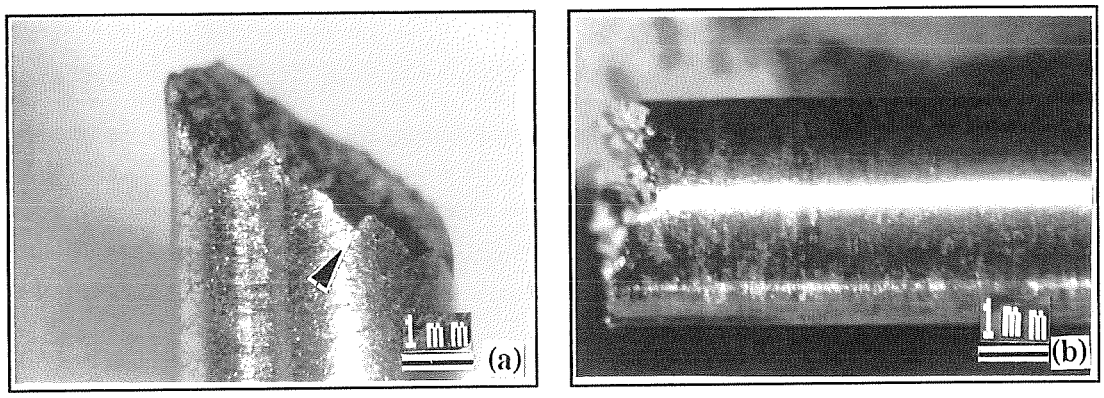

Fig. 1 Optical Macrographs of the Fracture Surfaces of Composites, (a)-Extruded (ARSE), (b)-As-cast (AOX3)

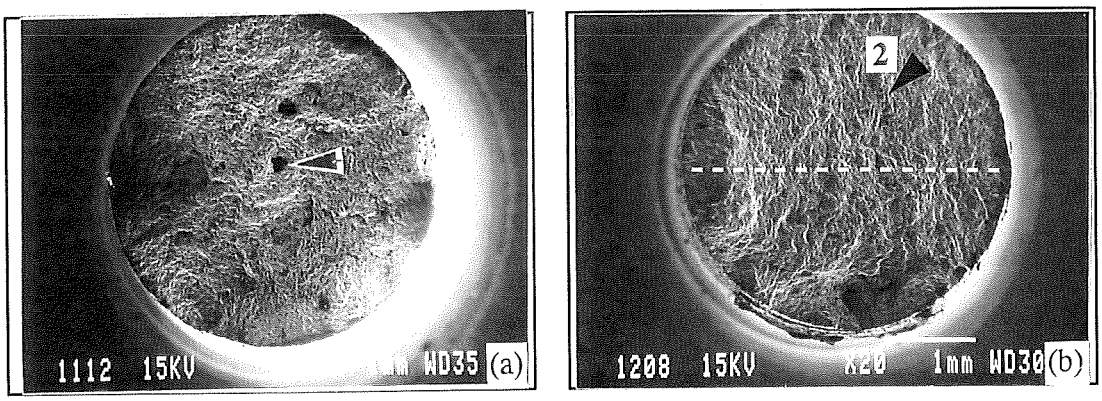

Fig. 2 Fracture Surfaces of Extruded Composites (at Room Temperature), Reinforced by As-received SiC ((a), ARSE) and Al_2O_3 Particles ((b), AROE) Respectively

Fig. 3 Fracture Surfaces of Extruded Composites, Matching Pairs: (a)-(b)&(c)-(d), Stereo-Pairs: (a)-(c)&(b)-(d) (ARSE)

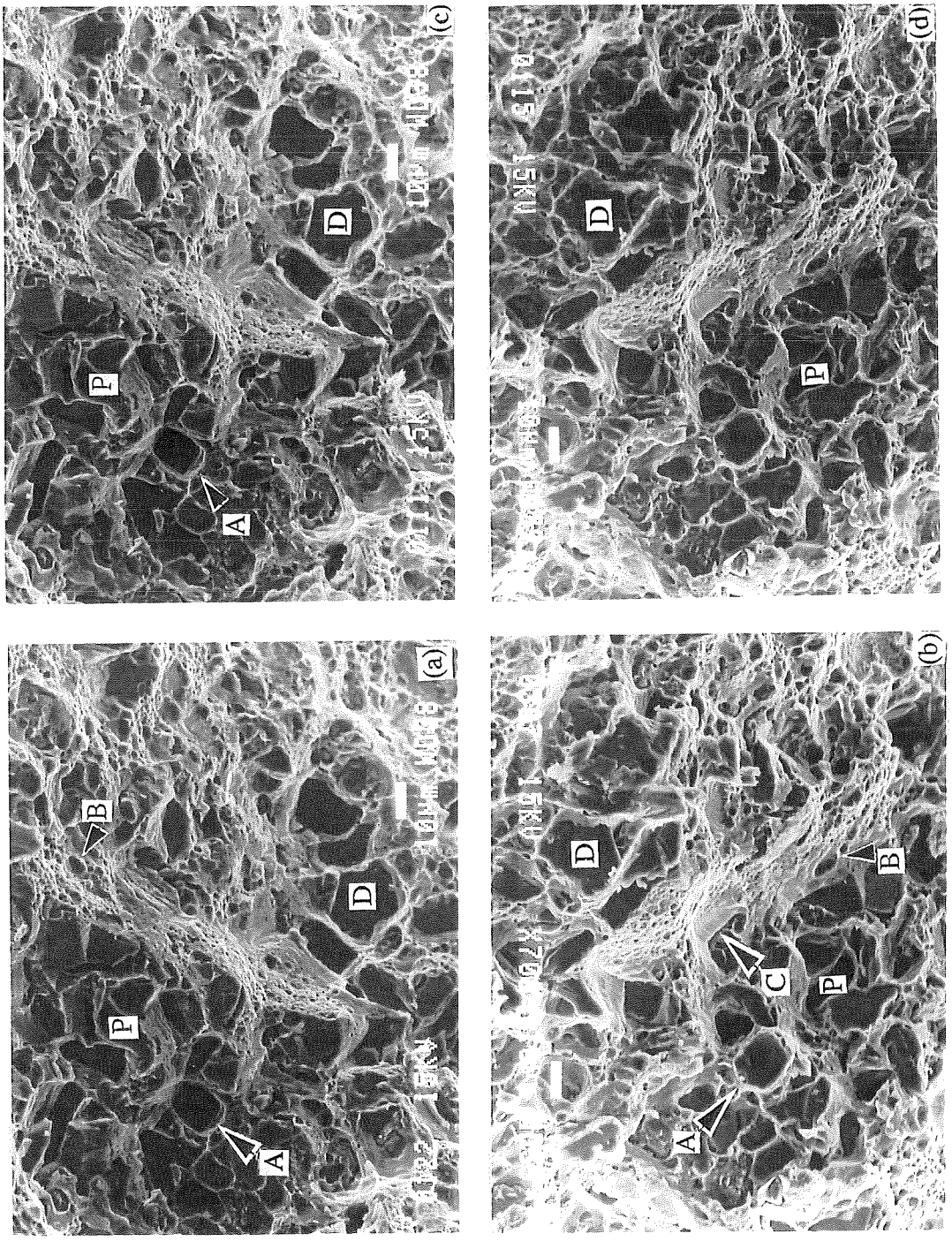

Fig. 4 Fracture Surfaces of Extruded Composites, Matching Pairs: (a)-(b)&(c)-(d), Stereo-Pairs: (a)-(c)&(b)-(d) (AOX3E)

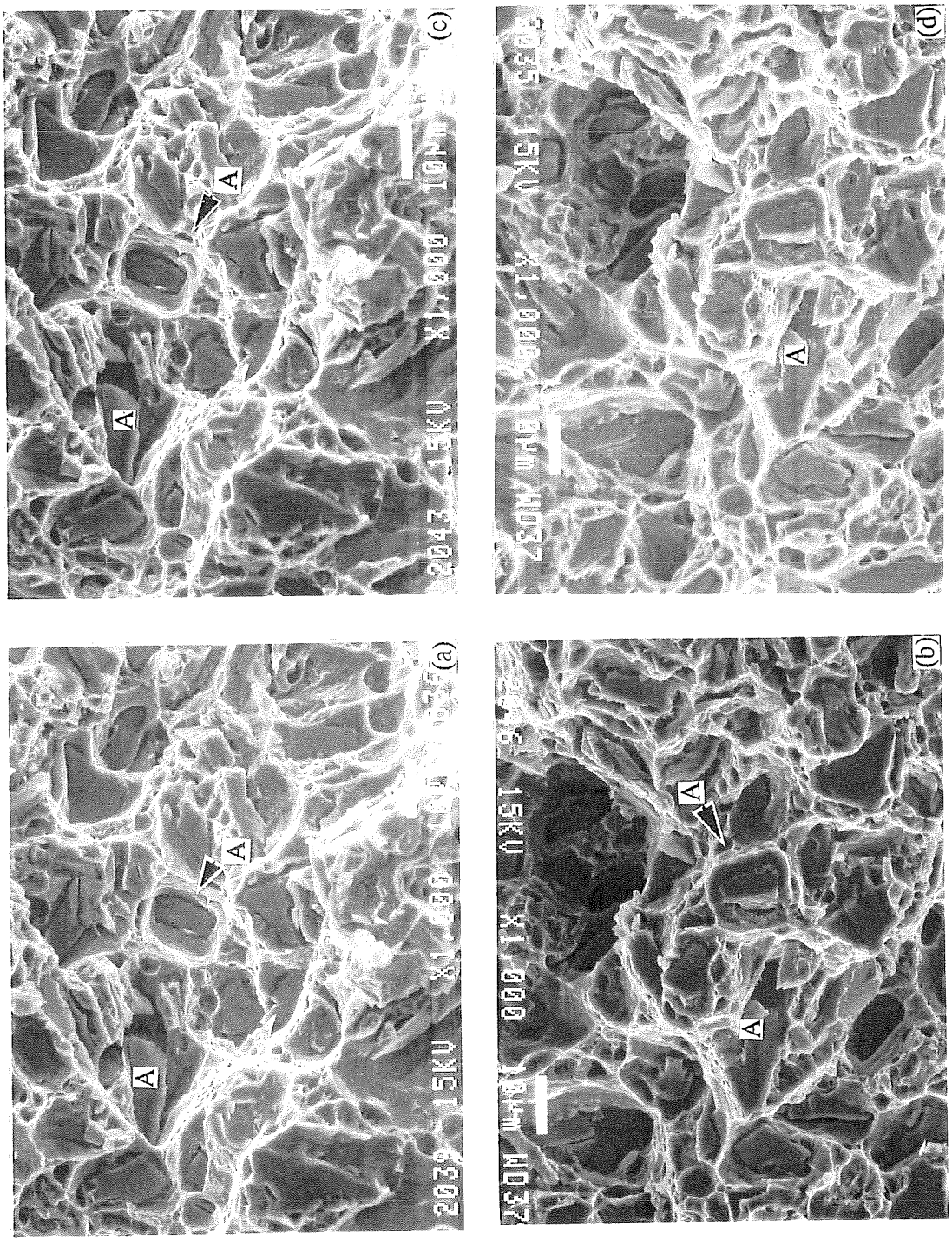

Fig. 5 Fracture Surfaces of Extruded Composites, Matching Pairs: (a)-(b)&(c)-(d), Stereo-Pairs: (a)-(c)&(b)-(d) (AROE)

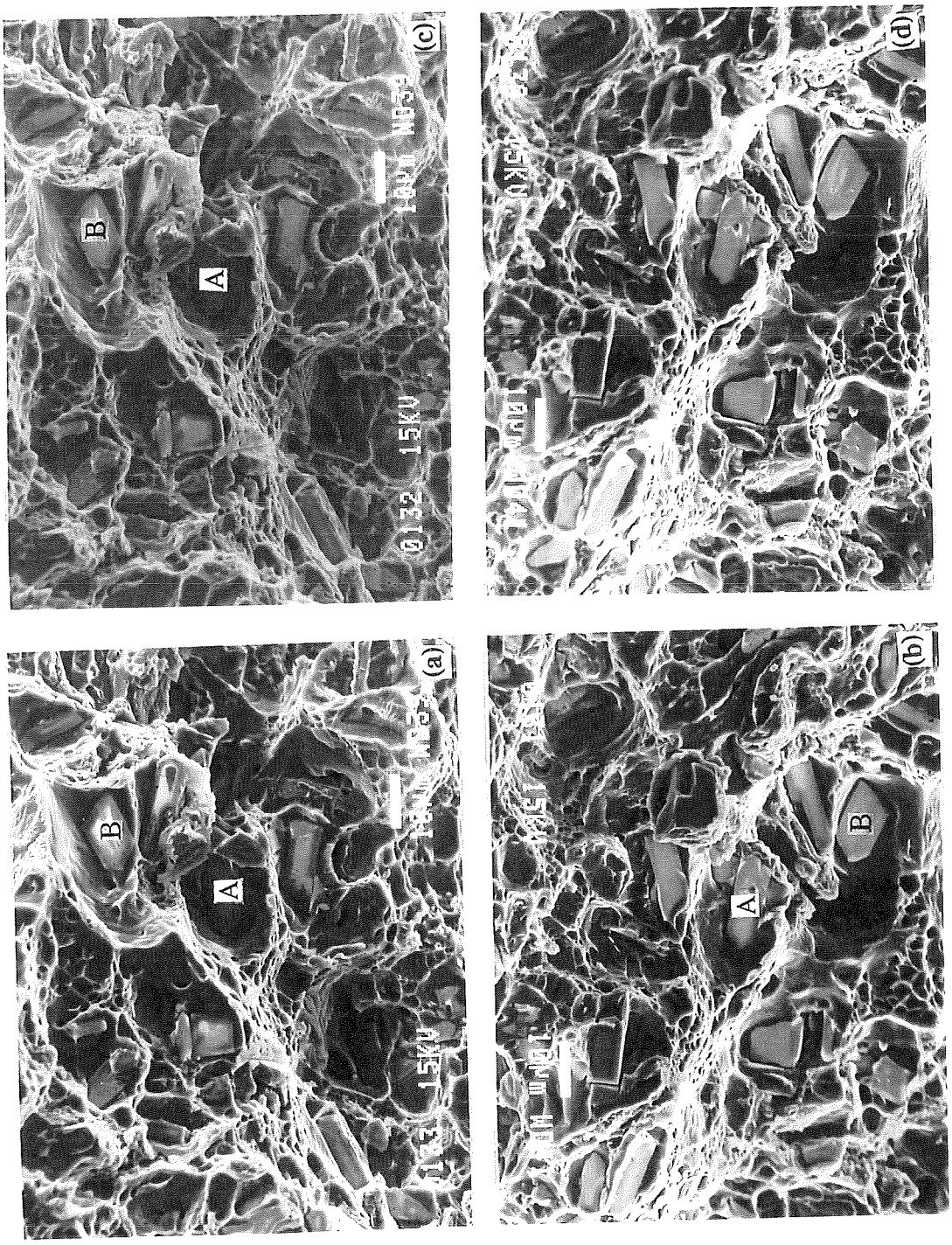

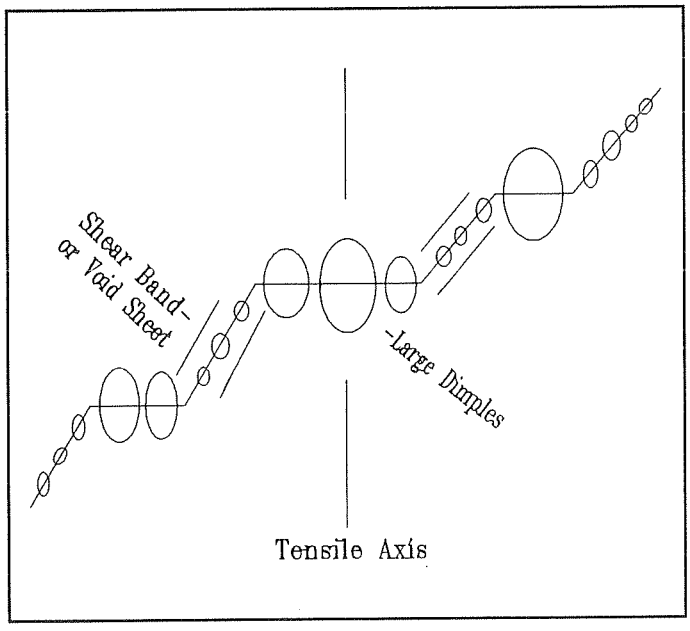

Fig. 6 Schematic Diagram of Dimple Formation

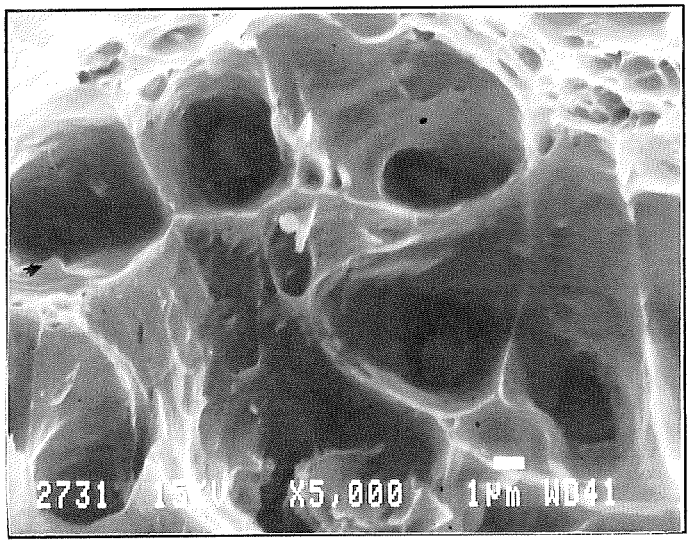

Fig. 7 SEM Micrograph Showing Small Elongated Dimples Caused by (Fe, Mn)-Rich Inclusions (ARSE)

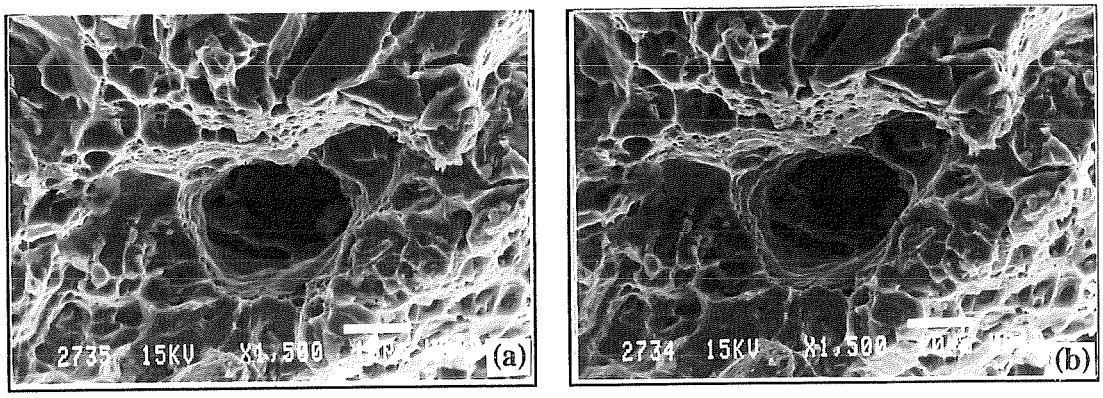

Fig. 8 (a),(b) Deep Dimple with Fine Striations on Its Wall
(SEM Stereo-Pairs, AOX3E, 25°C)

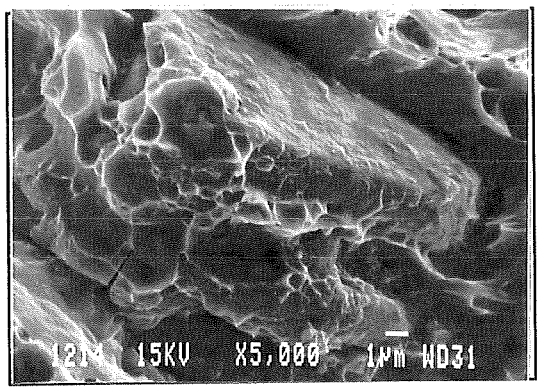

Fig. 9 Decohered Particle on a Fracture Surface (AROE, 25°)

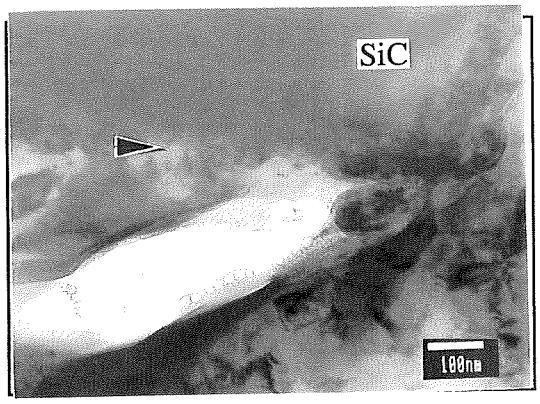

Fig. 10 TEM Micrograph Showing the Site of Decohesion
(Arrow Indicating the Reaction Zone, AOX3E)

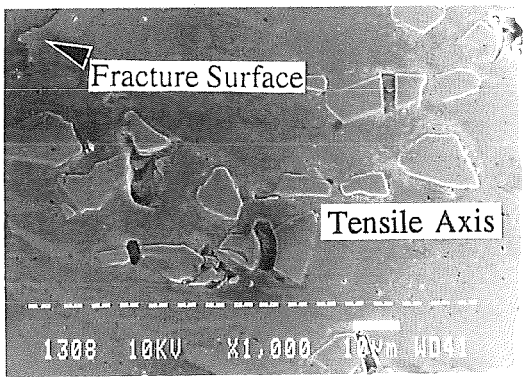

Fig. 11 SEM Micrograph of Longitudinal Section, Showing the Nucleation of Voids (ARSE)

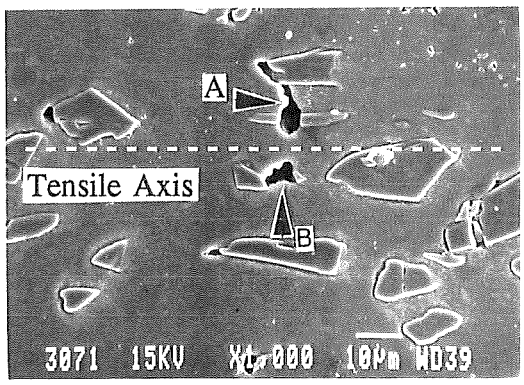

Fig. 12 SEM Micrograph of Longitudinal Section (1 mm from the Fracture Surface (AOX3E, 25°C))

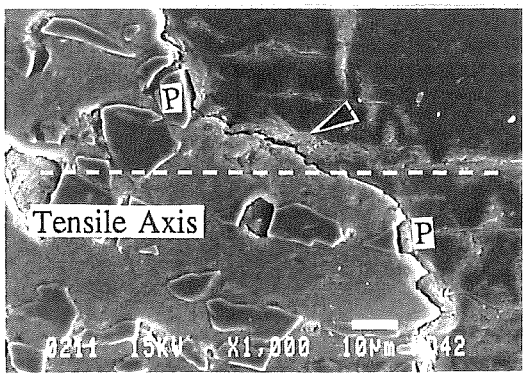

Fig.13 Particles (P) at Different Height Levels Joined by a Crack Propagating in the Matrix (ARSE)

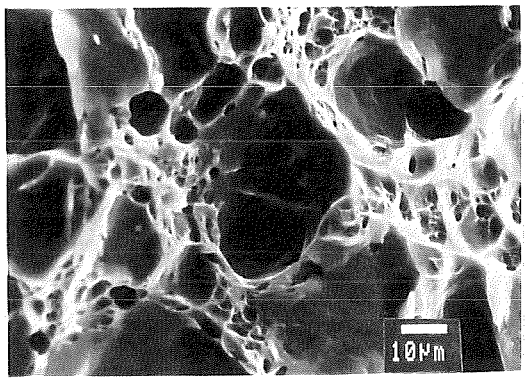

Fig. 14 Fracture Surface of the Extruded Monolithic 5083Al Alloy

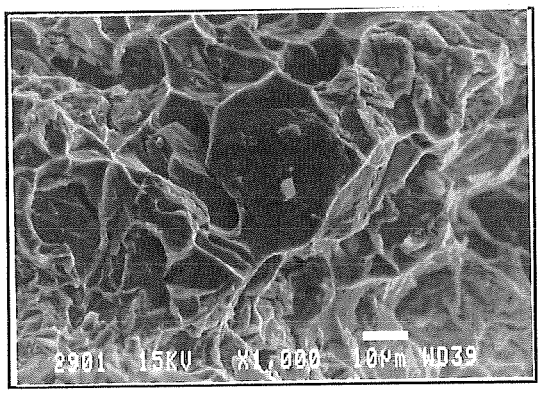

Fig.15 Decohered Particles on the Fracture Surface of the As-cast Composites (AOX3)

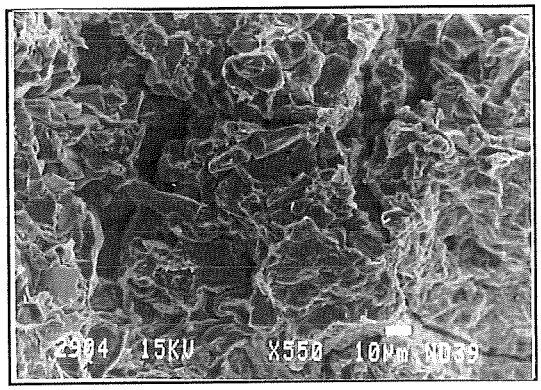

Fig.16 Secondary Cracks in a Cluster of Particles (AOX3)

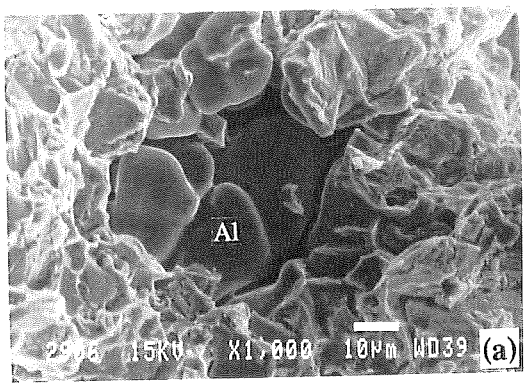

Fig. 17 (a) Cavity Observed at the Boundaries of the Dendrites
(b) Corresponding X-ray Maps (AOX3)

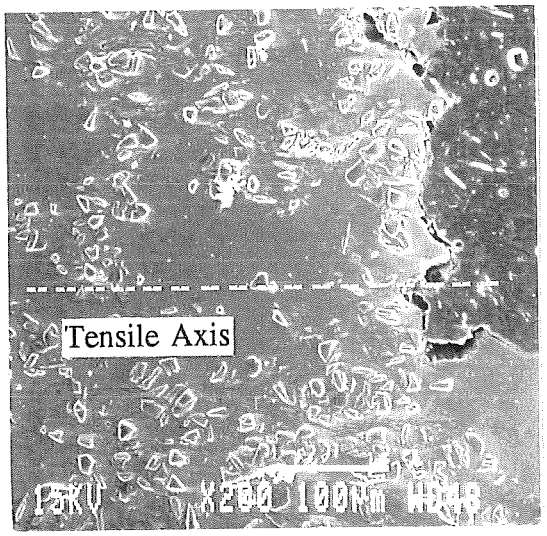

Fig. 18 Crack Formed in an Area with High Density of Particles (As-cast Composites, Longitudinal Section)

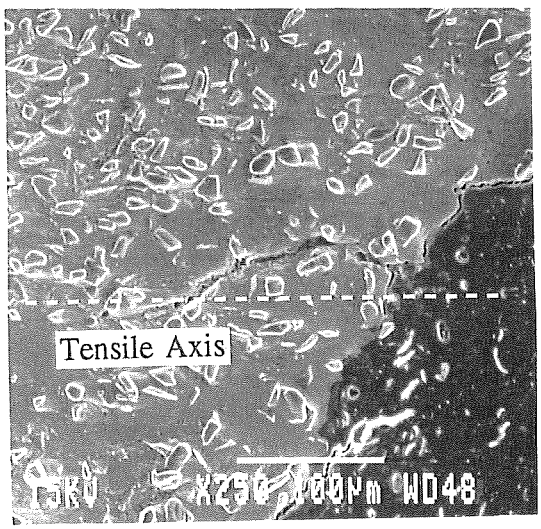

Fig. 19 Crack Parallel to Tensile Axis (AOX3)

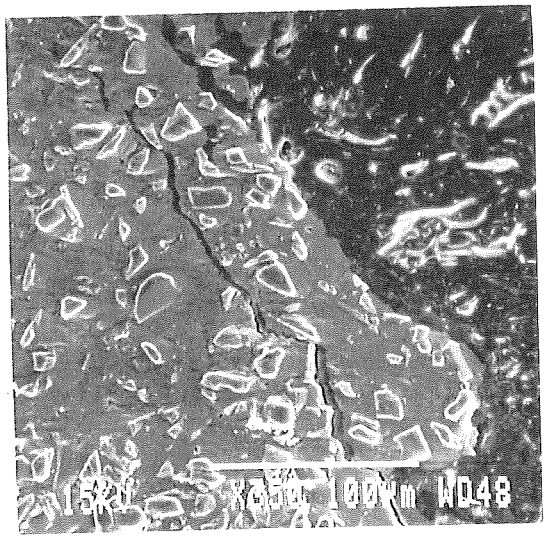

Fig. 20 Crack Parallel to Fracture Surface

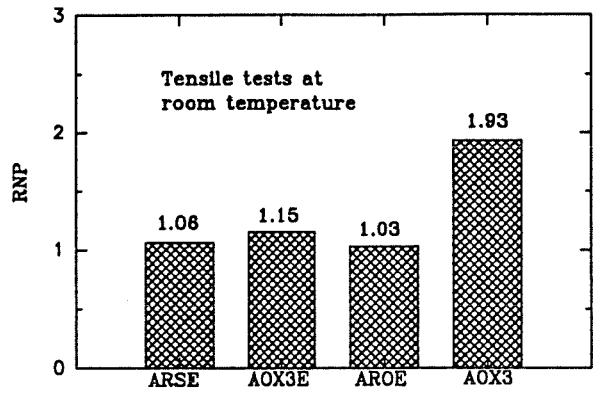

Fig. 21 Ratio of the Number of Particles on a Fracture Surface to that on a Polished Surface

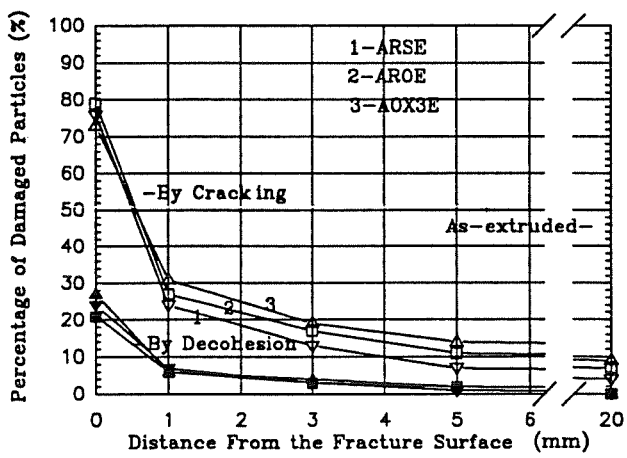

Fig. 22 Variation of the Number of Damaged Particles as a Function of Distance from the Fracture Surface

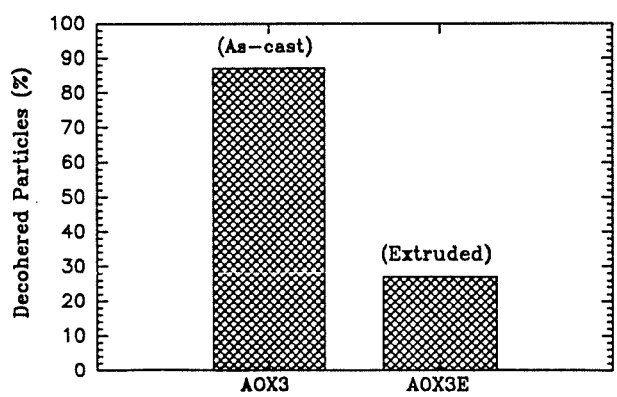

Fig. 23 Number of Decohered Particles on the Fracture Surfaces

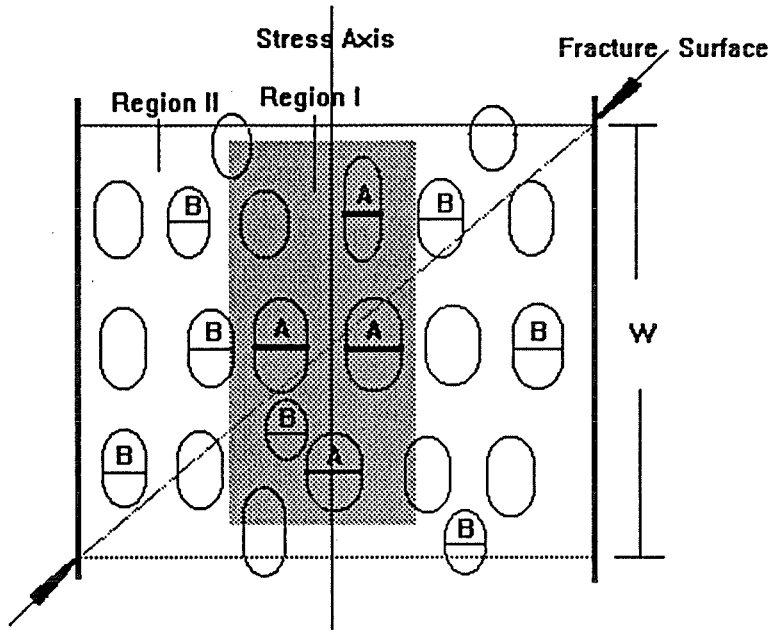

Fig. 24 Schematic Diagram of the Fracture Process in Extruded Particle-Reinforced Composites

(1) Particles(A) are cracked in **Region I** because of the geometrical factors (size, aspect ratio) and the stress state.
(2) Local plastic flow occurs in **Region I** because of the decrease of the constraint. The stress state between two cracked particles is also changed.
(3) **Region II** has to support more loads because of the unloading in **Region I**.
(4) Particles(B), mainly in **Region II**, are cracked.
(5) Plastic flow extends across the section in **Region W**.
(6) With the increase of plastic deformation in **Region W**, more particles are cracked and shear bands in the matrix between the cracked particles are formed.
(7) Coalescence of the small voids in the shear bands results in the final fracture of the composites.

3.4 The Portevin-Le Chatelier Effect in an Al-Mg (5083) Monolithic Alloy and Al-Mg (5083)/Particles Reinforced Composites

W.M. Zhong*, G. L'Espérance*, M. Suéry**

* Ecole Polytechnique de Montréal, Centre de Caractérisation Microscopique des Matériaux (CM)^2, Case Postale 6079, Succ. "A", Montréal, Québec, Canada H3C 3A7

**Institut National Polytechnique de Grenoble, Génie Physique et Mécanique des Matériaux, GPM2, URA CNRS 793 ENSPG, B.P.46, 38402 St Martin d'Heres Cedex, France

Abstract

In this paper, the Portevin-Le Chatelier effect in Al-Mg (5083) matrix composites (extruded) and the monolithic 5083 aluminum alloy are discussed. This effect has been found to be more pronounced in extruded composites than in the extruded monolithic alloy. Serration types are also different for different materials. Tensile tests were carried out at 25°C with strain rates in the range from 10^{-3} to $10^{-4}s^{-1}$. Three types of composites reinforced by as-received SiC particles, artificially oxidized SiC particles or Al_2O_3 particles were examined. Artificial oxidation of SiC particles (with 3.04 wt%

SiO_2) prior to their incorporation not only reduces both the UTS and the elongation to fracture of the composites but also greatly affects the serrated deformation of the composites.

1. Introduction

In our previous studies [1-5], interfacial reactions, dynamic recrystallization during extrusion, tensile properties and the fracture mechanisms of the 5083 Al matrix composites deformed at various temperatures were discussed. It was found that the microstructure, the tensile properties and the fracture behaviour of the composites are very different from those of the monolithic alloy. In addition, the properties of the composites are different for different reinforcements.

'Jerky flow' is often observed in the stress-strain curves of Al-Mg alloys [6-11]. The discontinuous yielding observed during serrated flow is known as the Portevin-Le Chatelier (PLC) effect. Both the micro- and macroscopic concepts of this effect have been discussed in many studies on monolithic alloys. However, a study of the PLC effect in metal matrix composites has not been reported to our knowledge.

The appearance of serrations in the stress-strain curves is usually associated with conditions for which the strain rate sensitivity of the flow stress becomes negative [6,12].

The microscopic reason for negative strain rate sensitivity is dynamic strain ageing (DSA) considered to arise from the interaction between diffusing solutes and mobile dislocations [10,11]. Gliding dislocations are temporarily held up by obstacles, e.g. forest dislocations. Solute atmospheres form on forest dislocations and then drain by pipe diffusion from the forest dislocations to mobile dislocations [11,12] (some models also assume that the atmospheres are formed on (mobile) dislocations by bulk diffusion during the waiting time). Since DSA is thermally activated, it occurs only within a certain range of temperatures and strain rates. The shape and amplitude of the serrations are affected not only by the amount of strain, strain rate and temperature during deformation, but also by the composition and the grain size of the alloys [13,14]. This phenomenon is observed at both room temperature and higher temperatures (e.g. 250-300°C [15]). In Al-Mg matrix composites, the introduction of reinforcements into the matrix often causes differences in the dislocation structure and other microstructural features as pointed out previously [4,5]. In this study, the effect of interfacial reactions, grain size and strength of reinforcement on the PLC phenomenon is presented.

2. Experimental Procedures

The 5083 matrix composites were fabricated using a modified compocasting technique (see [1-2] for details). The ingots were extruded at 480°C with an extrusion ratio of 16:1. Tensile tests were performed at a constant cross-head velocity at 25°C.

The initial strain rate was $1.6x10^{-3}s^{-1}$ at 25°C. The tensile samples had an initial 25 mm gauge length and a 4 mm diameter. Instron 1125 and Zwick 1474 tensile machines were used.

3. Results and Discussion

Serrated yielding was observed during tensile testing of the composites at room temperature as shown in figure 1. Table I gives the maximum serration amplitude and the serration peak distance for different materials. The strain rate sensitivity (*m*) of the flow stress was negative (about -0.02) as estimated by changing the initial strain rate from $1.6x10^{-3}s^{-1}$ to $8x10^{-1}s^{-1}$. Depending on the appearance of serrations, the serrations can be classified as type A (a rise above followed by a drop below the general stress level), B (near constant oscillations), C (sawtooth-shaped), D (plateaus), E (irregular serrations appear at high strains, or near the maximum load) and the possible combinations among these types (see figure 2) [6,14]. It has been reported that the type of serrations observed are a function of experimental conditions such as strain, strain rate and temperature etc. [6,12,14]. In our case, the types of serrations were found to be different in different materials. Thus, in the extruded monolithic alloy (5083E), type A serrations were observed, type (A+B) in the composites reinforced with as-received SiC (ARSE) and Al_2O_3 (AROE) particles, and type (D+B) in the composites reinforced with

oxidized SiC particles (AOX3E).

However, the amplitudes of serrations in the composites are much larger than those in the monolithic 5083 Al alloy. This is mainly caused by the large difference in grain size (50 μm in extruded monolithic alloy compared to 5 μm in extruded composites). Usually the serrations become more pronounced with decreasing grain size, since an increasing number of grain boundaries contributes to hold down (or slow down) the mobile dislocations and to increase the waiting time for each flight. As a result, there will be more solute atoms arriving at the dislocations and the locking strength will increase [13,14]. The magnitude of the serrations ($\Delta\sigma_s$) in Al-4 wt% Mg alloys is reported to satisfy the following relationship with the grain size (d) [13]:

$$\Delta\sigma_s = A + Bd^{-1/2} \qquad .....(1)$$

with A = 1.18-1.37 (MPa) and B = 0.735-0.755 (MPa $mm^{1/2}$) for a strain rate of $1.7x10^{-5}s^{-1}$. However, in our case, the strain rate used was $1.6x10^{-3}s^{-1}$ and the actual matrix compositions were about 3.9, 3.7 and 2.5-3.0 wt% Mg in the ARSE, AROE and AOX3E composites respectively, due to the different thicknesses of the reaction zone formed at the matrix/particle interface in the different composites, as discussed in [1,2] (it is 4.1 wt% Mg for the 5083E alloy). Thus, using these values for constants A and B may result in an over-estimation of the $\Delta\sigma_s$ because of the differences in strain rate and in alloy composition for the composites [13,16]. Using A=1.0 and B=0.7 for

simplicity, $\Delta\sigma_s$ is approximately equal to 4 MPa for 5083E (5083 monolithic alloy) and 11 MPa for the composites (see Table I). These calculated results are very close to our experimental results (Table I) for the 5083E sample (the calculated value is only 1 MPa larger than the experimental value owing to the larger strain rate used in our experiment). In the case of the composites, the over-estimation is larger than 1 MPa probably because of the relatively lower Mg contents in the matrix, however the calculated values are still less than the experimental values for AROE and particularly for ARSE samples.

Finally, the relatively smaller serration amplitude (about 5-7 MPa) in the AOX3E sample may be caused by its relatively lower Mg concentration (about 2.5-3 wt% Mg) in the matrix, and its relatively lower particle strength due to oxidation [2,3]. Usually, with increasing Mg content, the serration amplitude increases and the serration peak distance decreases [13]. The strength of the reinforcing particles may also affect the shape and amplitude of the serrations, because stronger particles will be more efficient to impede dislocation motion, whereas, weaker particles are more likely to break thereby allowing dislocations to annihilate at the crack surface. In addition to the effect of grain size, other factors may also contribute to serrated yielding. For example, the relatively large dislocation density and the presence of reinforcing particles in the composites will increase the possibility that moving dislocations are delayed by forest dislocations and particles, and will also decrease the flight distance (distance between serration peaks) compared to that of the monolithic alloy, as shown in Table I. The relationship between

the locking strength ($\Delta\sigma_{sc}$), the solute concentration (C_s) and the strength of obstacles is given as [16]:

$$\Delta\sigma_{sc}=Ef\mu C_s(Dt_w) \quad .....(2)$$

Here, E is a constant which depends on the interaction energy between the solute atoms and the dislocations, and constant f increases with increasing obstacle strength, μ is the shear modulus of the matrix, D is the diffusion coefficient of the solute atoms in the alloy and t_w is the dislocation waiting time. Thus, decreasing C_s and f will decrease $\Delta\sigma_{sc}$ - the locking strength.

Our results show that different types of serrations are observed in different materials under the same experimental conditions, indicating that the serration types may also be associated with the microstructure of different materials. The presence of type (A+B) serrations in the composites of ARSE and AROE in stead of type A as observed in the monolithic alloy may result from impediment of the dislocations by the reinforcing particles. It is interesting that type (D+B) is observed in the composite reinforced by oxidized SiC particles, indicating dislocations gradually break through the obstacles in this case instead of suddenly.

Above all, the characteristics of the DSA phenomenon in the composites can be explained by their smaller matrix grain size, their relatively larger dislocation densities,

the strength of the reinforcing particles and the extent of interfacial reactions which change the composition of the matrix. Finally, DSA will affect the strength of the composites. At higher strain rates, the flow strength will be lower due to its negative strain rate sensitivity. This may also promote localization of plastic deformation (in areas deformed at relatively large strain rates or forming PLC slip bands) and decrease the ductility of the composites.

4. Conclusions

The Portevin-Le Chatelier effect is more pronounced in extruded composites than in the monolithic 5083 alloy. It is observed that a small grain size, a large number of reinforcing particles and large dislocation densities contribute to an increase of the "locking strength". The change of the matrix composition caused by interfacial reactions also affects the amplitude and the shape of the serrations. The types of serrations observed are associated with the microstructure of the materials. The strength and the ductility of the composites are also likely to be affected by the strong DSA phenomenon.

Acknowledgements

The authors gratefully acknowledge the NATO International Scientific Exchange Programme (Grant no. CRG 900950) and the National Science and Engineering Research Council (NSERC) of Canada (strategic grants) for financial support. They thank E. Goiffon who took part in some of the experiments and L. Salvo and J.J. Blandin for their help in preparing the composite materials.

References

1. W.M. Zhong, G. L'Esperance, M. Suery, Interfacial Reactions in Al-Mg (5083) alloy/SiCp Composites During Fabrication and Remelting, (accepted by Metall. Trans. A)

2. W.M. Zhong, G. L'Esperance, M. Suery, Interfacial Reactions in Al-Mg (5083) alloy/Al_2O_3p Composites During Fabrication and Remelting, (accepted by Metall. Trans. A)

3. W.M. Zhong, G. L'Esperance, M. Suery, E. Goiffon and J.J. Blandin, Effect of Thermomechanical Processing on the Microstructure and the Mechanical Properties of Al-Mg (5083)/Particles Composites, part I, dynamic recrystallization of the composites, (accepted by Mater. Sci. Eng.)

4. W.M. Zhong, G. L'Esperance, M. Suery, Effect of Thermomechanical Processing on the Microstructure and the Mechanical Properties of Al-Mg (5083)/Particles Composites, part II, tensile properties at various temperatures, (accepted by Mater. Sci. Eng.)

5. W.M. Zhong, G. L'Esperance, M. Suery, Effect of Thermomechanical Processing on the Microstructure and the Mechanical Properties of Al-Mg (5083)/Particles Composites, part III, fracture behaviour of the composites, (accepted by Mater. Sci. Eng.)

6. J.M. Robinson and M.P. Shaw, Inter. Mater. Reviews, vol.39, No.3(1994), p.113

7. D. Park and J.G. Morris, Scripta Metall. and Mater. vol.29, No.3(1993),

p.365

8. S. Kumar, Scripta Metall. and Mater. vol.33, No.1(1995), p.81

9. J. Balik and P. Lukac, Acta Metall. vol.41, No.5(1993), P.1447

10. J.M. Robinson and M.P. Shaw, Mater. Sci. Eng. A159(1992), p.159

11. R.A. Mulford and U.F. Kocks, Acta Metall., vol.27(1979), p.1125

12. P. Hahner, Mater. Sci. Eng., A164(1993), p.23

13. H. Fujita, T. Tabata, Acta Metall., vol.25(1977), p.793

14. Encyclopedia of Mater. Sci. and Eng., eds. R.W. Cahn, Supp. vol.1(1988), p.505

15. G. L'Esperance, M.H. Loretto, W.T. Roberts, D. Price and D.V. Wilson, Metall. Trans. A, vol.15(1984), p.913

16. A. Van Den Beukel, U.F. Kocks, Acta Metall., vol.30(1982), p.1027

Table I Maximum Amplitude (MPa, calculated and experimental) and Peak Distance of Serrations (measured) for Different Materials

Materials	Calculated Stress Amplitude*	Experimental Stress Amplitude*	Peak Distance (converted to strain, %)
ARSE	11	16	0.59
AROE	11	12	0.52
AOX3E	11	7	0.52
5083E	4	3	1.0

* Stress Amplitude - MPa

** 5083O - annealed monolithic alloy, data from Metals Handbook 9th edition vol.2
5083E - extruded monolithic 5083 alloy
AOX3 - as-cast 5083/SiCp (oxidized 3.04 wt%)
ARSE - 5083/SiCp extruded
AROE - 5083/Al_2O_3p extruded
AOX3E - 5083/SiCp (oxidized 3.04 wt%) extruded

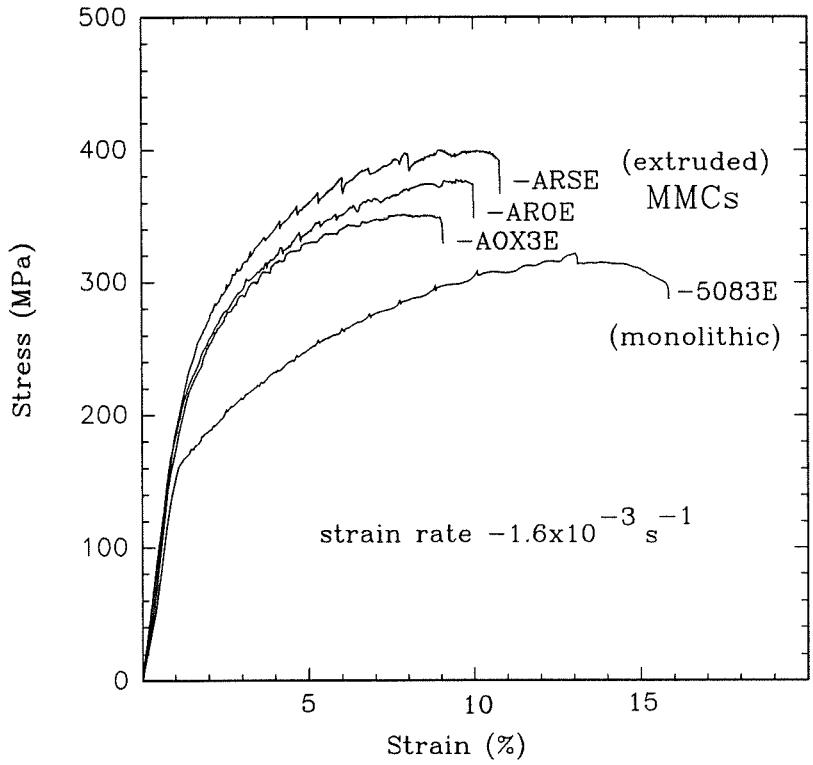

Figure 1 Tensile Test Curves Obtained at Room Temperature

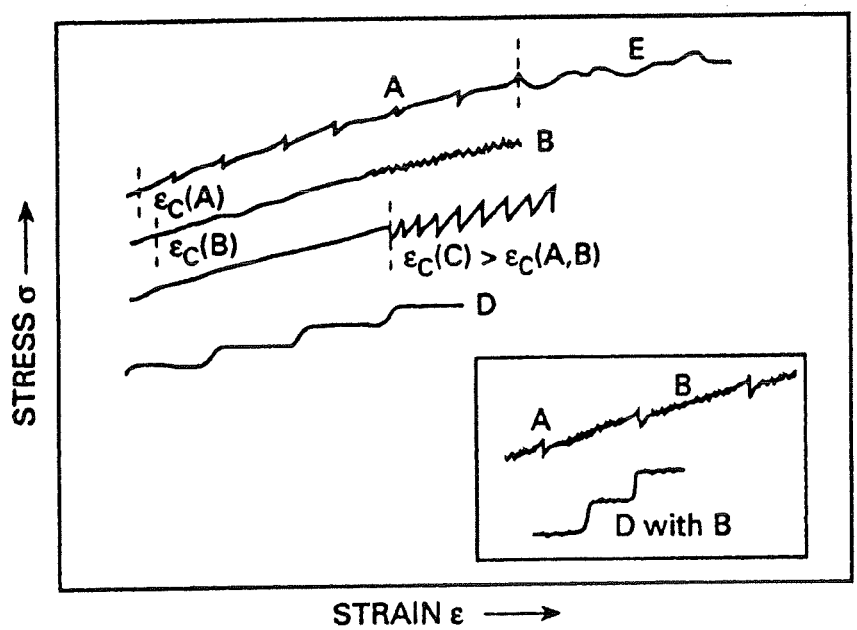

Figure 2 Examples of Different Types of Serrations [6]

3.5 Final Remarks in the Study of Deformation and Fracture of the Composites

From the results presented in this chapter, it can be seen that dynamic recrystallization occurs during extrusion of the composites owing to the large number of reinforcing particles incorporated in the matrix. As a result, the microstructure of the composites is changed after extrusion, with small grains (about 5 μm) appearing in the matrix. The UTS of the extruded composites can be as high as 360 to 400 MPa, and the elongation to fracture is near 10% at room temperature. These values are much larger than those of the as-cast composites. A large number of dislocations, a small grain size and a significant load transfer from the matrix to the particles all contribute to the strength of the composites. The fractographs of extruded composites are different from those of as-cast composites. It is shown that extrusion not only changes the microstructure of the composites, but also changes the fracture mechanisms of the composites.

Deformation at room temperature is influenced by the nature of the interfaces or the type of particles; however, it is controlled mainly by the deformation behaviour of the matrix at high temperatures. For example, at room temperature, the UTS and the elongation to fracture of the composite reinforced by artificially oxidized SiC particles are reduced, whereas, at high temperatures, such as 350° and 550°C, they are quite

similar to those of composites reinforced by SiC or Al_2O_3 particles. Moreover, the Portevin-Le Chatelier (PLC) effect observed for the composites deformed at room temperature is also related to the type of reinforcing particles. On the other hand, the fracture mechanism of the composites is changed with a change in deformation temperature.

Finally, in chapters 2 and 3, the interfaces and the mechanical properties of the 5083 aluminum matrix composites reinforced by different particles were discussed. In order to establish more complete relations between the different aspects of our study and to better understand the important factors in the fabrication and the processing of the composites, a general discussion and conclusions will be given in the next two chapters.

CHAPTER 4

GENERAL DISCUSSION

In the previous chapters, several important features during fabrication and deformation of the 5083 aluminum matrix composites reinforced by different particles have been discussed. In chapter 2, the interfacial reactions between 5083 aluminum alloy and particles of SiC, oxidized SiC and α-Al_2O_3 were studied. Chapter 3 presented and discussed the microstructure of the extruded composites and the tensile properties and the fracture behaviour of the different composites. The results of our studies indicate that the compocasting method may be used to produce high quality composites. The distribution of the reinforcing particles is relatively uniform on a macroscopical scale. Attack of the reinforcing particles by the matrix was well controlled due to the relatively low incorporation temperature and the short holding time when the alloy is completely molten during fabrication. In comparison, other fabrication methods, such as the vortex method or die casting, usually, require longer fabrication times and higher incorporation temperatures. However, segregation at dendritic boundaries and the oxide skins formed and trapped during incorporation of the particles are also observed in the composites fabricated using the compocasting method. Fortunately, these problems can be solved to a great extent by the subsequent extrusion stage. A further discussion of the improvement of the quality of the composites will be given in the following sections.

4.1 INTRODUCING A SiO_2 LAYER ON THE SURFACE OF SiC PARTICLES

As described in section 2.1, to produce a 500 nm thick layer of SiO_2 requires that the SiC particles are held at 1100 °C for more than ten hours in air. From our remelting experiments, we found that the artificially oxidized SiC particles are attacked by liquid aluminum more slowly. Both the SiO_2 layer, and the newly formed MgO or $MgAl_2O_4$ layer caused by the interfacial reaction between Mg and SiO_2, can delay the contact of liquid aluminum with SiC. From the protective point of view, it is expected that a thicker SiO_2 layer on the SiC surfaces will lead to a great protection. In our experiments, SiC particles oxidized to 14.06 wt% (the thickness of SiO_2 was then about 500 nm to 800 nm) were not attacked when held at 800 °C for 30 minutes. However, with only 3.06 wt% of SiO_2 on the surfaces of SiC particles, both the tensile strength and the plasticity of the composites decrease significantly, as seen in section 3.2. Because, as discussed in chapter 3, the SiO_2 layer changes the matrix composition, and probably the properties of particles and interfaces, the matrix composition and the total composite properties will become more difficult to control. In fact, in as-cast composites fabricated by the compocasting method, as-received SiC particles attacked by liquid aluminum are not observed. The interface is also stable during extrusion. Therefore, for the sake of mechanical properties and economy, artificial oxidization of SiC particles is unnecessary for as-cast materials. Of course, in certain cases, when the composites must be remelted and held for longer periods of time at high temperatures such as when the vortex method is used to fabricate the composites, protecting of SiC is required. In this case, we must

choose the thickness of the oxide layer carefully, using as thin an oxide layer as possible.

4.2 PROTECTIVE ROLE PLAYED BY THE INTERFACIAL REACTION PRODUCTS

In the discussion of the protective role of the newly formed MgO and $MgAl_2O_4$ crystals at the interfaces of both SiC/matrix and Al_2O_3/matrix in section 2.2, it was suggested that the MgO crystals protect the reinforcing particles better than the $MgAl_2O_4$ does. Forming MgO from SiO_2 leads to less volume shrinkage, and forming MgO from Al_2O_3 results in a larger volume expansion; thus, the diffusion path between these MgO crystals will be narrower than that between $MgAl_2O_4$ crystals. Increasing the Mg content in the matrix, decreasing the thickness of the reaction zone and decreasing the reaction time will increase the possibility of obtaining MgO crystals. It is usually found that the MgO crystals formed by interfacial reactions are much finer than the $MgAl_2O_4$ crystals (5 to 10 nm as compared to 0.5 to 1 μm). Although, smaller MgO crystals in the reaction zone will increase the area of crystal boundaries and thus enhance diffusion, the much larger volume expansion associated with formation of MgO, as discussed above, leads to narrower diffusion channels, that is, a much denser reaction zone, thus resulting in a better protective reaction layer compared to the $MgAl_2O_4$ crystals. In additions, the larger $MgAl_2O_4$ crystals will induce more stress concentration at the interface during deformation. It is, therefore, possible that forming MgO at the interface will have a less harmful effect on the properties of the composites.

4.3 EFFECT OF SEGREGATION OF SOLUTE ELEMENTS AND RESIDUAL STRESS

Segregation of Mg at interfaces was observed in our experiments. However, it is difficult to distingush the contribution of metallic Mg from that of MgO at interfaces between the matrix and the SiC or Al_2O_4 particles. Thus, more effort must be made to quantify the true metallic Mg concentration at the interface. From observations made after tensile tests at 550 °C, a Mg rich incipient phase could be seen on the surface of a decohered reinforcing particle. The liquid phase was formed during tensile testing because high Mg content at the interfaces decreases the local melting point of the matrix, as discussed in section 2.4 (an increase of 1 at% Mg reduces the melting point by about 6°). It has been reported, as mentioned in chapter 1, that this liquid phase may be one of the important factors in achieving a high strain rate superplasticity behaviour in composites. However, the effect of the segregation on the room temperature deformation behaviour seems different from that at high temperatures although experimental evidence is not available here, since Mg will distort the local lattice and harden the matrix at the interface, leading to larger stress concentrations near reinforcing particles thereby promoting cavitation at the interface.

The effect of residual stresses in metal matrix composites on their mechanical properties should not be ignored. As discussed in section 1.3.1, the average tensile residual stresses in an aluminum matrix can lead to a decrease of 20 to 30 MPa in the

yield strength. The residual stresses and the stress state near a SiC particle were determined using convergent beam electron diffraction (CBED); however, these results could not be related to the bulk stresses in composites because of the stress relaxation in TEM thin foils. Therefore, further work is necessary to relate directly the results obtained from CBED measurements to mechanical properties.

4.4 EXTRUSION AND PROPERTIES OF THE COMPOSITES

As shown in chapter 3, the effect of extrusion on mechanical properties of composites is significant. As discussed above, the main advantage of compocasting is the short fabrication time which prevents extensive interfacial reactions between the reinforcing particles and the matrix. However, the oxide skins formed during the incorporation of the particles into the matrix, the cavities formed during solidification, and the segregation of reinforcing particles and solute atoms at dendrites boundaries are still important issues in determining the quality of the castings. Extrusion increases not only the elongation to fracture, but also the tensile strength of the composites. The main effects of the extrusion, as discussed in chapter 3, are: to redistribute the particles, to break the oxide skins, to weld the cavities and change the size and shape of the matrix grains. From section 3.2, we can see that the microhardness of the composites increased about 25%. This increase is caused mainly by the small grain size and high dislocation density in the matrix. It was noticed that, at room temperature, the UTS of extruded composites increases more than 100% when compared to as-cast composites. This is also

related to the change in the fracture mechanism. On the fracture surface of as-cast composites, most of the reinforcing particles are decohered from the matrix; whereas, on the fracture surface of extruded composites, most of the reinforcing particles are cracked, as shown in section 3.3. The change of the matrix microstructure and the more uniform distribution of particles after extrusion delay the nucleation and growth of microcavities during tensile deformation, therefore, the matrix has more chance to be hardened by deformation. With the increase of matrix strength by work-hardening, there will be more load transferred to the reinforcing particles according to the shear lag model discussed in section 3.2. This is why the UTS of the composites increases and the elongation to fracture also increases. It is important to suppress the formation of large voids caused by particle cracking or interface decohesion, since these large voids will cause localization of plastic deformation in the matrix and promote the premature fracture of the composites. Thus, the quality of the reinforcing particles and the bond strength between the matrix and the particles are the important factors in order to have strong and tough composites.

Extrusion improves the properties of composites, however, it also causes the particles to align or to crack. Particle alignment causes anisotropy in the properties which reduces the advantages of the particle reinforced composites. As well, applications of composites will be limited. Therefore, it is important to improve the quality of as-cast composites. For example, in order to decrease oxygen entrapment during particle addition, the particles could be heated, cleaned and dried. Particles should be added in

a vacuum chamber. It is important to find a more effective way to uniformly distribute the particles in liquid Al. Increasing the cooling rate and increasing the pressure during casting may decrease the matrix grain size and the particle segregation. Using higher pressures can also decrease the cavities in composites.

Certainly, extrusion does improve the room temperature properties of composites. It is also expected that extrusion will directly affect the deformation and fracture of composites at high temperatures. Since an uniform distribution of particles and small grain sizes can facilitate deformation of the materials, decrease stress concentrations and promote grain boundary sliding at high temperatures, cavitation will be reduced and a large elongation to fracture will be obtained. In our experiments, the elongation to fracture of the composites was only about 50%, and the values of strain rate sensitivity in the temperature range from 350°C to 550°C are less than 0.3. It is believed that the size of the reinforcing particles was too large, resulting in large stress concentrations or a great resistance to the sliding of grain boundaries, thus promoting cavitation.

4.5 THE PORTEVIN-LE CHATELIER EFFECT IN Al-Mg MATRIX COMPOSITES

This is the first time that the Portevin-Le Chatelier (PLC) effect in composites has been reported. The role of the Portevin-Le Chatelier (PLC) effect in mechanical properties of composites is still not clear, although some relations between the

microstructure of the matrix, the properties of the reinforcing particles and the nature of the interfaces have been found. Usually, it is believed that the PLC effect decreases the plasticity of materials. Our experimental results show that the strongest PLC effect (highest stress amplitude) corresponds to the composite with the highest UTS and largest elongation to fracture. This implies that the effect of the PLC phenomenon on material properties is dominated by the increase of plasticity caused by delayed cavitation.

4.6 FINAL REMARKS ON APPLICATION OF THE COMPOSITES

We have systematically investigated the 5083 Al matrix composites from materials casting to materials processing and deformation and fracture behaviours. We believe that this type of composite has great commercial potential. As we have mentioned before, 5083 Al has a of good corrosion resistance and good weldability. With these properties, 5083 Al may be used in the marine industry or in the automobile and aerospace industries to make products such as oil tanks, shift parts etc.. Introducing ceramic particles into the 5083 Al alloy has shown a 30% increase of materials strength (for extruded composites). The composites have an elongation to fracture of about 8 to 10 % and show a large work-hardening rate during deformation. The extrusion force, at 480°C, is about 100 MPa which is not high for manufacturing purposes. Since the 5083 Al matrix has a high Mg content (about 4 to 4.5 wt%), during casting, a thin layer of fine MgO crystals is formed by interfacial reactions between the matrix and the particles (or a oxide layer on particle surfaces), which play an important role in protecting the

reinforcing particles from attack as discussed earlier. These reactions are also believed to improve the wettability of the Al melt to ceramic particles as pointed out in chapter 2. As seen from our experimental results, many particles are cracked during tensile testing, implying that the bond strength between the matrix and thee particles is very strong.

Further work would be necessary to determine the fatigue behaviour and the fracture toughness of the composites.

GENERAL CONCLUSIONS

Having discussed the 5083 Al matrix composites from materials casting to materials processing and the deformation and fracture behaviours of the materials, a general conclusion is give here. We will summarize the important conclusions from different chapters and different sections in this chapter.

1 MATERIALS CASTING AND INTERFACES

(1) In the as-cast composites, there is no attack of SiCp by molten Al whether the SiCp has been artificially oxidized or not prior to their incorporation, due to the relatively low incorporation temperature and the short holding time when the alloy is completely molten during fabrication using the compocasting method.

A reaction zone, consisting mainly of fine MgO crystals (5-20 nm), is found at the interface between the matrix and different reinforcements (including SiCp and Al_2O_3p particles). The thickness of the reaction zone increases with the thickness of the SiO_2 layer from about 30 nm to 200 nm and 500 nm for as-received SiCp, 3.04 wt% oxidized SiCp and 14.06 wt% oxidized SiCp respectively. At the interface between the matrix and Al_2O_3p, the width of the reaction zone is about 50-80 nm.

(2) In remelted composites with as-received SiCp, the particles are heavily attacked. However, attack of SiCp by molten Al is decreased with increasing thickness of the SiO_2 layer.

It is found that the possibility of obtaining $MgAl_2O_4$ during interfacial reactions increases with the thickness of the SiO_2 layer. The nature of the reaction product is related to the "dynamic" concentration of Mg in the matrix. Similar results are obtained in the reaction between Al_2O_3 and the matrix. MgO is formed at the beginning and $MgAl_2O_4$ eventually appears as the reaction proceeds.

(3) The newly formed MgO (or spinel) crystal boundaries are believed to be the diffusion paths (or channels) for the interfacial reactions to proceed. It was found that the reaction between Mg and Al_2O_3 is more difficult than that between Mg and SiO_2 because the former reaction leads to a volume expansion whilst the latter is asociated with a contraction. Moreover, the formation of MgO from SiO_2 will lead to less volume contraction and the formation of MgO from Al_2O_3 will result in a larger volume expansion compared to that of $MgAl_2O_4$ crystals. Thus, the diffusion paths between the MgO crystals will be narrower than that between $MgAl_2O_4$ crystals. Furthermore, MgO forms more easily when the Mg content in the matrix is high. Therefore, with a higher Mg content in the matrix, a denser MgO reaction zone will be formed more readily, and thus, will protect the particles better than the $MgAl_2O_4$ reaction zone.

(4) Segregation of Mg and Cu at the interfaces of aluminium alloys/SiCp or Si_3N_4w composites has been demonstrated using a graphical deconvolution method. Segregation of Mg or Cu at interfaces leads to a local decrease of the melting point of the matrix, resulting in the presence of a small amount of liquid phase around the particles during deformation of the composites at high temperatures.

(5) The residual stresses near the reinforcing particles were measured using the CBED technique. The effective stresses calculated by the Von Mises yield criterion are near the yield limit of the matrix and are larger near the SiCp and near the corners of the particles.

2 DEFORMATION AND FRACTURE BEHAVIOURS

(1) Large scale dynamic recrystallization was observed in all the extruded composites studied. The average grain size was about 5 μm. Reinforcing particles enhance the nucleation of the recrystallization and more than one grain was nucleated by a particle. In contrast, the microstructure of the extruded monolithic 5083 Al alloy consists mainly of a recovered microstructure.

(2) In the 5083/SiCp and 5083/Al_2O_3 composites, extrusion increases both the UTS (to about 400 MPa) and the elongation to fracture (to about 10%) at room temperature. THe microhardness of the extruded composites is also increased.

Increasing the reinforcement strength will increase both the UTS and the elongation to fracture. Artificial oxidation of the SiC particles (with 3.04 wt% SiO_2) reduces both the UTS and the elongation to fracture of the composites.

(3) At temperatures of 350°C and 550°C, the UTS of the composites decreases and the elongation to fracture increases to about 50%. Elongation to fracture does not increase as much as expected from the increase in the strain rate sensitivity when the deformation temperature increases from 350°C to 550°C, due to the greater possibility of cavitation at 550°C. The effect of different types of particles on the mechanical properties of the composites and on the fracture mechanisms is not obvious at higher temperatures.

(4) A change in the microstructure of the composites by extrusion corresponds to a change in the fracture mechanisms.

In as-cast composites, decohesion of the matrix/particle interface, cavities formed during solidification and fracture along the dendrite boundaries are all sources of void nucleation. Because of the large number of potential void nucleation sites in as-cast composites, premature fracture occurs during tensile testing.

In as-extruded composites, fracture of the reinforcing particles is the main source of void nucleation. Final failure occurs by shear coalescence of the small void sheets in

matrix between the large reinforcing particles (or clusters of particles). The large voids caused by reinforcing particles induce localized deformation in the matrix which accelerates the nucleation, growth and coalescence of the small voids in the matrix. Retarding the formation of the large voids, by improving the quality of reinforcing particles and increasing the interfacial bond strength between the matrix and reinforcements, for example, will increase both the strength and the elongation to fracture of the composites. As mentioned previously, composites with artificially oxidized SiCp particles have lower UTS and elongation to fracture compared to composites with as-received SiC particles. This is explained by the degradation of SiC particles during the oxidation and the thicker interfacial reaction zone consuming more Mg from the matrix thus reducing solute strengthening.

(5) At high deformation temperatures (350°C and 550°C), fracture of the composites is caused by interfacial decohesion between the reaction zone on the surface of the particle and the matrix. Both dimple fracture and intergranular fracture are observed at 350°C. At 550°C, the fracture is caused by cavitation at grain boundaries and near particles. Deformation associated with dislocation slip still plays an important role in the deformation mechanisms at 350°C; however, at 550°C, the deformation behaviour is mainly controlled by bulk diffusion, some grain boundary sliding, and particle/matrix interface decohesion. As well, at 550°C, cavitation at grain boundaries plays an important role in the fracture of composites, whereas, at 350°C, cavitation is greatly associated with reinforcing particles. Thus, more particles were observed on the

fracture surface of the composites deformed at 350°C.

(6) The Portevin-Le Chatelier effect is more pronounced in extruded composites than in the monolithic alloy. It is found that factors such as a smaller grain size of the matrix, a higher strength of the reinforcing particles and a larger density of dislocations are related to an increase of the "locking strength". The PLC effect is also related to the interfacial reactions which cause a variation of the Mg content of the matrix.

REFERENCE

1. L.SALVO, M.SUÉRY, J.G.LEGOUX AND G.L'ESPÉRANCE, Mater. Sci. and Eng. A 135(1991), p.129

2. H.RIBES, R.D.SILVA, M.SUÉRY AND T.BRETHEAU, Mater. Sci. and Tech., July(1990), Vol.6, p.621

3. F.DELANNAY AND L.FROYER, J. of Mater. Sci. 22(1987), p.1

4. C.MARUMO AND J.A.PASK, J. of Mater. Sci. 12(1977), p.223

5. J.G.LEGOUX, H.RIBES, G.L'ESPÉRANCE AND M.SUÉRY, Proc. of Interface in Metal-Ceramics Composites(1989), Anaheim, edited by R.Y.Lin, R.J.Arsenault

6. J.G.LEGOUX, G.L'ESPÉRANCE, L.SALVO AND M.SUÉRY, Proc. of Fabrication of Particulates Reinforced Metal Composites(1990), Montréal, edited by J.Masounave and F.G.Hamel, p.31

7. T.ISEKI, T.KAMEDA AND T.MARUYAMA, J. of Mater. Sci., 19(1984), p.1692

8. A.J.ARSENAULT AND C.S.PANDE, Scripta Metall. Vol.18,(1984), p.1131

9. S.R.NUTT AND R.W.CARPENTER, Mater. Sci. and Eng., 75(1985) p.169

10. P.J.WITHERS, W.M.STOBBS AND A.J.BOURDILLON, J. of Microscopy, Vol.151,(1988), p.159

11. B.HALLESTEDT, Z.K.LIU AND J.ÅGREN, Mater. Sci. and Eng., A 129(1990), p.135

12. R.Y.LIN AND K.KANNIKESWARAN, Proc. of Interfaces in Metal-Ceramics Composites(1989), edited by R.Y.Lin and R.J.Arsenault, Anaheim, p.153

13. K.KANNIKESWARAN AND R.Y.LIN, J. of Metal, 9(1987), p.17

14. D.J.LLOYD AND B.CHAMBERLAIN, Interfaces in Metal-Ceramics Composites, edited by R.Y.Lin and R.J.Arsenault(1989), Anaheim, p.263

15. GUNA SELVADURAY, RAY HICKMAN, Interfaces in Metal-Ceramics Composites, edited by R.Y.Lin and R.J.Arsenault(1989), Anaheim, p.271

16. A.MUNITZ, M.MITZGER AND R.MEHRABIAN, Metall. Trans A, Vol.10 A, 10(1979), p.1491

17. M.FISHKIS. J. of Mater. Sci. 261(1991), p.2651

18. M.STRANGEWOOD, C.A.HIPPLEY AND J.J.LEWANDOWSKI, Scripta Metall., Vol.24(1990), p.1483

19. T.MALIS AND M.C.CHATURVEDI, J. of Mater. Sci. 17(1982), p.1479

20. L.M.DIGNARD-BAILEY, T.F.MALIS, J.D.BOYD AND J.D.EMBURY, CIM Proc., Advanced Structure Materials, 9(1988), p.87

21. ANDREAS MORTENSEN, Mater. Sci. and Eng., A 135(1991), p.1

22. ANDREAS MORTENSEN, J.A.CORNIE AND M.C.FLEMINGS, J. of Metals, 2(1988), p.12

23. C.G.LEVI, G.J.ABBASCHIAN AND R.MEHRABIAN, Metall. Trans. A, Vol. 9A, 5(1978), p.697

24. P.K.GHOSH AND S.RAY, Proc. of fabrication of particulates reinforced metal composites, edited by J.Masounave and F.G. Hamel(1990), Montreal, p.23

25. B.F.QUIGLEY, G.J.ABBASCHIAN, R.WUNDERLIN AND R.MEHRABIAN, Metall. trans. A, Vol. 13A, 1(1982), p.93

26. M.FISHKIS, J. of Mater. Sci. 26(1991), p.2651

27. B.C.PAI AND S.RAY, Mater. Sci. and Eng. 24(1976), p.31

28. J.TAFTΦ, D.O.KARLSEN, Proc, Conf. on cast reinforced metal matrix composites, Chicago, Il, (1988), edited by S.G.Fishman and A.K.Dhingna, p.71

29. G.R.CAPPLEMAN, J.F.WATTS AND T.W.CLYNE, J. of Mater. Sci. 20(1985), p.2159

30. Y.LEPETITCORPS AND J.M.QUENISSAT, Mater. Sci. and Eng. A 135(1991), p.37

31. R.MOLINS, J.D.BARTOUT AND Y.BIENVENU, Mater. Sci. and Eng. A 135(1991), p.111

32. M.PFEIFER, J.M.RIGSBEE AND K.K.CHAWLA, J. of Mater. Sci. 25(1990) p.1563

33. B.S.BOKSTEIN, Defect and Diffusion Forum Vols. 66-69(1989) p.631

34. JENÖ HORVÁTH, Defect and Diffusion Forum Vols. 66-69(1989) p.207

35. A.D.MCLEOD, Proc. of fabrication of particulates reinforced metal composites, edited by J.Masounave and F.G. Hamel(1990), Montreal, p.17

36. P.A.LESSING AND R.S.GORDON, J. of Mater. Sci. 12(1977), p.2291

37. J.R.MICHAEL, J. Microscopy, Vol.147(1987), (3), p.289

38. P.DOIG, Microbeam Analysis, (1982), p.72

39. D.B.WILLIAMS AND A.D.ROMIG, Ultramicroscopy, Vol.30 (1989), p.38

40. J.R.MICHAEL, J. Microscopy, Vol.160(1990), (1), p.41

41. E.J.RAPPERPORT, Advances in electronics and electron physics, (1969), p.6

42. A.D.ROMIG, Analysis electron microscopy (1987), p.200

43. A.D.ROMIG, Metall. trans. Vol.19A(1988), p.35

44. J.G.LEGOUX, L.SALVO, H.RIBES, G.L'ESPERANCE AND M.SUERY, Interfaces in Metal-Ceramics Composites, Edited by R.Y.Lin and R.J.Arsinault (1990), p.187

45. M.VOLGELSANG, R.J. ARSENAULT AND R.M.FISHER, Met. Trans 17A (1986), p.379

46. D.J.LLOYD, Research Report (1989) Alcan International Limited Kingston Reseauch and Development Centre

47. A.LEVY AND J.M.PAPAZIAN, Metal and Ceramic Matrix Composites, Edited by R.B.Bhagat (1990), p.319

48. A.J.PORTER, R.C.ECOB AND R.A.RICKS, J. of Microscopy, vol.129 (1983), p.327

49. J.W.STEEDS, Introduction to Analytical Electron Microscopy, Edited by John, J.Hren, J.I.Goldstein, David C. Joy (1979), New York

50. S.J.ROZEVELD, Proceedings of ICEM-XII, Electron Microscopy, vol.2, (1990), Edited by L.D.Peachey and D.B.Williams, p.502

51. R.C.ECOB, M.P.SHAW AND A.J.PORTER, Phil. Mag. A44 (1981), p.1133

52. P. HIRSCH, Electron Microscopy of Thin Crystal, (1967) New York

53. M.M.J.TREACY, Philosophical Magizine A (1985), vol.51 No.3, p.389-417

54. P.M.JONES, G.M.RACKHAM AND J.W.STEEDS, Proc, E. Sic. Lond. A. 354 (1977), p.197

55. E.G.BITHELL AND W.M.STOBBS, Journal of Microscopy, vol. 153 (1989), p.39

56. J.D.ESHELBY, Pro. of the Royal soc. of London Series A. vol.241 (1957), p.376

57. Y. TAKEO AND M. TAYA, Trans. ASME (1985) 52, p.806

58. C. TEODOSIU, H. RIBES AND M. SUERY, Pro. of International conferece, RISϕ (1988), p.485

59. L.M. DIGNARD-BAILY, T.F. MALIS, J.D. BOYD, J.D. EMBURY, Advanced structural materials, CIM Proceedings, 9(1988), p.87

60. S. BRUSETHAUG, O. REISO, W. RUCH, Proc. of Fabrication of Particulates Reinforced Metal Composites(1990), Montréal, edited by J.Masounave and F.G.Hamel, p.173

61. T.M. OSMAN, J.J. LEWANDOWSKI, W.H. HUNT JR., Proc. of Fabrication of Particulates Reinforced Metal Composites(1990), Montréal, edited by J.Masounave and F.G.Hamel, p.209

62. D.L. DAVIDSON, Metall. Trans. A, vol.22(1991), p.113

63. R.J. ARSENAULT, N. SHI, C.R. FENG AND L. WANG, Mater. Sci. and Eng., A, vol.131(1991), p.55-68

64. J. LLORCA, A. NEEDLEMAN AND S. SURESH, Acta Metall. Mater. vol.39, No.10(1991), p.2317

65. T. SHEPPARD, N.C. PARSON AND M.A. ZAIDI, Metal Sci. vol.17, No.10(1983), p.481

66. T. SHEPPARD, M.G. TUTCHER, Metal Sci. vol.14, No.12(1980), p.579

67. D.L. MCDANELS, Metall. Trans. A, vol.16, No.6(1985), p.1105

68. Y. BRECHET, J.D. EMBURY, S. TAO, L. LUO, Acta Metall. Mater. vol.39, No.8(1991), p.1781

69. S.B. WU, R.J. ARSENAULT, Mater. Sci. and Eng. A, vol.138(1991), p.227

70. W.S. MILLER AND F.J. HUMPHREYS, Scripta Metall., vol.25(1991), p.33

71. P. MUMMERY, B. DERBY, Mater. Sci. and Eng. A, vol.135(1991), p.221

72. S.H. GOODS, L.M. BROWN, Acta Metall., vol.27(1979), p.1--15

73. J. GURLAND, Acta Metall., vol.20(1972), p.735

74. T.C. LINDLEY, G. OATES AND C.E. RICHARDS, Acta Metall., vol.18(1970), p.1127

75. V.C. NARDONE, K.M. PREWO, Scripta Metall., vol.20(1986), p.43

76. C.P.YOU, A.W. THOMPSON AND I.M. BERNSTEIN, Scripta Metall., vol.21(1987), p.181

77. B. ROEBUCK, J. of Mater. Sci. Letters, vol.6(1987), p.1138

78. F.J. HUMPHREYS, Proc. 9th. RISΦ, Denmark(1988), p.51

79. R.J. ARSENAULT, Proc. 9th. RISΦ, Denmark(1988), p.279

80. D.J. LLOYD, Acta Metall. Mater. vol.39, No.2(1991), p.59

81. Y. FLOM, R.J. ARSENAULT, Acta Metall. Mater. vol.37, No.9(1989), p.2413

82. W.J. CLEGG, Acta Metall. Mater. vol.36, No.8(1988), p.2141

83. T. CHRISTMAN, A. NEEDLEMAN, S. SURESH, Acta Metall. Mater. vol.37, No.11(1989), p.3029

84. M. MANOHARAN, J.J. LEWANDOWSKI, Acta Metall. Mater., vol.38, No.3(1990), p.489

85. S.V. KAMAT, J.P. HIRTH, R. MEHRABIAN, Acta Metall. Mater. vol.37, No.3(1989), p.2395

86. H.J. MCQUEEN, E. EVANGELISTA, J. BOWLES, G. CRAWFORD, Metal Sci. vol.18, No.8(1984), p.395

87. M. TAYA, R.J. ARSENAULT, Scripta Metall., vol.21(1987), p.349

88. S. CARON, J. MASOUNAVE, Proc. of Fabrication of Particulates Reinforced Metal Composites(1990), Montréal, edited by J.Masounave and F.G.Hamel, p.79

89. C. MILLIERE, M. SUERY, Mater. Sci. and Tech. vol.4, No.1(1988), p.41

90. Y. FLOM, R.J. ARSENAULT, Mater. Sci. and Eng., vol.79, (1985), p.151

91. R.J. ARSENAULT, N. SHI, Mater. Sci. and Eng., vol.81, (1986), p.175

92. T.B. COX, J.R. LOW, JR., Metall. Trans., A, vol.5, No.6(1974), p.1457

93. B. DERBY, J.R. WALKER, Scripta Met. vol.22(1988), p.529

94. W.H. HUNT JR., O. RICHMOND, R.D. YOUNG, Proc. ICCM6, vol.2(1987), p.2.209

95. R.J. ARSENAULT, Scripta Met. vol.25(1991), p.2617

96. M. TAYA, K.E. LULAY, D.J. LLOYD, Acta Metall. Mater., vol.39, No.1(1991), p.73

97. O.D. SHERBY, J. WADSWORTH, Progress in Mater. Sci., vol.33(1989), p.169

98. T.G. NIEH, J. WADSWORTH, Mater. Sci. and Eng., A, vol.147, (1991), p.129

99. J. PILLING, Scripta Met. vol.23(1989), p.1375

100. M. MABUCHI, T. IMAI, J. of mater. Sci. Letters, vol.9(1990), p.761

101. G. L'ESPERANCE, T. IMAI, H. BANDE, in press

102. T.G. NIEH, J. WADSWORTH, T. IMAI, Scripta Met. vol.26(1992), p.703

103. M.W. MAHONEY, A.K. GHOSH, Metall. Trans., A, vol.18, No.4(1987), p.653

104. H. IWASAKI, S. HAYAMI, K. HIGASH, S. TANIMURA, Superplasticity in Metal, Ceramics, and Intermerallics, MRS Proc. ed. by M. Mayo et al. 196(1990), p.233

105. F.A. GIROT, L. ALBINGRE, J.M. QUENISSET, R. NASLAIN, J. of Metals, No.11(1987), p.18

106. Metal Handbook, A.S.M., 9th Edition, vol.2(1979)

107. J.G. LEGOUX, Ph.D. Thesis (1991)

108. P.B. PRANGNELL, W.M. STOBBS, Proc. 12th Symp. Mater. Sci. RISΦ, Denmark (1991), p.603

109. A. KELLY, N.H. MACMILLAN, Strong Solids, 3rd Edn. Oxford Sci. Publications, 1986

110. H.L. COX, BR. J. Appl. Phys., vol.3(1952), p.72

111. P.J. WITHERS, D.J. JENSEN, H. LILHOLT, W.M. Stobbs, Proc. ICCM6 vol.2(1987), p.255

112. J.J. LEWANDOWSKI, D.S. LIU, AND C. LIU, Scripta Metall. et Mater., vol.25(1991), p.21

113. L.M. BROWN, J.D. EMBURY, Proc. 3rd Int. Conf. on Strength of Metals and Alloys, London, (1973), p.164

114. Y. FLOM, R.J. ARSENAULT, Proc. ICCM6 vol.2(1987), p.189

115. M. ALMAS F.J. HUMPHREYS, Proc. ICSMA8, Finland, 1988

116. M.Y. WU, O.D. SHERBY, Acta Metall. vol.39, No.9(1988), p.3088

117. P.Y. LIN, Proc. ICCM VII, Beijing, vol.2(1989), p.110

118. S. LI, R.J. ARSENAULT, P. JENA, Proc, Conf. on cast reinforced metal matrix composites, Chicago, Il, (1988), edited by S.G.Fishman, A.K.Dhingna, p.33

119. T. STEPHENSON, Y. LE PETITCORPS, J.M. QUENISSET, Mater. Sci. Eng., vol.135A(1991), p.101

120. K.J. BRONDYKE, J. of Am. Ceram. Soc., vol.36, No.5(1953), p.171

121. K. PRABRIPUTALOONG, M.R. PIGGOTT, J. of Am. Ceram. Soc., vol.56, No.4(1973), p.184

122. V. LAURENT, D. CHATAIN, N. EUSTATHOPOULOS, Mater. Sci. Eng., vol.135A(1991), p.89

123. C. MARUMO, J. PASK, J. of Mater. Sci. vol.12(1977), p.223

124. N. SHI, B. WILNER, R.J. ARSENAULT, Acta Metall. vol.40, No.11(1992), p.2841

125. D.M. KNOWLES, J.E. KING, Mater. Sci. & Tech., vol.8, No.6(1992), p.500

126. W.D. JOHNSTON, I.G. GREENFIELD, Proc, Conf. on cast reinforced Metal matrix composites, Chicago, Il, (1988), edited by S.G.Fishman, A.K.Dhingna, p.335

127. Y. LE PETITCORPS, T. STEPHENSON, F. GIROT, R. NASLAIN, Proc, Conf. on cast reinforced metal matrix composites, Chicago, Il, (1988), edited by S.G.Fishman, A.K.Dhingna, p.67

128. D.J. LLOYD, 3rd Int. Conf. Comp. Interfaces (ICCI-III) ed: H. Ishida, Elsevier, NY(1990), p.359

129. D.O. KARLSEN, J.B. BORRADAILE, J. GJΦNNES, J. TAFTΦ, Proc. Conf. RISΦ, Denmark (1988), p.421

130. J.S. CHO, S.I. KWUN, Scripta Metall. et Mater., vol.27(1992), p.789

131. T.B. SHAFFER, Plenum Press Handsbooks of High Temperature Materials, 1964

132. A.H. NAKAGAWA, M.N. GUNGOR, Fundamental Relations between Microstructure and Mechanical Properties of MMCs, eds. P.K. Lian, 1990, p.127

133. J.PACHNER, Handbook of Numerical Analysis Applications, McGraw-Hill Book Company, 1980

134. G.J.C. CARPENTER, M. CHAREST, O.T. WOO, EMSA Bulletin May(1988), p.57

135. P.M. MUMMERY, B. DERBY, C.B. SCRUBY, Acta Metall. Mater., vol.41, No.5(1993), p.1431

136. Grain Boundary Structure and Kinetics, American Socciety for Metals, 1980, p.373

137. Deformation and Freacture Mechanics of Engineering Materials, Eds. R.W. Hertzberg, 1983, p.155

138. Metal Handbook A.S.M., 9th Edition, vol.12(1979)

139. Elementary Engineering Fracture Mechanics, by David Broek, fourth edition, 1987

140. J. BALIK AND P. LUKAC, Acta Metall. vol.41, No.5(1993), P.1447

141. J.M. ROBINSO AND M.P. SHAW, Mater. Sci. Eng. A159(1992), p.159

142. R.A. MULFORD AND U.F. KOCKS, Acta Metall., vol.27(1979), p.1125

143. G. L'ESPERANCE, M.H. LORETTO, W.T. ROBERTS, D. PRICE AND D.V. WILSON, Metall. Trans. A, vol.15(1984), p.913

144. P. HAHNER, Mater. Sci. Eng., A164(1993), p.23

145. HIROSHI FUJITA, T. TABATA, Acta Metall., vol.25(1977), p.793

146. Encyclopedia of Mater. Sci. and Eng., eds. R.W. Cahn, Supp. vol.1(1988), p.505

147. D.A. WEIRAUCH, JR., J. Mater. Res. 3(4), Aug(1988), p.729

148. D.J. LLOYD, Metal Matrix Composites, Prcessing, Microstructure and Properties, Risφ,(1991), p.81

149. K. GARDNER, R. GRIMES, Mater. Sci. and Eng., vol.13(1979), p.216

150. A. VAN DEN BEUKEL, U.F. KOCKS, Acta Metall., vol.30(1982), p.1027

151. Z.M. SUN, J.B. LI, Z.G. WANG AND W.J. LI, Acta Metall. vol.40, No.11 (1992), p.2961

152. T.A. KUNTZ, H.N.G. WADLEY AND D.R. BLACK, Metall. Trans. vol.24A(1993), p.1117

153. L.C. DAVIS AND J.E. ALLISON, Metall. Trans. vol.24A(1993), p.2487

ECOLE POLYTECHNIQUE DE MONTREAL
3 334 00201512 5